The physical structure of Magellanic Cloud H II regions

On the cover: a false-colour image of the giant Large Magellanic Cloud H II region 30 Doradus taken by the Wide Field and Planetary Camera 2 on board the Hubble Space Telescope. The main power source of this H II region is the incredibly rich stellar cluster R 136 seen slightly below the center of the image.

Rijksuniversiteit Groningen

The physical structure of Magellanic Cloud H II regions

Proefschrift

ter verkrijging van het doctoraat in de
Wiskunde en Natuurwetenschappen
aan de Rijksuniversiteit Groningen
op gezag van de
Rector Magnificus, dr. F. Zwarts,
in het openbaar te verdedigen op
maandag 16 september 2002
om 14:15 uur

door

Ronald Vermeij

geboren op 18 augustus 1971
te Velsen

Promotor:	Prof. dr. J.M. van der Hulst
Beoordelingscommissie:	Prof. dr. J.-P. Baluteau
	Prof. dr. R.C. Kennicutt Jr.
	Prof. dr. A.G.G.M. Tielens

Contents

Chapter 1

Introduction

The sites of the most recent formation of massive stars are quite easily identified by their prodigious emission in the red Hα line. These patches of red light come in all shapes and sizes, ranging from nebulae spanning a significant fraction of a spiral arm powered by rich OB associations, all the way down to small nebulae containing only a few ionizing stars. Commonly refered to as H II regions, the large body of ionized gas of which the starformation site is comprised provides us with a wealth of spectral information. The large number of spectral lines emitted by the ionized gas gives us valuable information about the local physical conditions, and it is therefore not surprising that H II regions have always been a favourite tool with which to study the interstellar medium (ISM). A famous example of an H II region is shown in Fig. 1.1.

The spectrum of an H II region can in the first place be used to constrain the physical structure of the nebula itself. This structure includes the variation in electron temperature and density through the nebula, but also its ionization structure. The distribution of the elements over the various ionization stages is directly related to the energy distribution of the local radiation field, which is a signature of the nature of the main ionizing sources of the nebula. In the case of very young H II regions, the ionizing stars can not be observed directly, so clues about the stellar content of the nebula can only be obtained by these indirect means. This is often the only way in which some information can be obtained about the high-mass end of the initial-mass function.

The most important piece of information provided by the spectra of H II regions, however, is the chemical composition of the local ISM. Knowledge of the gas-phase abundances is important for constraining the nucleosynthetic and starformation history of the host galaxy; the sequence of generations of stars formed in the past is traced by the gradual build-up of heavy metals such as oxygen, and clues about the rates at which various elements have been synthesized are given by heavy element-to-oxygen ratios such as N/O. Large-scale abundance variations such as the radial abundance gradients often encountered in spiral galaxies reflect the bulk hydrodynamical flow of gas through a galaxy. We refer to Henry & Worthey (1999) for a nice review on the subject.

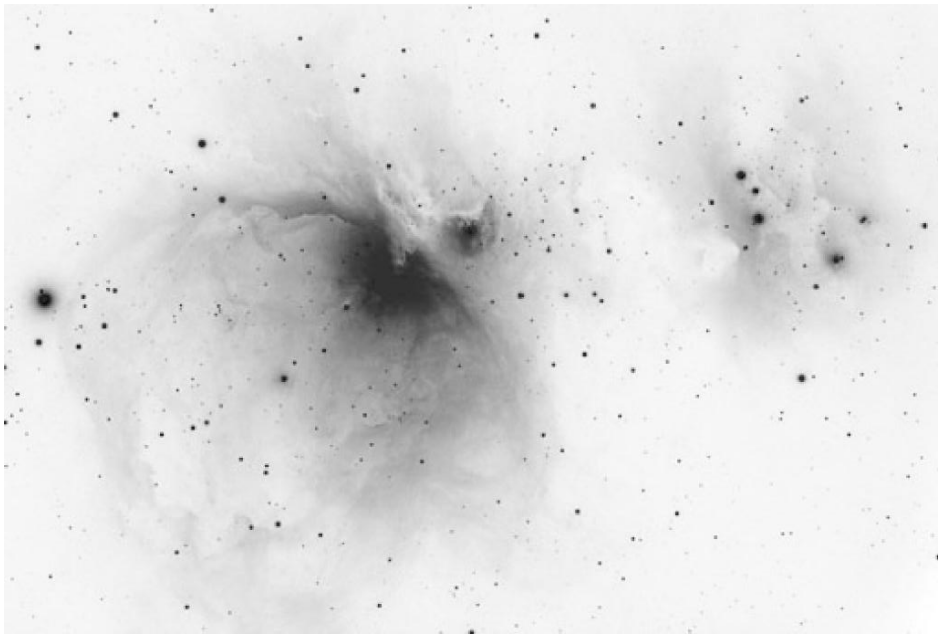

FIGURE 1.1— The most famous example of an H II region : the Orion nebula (M42).

1.1 The physics of starformation regions

The physical structure of an H II region mainly depends on three parameters. Possibly the most important of the three is the spectral-energy distribution (SED) of the main ionizing source(s) of the H II region; the ionization structure throughout the nebula is mostly determined by it. The second parameter, the ionization parameter, is also important for the ionization balance. This parameter ties together the local gas and photon density and is basically the ratio of ionizing photons to gas particles. The third important ingredient shaping the physics of an H II region is the chemical composition of the ionized gas, i.e. the metallicity. The metallicity regulates the cooling of the gas and hence determines the temperature structure of the nebula.

In this Section, a description of the basic physics of an H II region is given. Also, a sketch of the 'layout' of an H II region will be given that will serve as a template to be used throughout this thesis. For a very thorough discussion on the physics of photoionized astrophysical plasmas one should consult Osterbrock (1989).

1.1.1 Ionization structure

The dominant physical mechanism in setting up the ionization structure of an H II region is photoionization. With increasing distance from the ionizing source the radiation field steadily degrades, which leads to a more or less stratified ionization structure. We can divide this structure in roughly three parts or ionization zones, each with its own set of dominant ionic species. The general distribution of ions throughout an H II region is shown in Fig. 1.2.

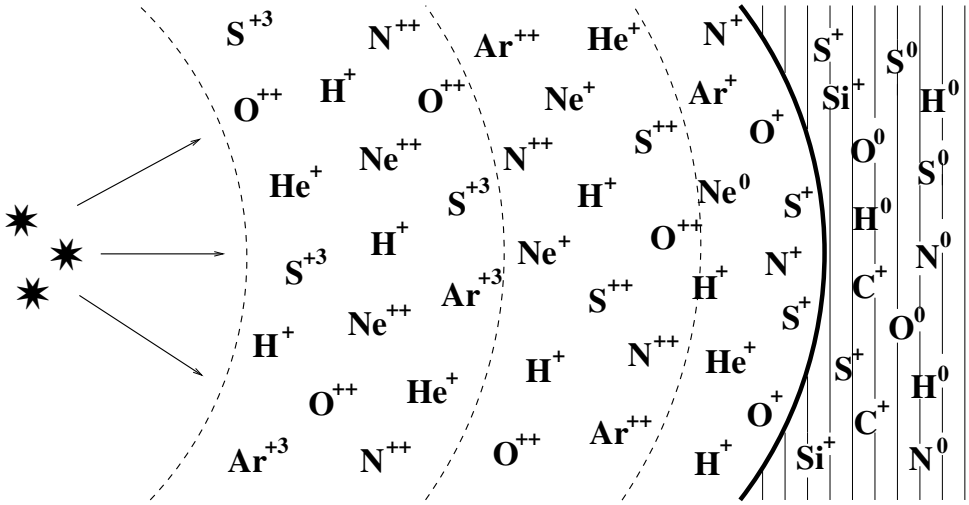

FIGURE 1.2— The ionization structure throughout an H II region. The rough boundaries of the three principal ionization zones inside an H II region are shown as dashed lines. The thick line designates the boundary of the H II region. The dashed area is the photodissociation region. The dominant ionic species in every zone are given.

Being the closest to the ionizing source, the core of the H II region is dominated by highly ionized species such as O^{++}, Ne^{++} and S^{+3}. These are also the most highly ionized species likely to be encountered in a regular H II region; not even the hottest main-sequence stars produce enough photons with energies in excess of 40 eV to give a significant amount of more highly ionized species. To give an idea of the energies involved, the ionization potential of O^{++} and He^{+} is $\sim$54 eV. For Ne^{++} and S^{+3} this is $\sim$41 eV and $\sim$48 eV, respectively.

Moving outwards, the photons with the highest energy become depleted, and a shift in the ionization balance occurs. The most important ions are now S^{++} and Ar^{++}. Some traces of O^{+} and Ne^{+} also appear, but the O^{++} ion is still dominant. The relevant ionization potentials are now in the order of 35 eV.

The most profound changes in the ionization structure occur near the edge of the H II region where the photon supply is nearly exhausted. Over a relatively small fraction of the total radius of the H II region, many ions that dominate the inner parts of the nebula recombine, and their dominant role is taken over by e.g. N^{+} and O^{+}. Helium that has thusfar been singly ionized now also appears in neutral form. When eventually the energy of the remaining photons drops below 13.6 eV, even hydrogen becomes fully neutral, and we have arrived at the outer boundary of the H II region. This boundary is refered to as the Strömgren radius.

At the interface of the H II region and the molecular cloud, we find the photodissociation region (PDR). Photon energies here are lower than the threshold 13.6 eV, and the photons are only energetic enough to dissociate small molecules and to ionize atomic species such as neutral sulfur. The dominating ions in the PDR are S^{+}, Si^{+} and C^{+}. It is also here in PDRs where large molecules such as Polycyclic Aromatic Hydrocarbons

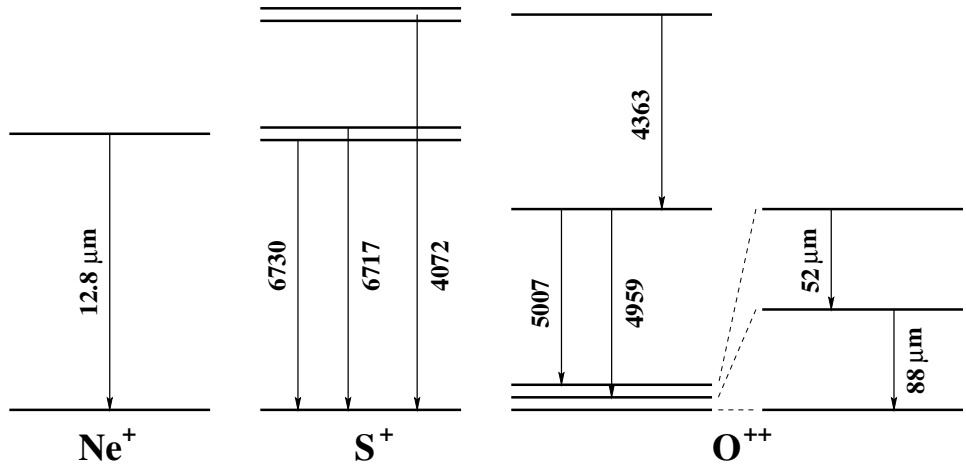

FIGURE 1.3— The three basic fine-structure level configurations of the ions usually found in H II regions. Shown are the configurations of Ne^{+}, S^{+} and O^{++}. The three low-lying levels in O^{++} are blown up for clarity.

(PAHs) are made to fluoresce.

In a real H II region the different ionization regimes are of course not so sharply defined; the different zones partially overlap and the transition between the different zones is smooth. Also, photoionization is not the only mechanism defining the ionization structure. Mechanisms such as charge-transfer reactions operate as well, especially in the low-ionization zone. This mechanism allows neutral oxygen to exist well inside the H II region despite its ionization potential of 13.6 eV. The presence of dust mixed in with the plasma also affects the ionization structure by absorbing some of the photons that would otherwise have ionized the gas.

1.1.2 Temperature structure

The local electron temperature in an H II region results from the two basic counteracting mechanisms of photoelectric heating and radiative cooling. Any excess energy of an ionizing photon is transfered to the released electron as kinetic energy, which is then distributed evenly over the electron gas through coulomb interactions. The electron gas loses this energy again through various radiative processes. This is either through direct means like free-free or recombination-line emission, or indirectly by collisional heating of dust which then emits this energy in the infrared.

By far the most effective radiative cooling mechanism is the one through fine-structure lines of heavy elements. These lines originate from low-lying energy levels in the ground state of ions, and the relative ease with which these lines are excited makes them an efficient 'sink' of energy. The efficiency with which a particular ion contributes to the cooling of the gas is directly related to its ground state level-configuration. Two-level ions such as S^{+3} and Ne^{+} or five-level ions such as O^{+} and S^{+} contribute relatively little to the total cooling. Five-level ions such as O^{++} on the other hand contribute much to the cooling rate. The crucial difference between the two groups of ions is the

TABLE 1.1— The most important diagnostic line ratios.

Line ratio	Measures	Line ratio	Measures
$(3727\,\text{Å} + 3730\,\text{Å})/(7320\,\text{Å} + 7330\,\text{Å})$	T_e [O II]	$3727\,\text{Å} / 3730\,\text{Å}$	n_e [O II]
$(5007\,\text{Å} + 4959\,\text{Å})/ 4363\,\text{Å}$	T_e [O III]	$52\,\mu\text{m} / 88\,\mu\text{m}$	n_e [O III]
$(5007\,\text{Å} + 4959\,\text{Å})/ 52\,\mu\text{m}$	T_e [O III]		
$(6717\,\text{Å} + 6730\,\text{Å})/(4068\,\text{Å} + 4076\,\text{Å})$	T_e [S II]	$6717\,\text{Å} / 6730\,\text{Å}$	n_e [S II]
$(9068\,\text{Å} + 9532\,\text{Å})/ 6312\,\text{Å}$	T_e [S III]	$18\,\mu\text{m} / 34\,\mu\text{m}$	n_e [S III]
$(9068\,\text{Å} + 9532\,\text{Å})/ 18\,\mu\text{m}$	T_e [S III]		

presence in the latter of a low-lying triplet of energy levels. The level configurations relevant for the ions commonly found in H II regions are shown in Fig. 1.3.

The fact that heavy elements are the major coolants in the nebula implies that the metallicity of the gas is also important for the cooling rate. That the metallicity of the gas as measured through its oxygen abundance is indeed one of the major factors determining the overall thermal balance becomes clear if we look at H II regions in environments with different metallicities. Going from our own Galaxy to the Large Magellanic Cloud and further to very low-metallicity galaxies such as I Zw 18, we see the global electron temperature increase from 9000 K and 10 000 K to $\sim$16 000 K for the lowest metallicities.

It is clear that the cooling efficiency of a plasma cell is determined by both the metallicity of the gas and the ionization structure. The temperature of the electron gas is therefore closely coupled to the local ionization structure, which results in a stratification of the electron temperature through the H II region. Analogous to the ionization structure, this temperature profile can be divided into zones that roughly coincide with the three ionization zones introduced in Sect. 1.1.1. The fact that oxygen is the most abundant elements after helium, and that its main ionization stage is O^{++} makes oxygen the main coolant in an H II region.

1.2 The diagnostic tools

Spectral lines form the raw material from which the basic nebular parameters are derived. The main diagnostic tool consists of line ratios, and it is therefore not surprising that the analysis methods are firmly rooted in atomic physics. For analysis purposes, a distinction should be made between recombination lines and fine-structure lines.

1.2.1 Properties of the electron gas

The basic properties of the electron gas, i. e. its density and temperature, are determined from ratios of fine-structure lines. The diagnostic power of line ratios stems from the fact that the differences in strength of the lines used in the analysis reflect the fractional distribution over the atomic levels of the particular ion. The fine-structure lines are mainly excited through collisions with electrons, so this distribution is determined by the properties of the electron gas. Both density and temperature have their own set of

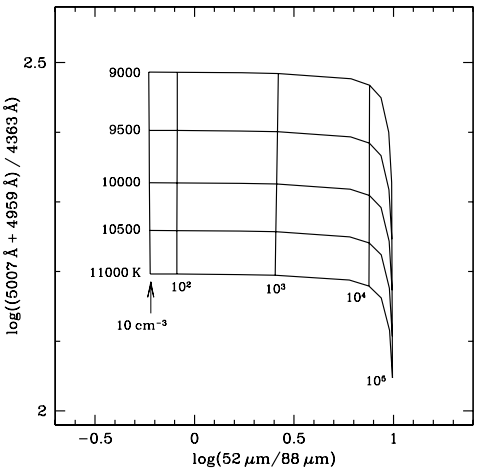

FIGURE 1.4— The diagnostic diagram for O^{++}. The electron density increases from left to right, the temperature from top to bottom. Note that the temperature-sensitive line ratio is nearly independent from the electron density and vice versa.

diagnostic line ratios. Examples of these are the [O III] 5007 Å /[O III] 4363 Å ratio and [S II] 6717 Å /[S II] 6730 Å ratio for the temperature and density, respectively. Whether the ratio is sensitive to either the temperature or the density is determined by the energy configuration of the relevant atomic levels. In Fig. 1.3 some examples of level configurations are given together with important fine-structure lines. A collection of diagnostic line ratios is given in Table 1.1.

In order to obtain the temperature or density from a line ratio, the fractional distribution over the various atomic levels corresponding to the measured line ratio has to be determined. The relative populations of the levels are calculated taking into account the mechanisms of collisional excitation and de-excitation by electrons, and radiative transitions, using either five or two levels depending on the ion. These are calculated by solving in an iterative manner for every level i the following set of coupled, detailed balance equations

$$N_i \sum_{j<i}(A_{ij} + n_e q_{ij}) + N_i \sum_{j>i} n_e q_{ij} = \sum_{j>i}(N_j A_{ji} + N_j n_e q_{ji}) + \sum_{j<i} N_j n_e q_{ji}, \qquad (1.1)$$

with n_e the electron density, A_{ij} the radiative transition rate, and q the temperature-dependent collisional (de-)excitation rate. Note that a reasonable starting value for either the electron density or temperature must be given. The closure relation is

$$\sum_i N_i = 1. \qquad (1.2)$$

This machinery can be applied to all the important ions in an H II region. It is therefore possible, with enough spectral information, to trace the run of the density and temperature throughout the nebula. A diagnostic diagram showing the power of these analysis tools is shown in Fig. 1.4 for O^{++}.

1.2.2 Elemental abundances

The derivation of elemental abundances is in general a two-step process. In the first step, the ionic fractions of an element are determined from ionic lines and summed.

More often then not, some ionization stages are missing from this sum, and for these missing ionization stages the sum has to be corrected in a second step. The end result is the full elemental abundance. The relevant astrophysical quantity is the particle density of an element relative to hydrogen, so in the derivation of the ionic fractions, both fine-structure lines as well as hydrogen recombination lines are used.

Given an electron density and, more importantly, an electron temperature, the ionic fraction X^+/H^+ can be derived from a fine-structure line with the following equation

$$\frac{X^+}{H^+} = \left[\frac{I_\lambda}{I_{H^+}}\right]\left[\frac{\epsilon\left(n_e, T_e\right)}{A_\lambda E_\lambda}\right]\left[\frac{n_e}{F\left(n_e, T_e\right)}\right], \tag{1.3}$$

with I_λ / I_{H^+} the line flux relative to a hydrogen recombination line, A_λ and E_λ the radiative rate of the transition from which the line originates and the energy of the photon, respectively, $\epsilon\left(n_e, T_e\right)$ the emissivity of the chosen hydrogen recombination line, n_e and T_e the electron density and temperature, and $F\left(n_e, T_e\right)$ the level-distribution function for the relevant atomic level as determined from Eqns. 1.1 and 1.2. This procedure is repeated for every ionic stage of an element after which the results are summed.

For elements such as oxygen of which every important ionization stage is observed, no correction of the sum abundance for missing ionization stages is needed. Elements such as argon and sulfur, however, are not fully represented in the optical so for these elements a correction is required. The factors used in this process are known as Ionization Correction Factors (ICFs).

1.3 Thesis outline

The importance of H II regions as an astrophysical tool is evident. However, the reliability of an H II region as a probe of the local gas-phase abundances is closely coupled to how well its structure is known. Despite a long history of studying the chemical composition of all kinds of photoionized plasmas, some very basic problems are still not solved. Among these are the need to correct for missing ionization stages of an element and, more seriously, the problem of temperature fluctuations in the plasma. On top of that, knowledge of the variation of the electron temperature and density through the ionization structure of an H II is often patchy. Any one of these problems has a severe impact on the reliability of the H II region as a probe and has serious consequences for the derived elemental abundances.

Some of these problems can be alleviated if not completely solved by combining spectral information from more spectral regimes than only the optical. Expanding the data base into these regimes gives access to otherwise unobservable ionic stages of important elements and makes it possible to study the physical structure of the H II region more thoroughly. Both these advantages lead to a more accurate determination of the chemical composition of the gas.

Two themes can be distinguished in this thesis. The first goal of the research presented in this thesis is to give a critical evaluation of the applicability and reliability of the diagnostic tools commonly used in nebular studies using a well-chosen sample of H II regions. The study is based on a spectroscopic data set covering both the optical regime and the infrared. The infrared data have been obtained using the spectrometers on board the *Infrared Space Observatory* (ISO, Kessler et al. 1996) as part of a

Guaranteed Time program on H II regions in Local Group Galaxies. In this thesis, the attention is focused on the Magellanic Clouds.

There are several reasons why the Magellanic Clouds are prime candidates for such studies. First of all, due to their close proximity, starformation sites can be studied in considerable detail. This makes it possible to study spatial variations in the structure of the H II regions. Knowledge of how various nebular diagnostics behave with spatial variations of nebular parameters becomes relevant in situations where the starformation sites are not spatially resolved. Secondly, the Magellanic Clouds are highly elevated above the Galactic plane. This makes a multi-wavelength study of the starformation regions in these galaxies possible, in contrast to studies in the Galactic plane where extinction limits the use of the optical spectral regime. This same problem also confines the study of Galactic H II regions to the nebulae in our close neighbourhood, whereas in the case of the Magellanic Clouds starformation regions can be studied on a galaxy-wide scale. Lastly, the Magellanic Clouds with their low-metallicity environment are of course themselves interesting in the context of nucleosynthetic and starformation history. The second goal of this thesis therefore is to present an improved determination of the chemical composition of the Magellanic Clouds.

The layout of the thesis is as follows. In chapter 2, the data used in this thesis are presented. The sample objects are described and a discussion on the reduction of the data is given. Also discussed are the main sources of uncertainty in the data. The analysis results from this data set are given in chapter 3. A case study of 30 Doradus based on optical longslit spectra covering the core of the nebula is given in chapter 4. Chapter 5 deals with the tools used to diagnose the stellar content of an H II region. The effects of both the stellar and nebular metallicity on the ionization structure of the H II region and, subsequently, the nebular spectrum is investigated, and the consequences for the analysis in terms of its stellar content are discussed. A slight detour from the main subject of this thesis is made in chapter 6. Using data obtained with the ISOPHOT (Lemke et al. 1996) instrument on board ISO, the properties of PAHs in the low-metallicity environment of the LMC are investigated and compared with those of PAHs in Galactic H II regions. Finally, a summary of this thesis and some thoughts about future developments are given in chapter 7.

References

Kessler, M.F., Steinz, J.A., Anderegg, M.E. et al. 1996, A&A **315**, L27
Henry, R.B.C., Worthey, G. 1999, PASP **111**, 919
Lemke, D., Klaas, U., Abolins, J. et al. 1996, A&A **315**, L64
Osterbrock, D.E. 1989, *Astrophysics of Gaseous Nebulae and Active Galactic Nuclei*, publ. University Science Books

Chapter 2

The physical structure of Magellanic Cloud H II regions : the data set

We present infrared and optical spectroscopic data for 11 H II regions and one Supernova Remnant in the Large and Small Magellanic Cloud. The infrared data have been obtained with the Short Wavelength Spectrometer and Long Wavelength Spectrometer on board the *Infrared Space Observatory* as part of a Guaranteed Time Program on H II regions in Local Group Galaxies. Aim of this project is to give a new and improved analysis of the physical structure of the sample H II regions by combining as much spectral data as possible. A detailed account is given here of the reduction process, and the quality and reliability of the presented fluxes are discussed.

2.1 Introduction

With a plethora of emission lines, from the far ultraviolet all the way to the far infrared, H II regions are a very rich source of spectral information. The huge amount of information contained in the emission lines makes these regions therefore ideally suited for investigating the properties of the local gas-phase interstellar medium (ISM). In principle, it is possible to deduce many of the important physical characteristics of an H II region from its spectrum.

Among such characteristics are the temperature and density of the electron gas, which can be derived from taking ratios of line fluxes. Well known examples of these are the often employed optical [O III] 5007 Å / 4363 Å and [S II] 6717 Å / 6730 Å line ratios for the electron temperature and density, respectively. Ratios from spectral lines emitted by different ionic species of the same element constrain the ionization structure inside the H II region. The ionization structure throughout the region reflects the hardness and density of the local radiation field which is a signature of the number and the mass of the major ionizing sources in the H II region. Given a set of electron temperatures and densities, the chemical composition of the gas can be derived from the spectral

lines. The abundances thus determined provide clues for the local nucleosynthetic and star-formation history.

The analysis of an H II region in terms of the physical structure, stellar content and chemical composition is, however, not without difficulties. The derivation of the physical structure is often limited to the electron temperature and density as found with the 'classical' ratios of lines from O^{++} and S^{+}, but by limiting the analysis to these lines, one is actually probing only a part of the total emitting volume of the H II region. This is the result of the stratified nature of the ion distribution within the region. The electron properties found are taken to be representative of the entire nebula, but the existence of density variations and temperature gradients throughout the nebula is not ruled out (the t^2 problem, Peimbert 1967). Gradients and fluctuations in the temperature structure are immediately reflected in the abundances one derives. The abundances are underestimated because of the tendency of temperature fluctuations to bias the temperatures found towards higher values.

The accurate determination of elemental abundances is also hampered by the limited number of ionization stages one can observe for a particular element. For many astrophysically important elements, one often has to make corrections for unseen ionization stages using Ionization Correction Factors (ICFs) in order to derive the total elemental abundance. Many prescriptions for these ICFs have appeared over the last thirty years, either based on coincidences in ionization potentials of various ions (Peimbert & Costero 1969) or on photoionization models (e.g. Grandi & Hawley 1978; Mathis & Rosa 1991). The most difficult element in this respect proved to be sulfur (Natta, Panagia & Preite-Martinez 1980; Garnett 1989).

Many different diagnostics have been proposed for constraining the effective temperature of the ionizing source of an H II region. Helium recombination line diagnostics like He I 5875/Hβ are robust but insensitive for T_* higher than 39000 K (Kennicutt et al. 2000). Single-element forbidden-line diagnostics, like [O III] 5007/Hβ and [Ne III] 3869/Hβ, as well as composite diagnostics, like the η' parameter (Vilchez & Pagel 1988), are also often used. These diagnostics, however, can be sensitive to abundance effects and to variations in the ionization parameter, especially in nebulae that are spatially resolved.

To address the problems described above, one needs to use as many spectral lines as possible. By extending the data base from the optical into other spectral regions, such as the infrared, many of the problems can at least be alleviated. The inclusion of more spectral lines makes it possible to derive electron temperatures and densities for more different ions, giving a better coverage of the temperature profile of the nebula. A larger spectral coverage gives us access to more different, otherwise unobservable, ionic species. This makes a direct calculation of the elemental abundance possible without having to resort to ICFs. It also puts more constraints on the ionization structure of the nebula and, therefore, on the nature of the ionizing sources.

For this purpose a large set of new optical and infrared spectroscopic data has been obtained of several bright H II regions in the Magellanic Clouds. The infrared spectra were taken with the *Short Wavelength Spectrometer* (SWS) and *Long Wavelength Spectrometer* (LWS) on board the *Infrared Space Observatory* (ISO, Kessler et al. 1996), as part of a comprehensive ISO Guaranteed Time Program on H II regions in Local Group Galaxies.

TABLE 2.1— The objects contained in the sample. Given are the coordinates of the ISO-SWS and ISO-LWS pointings. The designations, except for 30 Doradus, are those of Henize (1956).

Object	SWS Coordinates (J2000.0)			LWS Coordinates (J2000.0)		
	RA (h m s)	δ (^{o} $'$ $''$)	Date	RA (h m s)	δ (^{o} $'$ $''$)	Date
N66	0 59 03.7	−72 10 39.9	01-Apr-1996	0 59 08.0	−72 10 26	01-Apr-1996
N81	1 09 13.6	−73 11 41.1	14-May-1996	1 09 09.1	−73 12 07	22-Apr-1996
N88A	1 24 08.1	−73 09 02.5	14-May-1996	1 24 09.4	−73 09 16	22-Apr-1996
N79A	4 51 47.4	−69 23 47.6	10-Sep-1996	4 51 49.3	−69 24 36	29-Apr-1996
N4A	4 52 08.4	−66 55 23.4	29-Apr-1996	4 52 06.4	−66 55 27	29-Apr-1996
N83B	4 54 25.2	−69 10 59.8	14-May-1996	4 54 25.2	−69 10 59	01-Nov-1997
N11A	4 57 16.2	−66 23 18.3	22-Apr-1996	4 56 48.3	−66 24 11	17-Jul-1997
N159-5	5 40 02.4	−69 44 33.4	10-Jul-1996	5 40 04.2	−69 44 42	06-May-1996
N157B	5 37 51.6	−69 10 23.1	14-May-1996	5 37 51.8	−69 10 22	29-Apr-1996
30 Dor#1	5 38 33.5	−69 06 27.1	05-Dec-1997	5 38 33.5	−69 06 27	29-Apr-1996
30 Dor#2	5 38 35.5	−69 05 41.2	13-Apr-1996	5 38 43.8	−69 05 17	29-Apr-1996
30 Dor#3	5 38 46.0	−69 05 07.9	06-May-1996	5 38 45.8	−69 05 11	29-Apr-1996
30 Dor#4	5 38 54.2	−69 05 15.3	05-Aug-1997	5 38 54.2	−69 05 11	29-Apr-1996
N160A1	5 39 43.3	−69 38 51.4	10-Jul-1996	5 39 44.2	−69 38 42	06-May-1996
N160A2	5 39 46.1	−69 38 36.6	10-Jul-1996	5 39 44.2	−69 38 42	06-May-1996

The Magellanic Clouds form excellent targets for such studies. With their small distance of 55 kpc (LMC, e.g. Feast 1999) and 65 kpc (SMC, e.g. Kovács 2000), star formation and starforming regions can be studied in considerable detail, down to the scale of individual stars. Given their high elevation above the Galactic plane, the problem of extinction towards the Magellanic Clouds is less acute than for Galactic H II regions. The study of Galactic H II regions is often limited to the local neighbourhood because of the extinction in the Galactic plane, whereas in the Magellanic Clouds H II regions can be studied on a galaxy wide scale.

In this chapter, the data are presented. The data set comprises optical driftscan and stationary longslit spectra, as well as infrared spectra obtained with ISO. The layout is as follows. Section 2.2 gives an overview of the objects in the sample and their environment, section 2.3 gives a detailed account of the reduction of the optical and infrared spectra, and section 2.4 discusses the quality and reliability of the spectral data presented. A summary is given in section 2.5.

2.2 Sample objects

The selection of the sample objects had to be done with special consideration for the instruments used to observe them, and the use of the ISO satellite had in this respect the most serious impact on our choice of objects. The three main selection criteria for most of the objects in the sample were that they are bright enough to be detectable with ISO, that the geometry is relatively simple, and that the objects are small enough to fit into the four different ISO-SWS apertures.

Consequently, many of the objects in the sample are bright, highly excited compact blobs (HEBs), of which several have been discovered in the Magellanic Clouds in the

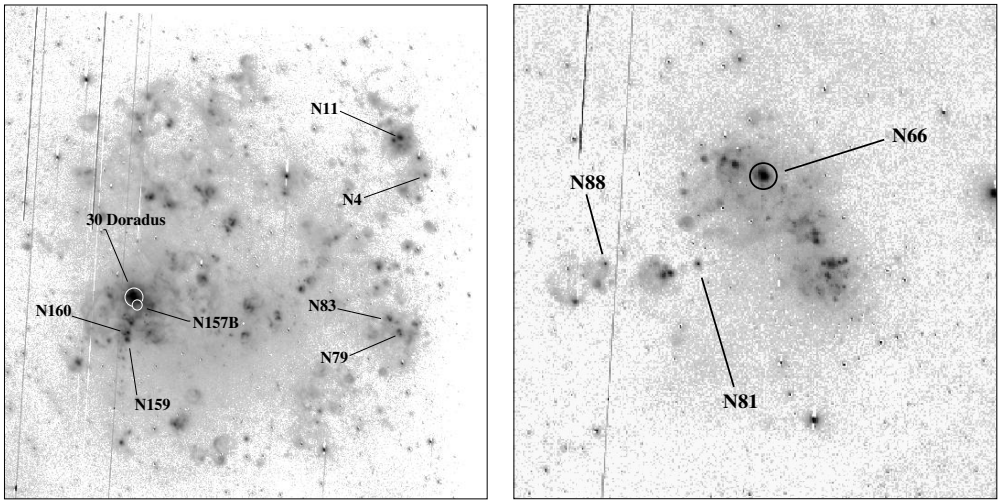

FIGURE 2.1— The Magellanic Clouds in Hα. The LMC is left and the SMC is right. Indicated are the H II regions in the sample. North is up and East is left. The images were obtained with the Parking Lot Camera (Kennicutt et al. 1995; Bothun & Thompson 1988).

last two decades (e.g. Heydari-Malayeri & Testor 1985). These HEBs are usually only a few arcseconds across, can have a rather large dust content (N88A, Kurt et al. 1999) and are small enough to be ionized by only a few massive stars (N81, Heydari-Malayeri et al. 1999c). These HEBs are thought to be the first step in the evolution from an ultracompact H II region towards more extended structures.

The objects observed in this study are given in Table 2.1 together with the ISO-SWS/LWS pointing coordinates and observation dates. The distribution of the sample H II regions across the Magellanic Clouds can be seen in Fig. 2.1. A short description of the sample objects, highlighting some of their features, is given below.

2.2.1 LMC : 30 Doradus

The giant H II region 30 Doradus (N157A) is the most conspicuous object in the Large Magellanic Cloud. Extending about $15'$ across the sky, the object is the closest extragalactic giant H II region. This makes 30 Dor very interesting and the nebula has therefore been the object of many different studies.

The morphology of 30 Dor is very complex, with filaments, bubbles and shells. A thorough kinematic study by Chu & Kennicutt (1994) revealed the presence of networks of high-velocity expanding shells in the inner parts of 30 Doradus. Hot bubbles inside the nebula make 30 Dor a strong diffuse X-ray emitter (e.g. Wang 1999).

Spectrophotometric studies of the region have been performed by e.g. Rosa & Mathis (1987) and Mathis, Chu & Peterson (1985). The spectra, taken at various locations, not only in the inner core of 30 Dor but also in the more diffuse outer parts, have shown the nebula to be chemically homogeneous. The ionization structure of the inner part of 30 Doradus has been investigated using narrow-band WFPC2 images in the Hα,

[O III] 5007 Å and the [S II] (6717+6731) Å lines (Scowen et al. 1998).

Studies of the stellar content of 30 Doradus have shown the nebula to be incredibly rich in massive stars (e.g. Parker & Garmany 1993; Hunter et al. 1995). Within the massive star cluster R136 at the core of 30 Doradus, about 39 O3 stars have been found, of which some are supergiants (Massey & Hunter 1998). At least five distinct epochs of consecutive star formation have been identified in 30 Doradus (Walborn & Blades 1997), of which the youngest is still ongoing. The detection of water maser activity near R136 betrays the presence of recently formed stars (Whiteoak et al. 1983; Van Loon & Zijlstra 2001). In this work, the pointings in 30 Doradus were chosen in a roughly semi-circular pattern centered on the massive central cluster R 136 (see Figure 2.2, upper left).

2.2.2 LMC : N4A

The object N4A is located a few arcminutes southwest from N11, and is the brighter of the two parts making up N4. The N4 region has been studied in detail by Heydari-Malayeri & Lecavalier des Etangs (1994). Their study of the morphology of N4A shows the presence of a bright compact structure embedded in fainter nebulosity extending towards the west (see Fig. 2.2, lower right). Associated with N4A is a molecular complex of which a sheet is located in front of the H II region. In a recent study of N4 with ISOCAM, the presence of emission from Polycyclic Aromatic Hydrocarbons (PAHs) and Very Small Grains (VSGs) was detected (Contursi et al. 1998).

2.2.3 LMC : N11A

Being the second largest H II region in the LMC after 30 Doradus, N11 lies quite isolated at about 4^o from the LMC bar. The region consists of several parts (N11 A-L, Henize 1956), of which N11B is the most prominent. Many rich stellar associations are located in the complex, like LH9 and LH10 (Lucke & Hodge 1970). The sample object N11A (Fig. 2.2, lower left), a blob of $\sim 12''$ in diameter, is located $1'$ east from N11B. The blob is highly excited, showing an [O III]/Hβ ratio in excess of 4 (Heydari-Malayeri & Testor 1983, present work), and is not heavily extincted. A study by Rosado et al. (1996) shows no evidence of disturbed kinematics inside N11A. An HST study of N11A revealed the presence of a tight cluster of stars in the center of the object (Heydari-Malayeri et al. 2001b).

2.2.4 LMC : N79A and N83B

The H II regions N79 and N83 in the LMC (Figure 2.3, upper left and right, respectively) both lie in the western part of the bar. With only the occasional appearance in larger samples for chemical abundance studies (e.g. Pagel et al. 1978), not much attention has been paid to either of these objects. A study of N83B by Heydari-Malayeri, Van Drom & Leisy (1990) has shown the presence of a very compact blob at the eastern part of the nebula (N83B-1). The morphological study of N83B has been extended using HST (Heydari-Malayeri et al. 2001a), resulting in two new compact blobs being added to the collection (N83B-2 and N83B-3). Both N83B-1 and N83B-2 are clearly visible in the upper right panel of Figure 2.3.

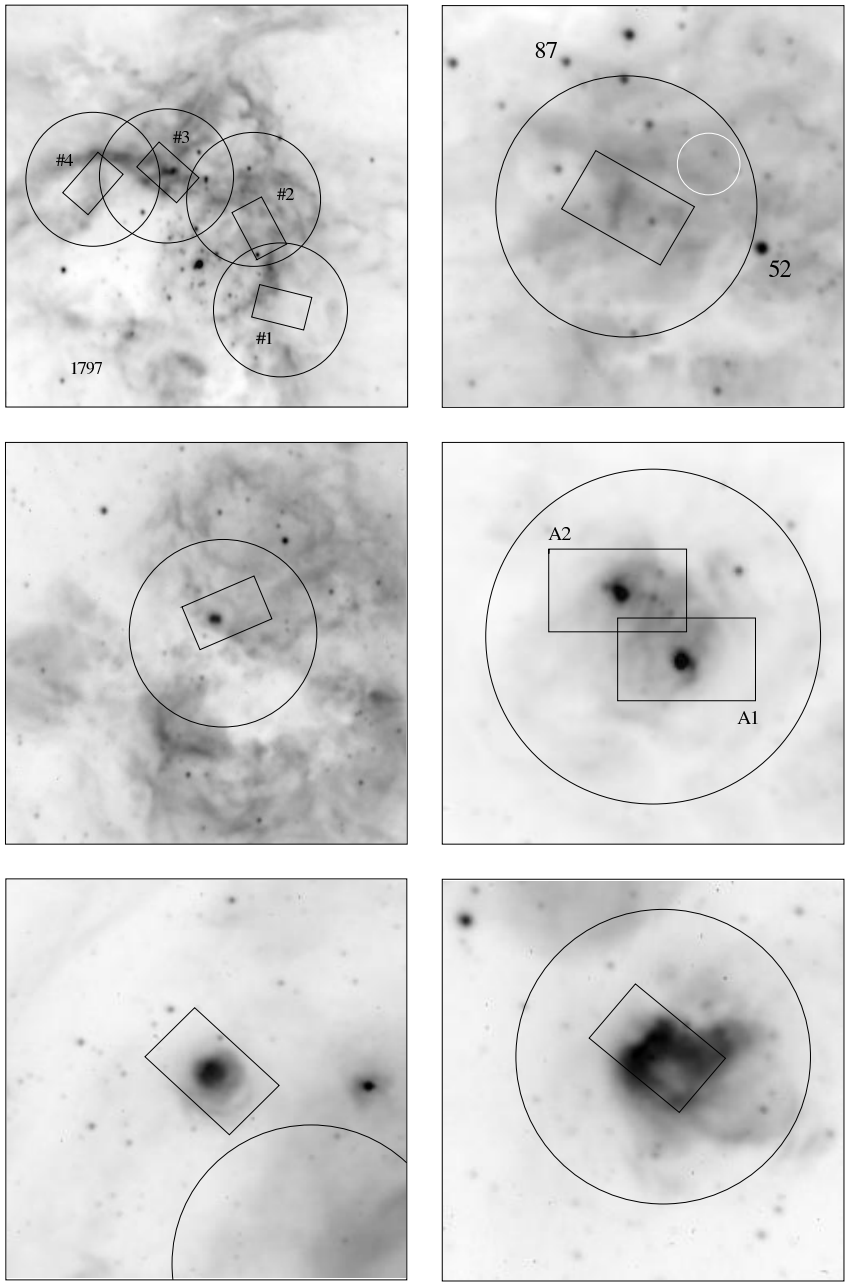

FIGURE 2.2— The LMC objects 30 Doradus (*upper left*), N157B (*upper right*), N159-5 (*middle left*), N160A (*middle right*), N11A (*lower left*) and N4A (*lower right*) in Hα. Shown are the ISO-SWS and ISO-LWS pointings in these objects. The SWS aperture plotted is $20'' \times 33''$ (band 4). The star 1797 in 30 Doradus is from Parker (1993). The stars 52 and 87 in N157B are from Shield & Testor (1992). The white circle shows the position of the X-ray source in N157B. North is up and East is left.

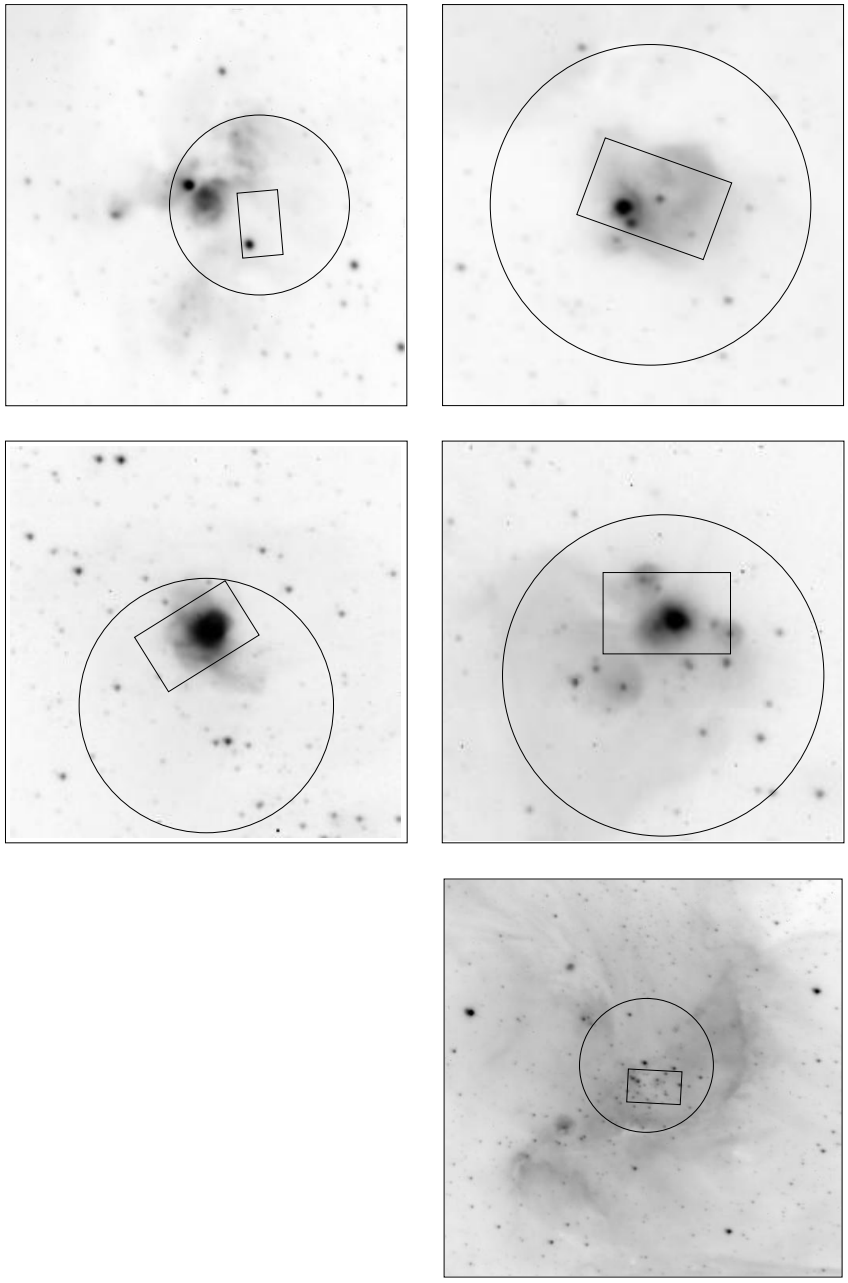

FIGURE 2.3— The LMC objects N79A (*upper left*) and N83B (*upper right*) and the SMC objects N81 (*middle left*), N88A (*middle right*) and N66 (*lower right*) in Hα. Shown are the ISO-SWS and ISO-LWS pointings in these objects. The SWS aperture plotted is $20'' \times 33''$ (band 4). North is up and East is left.

2.2.5 LMC : N157B

The object N157B, lying approximately 6′ south-west from 30 Doradus, is an interesting mix of an H II region and a supernova remnant (SNR). The complex was first recognized to contain an SNR through its Crab-like radio spectrum (Le Marne 1968; Mills et al. 1978), which was later confirmed by others (e.g. Dickel et al. 1994). The discovery of a bright X-ray source at this position by Long & Helfand (1979) established the nature of the object. An optical counterpart in [S II] emission showing signs of shock enhancement was detected by Danziger et al. (1981). It was on this optical counterpart that ISO was pointed (see Figure 2.2, upper right). The discovery of an X-ray pulsar with a period of only 16 ms by Marshall et al. (1998) has further strengthened the picture of N157B as a Crab-like SNR.

2.2.6 LMC : N159-5 and N160A

The H II regions N159 and N160, together with N158, form a nice chain of H II regions extending southwards from 30 Doradus. The regions lie approximately 30′ south from 30 Dor and are very complex. The N160 region is subdivided into two pairs of H II nebulosity, N160 B/C and N160 A/D. The two HEBs observed in this work (N160A1 and A2) are embedded within the component N160A, and clearly stand out in Hα images (see Fig. 2.2, center right). The H II region N159 roughly consists of two parts, a triangular shaped part (N159A) and a very complex H II structure at the east arching all the way to the north. The object N159-5 is located 6′ north-east of N159A (see Fig. 2.2, center left). High-resolution HST images of the blob show it to have a 'butterfly' like morphology (Heydari-Malayeri et al. 1999b). The HEBs in N160A and N159-5 have about the same angular size, 6″ for N159-5 and $\sim 4''$ for N160A1/A2. Both N159-5 and N160A1 are very highly excited, showing a very high [O III]/Hβ ratio of about 8, with N160A2 only slightly less. Locally, the extinction seen towards the objects is very high, with $A_{H\beta} = 1.7$ mag for N160A1 and as much as 2.9 mag for N159-5. Much of this extinction is internal, due to the presence of dust in the objects. In a recent HST study of N160A, the two blobs have been resolved and their stellar content determined (Heydari-Malayeri et al. 2002). The CO content of N159 and N160 has been studied by Johansson et al. (1998) as part of the ESO-SEST key programme.

2.2.7 SMC : N66

The SMC object N66 (NGC 346) is a giant H II region containing about 40 O stars (Massey, Parker & Garmany 1989). As can be seen in the lower right panel of Figure 2.3, the region has two distinct components. The first component is a semi-circular nebula showing a wealth of filaments and ridges. The second component, lying somewhat northeast from the main component of the nebula at the center of the circle, is formed by an isolated H II region known as N66A.

The region has been studied extensively in many wavelength regimes. In the optical, spectroscopic work has been done by e.g. Dufour & Harlow (1977) and Pagel et al. (1978). In a study by Taisheng, Turtle & Kennicutt (1991), a SNR and SNR candidate have been discovered in N66 by using Hα images and radio data at four frequencies. More recently, the nebula has been observed in the mid-infrared with ISOCAM, complemented by CO(2-1) and H_2 data (Contursi et al. 2000; Rubio et al. 2000).

TABLE 2.2— The log of the optical observations made in December 1995 and December 1996 at the ESO 1.52 meter telescope .

Observing date	Detector	Grating	Spectral Range	Slit width	Sptl/Spctrl res.
13/16 Dec 1995	Ford Aerospace 2048L 15 μm pixels	Grating #2 300 gr mm^{-1}	2880 Å -10550 Å	1.″7	0.″81 p^{-1} / 3.8 Å p^{-1}
2/5 Dec 1996	Loral/Lesser #39 15 μm pixels	Grating #5 900 gr mm^{-1}	3455 Å - 11150 Å	1.″7	0.″81 p^{-1} / 3.8 Å p^{-1}
		Grating #25 400 gr mm^{-1}	3977 Å - 9780 Å		2.8 Å p^{-1}

In their work, a detailed study is given of the photodissociation region associated with N66. The presence of PAHs has also been detected. In this work, the ISO satellite was pointed at a position halfway the two main components of N66 (see Figure 2.3, lower right).

2.2.8 SMC : N81 and N88A

The compact SMC H II regions N81 and N88 have been studied by e.g. Testor & Pakull (1985) and Heydari-Malayeri et al. (1988). The large scale morphology of the two objects is reasonably simple. In Hα, N81 shows up as a round object embedded, slightly off-center, in diffuse emission (Figure 2.3, center left). The object N88 is composed of four main components forming a roughly triangular shape. The dominant component N88A is a very compact blob of about 4″ in diameter (Figure 2.3, center right).

Both objects have been revisited by Heydari-Malayeri et al. (1999a, c) and Kurt et al. (1999) using the HST. The HST study of N81 revealed a small cluster of stars inside the core of the nebula, with the main exciting sources being two deeply embedded stars only 0.″27 apart. For N88A, the main exciting star could not be identified, which is due to the uncommonly high extinction. Both N81 and N88A show complex structures inside their cores, with dark lanes and bright and dark globules.

2.3 Data

2.3.1 Optical data

The optical spectra were secured during two observing runs in December 1995 and December 1996. The observations were carried out with the Boller & Chivens Spectrograph on the ESO 1.52 meter telescope. The instrumental setup in these two runs is given in Table 2.2. In all cases, the detector was windowed down to 300 × 2048 pixels, giving a slit length of 4.′1. In the second part of the December 1996 run, the grating was changed, which split the spectra in two sets, differing in wavelength range.

Of every H II region in our sample, longslit spectra and several driftscan spectra were taken. The longslit spectra were taken at intervals of 4-5″ in the direction perpendicular

to the slit so as to cover the whole object. The orientation of the slit was chosen such that the effects of differential refraction were minimized. The driftscan spectra scan areas ranging from $10''$ to $60''$, depending on scan speed and integration time, and are used to facilitate the combination of ISO and optical data. These driftscan spectra were obtained holding the slit in a fixed North-South direction. Unless stated otherwise, the reduction process described in this section is the same for both the longslit and the driftscan spectra.

The reduction of the optical spectra was done with the *Image Reduction and Analysis Facility* (IRAF) V2.11. The reduction involved bias subtraction, flatfielding using dome flats, and cosmic ray removal. A slit illumination function was created from sky flats to correct for illumination gradients in the dome flats along the spatial direction of the slit. These gradients, though, amounted to only a few percent going from one end of the slit to the other. Several Helium-Argon lamp exposures were made during every night for the wavelength calibration of the spectra. The Helium-Argon exposures were also used to correct for a slight misalignment of the slit with the dispersion lines of the detector.

For the flux calibration of the spectra, a response function of the total setup was derived using the combined spectra from the standard stars Feige 24, L 745-46A and G 99-37 (Oke 1974). The uncertainty in the response function, and hence in the flux calibration, was determined by overplotting the different 'sub' response functions as derived from the separate standard star exposures. The scatter in the combined 'sub' response functions as a function of wavelength was then determined. This scatter translated into an uncertainty in the flux calibration varying from 3% in the yellow, central part of the spectrum, to 5% in the red and blue parts at the ends. From the combined 'sub' response functions a master response function was derived. The 2D-spectra were then flux calibrated. A correction for atmospheric extinction was made with a standard extinction curve for the site using the airmass in mid-observation. Given the short exposure times of the spectra, the change in the airmass during the observation was negligible.

The background emission was subtracted from the 2D-spectra by fitting a constant function to every dispersion line. To this end, windows were placed along the slit where no nebular emission was present. In some of the spectra, however, the emission was seen to extend all across the slit, particularly in Hα and [O III] 5007 Å. In these cases, two 'versions' of the same spectrum were created, one with and one without the background emission removed. This procedure was necessary because of the multitude of nightsky lines in the far red which would otherwise make the identification of the nebular lines difficult.

From the spectra thus reduced a 1D-spectrum was extracted. For the stationary longslit spectra, the number of 1D-spectra extracted and their placing across the slit depend highly on the source under consideration. We therefore defer their discussion to future papers on the separate objects. As far as the driftscan spectra are concerned, the appropriate width and placing of the extraction window for every separate object was derived from the projection of the ISO-SWS band 4 aperture ($20'' \times 33''$) on the slit. Only for the object N159-5 the extraction window was made smaller to tightly fit the knot seen in the center panel of Fig. 2.2, this to increase the S/N ratio of the spectrum. Decreasing the width of the extraction window to match the projection of

the other three (smaller) apertures did not change the derived 1D-spectra significantly.

Fluxes were derived from the 1D-spectra with the SPLOT package. The flux of each line in the spectra was measured several times by fitting Gaussian profiles to the lines as well as by simple pixel integration. These measurements were repeated at least eight times for every line in order to get an estimate of the uncertainties in the line flux due to noise and continuum fitting. For most of the lines the profile was adequately described by a Gaussian, but for some of the stronger lines sometimes a small blue wing was seen. In such cases, the flux derived from the pixel integration was adopted, but the difference between the fluxes derived in the two different ways amounted to only a few percent.

In the case of a spectrum from which it was impossible to subtract the background emission, the line fitting procedure was a bit different. For those lines which did not extend all across the slit, the background subtracted version of the spectrum was used to derive the fluxes. These lines included the ones blue-wards from Hβ and red-wards from Hα. The lines extending all across the slit were measured in both versions of the 1D-spectrum. The difference in the fluxes derived for those lines was treated as an extra uncertainty.

The line fluxes were corrected for extinction using the Balmer-decrement Hα/Hβ. The only exception here was for some of the spectra of SMC-N81 for which the Hα line was sometimes saturated and Hδ/Hβ had to be used instead. For the unreddened decrements, the Baker & Menzel (1938) Case B values from Storey & Hummer (1995) were taken for $T_e = 10\,000$ Kelvin and $n_e = 100$ cm^{-3}. The correction was applied taking the extinction curve towards the Magellanic Clouds as parameterized by Howarth (1983), with the usual relation

$$\log(I_\lambda/I_\beta) = \log(F_\lambda/F_\beta) + C(H_\beta) f_\lambda, \tag{2.1}$$

with I_λ/I_β and F_λ/F_β the dereddened and reddened fluxes relative to Hβ, respectively, $C(H_\beta)$ the reddening parameter derived from the decrement Hα/Hβ, and f_λ the extinction curve. The amount of extinction in the driftscan spectra is generally low. Assuming an R_V of 3.1, the values for A_V range from ~ 0.1 magnitude for SMC-N66 to as high as 1.7 mag for the LMC object N159-5.

The line fluxes of a representative sub-sample of the driftscan spectra of the program objects are given in the Tables 2.3 to 2.5. For all the objects, the spectrum covering the wavelength range from 3400 Å to 10000 Å is given. For LMC-N83B, LMC-N11A and the pointings in 30 Doradus, however, only driftscan spectra covering the wavelength range from 4000 Å to 9800 Å were available. The error in the fluxes as given in the Tables is due to uncertainties in the flux calibration, noise and uncertainties arising from the continuum fitting and background subtraction. The error due to uncertainties in the applied reddening correction is not included, but a typical error for $E_{\beta-\alpha}$ resulting from the uncertainty in the Hα/Hβ decrement is in the order of 0.03 magnitude. An extra source of uncertainty exists in the fluxes redward from 8000 Å which is a spectral region that can be heavily affected by absorption from atmospheric water. This absorption was clearly present in the standard star exposures and in the objects with a strong continuum. The absorption was not 'divided' out of the spectra, but an attempt was made to derive the extra uncertainty in the flux arising from this problem (see section 2.4.2).

TABLE 2.3— The optical fluxes for the LMC objects N160A1, N160A2, N159-5, N157B and for 30 Doradus#1. The first and second column give the wavelength and identification of the lines, respectively. The fluxes are given relative to Hβ ($\times$100). Given in the last row is the reddening $E_{\beta-\alpha}$ in magnitudes. The flux uncertainties are coded as follows : A $< 5\%$, $5\% \leq$ B $< 7.5\%$, $7.5\% \leq$ C $< 10\%$, $10\% \leq$ D $< 12.5\%$, $12.5\% \leq$ E $< 15\%$, F $\geq 15\%$.

λ (Å)	Identifier	N160A1		N160A2		N159-5		N157B		30 Dor#1	
		I_λ/I_β	Err	I_λ/I_β	Err	I_λ/I_β	Err	I_λ/I_β	Err	I_λ/I_β	Err
3727	[O II]	165.5	C	164.6	C	246.0	C	223.0	B	–	–
3869	[Ne III]	29.4	B	26.5	C	29.5	E	19.9	D	–	–
3888	Hζ	17.4	C	16.5	C	17.3	E	15.8	D	–	–
3968	[Ne III]	23.6	B	22.2	C	25.2	F	21.3	E	–	–
4101	Hδ	24.7	B	24.2	B	24.6	F	23.3	C	24.1	B
4340	Hγ	44.4	B	44.1	B	47.0	D	42.4	C	50.5	A
4363	[O III]	2.4	D	1.8	E	–	–	4.8	F	4.8	B
4471	He I	3.8	C	3.6	D	–	–	3.5	F	4.2	C
4711	[Ar IV]	–	–	–	–	–	–	–	–	–	–
4861	Hβ	100.0	A	100.0	A	100.0	B	100.0	B	100.0	A
4959	[O III]	139.9	A	126.5	A	120.0	B	108.0	B	189.0	A
5007	[O III]	423.6	A	382.1	A	368.0	B	324.0	B	566.0	A
5200	[N I]	–	–	0.49	F	–	–	–	–	–	–
5270	[Fe III]	–	–	–	–	–	–	–	–	0.28	F
5517	[Cl III]	0.45	E	0.41	F	–	–	–	–	–	–
5537	[Cl III]	0.31	F	0.25	F	–	–	–	–	–	–
5754	[N II]	0.34	F	–	–	–	–	–	–	–	–
5875	He I	12.1	A	11.7	A	12.8	C	11.7	B	11.7	B
6302	[O I]	1.60	B	1.27	C	2.7	F	5.5	C	0.50	E
6312	[S III]	1.43	B	1.44	C	1.3	F	1.6	C	1.7	C
6362	[O I]	0.71	F	–	–	1.0	F	2.2	F	–	–
6563	Hα	286.0	A	286.0	A	286.0	B	286.0	B	286.0	A
6585	[N II]	18.7	B	18.3	B	21.0	B	22.2	C	5.2	B
6678	He I	3.3	B	3.2	B	3.4	C	3.8	D	3.3	B
6717	[S II]	12.7	C	11.7	C	18.1	B	29.1	B	3.7	B
6730	[S II]	10.1	C	9.3	C	14.3	B	24.5	B	3.2	B
7065	He I	3.2	B	3.3	B	4.5	C	2.4	E	3.5	B
7137	[Ar III]	11.9	A	11.2	A	12.4	B	10.5	B	11.5	A
7281	He I	0.61	E†	0.59	E†	–	–	–	–	0.46	E†
7320	[O II]	2.6	B†	2.5	B†	3.5	C†	–	–	1.3	C†
7330	[O II]	2.0	B†	2.0	B†	2.7	C†	–	–	1.2	C†
7450	[Fe II] (?)	3.0	C†	2.8	C†	2.4	F†	5.0	F†	–	–
7726	He I	0.57	D	0.45	E	–	–	–	–	0.35	F
7751	[Ar III]	3.1	B	2.8	B	3.0	D	–	–	2.9	B
8750	P 12	1.34	D‡	1.3	D‡	2.0	F‡	–	–	1.2	E‡
8862	P 11	2.10	D‡	2.0	C‡	2.4	F‡	–	–	1.6	D‡
9015	P 10	2.05	D‡	2.1	D‡	3.3	F‡	–	–	1.7	F‡
9069	[S III]	37.9	A‡	35.3	A‡	42.6	B‡	35.6	B‡	28.8	A‡
9229	P 9	3.53	B‡	3.4	C‡	4.1	F‡	–	–	3.4	C‡
9532	[S III]	87.1	A‡	82.2	A‡	91.6	B‡	85.8	B‡	79.4	A‡
	$E_{\beta-\alpha}$	0.27		0.30		0.59		0.25		0.40	

† : these lines sit in an absorption feature near 7200 Å.
‡ : the fluxes are affected by telluric absorption. This extra uncertainty is not included here.

TABLE 2.4— The optical fluxes for 30 Doradus#2, 30 Doradus#3 and 30 Doradus#4 and for the LMC objects N11A and N83B. The first and second column give the wavelength and identification of the lines, respectively. The fluxes are given relative to Hβ ($\times$100). Given in the last row is the reddening $E_{\beta-\alpha}$ in magnitudes. The flux uncertainties are coded as follows : A $< 5\%$, $5\% \leq$ B $< 7.5\%$, $7.5\% \leq$ C $< 10\%$, $10\% \leq$ D $< 12.5\%$, $12.5\% \leq$ E $< 15\%$, F $\geq 15\%$.

λ (Å)	Identifier	30 Dor#2		30 Dor#3		30 Dor#4		N11A		N83B	
		I_λ/I_β	Err	I_λ/I_β	Err	I_λ/I_β	Err	I_λ/I_β	Err	I_λ/I_β	Err
3727	[O II]	–	–	–	–	–	–	–	–	–	–
3869	[Ne III]	–	–	–	–	–	–	–	–	–	–
3888	Hζ	–	–	–	–	–	–	–	–	–	–
3968	[Ne III]	–	–	–	–	–	–	–	–	–	–
4101	Hδ	23.0	A	24.9	A	27.3	B	25.9	C	24.5	B
4340	Hγ	48.9	A	49.3	A	52.6	B	52.9	B	54.5	A
4363	[O III]	3.8	C	3.8	B	3.7	E	2.9	F	2.5	F
4471	He I	3.7	D	4.3	B	5.4	E	4.6	C	4.0	E
4711	[Ar IV]	–	–	0.88	E	–	–	–	–	–	–
4861	Hβ	100.0	A	100.0	A	100.0	A	100.0	A	100.0	A
4959	[O III]	167.0	C	168.0	A	151.0	A	128.0	A	92.1	A
5007	[O III]	502.0	C	497.0	A	457.0	A	387.0	A	277.0	A
5200	[N I]	–	–	–	–	–	–	–	–	–	–
5270	[Fe III]	–	–	0.26	F	–	–	–	–	–	–
5517	[Cl III]	0.55	F	0.56	D	–	–	–	–	–	–
5537	[Cl III]	0.44	F	0.37	D	–	–	–	–	–	–
5754	[N II]	–	–	–	–	–	–	–	–	–	–
5875	He I	13.1	A	12.7	A	12.1	A	12.3	B	11.4	A
6302	[O I]	–	–	0.59	C	1.2	C	1.7	D	1.3	D
6312	[S III]	1.7	F	1.7	B	1.7	C	1.5	D	1.4	C
6362	[O I]	–	–	0.29	F	0.68	F	–	–	–	–
6563	Hα	286.0	A	286.0	A	286.0	A	286.0	A	286.0	A
6585	[N II]	4.7	B	7.9	A	12.9	A	17.0	C	22.7	A
6678	He I	3.3	B	3.6	A	3.2	B	3.3	C	3.2	B
6717	[S II]	5.1	B	4.3	A	8.6	A	11.3	E	14.4	C
6730	[S II]	4.1	B	4.1	A	7.3	A	9.3	E	11.8	B
7065	He I	3.2	B	3.7	A	2.5	B	3.2	E	3.8	B
7137	[Ar III]	11.3	A	12.8	A	11.4	A	11.5	B	10.2	A
7281	He I	0.59	E†	0.60	C†	0.53	E†	–	–	–	–
7320	[O II]	1.2	B†	1.7	B†	1.9	B†	4.8	C†	4.0	B†
7330	[O II]	1.0	B†	1.4	B†	1.6	B†	3.8	C†	3.5	B†
7450	[Fe II] (?)	–	–	0.27	F†	–	–	–	–	–	–
7726	He I	–	–	0.37	E	–	–	–	–	–	–
7751	[Ar III]	2.9	C	3.3	B	2.7	B	3.3	D	2.7	C
8750	P 12	1.1	D‡	1.3	C‡	1.4	D‡	–	–	1.5	F‡
8862	P 11	1.5	D‡	1.8	C‡	1.6	E‡	–	–	1.7	F‡
9015	P 10	1.8	C‡	1.9	B‡	1.7	D‡	–	–	1.6	F‡
9069	[S III]	27.0	A‡	32.7	A‡	29.9	A‡	27.5	A‡	28.5	A‡
9229	P 9	3.1	C‡	3.8	B‡	3.1	C‡	–		3.8	F‡
9532	[S III]	–	–	97.5	A‡	85.3	A‡	77.8	A‡	81.5	A‡
	$E_{\beta-\alpha}$	0.35		0.33		0.59		0.25		0.27	

† : these lines sit in an absorption feature near 7200 Å.
‡ : the fluxes are affected by telluric absorption. This extra uncertainty is not included here.

TABLE 2.5— The optical fluxes for the LMC objects N79A and N4A, and for the SMC objects N88A, N66 and N81. The first and second column give the wavelength and identification of the lines, respectively. The fluxes are given relative to Hβ ($\times$100). Given in the last row is the reddening $E_{\beta-\alpha}$ in magnitudes. The flux uncertainties are coded as follows : A $< 5\%$, $5\% \leq$ B $< 7.5\%$, $7.5\% \leq$ C $< 10\%$, $10\% \leq$ D $< 12.5\%$, $12.5\% \leq$ E $< 15\%$, F $\geq 15\%$.

λ (Å)	Identifier	N79A		N4A		N88A		N66		N81	
		I_λ/I_β	Err	I_λ/I_β	Err	I_λ/I_β	Err	I_λ/I_β	Err	I_λ/I_β	Err
3727	[O II]	233.0	B	152.2	B	95.6	B	116.9	C	137.0	B
3869	[Ne III]	17.7	C	28.0	B	53.6	B	34.1	C	46.0	C
3888	Hζ	14.7	C	18.4	C	11.4	C	15.3	E	15.0	D
3968	[Ne III]	18.9	C	23.9	B	29.1	C	26.1	F	27.6	B
4101	Hδ	23.4	C	24.7	B	24.7	C	19.7	D	25.4	B
4340	Hγ	41.5	B	44.7	B	44.4	B	40.9	C	45.6	B
4363	[O III]	2.4	F	2.6	F	12.0	C	5.6	F	7.4	B
4471	He I	3.6	E	3.9	D	3.6	E	3.1	F	3.8	D
4711	[Ar IV]	–	–	–	–	–	–	–	–	–	–
4861	Hβ	100.0	B	100.0	A	100.0	A	100.0	B	100.0	A
4959	[O III]	101.0	A	142.0	A	222.0	A	156.0	B	175.0	A
5007	[O III]	306.0	A	430.0	A	672.0	A	469.0	B	528.0	A
5200	[N I]	–	–	–	–	–	–	–	–	0.4	F
5270	[Fe III]	–	–	–	–	–	–	–	–	–	–
5517	[Cl III]	–	–	–	–	–	–	–	–	–	–
5537	[Cl III]	–	–	–	–	–	–	–	–	–	–
5754	[N II]	–	–	0.41	F	–	–	–	–	–	–
5875	He I	11.4	A	12.4	A	12.9	B	11.0	C	10.9	B
6302	[O I]	1.8	C	1.2	C	1.6	C	2.3	E	1.1	C
6312	[S III]	1.3	C	1.5	C	1.6	C	1.8	E	1.6	C
6362	[O I]	0.76	F	–	–	–	–	1.4	F	–	–
6563	Hα	286.0	A	286.0	A	286.0	A	286.0	B	–	–
6585	[N II]	23.8	A	13.3	A	5.3	B	6.1	C	5.5	B
6678	He I	3.1	C	3.3	B	2.9	B	3.1	D	2.5	B
6717	[S II]	15.1	A	9.1	A	5.2	B	10.1	B	6.9	B
6730	[S II]	12.5	A	6.9	A	4.5	B	7.0	C	5.2	B
7065	He I	3.9	C	2.6	B	9.3	A	2.9	F	2.7	B
7137	[Ar III]	10.6	B	11.4	A	10.7	A	8.3	C	8.3	A
7281	He I	0.74	F†	0.68	F†	0.87	E†	–	–	0.6	F†
7320	[O II]	4.1	B†	2.2	C†	2.9	B†	2.1	E†	2.5	C†
7330	[O II]	3.3	B†	1.8	C†	2.2	B†	2.0	F†	1.9	C†
7450	[Fe II] (?)	5.9	C†	3.4	C†	1.7	F†	3.6	F†	–	–
7726	He I	–	–	0.66	E	0.6	F	–	–	1.2	D
7751	[Ar III]	2.7	C	2.9	B	2.2	D	–	–	2.0	C
8750	P 12	1.8	D‡	1.1	E‡	1.8	E‡	–	–	1.2	F‡
8862	P 11	2.7	F‡	1.9	E‡	1.7	E‡	–	–	1.5	F‡
9015	P 10	2.4	F‡	2.9	E‡	2.8	F‡	–	–	2.1	F‡
9069	[S III]	38.3	A‡	34.7	A‡	17.5	B‡	20.7	D‡	18.0	B‡
9229	P 9	4.0	D‡	–	–	4.0	D‡	–	–	3.0	C‡
9532	[S III]	90.4	A‡	75.8	A‡	20.7	B‡	45.7	D‡	37.7	B‡
	$E_{\beta-\alpha}$	0.13		0.27		0.01		0.26		$-0.08^\star$	

† : these lines sit in an absorption feature near 7200 Å.
‡ : the fluxes are affected by telluric absorption. This extra uncertainty is not included here.
$\star$: the H_α line was saturated. Given here is $E_{\beta-\delta}$.

TABLE 2.6— The ISO-SWS/LWS fluxes for the LMC objects N160A1, N160A2, N159-5, N157B and 30 Dor#1. The first and second column give the wavelength and identification of the lines. The fluxes are given in $10^{-16}\,\mathrm{W\,m^{-2}}$. The flux uncertainties are coded as follows : A < 5%, 5% ≤ B < 10%, 10% ≤ C < 15%, 15% ≤ D < 20%, 20% ≤ E < 30%, F ≥ 30%.

λ (μm)	Identifier	N160A1		N160A2		N159-5		N157B		30 Dor#1	
		Flux	Err	Flux	Err	Flux	Err	Flux	Err	Flux	Err
4.05	Brα	51.7	C	55.2	C	12.6	C	–	–	34.9	C
2.63	Brβ	24.0	B	28.4	B	5.98	C	3.65	C	16.0	B
7.46	Pfα	16.1	F	15.5	D	–	–	–	–	–	–
4.65	Pfβ	7.73	D	9.43	D	–	–	–	–	–	–
12.8	[Ne II]	112	E	124	E	51.0	E	28.5	E	70.4	E
15.6	[Ne III]	438	C	332	C	152	C	49.5	C	371	C
36.0	[Ne III]	70.6	F	55.9	F	17.9	F	7.35	F	109	F
18.7	[S III]	317	C	268	C	74.2	C	46.5	C	278	C
33.5	[S III]	643	F	491	F	204	F	116	F	785	F
10.5	[S IV]	289	C	194	C	56.7	C	11.7	C	246	C
34.8	[Si II]	111	F	120	F	80.5	F	44.0	F	152	F
6.98	[Ar II]	6.47	E	11.3	F	–	–	–	–	–	–
8.99	[Ar III]	70.3	C	76.2	C	19.9	C	8.72	D	49.3	C
25.99	[Fe II]	–	–	–	–	–	–	4.52	E	–	–
63.1	[O I]	890	B	890	B	540	B	106	B	910	B
145.5	[O I]	53	B	53	B	39	B	9	E	54	C
51.8	[O III]	3000	B	3000	B	1900	B	815	B	10000	B
88.3	[O III]	2700	B	2700	B	2250	B	1450	B	10200	B
25.91	[O IV]	–	–	–	–	–	–	5.09	D	–	–
121.8	[N II]	<22	⋆	<22	⋆	<23	⋆	<7	⋆	<26	⋆
57.3	[N III]	275	B	275	B	187	B	77	C	770	B
157.7	[C II]	595	B	595	B	560	B	170	B	575	B

⋆ : 3σ upper limit only

2.3.2 Infrared data

2.3.2.1 Short Wavelength Spectrometer (SWS)

The infrared data obtained with the Short Wavelength Spectrometer (de Graauw et al. 1996) on board ISO consist of separate line scans (AOT2, covering wavelength ranges from 0.02 to 0.6 μm), AOT6 scans (30 Doradus#1, covering wavelength ranges from 0.22 to 1.7 μm for wavelenghts shorter than 7.0 μm, and from 5.1 to 15 μm for longer wavelengths), and one archival full-grating scan (AOT1 speed 4, 30 Doradus #3). The observations were carried out during the revolutions 136 - 298 and 519 - 750. The total spectral coverage of the SWS instrument ranges from 2.4 μm to 45.2 μm. This range is roughly divided into 4 sub-ranges or bands associated with 4 separate detector blocks of 12 detectors each. Each band has its own aperture that increases in size with increasing wavelength. The positions of the band 4 ISO-SWS aperture (20″× 33″) on the sky are shown in the Figs. 2.2 and 2.3. The SWS AOT2 data were reduced using version 6.0

TABLE 2.7— The ISO-SWS/LWS fluxes for 30 Dor#2, 30 Dor#3, 30 Dor#4 and the LMC objects N11A and N83B. The first and second column give the wavelength and identification of the lines. The fluxes are given in $10^{-16}\,\mathrm{W\,m^{-2}}$. The flux uncertainties are coded as follows : A < 5%, 5% ≤ B < 10%, 10% ≤ C < 15%, 15% ≤ D < 20%, 20% ≤ E < 30%, F ≥ 30%.

λ (μm)	Identifier	30 Dor#2		30 Dor#3		30 Dor#4		N11A		N83B	
		Flux	Err	Flux	Err	Flux	Err	Flux	Err	Flux	Err
4.05	Brα	53.5	C	95.9	C	26.6	C	–	–	12.3	D
2.63	Brβ	27.0	B	45.8	B	12.7	C	–	–	6.53	B
7.46	Pfα	19.6	C	38.3	C	12.7	D	–	–	–	–
4.65	Pfβ	–	–	20.2	D	–	–	–	–	–	–
12.8	[Ne II]	100	E	169	E	72.0	E	18.9	E	18.9	E
15.6	[Ne III	689	C	1120	C	404	C	42.6	C	26.7	C
36.0	[Ne III]	123	F	194	F	87.1	F	6.22	F	4.92	F
18.7	[S III]	381	C	554	C	270	C	36.1	C	28.8	C
33.5	[S III]	921	F	1650	F	754	F	60.3	F	52.2	F
10.5	[S IV]	448	C	761	C	186	C	23.3	C	18.1	C
34.8	[Si II]	107	F	1440	F	116	F	14.4	F	15.1	F
6.98	[Ar II]	–	–	–	–	–	–	–	–	–	–
8.99	[Ar III]	71.9	C	146	C	45.7	C	11.6	C	10.7	C
25.99	[Fe II]	–	–	–	–	–	–	–	–	–	–
63.1	[O I]	970	B	1140	B	830	B	270	B	153	C
145.5	[O I]	56	E	78	C	70	C	8.3	D	8.3	D
51.8	[O III]	12000	B	12200	B	8800	B	1140	B	130	C
88.3	[O III]	11700	B	11700	B	9400	B	1710	B	140	C
25.91	[O IV]	–	–	–	–	–	–	–	–	–	–
121.8	[N II]	<19	⋆	<25	⋆	<24	⋆	<14	⋆	<6	⋆
57.3	[N III]	910	B	970	B	810	B	133	C	<35	⋆
157.7	[C II]	500	B	600	B	610	B	270	B	156	B

⋆ : 3σ upper limit only

of the Standard Product Generation pipeline as implemented in Interactive Analysis (IA^3). The AOT6 and AOT1 data were processed with version 8.7. A recalibration of the AOT2 data with pipeline version 8.7 did not change the reduction results from version 6.0, so the first ones were retained. In all cases, the reduction process started at the *Standard Processed Data* (SPD) level.

The reduction of every SPD involved the steps of a zeroth order correction for memory effects, dark current subtraction, response calibration, flux calibration, and a correction for the velocity of the ISO spacecraft in the line of sight towards the object. Special attention was paid to the dark current subtraction step where, when possible, a correction was made for variations in the dark current during a scan. The absence of a continuum in most of the scans made this not too difficult. After the dark current subtraction, the separate up and down scans were checked for symmetry. Finally, bad detectors were removed from the SPD and an *Auto Analysis Result* (AAR) was extracted. The AAR was then flatfielded, sigma clipped to remove spurious points from

TABLE 2.8— The ISO-SWS/LWS fluxes for the LMC objects N79A and N4A, and the SMC objects N88A, N66 and N81. The first and second column give the wavelength and identification of the lines. The fluxes are given in $10^{-16}\,\mathrm{W\,m^{-2}}$. The flux uncertainties are coded as follows : A < 5%, 5% ≤ B < 10%, 10% ≤ C < 15%, 15% ≤ D < 20%, 20% ≤ E < 30%, F ≥ 30%.

λ (μm)	Identifier	N79A		N4A		N88A		N66		N81	
		Flux	Err	Flux	Err	Flux	Err	Flux	Err	Flux	Err
4.05	Brα	–	–	10.7	E	–	–	–	–	–	–
2.63	Brβ	–	–	10.8	B	8.45	C	1.83	F	5.60	D
7.46	Pfα	–	–	6.50	D	–	–	–	–	–	–
4.65	Pfβ	–	–	–	–	–	–	–	–	–	–
12.8	[Ne II]	–	–	41.1	E	–	–	4.77	E	2.90	E
15.6	[Ne III]	5.39	C	121	C	25.1	C	15.0	C	21.4	C
36.0	[Ne III]	–	–	20.4	F	6.75	F	–	–	1.60	F
18.7	[S III]	1.64/6.32	F/C	93.6	C	8.99	C	7.18	C	14.1	C
33.5	[S III]	24.8	F	212	F	8.86	F	20.1	F	23.2	F
10.5	[S IV]	2.49	C	75.9	C	55.1	C	9.71	C	15.9	C
34.8	[Si II]	14.2	F	32.5	F	13.1	F	–	–	6.20	F
6.98	[Ar II]	–	–	–	–	–	–	–	–	–	–
8.99	[Ar III]	–	–	25.8	C	8.07	D	3.55	E	3.90	C
25.99	[Fe II]	–	–	–	–	–	–	–	–	–	–
63.1	[O I]	63	C	182	B	86	B	105	D	37	B
145.5	[O I]	3.5	D	13	C	3	F	5	C	<2	–
51.8	[O III]	151	C	800	B	85	D	340	D	67	E
88.3	[O III]	275	C	850	C	22	F	590	C	74	E
25.91	[O IV]	–	–	–	–	–		–	–	–	–
121.8	[N II]	<5	⋆	<7.5	⋆	<4.5	⋆	<7	⋆	<2.5	⋆
57.3	[N III]	20	F	67	C	<32	⋆	<67	⋆	<38	⋆
157.7	[C II]	81	B	160	B	35	B	58	C	14	E

⋆ : 3σ upper limit only

the scans and rebinned to the default resolution for the particular observing template (3000 for AOT2/AOT6 and 2000 for AOT1 speed 4). This was done for the up and down scans separately, as well as for the combined data.

Fluxes were derived from the AAR by fitting Gaussians to the line profiles using the line-fitting routines within the *ISO Spectral Analysis Package* (ISAP). The fluxes were independently checked with self-developed line-fitting software. In all cases, both flux measurements agreed well. The fluxes were measured in the separate up and down scans as well as in the combined spectra. The fluxes derived with the ISAP routines from the combined up and down scans are given in the Tables 2.6 to 2.8. The fluxes have not been corrected for possible extinction. The highest Brα/Brβ ratio found in our SWS spectra is 2.18±0.32, which is comparable with the Storey & Hummer (1995) Case B value of 1.76 for T_e = 10 000 Kelvin and n_e = 100 $\mathrm{cm^{-3}}$. For some of our objects no estimate of the possible extinction could be made because of the absence of suitable hydrogen recombination lines. The uncertainties in the line fluxes arise mainly

from noise, uncertainties in the flux calibration and from the differences in the fluxes as measured from the separate up and down AARs. For most of the objects, the main contributor to the error in the flux is the uncertainty in the flux calibration, which can be as high as 30% for the band 4 lines.

2.3.2.2 Long Wavelength Spectrometer (LWS)

The Long Wavelength Spectrometer (Clegg et al. 1996) on board ISO was used in AOT1 mode to get full-grating scan spectra covering the wavelength range from 43 μm to 196 μm. Over this spectral range, the resolving power varies from 140 to 330. The total spectral range covered is split into two sets of five parts each, a Short Wavelength part (SW, 43 - 93 μm) and a Long Wavelength part (LW, 84 - 196 μm). Both the SW and LW part have their own set of 5 detectors (SW 1-5 and LW 1-5). The total spectrum is formed by adding the subspectra from each of the ten separate detectors in LWS. For each source and for each of the ten detectors, six scans were obtained. The positions of the LWS beam on the sky are shown in the Figs. 2.2 and 2.3.

The spectra were reduced with LWS Interactive Analysis (LIA) V8.7, starting at the SPD level. The reduction process involved six separate steps. In the first reduction step, the absolute response of the detectors was calibrated using the illuminator flashes bracketing every observation. Following this was a correction for the drift in responsivity of every detector. The conversion from photocurrents ($\mathrm{V\,s^{-1}}$) to flux units ($\mathrm{W\,cm^{-2}\,\mu m^{-1}}$) was done in two steps : the relative response correction and the spectral element correction. The first of these two steps corrects for the wavelength-dependent responsivity of every separate detector, while the second step corrects for the size of its spectral element. Next, a dark-current correction was applied. The last reduction steps were the wavelength calibration of the spectra and a correction for the line-of-sight velocity of the ISO spacecraft towards the object. For those objects for which the continuum was very weak (flux density lower than 300 Jy at 100 μm) the dark current subtraction was done a second time with extra care. This was done to prevent the baselines of the separate scans from becoming negative as a result of inaccurate dark-current subtraction. The thus reduced spectra were further processed in ISAP, where they were manually deglitched, sigma clipped to remove the remaining outlying points and corrected for fringes. The up and down scan spectra were reduced separately and in combined form. The ten subspectra were then combined to give the total spectrum. The different subspectra were not corrected for detector-to-detector jumps in the baseline (stitching).

The line fluxes were measured in the same way as the SWS lines by fitting Gaussians (see section 2.3.2.1). The approximation of the LWS lines by Gaussians introduces errors in the measured flux of less than 2.5% (Gry et al. 2000). The FWHM of the fitted Gaussians was held constant at 0.283 μm for the SW detectors and at 0.584 μm for the LW detectors. Extensive calibration of LWS has shown the FWHM of the lines to be constant for both sets of detectors (Gry et al. 2000). The fluxes were measured in the separate up and down scans and in the combined spectra. The fluxes from the combined up and down scans are given in the Tables 2.6 to 2.8. For lines of which the flux was less than three times the noise level only an upper limit is given. No extinction correction has been applied to the LWS fluxes (see Sect. 2.3.2.1). Sources of uncertainty

in the line fluxes include noise, differences between the fluxes measured in the up and down scan and the uncertainty in the absolute flux calibration. The uncertainty due to noise was determined from line-fit residuals. The main source of error is the uncertainty in the flux calibration. For strong sources, this uncertainty is in the order of 10%. For weak sources or for sources with a complex morphology, however, this uncertainty can be as high as 30%. These numbers apply to every detector except the detectors SW1 and LW2 for which the calibration is less clear.

2.3.3 The spectra

Examples of the spectra are given for the LMC objects N159-5 (Fig. 2.4) and N83B (Fig. 2.5). Shown in these Figures are the optical spectrum (upper left panel), the LWS spectrum (upper right panel) and the separate SWS line scans (lower panel). Also shown in Fig. 2.6 are the combined optical and infrared spectra of 30 Doradus#1. These spectra serve as an example of the general quality of our data, where the spectra of LMC-N83B represent the lower end of the quality scale. It is worth noting that the spectral coverage of the 30 Doradus#1 spectra is almost continuous and spans three decades.

2.4 Discussion

The line fluxes presented in this paper suffer from a number of extra uncertainties, which break down into two groups. One has to do with the extinction correction of the fluxes, the other with the problem of different instrumental beams and the size of the sample objects. The problems connected with the extinction correction are the most important for the optical line fluxes. For the infrared data the extinction is negligible.

2.4.1 Extinction correction

The optical spectra given in this chapter are all driftscan spectra. The surface integrated spectra make the comparison between the optical and infrared fluxes easier, but they also present a problem for the extinction correction of the line fluxes. This has to do with the non-uniform nature of the extinction across an object, which is especially a problem in very complex environments like starforming regions, where the extinction can change drastically from one point to another. A good example in this respect is the SMC object N88A. In a recent paper, Heydari-Malayeri et al. (1999a) showed that even within an object with such a small angular size ($3\farcs5$), the Hα/Hβ intensity ratio can change drastically within a few arcseconds. This general 'patchiness' of the extinction across the face of an object, however, is smeared in a driftscan spectrum. The resulting Balmer-decrements on which the extinction correction is based are therefore just a complicated 'weighted average' that reflects the variation in extinction properties encountered across the area scanned.

Related to the problem of the non-uniformity of the extinction, is the issue of what extinction curve to apply. In this work, a general extinction curve was used for the reddening correction of the optical data. The assumption made in the correction applied was that all the extinction can be ascribed to foreground extinction. Furthermore, an implicit assumption made is that the properties of the absorbing matter are the

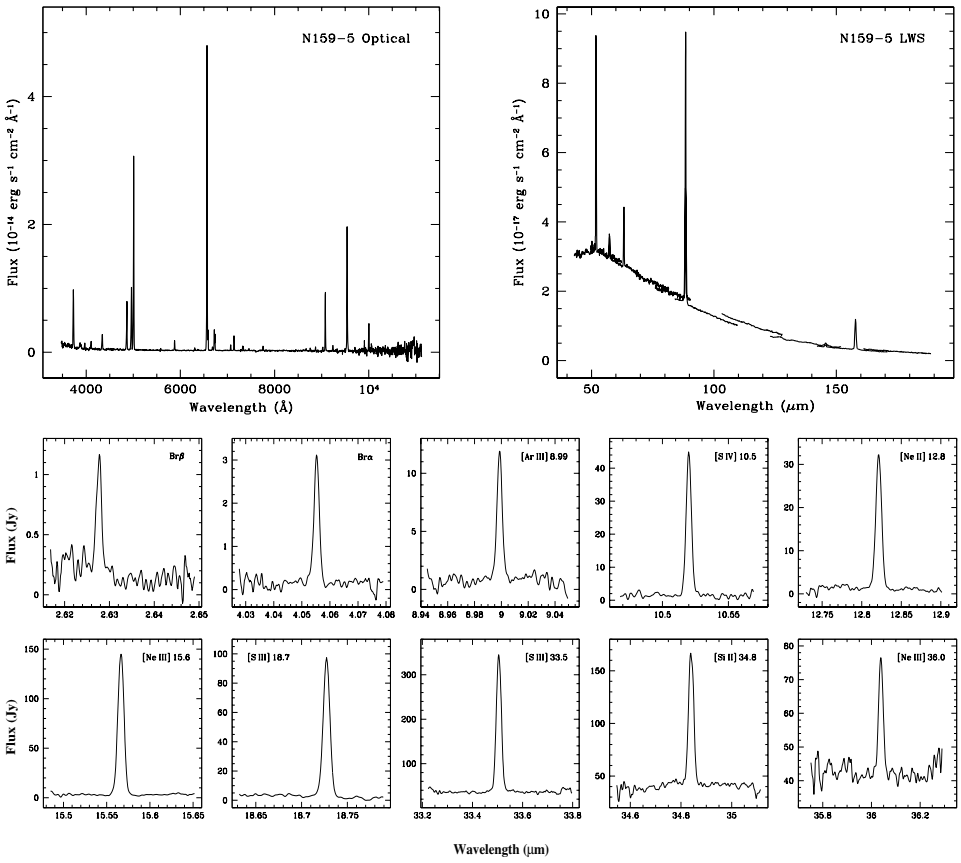

FIGURE 2.4— The optical and infrared spectra from N159-5. The top part shows the optical (*left*) and LWS (*right*) spectra, the bottom part the SWS line scans.

same everywhere, which is reflected in the 'unchangeable' shape of the extinction curve adopted in the correction.

The assumptions about the origin of the extinction and the shape of the extinction curve are invalidated when extinction within the source itself also becomes important. The absorption and scattering properties of the matter inside the source can be different from those of the matter external to the source, this as a result of the drastically different environment within the source. In this case, the shape of the extinction curve will be modified. A situation where this can become important is when dust is mixed with the emitting gas of an object. Objects in the sample which are known to have internal dust are SMC-N88A (Kurt et al. 1999), and the LMC objects N159-5 and N160A1. Furthermore, any dust mixed with the ionized gas can decrease the Balmer-decrements found in the spectrum (Mathis 1983).

Both of the uncertainties described here will have repercussions for the line fluxes given. The smearing of the extinction in a driftscan spectrum will lead to an under-

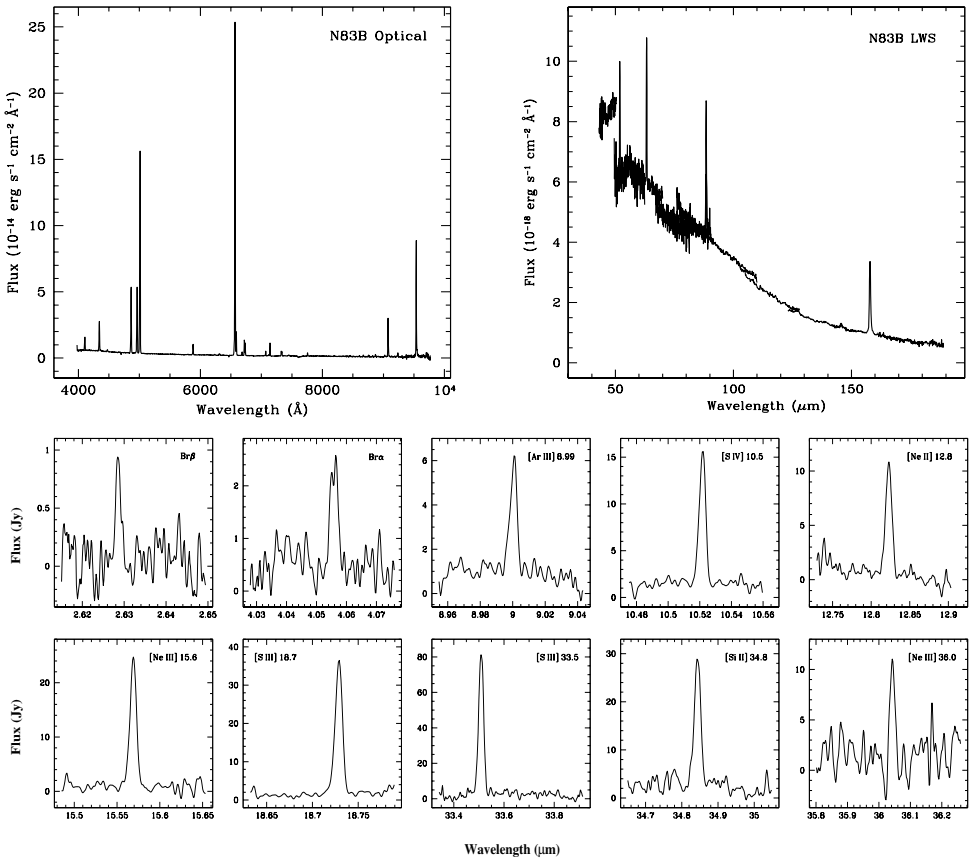

FIGURE 2.5— The optical and infrared spectra from N83B. The top part shows the optical (*left*) and LWS (*right*) spectra, the bottom part the SWS line scans.

estimate of the correction to apply, while the unknown variations in the shape of the extinction curve will give unknown wavelength dependent variations in the total extinction correction. One should bear in mind, however, that everything said in this Section will only affect the fluxes which have actually been corrected for extinction (i.e. the optical fluxes). The same problems also affect the extinction correction of the infrared lines but no correction has been applied here.

2.4.2 Telluric absorption

An additional problem affecting the optical line fluxes is the absorption from water in the atmosphere. The line fluxes red-wards from 8000 Å are affected by it, and it is especially important for the [S III] 9068 Å and [S III] 9532 Å lines. The presence of this absorption is clearly visible in the standard star spectra and in some of the object spectra. The amount of telluric absorption is difficult to asses, because it depends

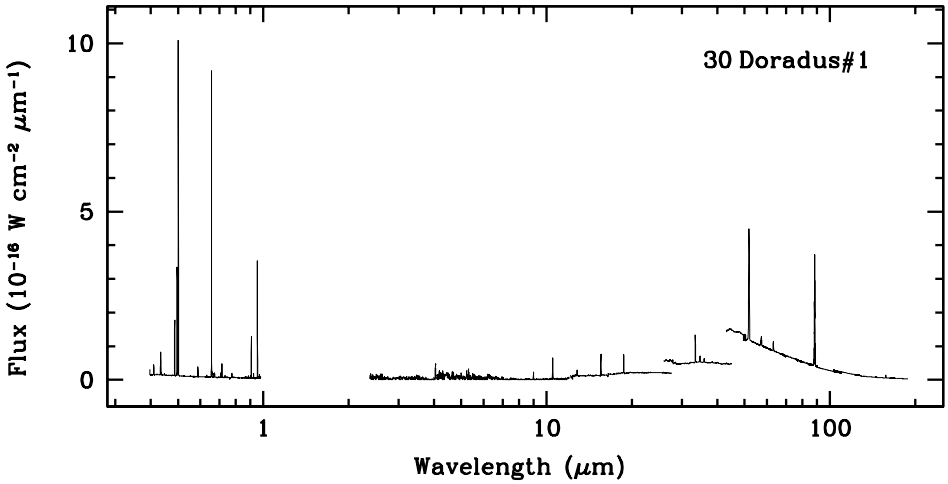

FIGURE 2.6— The optical and infrared spectra from 30 Doradus#1. Note the almost continous spectral coverage over three decades.

critically on the degree of overlap between the telluric and the spectral lines. Also, given the low spectral resolution of our spectra of about 4 Å, the narrow telluric lines are blended and only a broad absorption feature is seen. We can, therefore, only give a rough estimate of the extra uncertainty on our line fluxes introduced by this absorption, and did not attempt to actually correct the fluxes for this. We thereby focussed our attention exclusively on the crucial [S III] lines.

To get a rough idea of the magnitude of the telluric extinction, the depths of the absorption features seen in the standard star exposures were measured. The absolute values of the amount of absorption themselves were not very useful because of the changes in the atmospheric conditions from night to night, but it was possible to establish a ratio for the absorption near [S III] 9068 Å and near [S III] 9532 Å. It turned out that the absorption at [S III] 9532 Å was in all cases roughly three times larger than at [S III] 9068 Å. The absorption near [S III] 9068 Å was at most 0.1 magnitude.

The actual estimation of the extra uncertainty on our line fluxes involved the use of the theoretical line flux ratio of the two [S III] lines. The theoretical ratio [S III] 9532/[S III] 9068 is 2.44, the ratio of the transition probabilities. The observed [S III] 9532/[S III] 9068 ratio was compared with the theoretical one, and the correction factor needed to arrive at the theoretical ratio was derived. The deviation of the observed ratio from the theoretical one is (most likely) due to absorption in both the [S III] lines. The correction factor described above, therefore, depends on the effect of the (unknown) absorption on *both* the lines. Taking this dependency into account, we derived a matrix of correction factors for the [S III] 9532 Å and the [S III] 9068 Å line flux from which the uncertainty was estimated.

Taking into account the relative difference in absorption near the two lines and the

fact that the [S III] 9068 Å line appeared more reliable than the [S III] 9532 Å line, the investigation of the parameter space of correction factors led us to estimate that there is an extra uncertainty in the line fluxes of up to 20%. This uncertainty is not included in the error given for these lines in the Tables 2.3 to 2.5.

2.4.3 Apertures and beams

An important issue, concerning the infrared line fluxes, is the question whether or not the sample objects are pointlike or extended compared to the ISO-SWS/LWS apertures. Any deviation of the source morphology from a perfect point source gives rise to a set of inter-related problems, resulting from the multitude of apertures and beams involved with the ISO spectrometers.

The total spectral coverage of the ISO spectrometers is subdivided into several subregions or bands, and all these different parts of the spectrum are observed using different apertures. The four rectangular ISO-SWS apertures through which the different spectral ranges are observed cover an area on the sky of $14'' \times 20''$ (2.38 - 12.0 μm), $14'' \times 27''$ (12.0 - 27.5 μm), $20'' \times 27''$ (27.5 - 29.0 μm) and $20'' \times 33''$ (29.0 - 45.2 μm), respectively. The circular ISO-LWS aperture is about $80''$ in diameter. The result of the subdivision is that, depending on wavelength, different spatial areas of a sample object are observed.

All these apertures also have their own wavelength dependent throughput or beam profile. The beam profiles drop off sharply when one moves away from the centre of the aperture, which can lead to a significant loss of flux. In the ideal cases of an infinitely extended and homogeneous object or a point source, a correction for the loss of flux can be made. However, for a realistic object, where the flux is the result of a complex convolution of the beam profile and the source morphology, it is very difficult to make such corrections.

With these two facts in mind, it will also be clear that not only the source morphology is of importance but also the position of the source in the aperture. If an object is located at the edge of one or more of the apertures, the flux losses can be severe. These losses can hardly be traced or restored. It is therefore important that the intended target is in the centre of the aperture. Objects in our sample not satisfying this requirement are SMC-N81 and SMC-N88A, which are lying near the edge of the LWS aperture (see Fig. 2.3, center).

In this respect, a comment must be made about the pointings of the two ISO spectrometers for the sample sources. As can be seen in Table 2.1 and even more clearly in the Figs. 2.2 and 2.3, there are sometimes considerable differences between the pointings of SWS and LWS, despite the fact that the pointings were meant to be exactly the same. The most serious cases are LMC-N11A (Fig. 2.2, lower left), where LWS was actually pointed at LMC-N11B, and the object LMC-N79A which falls outside the SWS beam completely (Fig. 2.3, upper left). In many cases, though, the pointing differences are only slight.

The problems described above raise the issue of flux (in)compatibility. This is a serious handicap for the analysis done with the line fluxes, which is primarily based on flux ratios of different fine-structure and recombination lines. The impact of the flux incompatibility on the analysis depends on the lines used. For lines observed through

the same aperture, where the degree of incompatibility is likely to be small (e.g. Brβ and [S IV] 10.5 μm), the result will be more reliable than for lines observed through different apertures (e.g. [S III] 18.7 μm and [S III] 33.5 μm). It is obvious that any analysis based on the infrared line fluxes should be done with these caveats in mind.

2.5 Summary

As part of an ISO Guaranteed Time Program on H II regions in Local Group Galaxies a sample of Magellanic Cloud H II regions has been observed with the spectrometers onboard ISO. Complementary to the infrared data is a large set of optical spectra. Aim of the project is to give a new and improved analysis of the physical structure of the sample H II regions by combining as much spectral data as possible.

In this first of a set of papers, the sample objects and the data set are presented. An account is given of the reduction of the data and a discussion about the reliability of the line fluxes is presented. In this discussion, attention has been paid to problems regarding extinction and to problems generated by the SWS/LWS instruments themselves. The analysis based on this data set will be given in different papers. The results on the large-scale temperature stratification, the elemental abundances and the ionization structure of the sample H II regions will be presented in Vermeij & Van der Hulst (in press). The analysis of the photodissociation regions based on the LWS lines will be given in Damour et al. (in prep.).

Acknowledgements

The ISO Spectral Analysis Package (ISAP) is a joint development by the LWS and SWS Instrument Teams and Data Centers. Contributing institutes are CESR, IAS, IPAC, MPE, RAL and SRON. IA^3 is a joint development of the SWS consortium. Contributing institutes are SRON, MPE, KUL and the ESA Astrophysics Division. LIA is a joint development of the LWS consortium. Contributing institutes are DRAL, CESR and the ESA Astrophysics Division.

References

Baker, J.G., Menzel, D.H. 1938, ApJ **88**, 52
Bothun, G.D., Thompson, I.B. 1988, AJ **96**, 877
Clegg, P.E., Ade, P.A.R., Armand, C. et al. 1996, A&A **315**, L38
Contursi, A., Lequeux, J., Hanus, M. et al. 1998, A&A **336**, 662
Contursi, A., Lequeux, J., Cesarsky, D. et al. 2000, A&A **362**, 310
Chu, Y.-H., Kennicutt Jr, R.C. 1994, ApJ **425**, 720
Danziger, I.J., Goss, W.M., Murdin, P. et al. 1981, MNRAS **195**, 33
Dickel, J.R., Milne, D.K., Kennicutt, R.C. et al. 1994, AJ **107**, 1067
Dufour, R.J., Harlow, W.V. 1977, ApJ **216**, 706
Feast, M.W. 1999, PASP **111**, 775
de Graauw, Th., Haser, L.N., Beintema, D.A. et al. 1996, A&A **315**, L49
Garnett, D.R. 1989, ApJ **345**, 282
Grandi, S.A., Hawley, S.A. 1978, PASP **90**, 125
Gry, C. et al. 2000, LWS handbook SAI/99-077/Dc V1.1

Henize, K.G. 1956, ApJS **2**, 315
Heydari-Malayeri, M., Testor, G. 1983, A&A **118**, 116
Heydari-Malayeri, M., Testor, G. 1985, A&A **144**, 98
Heydari-Malayeri, M., Le Bertre, T., Magain, P. 1988, A&A **195**, 230
Heydari-Malayeri, M., Van Drom, E., Leisy, P. 1990, A&A **240**, 481
Heydari-Malayeri, M., Lecavalier des Etangs, A. 1994, A&A **291**, 960
Heydari-Malayeri, M., Charmandaris, V., Deharveng, L. et al. 1999a, A&A **347**, 841
Heydari-Malayeri, M., Rosa, M.R., Charmandaris, V. et al. 1999b, A&A **352**, 665
Heydari-Malayeri, M., Rosa, M.R., Zinnecker, H. et al. 1999c, A&A **344**, 848
Heydari-Malayeri, M., Charmandaris, V., Deharveng, L. et al. 2001a, A&A **372**, 495
Heydari-Malayeri, M., Charmandaris, V., Deharveng, L. et al. 2001b, A&A **372**, 527
Heydari-Malayeri, M., Charmandaris, V., Deharveng, L. et al. 2002, A&A **381**, 941
Howarth, I.D. 1983, MNRAS **203**, 301
Hunter, D.A., Shaya, E.J., Holtzman, J.A., Light, R.M. 1995, ApJ **448**, 179
Johansson, L.E.B., Greve, A., Booth, R.S. et al. 1998, A&A **331**, 857
Kennicutt Jr, R.C., Bomans, D.J., Bothun, G.D., Thompson, I.B. 1995, AJ **109**, 594
Kennicutt Jr, R.C, Bresolin, F., French, H., Martin, P. 2000, ApJ **537**, 589
Kessler, M.F., Steinz, J.A., Anderegg, M.E. et al. 1996, A&A **315**, L27
Kovács, G. 2000, A&A **360**, L1
Kurt, C.M., Dufour, R.J., Garnett, D.R. et al. 1999, ApJ **518**, 246
Long, K.S., Helfand, D.J. 1979, ApJ **234**, L77
Lucke, P.B., Hodge, P.W. 1970, AJ **75**, 171
Le Marne 1968, MNRAS **139**, 461
Marshall, F.E., Gotthelf, E.V., Zhang, W. et al. 1998, ApJ **499**, L179
Massey, P., Hunter, D.A. 1998, ApJ **493**, 180
Massey, P., Parker, J.W., Garmany, C. 1989, AJ **98**, 1305
Mathis, J.S. 1983, ApJ **267**, 119
Mathis, J.S., Chu, Y.-H., Peterson, D.E. 1985, ApJ **292**, 155
Mathis, J.S., Rosa, M.R. 1991, A&A **245**, 625
Mills, B.Y., Turtle, A.J., Watkinson, A. 1978, MNRAS **185**, 263
Natta, A., Panagia, N., Preite-Martinez, A. 1980, ApJ **242**, 596
Oke, J.B. 1974, ApJS **27**, 21
Pagel, B.E.J., Edmunds, M.G., Fosbury, R.A.E. et al. 1978, MNRAS **184**, 569
Parker, J.Wm. 1993, AJ **106**, 560
Parker, J.Wm., Garmany, C.D. 1993, AJ **106**, 1471
Peimbert, M. 1967, ApJ **150**, 825
Peimbert, M., Costero, R. 1969, *Bol. Obs. Tonantzintla y Tacubaya* **5**, 3
Rosa, M., Mathis, J.S. 1987, ApJ **317**, 163
Rosado, M., Laval, A., Le Coarer, E. et al. 1996, A&A **308**, 588
Rubio, M., Contursi, A., Lequeux et al. 2000, A&A **359**, 1139
Taisheng, Y., Turtle, A.J., Kennicutt Jr, R.C. 1991, MNRAS **249**, 722
Schild, H., Testor, G. 1992, A&AS **92**, 729
Scowen, P.A., Hester, J.J., Sankrit, R. et al. 1998, AJ **116**, 163
Storey, P.J., Hummer, D.G. 1995, MNRAS **272**, 41
Testor, G., Pakull, M. 1985, A&A **145**, 170
Van Loon, J.Th., Zijlstra, A.A. 2001, ApJ **547**, L61

Vermeij, R., Van der Hulst, J.M. 2002, A&A, in press
Vilchez, J.M., Pagel, B.E.J. 1988, MNRAS **231**, 257
Walborn, N.R., Blades, J.C. 1997, ApJS **112**, 457
Wang, Q.D. 1999, ApJ **510**, L139
Whiteoak, J.B., Wellington, K.J., Jauncey, D.L. et al. 1983, MNRAS **205**, 275

Chapter 3

The physical structure of Magellanic Cloud H II regions : elemental abundances

BASED on a new data set of optical and infrared spectra described in chapter 2, we analyse the gas-phase elemental abundances of a sample of H II regions in the Large and Small Magellanic Cloud. The combined optical and infrared data set gives us access to all the ionization stages of astrophysically important elements such as sulfur and oxygen. We self-consistently determine the electron temperatures and densities for the O^+, S^{++} and O^{++} ionization zones, and use these parameters in the derivation of the ionic fractions. We discuss the uncertainties on these ionic fractions. The different relations between the electron temperatures as proposed by Garnett (1992) and Thuan et al. (1995) are confronted with our results. We find our electron temperatures to be consistent with these relations, although the relation between T_e [S III] and T_e [O III] might be slightly steeper than predicted. We investigate the reliability of the Ionization Correction Factors (ICFs) used in the derivation of the full elemental abundances of sulfur and neon. We conclude that the prescription for the ICF used to derive the sulfur abundance as given by Stasińska (1978) for $\alpha = 3$ is accurate for $O^+/O > 0.20$. No conclusions could be drawn for neon. Avoiding the use of ICFs as much as possible, we then proceed to derive the full elemental abundances. We calculate a grid of general photoionization models to compare our results with the 'bright-line' abundance diagnostics for oxygen (R23) and sulfur (S23(4)). The reliability of the newly proposed S234 parameter (Oey & Shields 2000) which includes emission lines from S^+, S^{++} and S^{+3} is checked. We find a very good agreement between the S234 models and our analysis results. Finally, we compare the heavy element-to-oxygen ratios of our sample objects to those of giant H II regions in a large sample of low-metallicity blue dwarf galaxies (Izotov & Thuan 1999) and with the results from Kobulnicky & Skillman (1996, 1997) for the irregular galaxies NGC 1569 and 4214.

3.1 Introduction

Because of their often very rich emission-line spectra, astrophysical plasmas are an important tool for studying the gas-phase interstellar medium (ISM). Starforming or H II regions are therefore well suited for deriving the properties of the ISM. These properties include the density and temperature of the ionized plasma, but, more importantly, also the gas-phase elemental abundances. Knowledge of the chemical composition of the ISM provides an important constraint on the star-formation history and chemical evolution of a galaxy and should therefore be accurately known (e.g. Russell & Dopita 1992; Tsujimoto et al. 1995; Pagel & Tautvaišienė 1998).

An important prerequisite for the correct derivation of abundances is a good determination of the electron density and temperature. Of these two, the temperature is the most crucial. The electron temperature that has traditionally been used for deriving abundances is the one derived from the optical lines of O^{++}, but this simple approach of assuming one and the same temperature for every element is oversimplified. Any good derivation of elemental abundances should take into account that different ionic species, residing in their own ionization zone, can have their own electron temperature (Garnett 1992), and that these temperatures can be biased towards higher values because of small-scale temperature fluctuations (Peimbert 1967). Failing to do so can lead to serious errors in the derived abundandes.

The reliability of the derived elemental abundances is also compromised by the fact that not every ionic stage of an element has suitable emission lines to derive an ionic fraction from. Not taking into account these unobserved ionization stages leads to an underestimate of the total abundance. The usual way to 'remedy' this problem is by the use of Ionization Correction Factors (ICFs). Many descriptions of these ICFs have appeared for the different elements, either based on coincidences in the atomic properties of the various ionic species involved (e.g. Peimbert & Costero 1969) or on photoionization models (e.g. Stasińska 1978). The proper correction for the missing ionization stages to make, however, is not always clear and has proven to be difficult for important elements such as sulfur (Natta et al. 1980; Dennefeld & Stasińska 1983).

Both these problems can be alleviated, if not solved, by extending the usual optical data base into the infrared. The inclusion of the fine-structure lines in the infrared makes it possible to derive plasma properties for more different ionization zones, giving a better coverage of the temperature and density profile of the nebula. The larger spectral coverage also gives us access to more different, otherwise unobservable, ionic species which makes a direct calculation of the elemental abundance possible without having to resort to ICFs. The *Infrared Space Observatory* (ISO, Kessler et al. 1996) has now opened up this infrared window and has allowed us to combine the optical and infrared spectral regimes.

Using a new data base of infrared and optical spectroscopical data described in the previous chapter, we re-examine the elemental abundances of a sample of H II regions in the Magellanic Clouds. We use the H II regions in our sample primarily in their role as probe of the local gas-phase abundances, but we also address their large-scale temperature stratification. The chapter is organized as follows. A short description of the data used in this work is given in Sect. 3.2. In Sect. 3.3 the analysis in terms of electron gas properties and abundances is presented. A discussion on the derived

electron gas properties with emphasis on the large-scale temperature stratification is given in Sect. 3.4. Also given in this section is a discussion on the reliability of the derived ionic fractions and total abundances, and on the ionization correction factors used to derive these. In Sect. 3.5, we take a look at the different 'bright line' methods for deriving abundances, and in Sect. 3.6 we briefly discuss the nucleosynthetic aspects. Section 3.7 gives a summary.

3.2 Data

The data set used in the analysis presented here is described in chapter 2 of this thesis, where a detailed account of the reduction process as well as a discussion regarding the reliability and the quality of the data is given. Here we will only give a short summary of the most relevant points.

The data set consists of two parts. The first part is made up of a large set of optical driftscan and stationary longslit spectra. These were obtained in December 1995 and December 1996 with the Boller & Chivens spectrograph on the ESO 1.52 meter telescope. The optical spectra cover various spectral ranges, varying from 2880 Å to 11150 Å and from 3977 Å to 9780 Å. All spectra include the [O III] 4363 Å, [S III] 6312 Å and [O II] (7320 + 7330) Å lines important for deriving electron temperatures. Also included are the [S III] 9068 Å and [S III] 9532 Å lines. An assessment of the impact of telluric absorption on the latter two lines was made.

The optical data are complemented by infrared spectra obtained with the *Short Wavelength Spectrometer* (SWS, de Graauw et al. 1996) and *Long Wavelength Spectrometer* (LWS, Clegg et al. 1996) on board the Infrared Space Observatory (ISO) as part of a Guaranteed Time Program of H II regions in Local Group Galaxies. The SWS data were obtained using mainly the AOT2 line-scanning mode. The infrared lines observed include amongst others the [Ne II] 12.8 μm, [S IV] 10.5 μm, [Ne III] 15.6 μm, [S III] 18.7 μm and [O III] 52 μm lines.

3.3 Analysis

For the analysis involving the fine-structure lines, a five-level atom was used as a model. The relative populations of the five levels were calculated by taking into account the (de)population mechanisms of collisional excitation and de-excitation by electrons, and radiative transitions. In those cases where the electron densities and temperatures were derived from lines of the same ionic species, this has been done in a self-consistent, iterative manner. The slow variation of the effective collision strengths with temperature has been included in the model.

The effective collision strengths and radiative transition probabilities have mainly been taken from the IRON project. Effective collision strengths have been taken from Saraph & Tully (1994, Ne^{+}), Butler & Zeippen (1994, Ne^{++}), Pelan & Berrington (1995, Ar^{+}), Galavis et al. (1995, Ar^{++}, S^{++}), Cai & Pradhan (1993, S^{+}), Saraph & Storey (1999, S^{+3}), Lennon & Burke (1994, N^{+}, O^{++}) and McLauglin & Bell (1998, O^{+}). The radiative transition probabilities have been taken from Cai & Pradhan (1993, S^{+}), Biemont & Bromage (1983, S^{++}), Galavis et al. (1997, N^{+}, O^{++}, Ne^{++}), Mendoza & Zeippen (1983, Ar^{++}) and Mendoza (1983, Ne^{+}, Ar^{+}, S^{+3}). The O^{+} transition probabilities have been taken from the CHIANTI database.

3.3.1 Properties of the electron gas

The electron temperatures were determined from optical line ratios only, and were derived for the O^+, O^{++} and S^{++} emitting zones. We used the [O III] $(5007 + 4959)/\,4363$, the [S III] 9068/6312 and the [O II] $(3727 + 3730)/(7320 + 7330)$ line ratios for this. When more than one scan spectrum was available for an object, we determined the temperature from the average of the line ratios from the different spectra. The [N II] 5755 Å and [S II] 4068, 4076 Å lines were not detected or were too weak to derive a T_e [N II] or T_e [S II] from. No attempt was made to derive electron temperatures from line ratios combining the optical and the infrared lines. The different ways in which the optical and various infrared lines were observed would make such ratios very hard to interpret.

The driftscan spectra for the sources N83B, N11A and for the pointings in 30 Doradus did not include the [O II] $(3727 + 3730)$ Å or [Ne III] 3869 Å lines so no T_e [O II] could be derived from them. We therefore used our stationary longslit spectra centered on N83B and N11A to cure that problem. In order to obtain a T_e [O II] for the 30 Dor positions, we used the results from an extensive spectroscopic study of 30 Doradus with spectral positions covering the face of the nebula (Vermeij & Van der Hulst, in prep.). This was unfortunately not possible for the pointing 30 Dor#1.

The electron density in the S^+ zone was derived from the classical optical ratio of [S II] 6717/6730. The ratio was not taken from the scan spectra but from longslit spectra centered on the same position as the scan spectra. This was necessary because in the scan spectra the line ratio is always in the low-density regime where it loses its sensitivity to the electron density. In the few cases where this was not possible, an electron density of 500 cm^{-3} was adopted.

The electron densities in the S^{++} and O^{++} zones were derived from the infrared lines. The O^{++} density was derived from the [O III] 52 μm/88 μm and the S^{++} density from the [S III] 18 μm/33 μm ratio. In almost all cases, the [O III] 52 μm/88 μm line ratio was in the low-density regime. For the [S III] 18 μm/33 μm ratio, an aperture correction had to be applied, because all the ratios, except for N88A, were unphysically low. The derived electron densities and temperatures are given in Table 3.1.

3.3.2 Ionic fractions

The ionic fractions were calculated from the forbidden lines with the usual equation

$$\frac{X^+}{H^+} = \left[\frac{I_\lambda}{I_{H^+}}\right]\left[\frac{\epsilon\,(n_e, T_e)}{A_\lambda E_\lambda}\right]\left[\frac{n_e}{F\,(n_e, T_e)}\right], \tag{3.1}$$

with $X^+/\,H^+$ the ionic fraction, $I_\lambda/\,I_{H^+}$ the line flux relative to the hydrogen recombination line Brβ or Hβ, A_λ and E_λ the radiative rate and energy of the transition from which the line originates, $\epsilon\,(n_e, T_e)$ the emissivity of the hydrogen recombination line taken from Storey & Hummer (1995), n_e and T_e the electron density and temperature, and $F\,(n_e, T_e)$ the level-distribution function.

For some ionic species the fraction could be calculated from the infrared as well as from the optical line flux. This is the case for species of which the infrared lines have a suitable hydrogen recombination line available. The S^{++}, Ar^{++} and Ne^{++} ionic fractions could be calculated this way. The hydrogen recombination line used in all cases was the Brβ line. To get the best possible aperture match with the Brβ flux, the

TABLE 3.1— The electron temperatures (K) and densities (cm^{-3}) of the O^{++}, S^{++} and O^{+} zones. The temperatures were all derived from optical spectra. The O^{++} and S^{++} electron densities were derived from ratios of infrared lines, whereas the S^{+} densities are based on optical longslit spectra. The uncertainties in the derived parameters are included in parentheses.

#	Object	T_e [O III]	n_e [O III]	T_e [S III]	n_e [S III]	T_e [O II]	n_e [S II]
1	N81	13320 (170)	140 (100)	13960 (1150)	750 (650)	11900 (1800)	400 (90)
2	N88A	14990 (240)	1960 (700)	14830 (1170)	2200 (1750)	11000 (2200)	1620 (270)
3	N66	12300 (500)	–	13750 (2800)	–	11980 (1000)	500†
4	N79A	10640 (700)	–	9000 (1000)	–	11200 (1000)	500†
5	N4A	10100 (290)	150 (30)	9800 (700)	360 (300)	11700 (2000)	220 (120)
6	N83B	11270 (700)	150 (30)	9800 (1000)	620 (500)	16610 (6300)	680 (170)
7	N11A	9690 (200)	–	10400 (1400)	750 (600)	10990 (2090)	370 (70)
8	N159-5	11300 (900)	120 (20)	8000 (1500)	270 (160)	10600 (2800)	370 (210)
9	N157B	13500 (1300)	–	9600 (1200)	200 (200)	–	500†
10	30 Dor#1	10990 (600)	170 (20)	10470 (1500)	–	–	500†
11	30 Dor#2	10640 (500)	190 (20)	10730 (1900)	190 (190)	10180 (1100)*	460 (120)*
12	30 Dor#3	10570 (500)	190 (20)	9970 (1000)	–	11640 (1340)*	570 (120)*
13	30 Dor#4	10970 (500)	150 (30)	10860 (1600)	–	11200 (1320)*	400 (100)*
14	N160A1	9970 (200)	220 (30)‡	9230 (600)	450 (400)	10200 (1600)	610 (120)
15	N160A2	9710 (180)	220 (30)‡	9140 (600)	620 (500)	10000 (1600)	660 (130)

† : adopted value. ‡ : the objects fall within the LWS beam simultaneously.
* : derived from longslit spectra from Vermeij & Van der Hulst, in prep.

[Ne III] 15.6 μm and [S III] 18.7 μm lines were used instead of the [Ne III] 36.0 μm and [S III] 33.4 μm lines. The absence of a suitable hydrogen recombination line in the LWS spectral range made it impossible to derive an O^{++} ionic fraction from the [O III] 52 μm and [O III] 88 μm lines. For the remainder of this chapter, the differently derived ionic fractions will be referred to as the optical and infrared ionic fractions, respectively.

No Brβ flux was available for N11A so we had to derive it from the Hβ line in the optical driftscan spectra. This procedure, however, introduced a severe 'aperture' mismatch between the derived Brβ flux and the infrared line fluxes. The flux in the 1D driftscan spectrum of N11A is the sum from an area of the sky covering $24'' \times 36''$ whereas the infrared line fluxes are observed through apertures of $14'' \times 20''$ and $14'' \times 27''$. We therefore calculated the infrared ionic fractions for N11A in two different ways. A lower limit of the ionic fraction was derived by just using the derived Brβ flux. A second value for the ionic fraction was derived by scaling the infrared line fluxes to the Brβ aperture. Both ionic fractions are given in Table 3.2.

Because of the smaller spectral coverage of the scan spectra of N11A, N83B and 30 Doradus, the O^{+}_{opt} and Ne^{++}_{opt} ionic fractions had to be derived from their stationary longslit spectra and from the spectra of the more extensive study of 30 Doradus already mentioned in Section 3.3.1. The O^{+}_{opt} fraction for the pointings in 30 Dor was determined from the relation between the (S^{++}/S^{+}) and (O^{++}/O^{+}) ratios derived in the study of this object using the $(S^{++}/S^{+})_{opt}$ ratio and O^{++}_{opt} ionic fraction from the present work. We used the [Ne III] 3869 Å line from these spectra to derive the Ne^{++}_{opt} fraction for our positions in 30 Doradus.

TABLE 3.2— The ionic fractions X^{+i}/H^+ as derived from the optical and infrared line fluxes. For N11A, the two differently derived infrared ionic fractions are given (see Sect. 3.3.2). No infrared ionic fractions could be derived for N79A. The notation a(−b) is shorthand for a×10^{-b}.

Object	O^+_{op}	O^{++}_{op}	N^+_{op}	S^+_{op}	S^{++}_{op}	S^{++}_{ir}	S^{+3}_{ir}
N81	1.84 (−5)	7.33 (−5)	5.26 (−7)	1.49 (−7)	1.20 (−6)	8.31 (−7)	2.13 (−7)
N88A	1.24 (−5)	6.56 (−5)	3.91 (−7)	3.57 (−8)	1.06 (−6)	3.53 (−7)	4.75 (−7)
N66	2.20 (−5)	8.32 (−5)	7.59 (−7)	2.45 (−7)	1.53 (−6)	1.30 (−6)	4.19 (−7)
N79A	6.34 (−5)	8.28 (−5)	3.43 (−6)	5.13 (−7)	6.38 (−6)	–	–
N4A	6.09 (−5)	1.36 (−4)	2.50 (−6)	3.53 (−7)	4.55 (−6)	4.32 (−6)	6.54 (−7)
N83B	4.87 (−5)	1.14 (−4)	3.25 (−6)	5.22 (−7)	4.36 (−6)	2.25 (−6)	2.40 (−7)
N11A[1]	6.82 (−5)	1.41 (−4)	3.54 (−6)	5.15 (−7)	4.03 (−6)	2.47 (−6)	2.88 (−7)
N11A[2]						4.33 (−6)	6.80 (−7)
N159-5	6.65 (−5)	7.37 (−5)	3.23 (−6)	6.91 (−7)	7.00 (−6)	6.81 (−6)	8.03 (−7)
N157B	1.08 (−4)	4.31 (−5)	4.77 (−6)	1.18 (−6)	5.17 (−6)	4.29 (−6)	2.35 (−7)
30 Dor#1	3.71 (−5)[3]	1.39 (−4)	8.93 (−7)	1.28 (−7)	3.52 (−6)	7.56 (−6)	1.32 (−6)
30 Dor#2	5.06 (−5)[3]	1.37 (−4)	7.73 (−7)	1.61 (−7)	3.19 (−6)	6.15 (−6)	1.46 (−6)
30 Dor#3	3.93 (−5)[3]	1.40 (−4)	1.53 (−6)	1.67 (−7)	4.36 (−6)	5.54 (−6)	1.48 (−6)
30 Dor#4	7.01 (−5)[3]	1.15 (−4)	2.00 (−6)	2.85 (−7)	3.36 (−6)	8.73 (−6)	1.27 (−6)
N160A1	6.96 (−5)	1.45 (−4)	3.28 (−6)	5.07 (−7)	5.68 (−6)	6.57 (−6)	1.15 (−6)
N160A2	7.94 (−5)	1.45 (−4)	3.61 (−6)	5.34 (−7)	5.67 (−6)	4.84 (−6)	6.70 (−7)

Object	Ar^+_{ir}	Ar^{++}_{op}	Ar^{++}_{ir}	Ne^+_{ir}	Ne^{++}_{op}	Ne^{++}_{ir}	He^+_{op}
N81	–	3.95 (-7)	2.35 (-7)	2.47 (-6)	1.51 (-5)	7.86 (-6)	0.082
N88A	–	3.74 (-7)	3.15 (-7)	–	1.33 (-5)	5.60 (-6)	0.089
N66	–	3.81 (-7)	6.57 (-7)	1.27 (-5)	1.57 (-5)	1.74 (-5)	0.084
N79A	–	1.25 (-6)	–	–	1.39 (-5)	–	0.084
N4A	–	1.11 (-6)	1.13 (-6)	2.28 (-5)	2.69 (-5)	2.87 (-5)	0.088
N83B	–	1.09 (-6)	8.05 (-7)	1.58 (-5)	1.65 (-5)	9.60 (-6)	0.084
N11A[1]	–	1.18 (-6)	7.07 (-7)	1.63 (-5)	3.48 (-5)	1.60 (-5)	0.089
N11A[2]			1.67 (-6)	2.86 (-5)		2.80 (-5)	
N159-5	–	1.39 (-6)	1.68 (-6)	4.63 (-5)	1.83 (-5)	5.97 (-5)	0.093
N157B	–	1.04 (-6)	1.13 (-6)	3.50 (-5)	6.69 (-6)	2.66 (-5)	0.097
30 Dor#1	–	9.37 (-7)	1.34 (-6)	2.33 (-5)	–	5.34 (-5)	0.087
30 Dor#2	–	8.85 (-7)	1.14 (-6)	2.02 (-5)	3.63 (-5)	6.04 (-5)	0.091
30 Dor#3	–	1.16 (-6)	1.45 (-6)	2.03 (-5)	3.79 (-5)	5.84 (-5)	0.094
30 Dor#4	–	8.46 (-7)	1.50 (-6)	3.02 (-5)	3.88 (-5)	7.37 (-5)	0.086
N160A1	1.04 (−7)	1.34 (-6)	1.42 (-6)	2.82 (-5)	3.00 (-5)	4.72 (-5)	0.087
N160A2	1.58 (−7)	1.37 (-6)	1.33 (-6)	2.68 (-5)	3.04 (-5)	3.07 (-5)	0.084

1 : infrared ionic fractions calculated with the Brβ flux as derived from the Hβ line (see Sect. 3.3.2).
2 : ionic fractions calculated from infrared line fluxes scaled to the Brβ aperture (see Sect. 3.3.2).
3 : derived from the $(S^{++}/S^+) - (O^{++}/O^+)$ relation from Vermeij & Van der Hulst, in prep.

For the calculation of the He^+ ionic fraction the following equation was used

$$\frac{He^+}{H^+} = \left[\frac{I_\lambda}{I_{H_\beta}}\right]\left[\frac{\epsilon_\beta\,(n_e, T_e)}{\epsilon_\lambda\,(n_e, T_e)}\right], \tag{3.2}$$

with $I_\lambda/I_{H\beta}$ the helium line flux relative to the Hβ line, $\epsilon_\beta\,(n_e, T_e)$ the Hβ emissivity from Storey & Hummer (1995), and $\epsilon_\lambda\,(n_e, T_e)$ the helium recombination line emissivity from Benjamin et al. (1999). The He I recombination lines used in the derivation were the $\lambda\,5875$ Å and the $\lambda\,6680$ Å lines. The He^+ fraction derived from the two different lines was then averaged to produce the final result.

Where possible, the ionic fractions have been calculated using the electron density and temperature appropriate for the zone in which the particular ion resides. The T_e [O II] is, however, so sensitive for the electron density used that this one has not been used for this purpose. The S^{++} and Ar^{++} ionic fractions have been calculated with T_e [S III], while for the other ions T_e [O III] has been used. The ionic fractions are given in Table 3.2.

3.4 Discussion

3.4.1 Electron temperatures

The various electron temperatures derived for our sources are given in Table 3.1. All these temperatures have values near or higher than 10 000 Kelvin. The SMC sources are slightly hotter than the LMC ones, but this is a known effect of their different metallicities. The T_e [O III] are generally somewhat higher than found in the literature for our sources, which is the result of different line ratios and more recent atomic data. The T_e [S III] are comparable to the [O III] temperatures, but the uncertainties are somewhat larger. This is due to the lines used in their derivation; the [S III] 6312 Å line is quite weak (typically $\sim$ 1.5 % of Hβ) and the uncertainty on the [S III] 9068 Å is increased due to an unknown amount of telluric absorption. The T_e [O II] have uncertainties between 10 and 20%. This results from the fact that for a given [O II] $(3727 + 3730)/(7320 + 7330)$ ratio the derived temperature is very sensitive to the electron density; an uncertainty in the electron density of 100 cm^{-3} translates into an uncertainty in T_e [O II] of as much as 500 Kelvin.

It is important to point out that the electron temperatures have been derived from optical *drift*scan spectra. Any small temperature fluctuation across the area covered by the spectra weighs the flux of the temperature-sensitive lines towards regions where the temperature is slightly higher, which can increase the temperatures found in this analysis.

3.4.1.1 Temperature stratification

The electron temperature is a crucial ingredient in the derivation of elemental abundances, and the high sensitivity of the abundances to the temperatures makes a good determination of these very important. Large-scale temperature gradients and small-scale temperature fluctuations have a large impact on the abundances one derives.

The once widely adopted assumption in abundance studies of an isothermal H II region has been replaced by a more sophisticated two-zone treatment of the large-scale

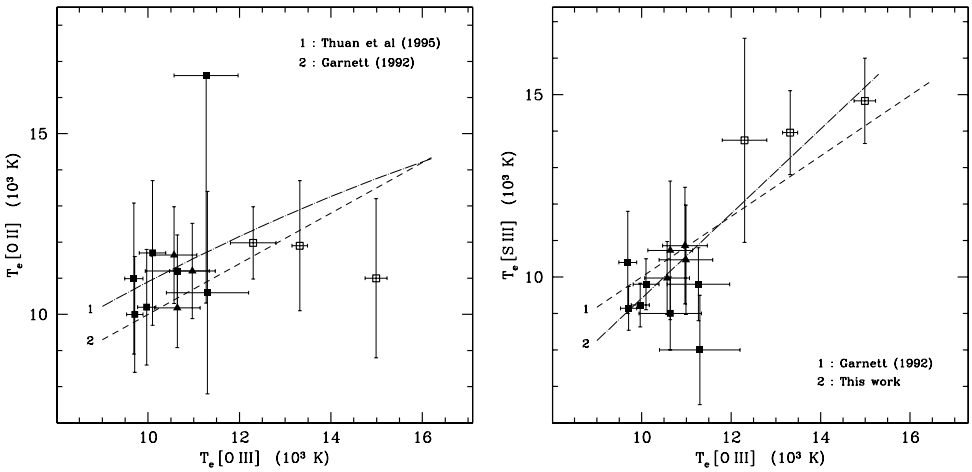

FIGURE 3.1— The correlation between $T_e\,[O\,III]$ and $T_e\,[O\,II]$ (*left*) and $T_e\,[S\,III]$. The SMC sources are given as open squares, the 30 Doradus pointings as solid triangles and the other LMC sources as solid squares.

temperature stratification. In this treatment, a subdivision has been made in a $T_e\,[O\,II]$ zone for N^+ and O^+ and a $T_e\,[O\,III]$ zone for Ne^{++}, O^{++}, Ar^{++} and S^{++}. A further refinement to this scheme was later introduced by Garnett (1992), treating Ar^{++} and S^{++} in their own, separate third temperature zone.

Given the importance of the electron temperature for the correct derivation of the abundances, attempts have been made to find relations between the different temperatures. Garnett (1992) derives the following relations between these from fits to photoionization models covering a large range of metallicities

$$t_e\,[O\,II] = 0.70\,t_e\,[O\,III] + 0.30 \tag{3.3}$$

$$t_e\,[S\,III] = 0.83\,t_e\,[O\,III] + 0.17 \tag{3.4}$$

with t_e in units of 10^4 K. An alternative relation for $t_e\,[O\,II]$ derived by Thuan et al. (1995) is

$$t_e\,[O\,II] = 0.243 + t_e\,[O\,III]\,(1.031 - 0.184\,t_e\,[O\,III]). \tag{3.5}$$

These relations are shown in Figure 3.1 together with our measured temperatures.

The derived electron temperatures for the O^{++} and O^+ zone generally fall right in between the relations given by Eqns. 3.3 and 3.5 (Fig. 3.1, left panel), with the latter relation predicting a higher $T_e\,[O\,II]$ than the former for temperatures up to about 16 000 K. The grossly deviating point is that of N83B. The N88A temperature-pair is lower than the relations predict but is still within $1.5\,\sigma$ from them. The $T_e[O\,II]$ for N88A, however, might have been depressed a bit because of the very high $n_e[S\,II]$ found for this object.

The same general agreement with the predictions is seen in the righthand panel of Figure 3.1 for $T_e\,[S\,III]$ as a function of $T_e\,[O\,III]$. The temperatures agree reasonably well with Eqn. 3.4, especially near 10 500 K. However, despite the fact that the derived

temperature-pairs are consistent within their errors with the theoretical relation from Garnett (1992), most of the low-end points fall below this relation whereas the SMC high-end points all lie above it. We therefore derived a new linear empirical relation between T_e [S III] and T_e [O III]. To this end, a least-squares fit has been made to the data points taking into account the errors in both the temperatures. The procedure followed is the one given by Reed (1989). The derived fit is plotted in Figure 3.1. The fit parameters for the slope and the intercept are 1.16 ± 0.12 and -0.22 ± 0.13, respectively, in units of 10^4 K. The inclusion of the point for N159-5 with its low T_e [S III] did not change these parameters much. The large uncertainty on the derived intercept is mainly the result of the often substantial errors on T_e [S III].

The fact that our sample objects are located in the Magellanic Clouds limits our discussion of the temperature relations to the low-metallicity end of these, but we can conclude that at least in this regime the different relations between the electron temperatures derived from photoionization models are quite accurate. The relation between T_e [S III] and T_e [O III], however, could be a bit steeper than predicted.

We did not address the subject of small-scale temperature fluctuations, although the optical and infrared fine-structure lines in our database combined, in principle, make it possible to determine their presence and, if there are any, to measure their size. However, the multitude of different instruments, beams and apertures used in obtaining our optical and infrared fluxes makes the interpretation of the optical/infrared ratios necessary for this analysis extremely difficult. We therefore could not carry out this analysis here.

3.4.2 Electron densities

The electron densities presented in Table 3.1 are all lower than 1000 cm^{-3} except for the object N88A. The O^{++} electron densities were derived from lines observed through the large LWS beam, which samples the more diffuse part of many of our objects. All the O^{++} densities are therefore quite low. The infrared lines used in the determination of n_e[S III] were observed through two different ISO-SWS apertures. In nearly all cases, this resulted in a [S III] 18.7 μm/[S III] 33.4 μm ratio that was unphysically low, i.e. the line ratio was lower than possible given the atomic physics of the S^{++} ion. We therefore scaled the [S III] 18.7 μm line flux with a factor equal to the ratio of the areas covered by the two apertures. The electron densities derived for N88A are all in the order of $\sim$ 2000 cm^{-3}, this despite the ambiguities in the [O III] and [S III] line ratios. The [Ne III] 15.6 μm/[Ne III] 36.0 μm density diagnostic could not be used for our objects because of the high critical density (10^{4-5} cm^{-3}) of the ratio.

3.4.3 Full elemental abundances and ICFs

3.4.3.1 Error budget of the ionic fractions

The factors that contribute to the uncertainty in the derived ionic fractions include errors in the used temperature and density, uncertainties in the fluxes, and uncertainties in the used atomic data. This last source of error is rather intractable, however, and shall not be discussed further here.

The contribution of the flux uncertainties to the total error budget is relatively low for the optical lines. With errors of typically 5% for the strong optical line fluxes,

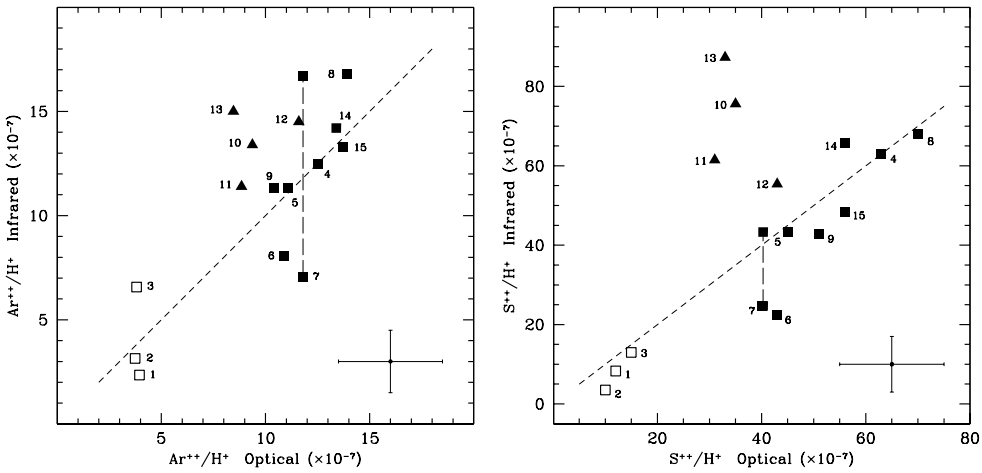

FIGURE 3.2— The comparison between the S^{++} and Ar^{++} ionic fractions as derived from the optical and infrared fluxes. The SMC sources are given as open squares, the 30 Doradus pointings as solid triangles and the other LMC sources as solid squares. The numbering of the objects is according to Table 3.1. The vertical dashed line connects the two differently derived infrared ionic fractions of N11A (see Sect. 3.3.2). Shown in the right lower corner is a typical error bar.

the optical ionic fractions are hardly affected by it. The exception in this case is the [S III] 9068 Å flux from which the S^{++}_{opt} ionic fraction is calculated. This line suffers from telluric absorption that can increase the uncertainty on the flux with $\sim 20\%$ (see chapter 2). As far as the infrared line fluxes are concerned, the instrumental setup of the ISO spectrometers imposes its own typical set of uncertainties on the lines (see chapter 2 for a discussion), but if one confines oneself to the combined uncertainty in the flux calibration and flux measurement, the uncertainties in the used infrared fluxes are commonly around 10%.

The uncertainties in the applied electron temperature and density both have their own different impact on the ionic fractions. Furthermore, not every ion reacts the same to changes in these parameters. Although it is very difficult to propagate the error in the ionic fractions through Equation 3.1 in a formal manner, an estimate of the resulting error can be obtained by varying the temperature and density within their error bars.

The size of the contribution to the total error in the ionic fractions due to uncertainties in the electron density depends on the fine-structure level configuration of the relevant ion; five-level ions with a low-lying triplet like O^{++} are much less sensitive to the density than those with a low-lying singlet (O^{+} and S^{+}). It turns out that for the generally low densities observed in our sample objects, an uncertainty of 200 cm^{-3} in the density will translate into less than 1% error in the ionic fraction of O^{++}_{opt}, Ne^{+}_{ir}, Ne^{++}_{opt}, Ne^{++}_{ir}, S^{++}_{opt}, Ar^{+}_{ir}, Ar^{++}_{opt}, Ar^{++}_{ir} and N^{+}_{opt}. For O^{+}_{opt} and S^{+}_{opt} though this error increases to 4% and 10% respectively, while both the S^{++}_{ir} and S^{+3}_{ir} fractions have their errors increased by about 4%.

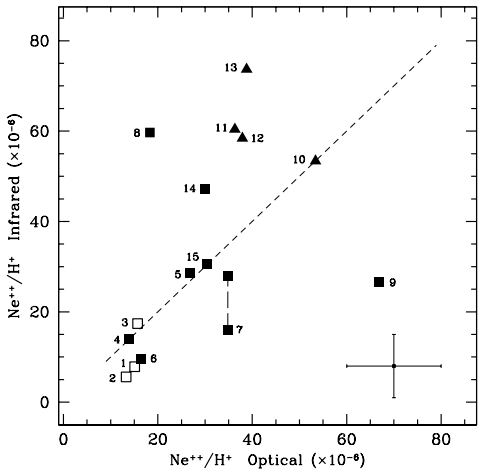

FIGURE 3.3— The comparison between the Ne^{++} ionic fractions as derived from the optical and infrared fluxes. For an explanation of the symbols and labels see Figure 3.2. The vertical dashed line connects the two differently derived infrared ionic fractions of N11A (see Sect. 3.3.2). Shown in the right lower corner is a typical error bar.

The largest contribution to the total error is produced by the uncertainty in the electron temperature. A variation of 900 K in temperature can produce an error of $\sim 20\%$ for O^{+}_{opt}, O^{++}_{opt} and Ne^{++}_{opt}, and $\sim 10\%$ for S^{+}_{opt} and S^{++}_{opt}. The error is $\sim 15\%$ for Ar^{++}_{opt} and N^{++}_{opt}. The ionic fractions derived from the infrared lines suffer much less from errors in the electron temperature. The impact of the uncertainty in the electron temperature here is about 5% for all the infrared ionic fractions.

Taking into account both of the sources of error discused here, we derived a typical error of 15% for the optical ionic fractions and of 10% for the infrared ones. For some specific cases like S^{++}_{opt} this error increases to $\sim$ 25%. The estimates are probably somewhat conservative because both the electron properties and ionic fractions are ultimately derived from the same set of line fluxes so some cancellation is possible. A quick glance at Eqn. 3.1 suffices to see that the errors are not independent.

The error analysis given above only applies to the ionic fractions derived from fine-structure lines. The uncertainty in the He^{+} ionic fraction, which is derived from recombination lines, arises from the impact of the uncertainty of the electron temperature on the helium line-emissivities. This impact is, however, small. A variation of 900 K in temperature translates itself into an uncertainty of $\sim$3% in the ionic fraction. The uncertainty on the helium line fluxes is larger (between 5 and 10%).

3.4.3.2 Comparison between the optical and infrared ionic fractions

An extra check on the reliability of the S^{++}, Ar^{++} and Ne^{++} ionic fractions was performed by comparing the optical fractions with the infrared ones. As the Figures 3.2 and 3.3 show, there is in general a reasonable agreement between the different S^{++} and Ar^{++} ionic fractions. The Ne^{++} ionic fraction is the least certain of the three showing a large scatter. The largest differences are found for the more extended objects.

The use of T_e [S III] rather than T_e [O III] in the derivation of the S^{++} and Ar^{++} ionic fractions cannot explain the differences. For many of our sample objects, and especially for our pointings in 30 Doradus, the T_e [S III] and T_e [O III] are rather similar. Also, in order to get equal optical and infrared ionic fractions for e.g. the pointings

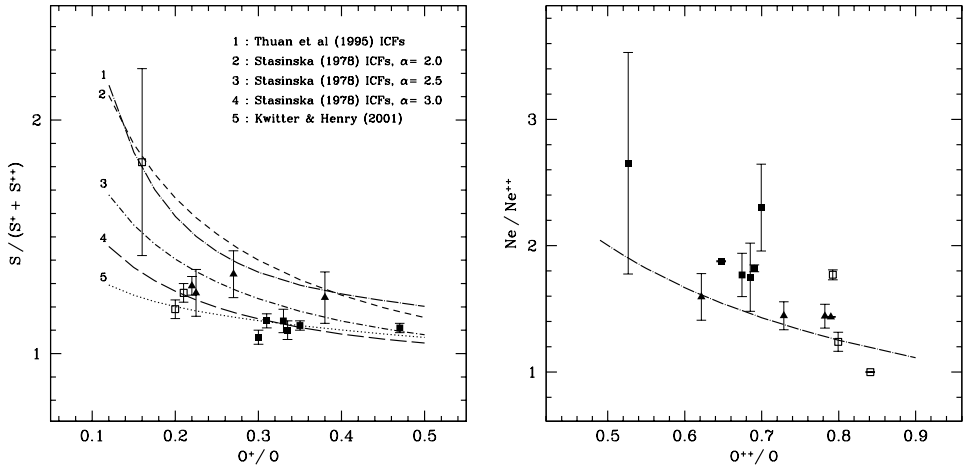

FIGURE 3.4— The observed ratios $S / (S^+ + S^{++})$ and Ne / Ne^{++} compared with the theoretical ratios. The error bars show the extremes when using either the optical or infrared S^{++} and Ne^{++} ionic fraction. The objects N157B and N79A are not shown here. For an explanation of the symbols see Figure 3.2.

in 30 Doradus one has to lower the T_e [S III] which would in turn make the relation between T_e [S III] and T_e [O III] derived in Sect. 3.4.1.1 even steeper.

The most likely explanation for the differences between the optical and infrared ionic fractions is the difference in the area of the sky covered by the optical driftscan spectra and the ISO-SWS beams. The optical driftscan spectra usually cover a somewhat larger area than the SWS apertures through which the infrared line fluxes have been observed. Our sample objects are all spatially resolved and variations in the ionization structure across the beam can play an important role. This problem is the most severe for large extended objects such as 30 Doradus (positions 10-13 in Figs. 3.2 and 3.3).

3.4.3.3 Ionization correction factors

The most difficult step in the derivation of elemental abundances is the correction one has to make for the unobserved ionic species of an element. The factors used in this correction are commonly called Ionization Correction Factors (ICFs).

An early prescription for ICFs was given by Peimbert & Costero (1969). Based on coincidences of ionization potentials a scheme for the ICFs was developed in which the H II region was divided into two parts. The boundary between these two parts is defined by the ionization potential of O^+ (35.1 eV) and S^{++} (34.8 eV). In this scheme, the low-ionization (N^+, S^+, O^+, Ne^+) and high-ionization species (like O^{++} and Ne^{++}) reside in their own separate parts of the nebula. The ICF for a particular element was then taken to be O/O^+ or O/O^{++} for the low and high-ionization species, respectively.

The simple two-zone model for the ICFs, however, soon broke down. The inclusion of more atomic properties than only the ionization potential (e.g. Natta et al. 1980) and of more processes playing a role in determining the ionization structure (e.g. charge-

transfer reactions) showed the scheme to be oversimplified. This is best seen in the case of sulfur and also argon, for which more elaborate prescriptions for the ICFs had to be constructed.

As a legacy of these early attempts, ionization correction factors are usually given as a function of the fraction O^+/O or O^{++}/O combined with the assumption that $O = O^+ + O^{++}$. The neon and nitrogen abundances are then calculated from the relation

$$\frac{Ne}{Ne^{++}} = \frac{O}{O^{++}} \tag{3.6}$$

and with

$$\frac{N}{N^+} = \frac{O}{O^+}, \tag{3.7}$$

where the ICFs are simply the inverted O^{++}/O and O^+/O fractions.

The correction factors for sulfur and argon are usually derived from fits to photoionization models. Fits to models from Stasińska (1978) give for the sulfur ICFs the relation

$$\frac{S}{S^+ + S^{++}} = \left[1 - \left(1 - \frac{O^+}{O}\right)^{\alpha}\right]^{-1/\alpha} \tag{3.8}$$

with $2 \leq \alpha \leq 3$. This ionization correction factor is also employed for argon (e.g. Oey & Shields 2000). More elaborate prescriptions for sulfur and argon given by Thuan et al. (1995) are

$$\frac{S}{S^+ + S^{++}} = 0.013 + x(5.10 - x(12.78 - x(14.77 - 6.11x)))^{-1} \tag{3.9}$$

$$\frac{Ar}{Ar^{++}} = [\,0.15 + x(2.39 - 2.64x)\,]^{-1} \tag{3.10}$$

with $x \equiv O^+/O$. With our data base including fine-structure lines from species like Ne^+ and S^{+3} it is possible to check the ICFs for neon and sulfur as given in these equations.

The sulfur ICFs as defined in Eqns. 3.8 and 3.9 have been compared with the observed ratio $(S^+ + S^{++} + S^{+3}) / (S^+ + S^{++})$. The results are shown in the left panel of Fig. 3.4. Also shown in this figure is a more recent prescription for the sulfur ICF from Kwitter & Henry (2001). The error bars in this figure give the range of the plotted ratio when using either the optical or infrared S^{++} ionic fraction in the sum.

As can be seen in this figure, the observed sum abundances compare reasonably well with the total abundances predicted by the theoretical ICFs. Many of the observed sulfur abundances agree well with the ICF from Eqn. 3.8 using $\alpha = 3$, and with the ICF from Kwitter & Henry (2001). The prescription for the ICF from Thuan et al. (1995) clearly overpredicts the amount of 'missing' sulfur. The value for α to adopt in Eqn. 3.8 is not completely clear. In the original prescription by Stasińska (1978) the value of 3 was used, but French (1981) took α to be 2. Garnett (1989) pointed out, however, that the use of $\alpha = 2$ severely overpredicts the amount of unobserved sulfur for O^+/O in the range from 0.1 to 0.3. This is clearly seen in Fig. 3.4 where the $\alpha = 2$ ICF is even larger than the one from Thuan et al. (1995). It was also noted by Garnett (1989) that although the use of $\alpha = 3$ gives a good correction for the unobserved sulfur, it seemed to underestimate the missing sulfur for $O^+/O < 0.2$. The ICF from Kwitter & Henry (2001) is even lower in this range.

Given our observational results, we conclude that the prescription for the sulfur ICF given in Eqn. 3.8 with $\alpha = 3$ is fairly accurate for $O^+/O > 0.2$. For $O^+/O < 0.2$ the case is less clear, but one might argue that the ICF as a function of O^+/O is steeper in this range. It is, however, difficult to check this last statement in this work because our only point with $O^+/O < 0.2$ shows a large variation in the $(S^+ + S^{++} + S^{+3}) / (S^+ + S^{++})$ ratio. The number of ionization stages included in the $\sum S^{+i} / (S^+ + S^{++})$ ratio has of course some influence on our results, but with the ionization potential of S^{+3} as high as it is (47.3 eV), we do not think that the inclusion of ionization stages higher than this will change our conclusions.

Shown in the right panel of Figure 3.4 is the comparison between the ICF from Eqn. 3.6 and the $(Ne^+ + Ne^{++}) / Ne^{++}$ ratio. For the error bars in this figure the same remarks apply as for sulfur. The large scatter and uncertainty in the Ne^{++} ionic fraction already noted (cf. section 3.4.3.2) make the situation rather unclear. At first sight, the theoretical ICF for neon seems to underestimate the true neon abundances. The observed Ne / Ne^{++} ratio, however, strongly depends on the ionization structure one happens to find in the beam (i.e. the ratio Ne^+ / Ne^{++}). If for whatever reason the Ne^+/Ne^{++} ratio is increased, the observed Ne / Ne^{++} ratio can quite easily exceed the value predicted by the theoretical ICF. This problem, of course, also plays a role for sulfur, but in this case the S^{+3} ionic fraction is compared to the sum of *two* other ionization stages (of which S^{++} is dominant) so the impact is less. Given this confused state of affairs, we feel that we cannot draw any strong conclusion about the (un)reliability of the neon ICF given in Equation 3.6.

The Ar^+ ionic fraction could unfortunately only be calculated for two of our sample objects, so a comparison of the argon abundance with the theoretical ICFs is difficult. The observed ratio $(Ar^+ + Ar^{++}) / Ar^{++}$ for N160A1 and N160A2 are 1.08 and 1.12, respectively. The argon ICFs for N160A1 and N160A2 are 1.54 and 1.51 using the prescription in Eqn. 3.10. Using Eqn. 3.8, the ICFs are 1.20 and 1.18 for $\alpha = 2.5$, and 1.18 and 1.11 for $\alpha = 3.0$. The latter ICFs are quite close to the $(Ar^+ + Ar^{++}) / Ar^{++}$ ratios found for N160A1 and N160A2, but whether this means that this particular ICF is 'correct' is not clear; the presence of Ar^{+3} would raise the $\sum Ar^{+i} / Ar^{++}$ ratio. The ionization potential of Ar^{++} is about the same as that of Ne^+ (~ 40 eV), so it is conceivable that some Ar^{+3} is present in the source.

The only source for which the presence of Ar^{+3} was detected is 30 Doradus#3 where it showed up in the form of the [Ar IV] 4711 Å line. To get an estimate of the influence of the Ar^{+3} ionic fraction on the $\sum Ar^{+i} / Ar^{++}$ ratio, we derived it for 30 Dor#3. The [Ar IV] 4711 Å line flux in the optical spectra of 30 Dor#3 had a strength of 0.009 relative to Hβ. Using the electron temperature T_e[O III] and density n_e[S II] for this source this gave an Ar^{+3} ionic fraction of 2×10^{-7}. With this fraction, we arrived at an Ar^{+3}/Ar^{++}_{opt} ratio of ~ 0.17. The result of this little exercise clearly shows that the relative contribution of Ar^{+3} to the total Ar abundance can be significant. The warning issued in the previous paragraph is therefore warranted. On the other hand, it should be noted that the derived Ar^{+3} ionic fraction is an upper limit because the [Ar IV] 4711 Å line is blended with the He I 4713 Å line.

The results for the object N157B have not been included in this discussion about the ICFs. This is because the recipes for the ICFs are based on the assumption that the ionization structure within the source is in *photo*ionization equilibrium. The sample

object N157B, however, is a supernova remnant and our line fluxes originate from a radiative shock; the optical spectra of this object show clear evidence of shock enhancement. The ionization structure in a radiative shock is dominated by collisional processes and is not in equilibrium. The ICFs discussed here are therefore not applicable.

3.4.3.4 The full elemental abundances

In the derivation of the full elemental abundances the use of ICFs has been kept to a minimum. No ICF was used to derive the elemental abundance of oxygen, sulfur, helium and neon. The sulfur and neon abundances have been derived by simply summing the ionic fractions. Where optical and infrared ionic fractions were available for the same ion, their average has been used in the sum. For the derivation of the full abundance of nitrogen the ICF given in Eqn. 3.7 was used, and for argon the one in Eqn. 3.8 with $\alpha = 3.0$. The results are given in Table 3.3 together with abundances from the literature. In the case of N79A for which no infrared ionic fractions could be calculated, we also used ICFs for deriving the sulfur and neon abundances. We used the ICFs in Eqn. 3.6 and Eqn. 3.8 with $\alpha = 3.0$, respectively. For N157B only the sum abundances are given because the standard ICFs cannot be applied in the case of an SNR (cf. section 3.4.3.3).

A first look at Table 3.3 shows that within the two subsets of sources (SMC and LMC) the different abundances do not show much variation from source to source; the chemical composition of the sample is rather homogeneous. The nitrogen abundance for the positions in 30 Doradus, however, are lower than those for the other LMC sources. The difference in metallicity between the SMC and LMC is also clearly visible. The average abundances of the SMC are in general a factor 2 to 4 lower than those in the LMC. This is not the case for the helium abundance though which is basically constant throughout the entire sample. A few remarks must be made for some of the elemental abundances.

The oxygen abundance was derived with the assumption that the only two ionization stages of importance were O^+ and O^{++}. This assumption is quite safe because of the high ionization potential of O^{++} (~ 54 eV). The complete absence of He II recombination lines in our optical spectra shows that not many of these high-energy photons are present. The only object for which this assumption might lead to an underestimate of the oxygen abundance is N157B; the [O IV] 25.91 μm line has been detected for this object. The oxygen abundance found throughout the sample is lower than that quoted in the literature. This is mainly the result of the higher electron temperatures T_e [O III] derived in this work which lowers the abundance.

With the ionization potential of neutral sulfur at 10.4 eV and that of S^{+3} at 47.3 eV, the three ionic species S^+, S^{++} and S^{+3} contain most if not all of the sulfur within the H II region. The largest contributor to this abundance is S^{++}. Given the large ionization potential of S^{+3}, we estimate the possible contribution of S^{+4} to the total abundance to be not more than a few percent for the LMC sources. For the SMC sources, this contribution could be slightly larger given the high excitation of these sources ($O^{++}/O \simeq 0.80$). The high sulfur abundance of the object N159-9 is the result of the low T_e [S III] used in the derivation of the S^{++} ionic fraction. The sulfur abundances of N4A and N160A from Pagel et al. (1978) exceed the value found here by a factor of three. However, their sulfur abundance was derived by using the traditional

TABLE 3.3— The full elemental abundances of O, N, S, Ar, Ne and He. A comparison is made with abundances from the literature. The first row for every entry gives the abundances from the present work. The use of ICFs has been limited to the derivation of the full N and Ar abundances. For N79A, however, ICFs have also been used for the derivation of the full elemental abundances of S and Ne (see text).

Object	O/H (10^{-4})	N/H (10^{-6})	S/H (10^{-6})	Ar/H (10^{-6})	Ne/H (10^{-5})	He/H
N81	0.917	2.63	1.38±0.18	0.400±0.102	1.40±0.36	0.082
	0.791[1]	2.16[1]	1.12[1]	0.758[1]	1.49[1]	0.088[1]
	0.994[4]	3.14[4]		0.808[4]	1.73[4]	
N88A	0.780	2.44	1.22±0.35	0.465±0.040	0.945†±0.039	0.089
	1.11[2]	2.20[4]	3.47[2]		2.19[2]	0.078[2]
	0.781[4]				1.42[4]	
N66	1.05	3.61	2.08±0.12	0.650±0.173	2.93±0.09	0.084
	1.66[3]	3.16[3]	6.61[3]	0.812[3]	3.02[3]	0.072[3]
	1.12[4]	4.17[4]			1.95[4]	
N79A	1.46	7.91	7.37	1.34	2.45	0.084
	2.54[4]	10.6[4]			3.63[4]	
N4A	1.97	8.07	5.45±0.12	1.29±0.01	5.06±0.09	0.088
	2.66[5]	11.3[5]	5.99[5]	1.53[5]	3.21[5]	0.08[5]
	2.77[4]	9.83[4]	17.9[4]		5.28[4]	
N83B	1.63	10.8	4.07±1.05	1.09±0.16	2.89±0.35	0.084
	1.94[6]	7.00[6]	4.40[6]		4.00[6]	0.10[6]
N11A(1)	2.09	10.7	4.05±0.78	1.07±0.26	4.17±0.94	0.089
	2.79[7]	7.31[7]	3.89[7]±1.06		5.06[7]	0.085[7]
N11A(2)			5.38±0.15	1.61±0.28	6.00±0.34	
N159-5	1.40	6.87	8.40±0.10	1.62±0.15	8.53±2.07	0.093
	2.33[7]	7.68[7]	3.78[7]±0.84		1.90[7]	0.092[7]
	2.09[4]	6.98[4]			3.98[4]	
N157B	1.51	4.77‡	6.15±0.44	1.09‡±0.05	5.17±1.00	0.097
30 Dor#1	1.76	4.25	6.99±2.02	1.43±0.25	7.67	0.087
	2.12[8]	7.63[8]	5.09[8]	1.06[8]	3.58[8]	0.081[9]
	2.03[9]	5.71[9]	4.63[9]±0.09	1.79[9]±0.17	6.08[9]±0.88	
	2.57[3]	6.17[3]	7.94[3]	1.38[3]	5.13[3]	
30 Dor#2	1.88	2.86	6.29±1.48	1.19±0.15	6.86±1.21	0.091
30 Dor#3	1.79	6.96	6.60±0.59	1.62±0.18	6.85±1.03	0.094
30 Dor#4	1.85	5.26	7.61±2.69	1.28±0.36	8.65±1.75	0.086
N160A1	2.15	9.94	7.79±0.45	1.48⋆±0.04	6.68±0.86	0.087
	2.76[7]	8.08[7]	6.57[7]±1.92	1.26[4]	6.33[7]	0.087[7]
	2.78[4]	8.13[4]	18.2[4]		5.01[4]	
N160A2	2.24	10.3	6.46±0.42	1.51⋆±0.02	5.73±0.02	0.084
	2.16[7]	6.57[7]	4.88[7]±1.32	1.26[4]	4.48[7]	0.081[7]
	2.78[4]	8.13[4]	18.2[4]		5.01[4]	

† : only the Ne^{++} fraction is given. ‡ : no ICF was used. ⋆ : the sum abundance $Ar^{+} + Ar^{++}$ is given.
1 : Heydari-Malayeri et al. (1988) 2 : Testor & Pakull (1985) 3 : Shaver et al. (1983) 4 : Pagel et al. (1978)
5 : Heydari-Malayeri & Lecavalier des Etangs (1994) 6 : Heydari-Malayeri, Van Drom & Leisy (1990)
7 : Heydari-Malayeri & Testor (1986) 8 : Rosa & Mathis (1987) 9 : Mathis, Chu & Peterson (1985)

ICF (O/O^+) which severely overestimates the missing sulfur.

Except for our sample objects N160A1 and A2, the argon abundance was derived by using an ICF. Our abundances agree well with the literature values, but for N81 our argon abundance is off by a factor of two when compared with the results from Heydari-Malayeri et al. (1988) and Pagel et al. (1978). These authors, however, assumed an argon ICF ≥ 2 which is quite likely too high (cf. section 3.4.3.3).

No correction has been made for the possible presence of neutral helium. We think that given the high excitation of our sample sources ($0.53 < O^{++}/O < 0.84$) the contribution of the neutral species is negligible. Furthermore, all the optical spectra used in this study show He I 5875 / Hβ to be ~ 12 which indicates helium to be singly ionized throughout the H II region (e.g. Kennicutt et al. 2000).

For the uncertainty on the full elemental abundances we made the following estimates. The oxygen abundance is reliable within $\sim 20\%$, and the uncertainty on the sulfur abundance is in the order of 40%. The case for neon is complicated because of the large uncertainties on the Ne^{++} ionic fraction and the relative contribution of Ne^+ to the total neon abundance. We assigned an uncertainty of at least 50% to the neon abundance. The uncertainty on the helium abundance is estimated to be $\leq 10\%$. For the abundance of argon and nitrogen the assessment of the uncertainty is more difficult because of the use of an ICF to derive them. The total error on these abundances stems from the error on the ionic fractions (N^+, Ar^{++}) and from the uncertainty in the O/O^+ ratio used in the ICF. Given a typical error of $\sim 20\%$ on the O/O^+ ratio and of 12% on the N^+ ionic fraction the uncertainty on the nitrogen abundance is estimated to be 25%. The propagation of the errors on the Ar^{++} ionic fraction and on the O/O^+ ratio through Eqn. 3.8 yielded a typical uncertainty of $\sim 20\%$ on the total argon abundance.

3.5 The R23 and S23(4) abundance indicators

To derive reliable elemental abundances, a good determination of the electron temperature is needed. Other means of deriving abundances must be employed if no temperature can be derived. This is for example the case for H II regions in metal-rich galaxies where the [O III] 4363 Å line is seldom detected. The best known of these alternative methods is the so called 'bright-line' method, where the bright emission lines from all the important ionization stages of an element are summed to get an estimate of its abundance. Examples of these are the R23 and S23 parameters for the oxygen and sulfur abundance, respectively (e.g. Pagel et al. 1979; Vílchez & Esteban 1996). The R23 parameter is defined as

$$\mathrm{R23} = \frac{[\mathrm{O\,III}]\,5007, 4959 + [\mathrm{O\,II}]\,3727}{\mathrm{H}\beta}, \tag{3.11}$$

and the S23 parameter as

$$\mathrm{S23} = \frac{[\mathrm{S\,III}]\,9068, 9532 + [\mathrm{S\,II}]\,6717, 6730}{\mathrm{H}\beta}. \tag{3.12}$$

The link between the observed R23 and S23 parameters and the actual O and S abundances is usually provided by photoionization models.

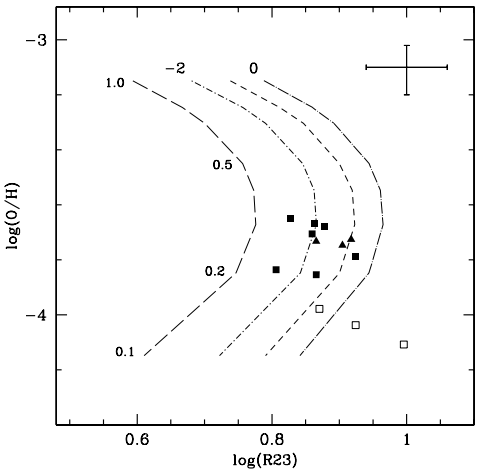

FIGURE 3.5— The O abundance plotted against the R23 diagnostic. The model calculations for $\log U = 0$, -1, -2 and -3 are shown. Shown in the upper right corner is a typical errorbar. For an explanation of the symbols see Figure 3.2.

Although the R23 and S23 parameters have proven themselves to be useful abundance indicators, they suffer from a few problems. The worst of these is the degenerate nature of the indicators, showing a low and a high-metallicity branch (see Fig. 3.5). This degeneracy can only be broken by invoking some other parameters like the [O III] 5007/[N II] 6583 ratio (Edmunds & Pagel 1984) for R23. In addition to this problem, the location of the inflection point of the parameter is poorly constrained, and the low-metallicity branch is very sensitive to changes in nebular parameters (especially to changes in the ionization parameter U).

These problems with the R23 and S23 parameters have prompted several authors to calibrate the abundance indicators empirically (e.g. Dopita & Evans 1986; McGaugh 1991; Díaz & Pérez-Montero 2000). We do not have enough data points to perform such a calibration here, but we can check the robustness of these parameters to the effects of incomplete spatial coverage of the objects and to variations in the spatial extent of the observed objects. We therefore plot our oxygen and sulfur abundances against the R23 and S23 parameters as defined in Eqns. 3.11 and 3.12 in Figure 3.5 and the lefthand panel of Figure 3.6, respectively. We overplot our points with a small grid of general photoionization models, which was calculated using CLOUDY for a range of metallicities between 0.05 and 2.0 $Z_\odot$, and for the ionization parameters $\log U = -3$, -2, -1 and 0. The stellar atmosphere used was the D2 CoStar model from Schaerer & de Koter (1997). The hydrogen density was fixed at 500 cm^{-3} and the inner radius of the central cavity of the model was set at 10^{17} cm.

As can be seen in Fig. 3.5, our LMC sources lie in the turnabout region of the R23 relation which is located around $12 + \log(\mathrm{O/H}) = 8.4$. All the LMC objects have about the same oxygen abundance (a bit lower for N79A and N159-5) and, within the uncertainties, also the same value for the R23 parameter. A similar good correspondence between the oxygen abundance and the R23 parameter is also found for our pointings in 30 Doradus. Given the fact that our spectra undersample this object spatially and that the different pointings in 30 Dor are spaced widely apart, this is encouraging. The case is less clear for our SMC sources though. The SMC object N66 falls between the model

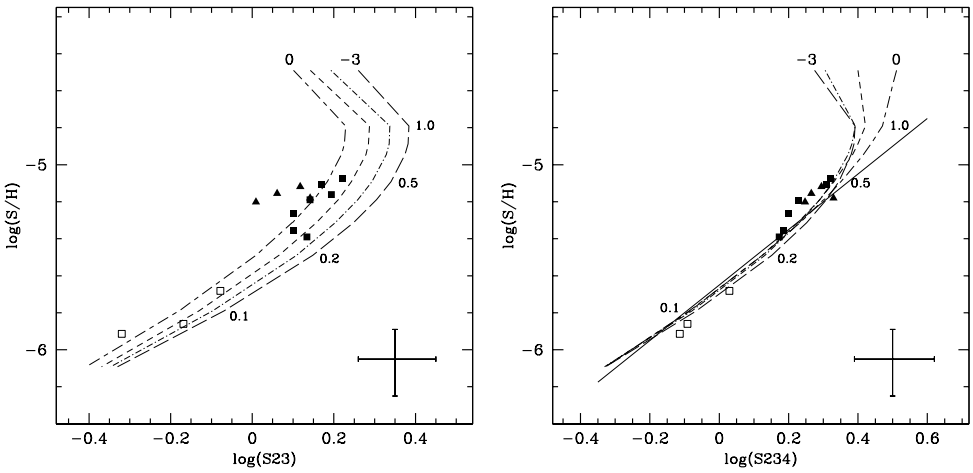

FIGURE 3.6— The S abundance plotted against the S23 and S234 diagnostics, respectively. The model calculations for $\log U = 0$, -1, -2 and -3 are shown. The fit to the models of S234 is shown as a solid line. Shown in the lower right corner is a typical errorbar. For an explanation of the symbols see Figure 3.2.

curves for $\log U = 0$ and -1, but although the oxygen abundance is lower, the object has about the same value for the R23 parameter as most of our LMC sources. The strong dependence of the low-metallicity branch of the R23 relation on the ionization parameter likely plays a role here. The SMC sources N81 and especially N88A deviate substantially from the model curves, but this is the result of the high [O III]/Hβ line ratio for these objects (see chapter 2).

We might conclude that when looking at the LMC sources the R23 parameter seems to be robust to variations in spatial extent and coverage of the object. The uncertainties in the calibration of the low-metallicity branch of R23 and the exceptionally strong [O III] lines in the spectra of N81 and N88A, however, prevent us from extending this conclusion to the SMC sources. It should be mentioned that the different oxygen abundances and R23 parameters have been derived from a mix of stationary longslit and driftscan spectra.

The S23 parameter is, just like R23, double-valued, but the turnabout point lies at a higher metallicity (~ 0.5 Z$_\odot$). The values of the S23 parameter for our sources plotted in the left panel of Fig. 3.6 show a similar picture as R23; there is a rough correspondence between a given value of S23 and the sulfur abundance. The conclusion as drawn for R23, however, is substantially less solid for S23 because of the much larger uncertainties on both the observed S23 parameter and the sulfur abundance. Note that the direction in which the ionization parameter increases for S23 is reversed when compared to the R23 parameter. Also note that the $\log U$ predicted by S23 is slightly higher than for the R23 parameter. Whether or not the low-metallicity branch of the S23 relation is less sensitive to the ionization parameter than for R23 is stil unclear. We find it to be less sensitive for our models.

Because of the similar ionization potentials of O^+ and S^{++} it might be expected

that S^{+3} plays an important role in the ionization balance. The S23 parameter has therefore been refined by including this ion in the expanded parameter S234 (Oey & Shields 2000). The new parameter S234 was defined as

$$\mathrm{S234} = \mathrm{S23} + \frac{[\mathrm{S\,IV}]\,10.5\,\mu\mathrm{m}}{\mathrm{H}\beta}, \tag{3.13}$$

including the [S IV] 10.5 μm line. A grid of generalized photoionization models calculated by Oey & Shields (2000) showed the S234 parameter to be very robust to changes in the ionization parameter U, which greatly enhances the usefulness of S234 as an abundance indicator. The lack of [S IV] 10.5 μm fluxes and of directly determined S^{+3} ionic fractions made it, however, difficult for these authors to check the reliability of the S234 parameter.

Our new sulfur abundances and the availability of the [S IV] 10.5 μm line in our data base allow such a check. The correlation between the sulfur abundances and the observed values for S234 is shown in the right panel of Figure 3.6. Our analysis results agree well with the theoretical tracks. The insensitivity of the S234 parameter to changes in the ionization parameter as noted by Oey & Shields (2000) is confirmed by our models; for low metallicities, the different $\log U$ tracks almost completely overlap. For metallicities higher than about 0.5 $Z_\odot$, however, the models start to diverge. This is also roughly the location where the relation starts to bend back on itself. These results prove the usefulness and reliability of the newly proposed abundance indicator.

Given the tight overlap between the different $\log U$ curves we made a rough fit to the theoretical models. The following relation was found between log(S234) and log(S/H)

$$\log(\mathrm{S/H}) = -5.65 + 1.50\,\log(\mathrm{S234}). \tag{3.14}$$

The fit is plotted in the right panel of Figure 3.6 (solid line). Our fit to the models is steeper and has its intercept at a somewhat lower sulfur abundance than the one found by Oey & Shields (2000). One should be cautious with the use of this relation for $\log(\mathrm{S234}) \geq 0.3$, because here the (S/H)−(S234) relations predicted by the various models start to diverge. Its use is therefore limited to metallicities lower than $\sim 0.5\,Z_\odot$.

3.6 Nucleosynthetic aspects

Important constraints to stellar nucleosynthesis and to the star-formation history of a galaxy are provided by the ratio of the heavy element abundances to the oxygen abundance. The heavy element-to-oxygen ratios of elements like sulfur and neon provide information about the different rates at which these are produced in stars, whereas the nitrogen-to-oxygen ratio gives information about the initial mass function of generations of stars formed in the past (e.g. Henry & Worthey 1999). The heavy element-to-oxygen abundance ratios for sulfur, nitrogen, argon and neon for our sample objects are shown in Figure 3.7. Also plotted in this figure are the values from Kobulnicky & Skillman (1996, 1997) and Izotov & Thuan (1999, IT99). The sample of IT99 consists of observations of giant H II regions in low-metallicity blue compact galaxies with oxygen abundances $12 + \log(\mathrm{O/H})$ between 7.1 and 8.3. The Magellanic sources in the present work add to the high-metallicity end of this range.

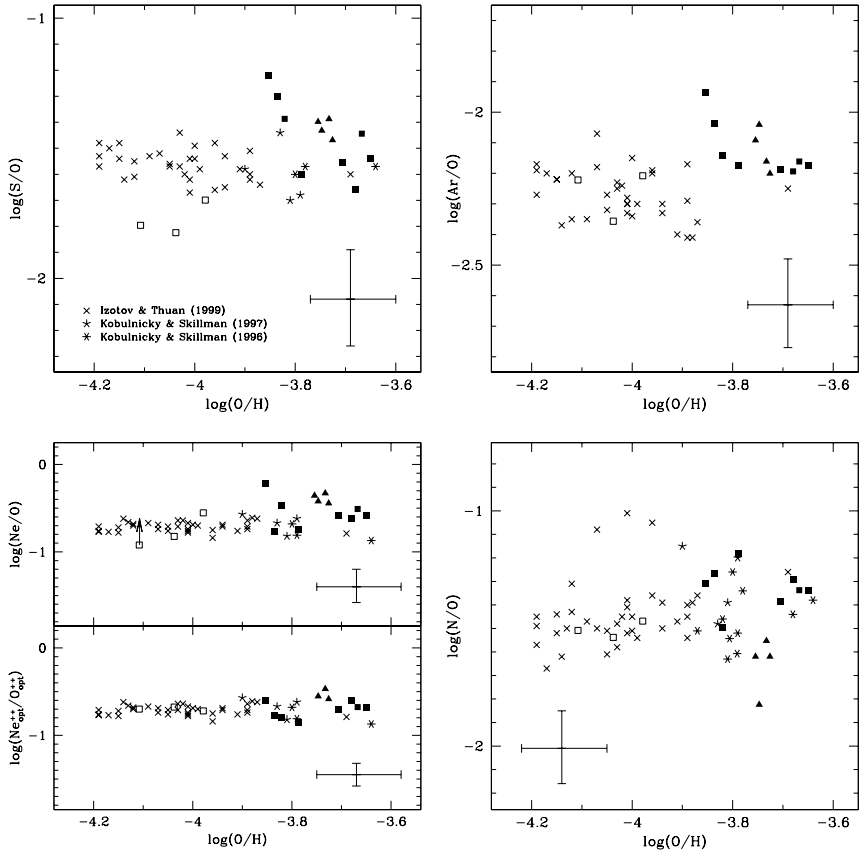

FIGURE 3.7— The heavy element-to-oxygen abundance ratios S/O, Ar/O, Ne/O and N/O for our sample objects. Also shown in the lower left panel is the ($Ne^{++}_{opt}/O^{++}_{opt}$) ratio. In every panel a typical error bar is shown. For an explanation of the symbols designating the Magellanic sources see Figure 3.2.

All the heavy element-to-oxygen abundance ratios found for our sample are comparable to the ones in the literature. They show no dependency on the oxygen abundance which indicates the primary origin of the heavy elements. We find -1.48 ± 0.18 for log<S/O> and -2.14 ± 0.10 for log<Ar/O>. These values are very similar to the -1.55 ± 0.06 and -2.27 ± 0.10, respectively, found by IT99 for their high-metallicity subsample ($12+\log(O/H)>7.6$). Note that our Ar/O values are all at the high end of the distribution of values.

The log<Ne/O> for our sources of -0.52 ± 0.20 is higher than the -0.72 ± 0.06 found by IT99. However, the neon abundance derived for our sources is rather uncertain because of the sometimes large discrepancies between the infrared and optical Ne^{++} ionic fractions and of the suspiciously large relative contribution of Ne^{+} to the total neon abundance. This uncertainty is clearly seen in our Ne/O ratios which show a

large scatter (see lower left panel of Fig. 3.7, upper half). In the derivation of the Ne/O abundance ratio both Kobulnicky & Skillman (1996, 1997) and IT99 use the equality $Ne^{++}/O^{++} = Ne/O$ (see also Eqn. 3.6). We can therefore test our suspicion by plotting our $Ne^{++}_{opt}/O^{++}_{opt}$ ratios together with the Ne/O ratios from these authors (lower left panel of Fig. 3.7, lower half). It is pretty obvious from this figure that the scatter is greatly reduced when compared to the upper half of the panel. The $\log<Ne^{++}_{opt}/O^{++}_{opt}>$ is -0.66 ± 0.12, in agreement with the $\log<Ne/O>$ of IT99.

The evolution of nitrogen has long been a subject of debate, not only because of the bimodal nature of the element (primary/secondary), but also because of the precise origin of the primary component of the total nitrogen abundance (IT99; Henry et al. 2000). The average N/O abundance ratio for the objects in our sample is $\log<N/O>=-1.42 \pm 0.20$ (compare with IT99 -1.46 ± 0.14), and no correlation with the oxygen abundance is seen (see Fig. 3.7, lower right). This shows the nitrogen to be of mostly primary origin, which is in line with predictions that the contribution of secondary nitrogen to the total abundance is negligible for metallicities lower than $12 + \log(O/H) < 8.3$ (e.g. Shields et al. 1991).

Despite the fact that all our oxygen abundances for the LMC lie in a very narrow range we see some considerable scatter in the N/O ratio. Variations in the N/O ratio at a given metallicity have been established by several authors (e.g. Vila-Costas & Edmunds 1993; Marconi et al. 1994), but the underlying cause for this scatter is unsure. Pollution of the interstellar gas by W-R stars has been proposed as a mechanism for the observed local enhancements in the N/O ratio (Pagel et al. 1986), but Kobulnicky & Skillman (1998) oppose this view. The different time-scales in which nitrogen and oxygen are released into the interstellar medium also play an important role, but here things are unclear because of the question whether primary nitrogen is exclusively formed in intermediate-mass stars or is also produced in significant amounts in high-mass stars. Variations in the efficiency with which the newly produced nitrogen is dispersed through a galaxy and the possibility of differential outflow of nitrogen and oxygen add yet another layer of uncertainty. It is outside the scope of this paper to discuss which of these possible scenarios might be applicable to the LMC. Moreover, the uncertainties in our derived abundances are such that it is hard to say whether the scatter is really due to local enrichment.

3.7 Summary

Based on optical spectra and infrared data obtained with ISO-SWS/LWS, the temperature and density structure of a sample of Magellanic Cloud H II regions was determined. From this structure, new elemental abundances have been calculated for our sources.

The electron temperatures were derived for the O^+, O^{++} and S^{++} ionization zones from optical/optical line ratios. These were confronted with relations between the various temperatures from the literature. We concluded that the relation between T_e[O III] and T_e[O II] is fairly accurate. The relation between T_e[O III] and T_e[S III], however, appeared to be slightly steeper, so we derived a new, empirical relation between these two temperatures. The issue of small-scale temperature fluctuations within an emitting zone (the t^2 problem) could not be addressed through optical/infrared line ratios because of the incompatibility of the optical and infrared line fluxes. Electron densities

were derived for the same ionization zones as the temperatures using optical/optical and infrared/infrared line ratios. The derived densities for the different zones were all comparable, but suffered from the fact that the various fine-structure lines used in their derivation have been observed through various apertures.

Using these electron gas properties and our combined optical/infrared data base, we derived a new set of elemental abundances. Where possible, the individual ionic fractions were calculated with the electron gas properties of the corresponding ionization zone. An estimate of the uncertainties on the different ionic fractions was given. We compared the Ar^{++} and S^{++} ionic fractions as derived from the infrared and optical lines and found them to agree well. However, the infrared and optical Ne^{++} ionic fractions sometimes differed considerably. The full elemental abundances were calculated, when possible, without using ICFs. We compared the commonly used recipes for the sulfur and neon ICFs with the abundances derived from adding the different ionic fractions. We concluded that the sulfur ICF from Stasińska (1978) with $\alpha = 3$ is fairly accurate for $O^+/O > 0.2$. The validity of this ICF for $O^+/O < 0.2$ was less clear. Given the uncertainty in the neon abundance and the absence of an Ar^+ ionic fraction, no reliable comparison with the ICFs for neon and argon could be made.

We compared our spectra and the newly derived abundances with the bright-line abundance indicators R23 and S23(4). For this purpose, we computed a small grid of photoionization models. The small number of data points prevented us from calibrating these indicators empirically, but we checked their robustness for spatial undersampling of the sample objects and variations in their spatial extent. The [S IV] 10.5 μm line in our data base and the S^{+3} ionic fraction directly derived from this allowed us to check the newly proposed abundance indicator S234 empirically. The S234 data points from our sample agreed well with the models, which show the S234 abundance indicator to be highly insensitive to the ionization parameter.

The heavy element-to-oxygen abundance ratios from our sources have been compared with those found for giant extragalactic H II regions in a large sample of low-metallicity blue compact galaxies (IT99). With our Magellanic Cloud sources we add to the high-metallicity end of this sample. Also included in the comparison are the results from Kobulnicky & Skillman (1996, 1997) for the irregular galaxies NGC 1569 and 4214. The average element-to-oxygen abundance ratios from our sources were comparable to the ones found in the literature and none of these showed any correlation with the oxygen abundance.

References

Benjamin, R.A., Skillman, E.D., Smits, D.P. 1999, ApJ **514**, 307
Biemont, E., Bromage, G.E. 1983, MNRAS **205**, 1085
Butler, K., Zeippen, C.J. 1994, A&AS **108**, 1
Cai, W., Pradhan, A.K. 1993, ApJS **88**, 329
Clegg, P.E., Ade, P.A.R., Armand, C. et al 1996, A&A **315**, L38
de Graauw, Th., Haser, L.N., Beintema, D.A. et al. 1996, A&A **315**, L49
Dennefeld, M., Stasińska, G. 1983, A&A **118**, 234
Díaz, A.I., Pérez-Montero, E. 2000, MNRAS **312**, 130
Dopita, M.A., Evans, I.N. 1986, ApJ **307**, 431

Edmunds, M.G., Pagel, B.E.J. 1984, MNRAS **211**, 507
French, H.B. 1981, ApJ **246**, 434
Galavis, M.E., Mendoza, C, Zeippen, C.J. 1995, A&AS **111**, 347
Galavis, M.E., Mendoza, C, Zeippen, C.J. 1997, A&AS **123**, 159
Garnett, D. 1989, ApJ **345**, 282
Garnett, D. 1992, AJ **103**, 1330
Henry, R.B.C., Worthey, G. 1999, PASP **111**, 919
Henry, R.B.C., Edmunds, M.G., Köppen, J. 2000, ApJ **541**, 660
Heydari-Malayeri, M., Testor, G. 1986, A&A **162**, 180
Heydari-Malayeri, M., Le Bertre, T, Magain, P. 1988, A&A **195**, 230
Heydari-Malayeri, M., Van Drom, E., Leisy, P. 1990, A&A **240**, 481
Heydari-Malayeri, M., Lecavelier des Etangs, A. 1994, A&A **291**, 960
Izotov, Y.I., Thuan, T.X. 1999, ApJ **511**, 639
Kennicutt Jr, R.C., Bresolin, F., French, H., Martin, P. 2000, ApJ **537**, 589
Kessler, M.F., Steinz, J.A., Anderegg, M.E. et al. 1996, A&A **315**, L27
Kobulnicky, H.A., Skillman, E.D. 1996, ApJ **471**, 211
Kobulnicky, H.A., Skillman, E.D. 1997, ApJ **489**, 636
Kobulnicky, H.A., Skillman, E.D. 1998, ApJ **497**, 601
Kwitter, K.B., Henry, R.B.C. 2001, ApJ **562**, 804
Lennon, D.J., Burke, V.M. 1994, A&AS **103**, 273
Marconi, G., Matteucci, F., Tosi, M. 1994, MNRAS **270**, 35
Mathis, J.S., Chu, Y.-H., Peterson, D.E. 1985, ApJ **292**, 155
Mendoza, C. 1983, IAU Symp. 103 : Planetary Nebulae, 143
Mendoza, C., Zeippen, C.J. 1983, MNRAS **202**, 981
McGaugh, S.S. 1991, ApJ **380**, 140
McLauglin, B.M., Bell, K.L. 1998, J. Phys. B **31**, 4317
Natta, A., Panagia, N., Preite-Martinez, A. 1980, ApJ **242**, 596
Oey, M.S., Shields, J.C. 2000, ApJ **539**, 687
Pagel, B.E.J., Edmunds, M.G., Fosbury, R.A.E. et al. 1978, MNRAS **184**, 569
Pagel, B.E.J., Edmunds, M.G., Blackwell, D.E. et al. 1979, MNRAS **189**, 95
Pagel, B.E.J., Terlevich, R.J., Melnick, J. 1986, PASP **98**, 1005
Pagel, B.E.J., Tautvaišienė, G. 1998, MNRAS **299**, 535
Pelan, J., Berrington, K.A. 1995, A&AS **110**, 209
Peimbert, M. 1967, ApJ **150**, 825
Peimbert, M., Costero, R. 1969, *Bol. Obs. Tonantzintla y Tacubaya* **5**, 3
Reed, B.C. 1989, AmJPh **57**, 642
Rosa, M., Mathis, J.S. 1987, ApJ **317**, 163
Russell, S.C., Dopita, M.A. 1992, ApJ **384**, 508
Saraph, H.E., Tully, J.A. 1994, A&AS **107**, 29
Saraph, H.E., Storey, P.J. 1999, A&AS **134**, 369
Schaerer, D., de Koter, A. 1997, A&A **322**, 598
Shaver, P.A., McGee, R.X., Newton, L.M. et al. 1983, MNRAS **204**, 53
Shields, G.A., Skillman, E.D., Kennicutt, R.C. 1991, ApJ **371**, 82
Stasińska, G. 1978, A&A **66**, 257
Storey, P.J., Hummer, D.G. 1995, MNRAS **272**, 41
Testor, G., Pakull, M. 1985, A&A **145**, 170

Tsujimoto, T., Nomoto, K., Yoshii, Y. et al. 1995, MNRAS **277**, 945
Thuan, T.X., Izotov, Y.I., Lipovetsky V.A. 1995 **ApJ**, 445, 108
Vila-Costas, M.B., Edmunds, M.G. 1993, MNRAS **265**, 199
Vílchez, J.M., Esteban, C. 1996, MNRAS **280**, 720

Chapter 4

The physical structure of Magellanic Cloud H II regions : the giant LMC H II region 30 Doradus[1]

BASED on 35 spectral positions in the core of the giant LMC H II region 30 Doradus, we investigate the variation in spectral characteristics and chemical composition of the nebula as a function of the projected radial distance from the ionizing source R 136. The robustness of spectral parameters commonly used in nebular studies when measured at various positions in a spatially resolved nebula is investigated. We find the following results: (*a*) good correlations exist between the various high and low-ionization lines of the different spectra, which is indicative of a well-defined ionization structure. The ionization parameter as traced by the [O II]/[O III] and [S II]/[S III] line ratios is well constrained across the nebula, and the Vilchez & Pagel (1988) η' parameter turns out to vary only slightly from position to position. (*b*) There is no evidence for chemical enrichment in 30 Dor, and no variation of the abundances with increasing projected radial distance from R 136 is seen. The heavy element-to-oxygen ratios for sulfur, argon and neon do not deviate from the commonly found values. However, we do find a radial increase in the nitrogen abundance and N/O ratio. We discuss the role of line-of-sight effects in producing these gradients, and we conclude that the observed gradients are not real. (*c*) The bright-line abundance parameters for oxygen and sulfur are very constant across the nebula, and show a well defined connection between their measured value and the directly derived abundances. (*d*) To investigate to what extent the analysis results from spatially resolved spectra compare to those derived from a spatially integrated spectrum, we created an artificial global spectrum for 30 Doradus by summing the fluxes from the separate spectra. All the analysis results from the global spectrum agree very well with those derived from the separate spectra.

[1]Based on Vermeij, R. & Van der Hulst, J.M., in preparation

4.1 Introduction

The giant H II region 30 Doradus is quite easily one of the most productive sites of star formation in the Large Magellanic Cloud. Powered by the incredibly rich stellar cluster R 136, the nebula can be considered to be the result of a miniature starburst. This central engine of 30 Dor is one of the more recent products of the ongoing star formation in the complex, and it contains more than 30 of the most massive stars known (Massey & Hunter 1998). Apart from the burst of star formation that spawned R 136, at least four other phases of star formation have been identified (Walborn & Blades 1997). Any one of these phases of star formation leaves its mark on the chemical composition of the local interstellar medium (ISM), either through supernova explosions enriching the ISM or through mass-loss of massive stars. Nebular abundance studies are therefore an important tool for unravelling the complicated star-formation history of the region.

In a similar way, nebular abundance studies of H II regions in more distant galaxies provide us with information on the star-formation history of their hosts. Unlike studies of relatively nearby H II regions, however, these extragalactic abundance studies are often based on spatially *un*resolved spectra, with the inevitable result that the observational beam encompasses entire complexes of giant H II regions. Variations across the beam in e.g. excitation conditions are smeared out, and one key question is whether these spatially integrated spectra are truly representative for the global conditions in the H II region as a whole. These problems hamper the interpretation of the derived chemical composition of the nebula. More often than not in extragalactic studies, abundance parameters based on bright spectral lines are the only means by which abundances can be derived (Pagel et al. 1979; Vílchez & Esteban 1996). The usefulness of these common nebular tools in the case of spatially unresolved spectra is therefore a major issue.

We present in this chapter a new set of optical longslit spectra covering the central region of 30 Doradus. The goal of this chapter is twofold. Our main goal is to give a new analysis of the chemical composition of the nebula and to examine the spatial variation of the abundances as a function of projected radial distance from R 136. Secondly, using 30 Doradus as a template object for more distant giant H II regions, we use the spatially resolved spectra to check the reliability of important nebular analysis tools when measured at various positions in the nebula. The organisation of the chapter is as follows. In Sect. 4.2 we introduce the data set. The abundance analysis is described in Sect. 4.3. The ionization structure of 30 Dor as reflected in its spectral characteristics and the results of the abundance analysis are discussed in Sect. 4.4. Using the newly derived abundances, we investigate the robustness of the oxygen and sulfur 'bright-line' abundance parameters in Sect. 4.5. By way of an experiment, we analyze in Sect. 4.6 an 'integrated' global spectrum of 30 Doradus and compare the results with those found from the separate spectra. Finally, in Sect. 4.7 we give a summary of our results.

4.2 Observations and data reduction

The data used in this work consist of twelve longslit spectra obtained with the Boller & Chivens Spectrograph on the ESO 1.52m telescope in the course of three nights in December 1995. The log of the setup used in these observations is given in Table 4.1. The slit length was set to 4.′1 by windowing down the detector to 300×2048 pixels.

TABLE 4.1— The log of the observations made in December 1995.

Observing date	13/16 Dec 1995	Slit width	1″.7
Detector	Ford Aerospace 2048L, 15 μm pixels	Slit length	4′.1
Grating	Grating #2, 300 gr mm^{-1}	Spatial resolution	0″.81 pix^{-1}
Spectral range	2880 Å - 10550 Å	Spectral resolution	3.8 Å pix^{-1}

The slit positions were taken at intervals of about 4-5″ covering the whole inner part of 30 Doradus. Care was taken to minimize the effects of differential refraction. During the observation of slit positions VI and VII (see Fig. 4.1) conditions were not completely photometric due to cirrus. For reasons that will be explained later, the 1D-spectra extracted from the longslit spectra have been divided into two groups.

The data were reduced with the *Image Reduction and Analysis Facility* (IRAF) V2.11. The first reduction steps consisted of the usual ones of bias subtraction, flatfielding and cosmic ray removal. Wavelength calibration was achieved with Helium-Argon lamp exposures taken at various times every observing night. For the flux calibration, spectra were taken from the standard stars Feige 24, L 745-46A and G 99-37. A correction for atmospheric extinction was made with a standard extinction curve for the site. A full and detailed account of the reduction proces is given in chapter 2 of this thesis.

The subtraction of nightsky lines was difficult because the nebulosity frequently filled the whole slit. This problem was most severe for the Hα, Hβ, [O III] 5007 Å and [O III] 4959 Å lines. The identification of lines in the far red would be very difficult without nightsky subtraction, so this reduction step could not be skipped. However, to be able to asses the impact of the nightsky subtraction on the flux of the affected lines, two versions of the fully reduced 2D-spectra were made, one with and one without the nightsky lines subtracted. The effect of the nightsky subtraction on the hydrogen and [O III] line fluxes was determined by measuring their fluxes in both versions of the spectrum. Any differences found in the fluxes of these lines was treated as an extra source of uncertainty.

The nightsky subtraction was not alway completely perfect. Near the He I 5875 Å, [O I] 6302 Å and [S III] 6312 Å lines, the nightsky lines were sometimes clearly oversubtracted. The important [S III] 6312 Å line is therefore limited in its use of an electron temperature indicator.

The 1D-spectra were extracted with apertures of typically 20-30 pixels wide (16-24 arcseconds). The placing of every aperture is shown in Fig. 4.1. Examples of the resultant reddened 1D-spectra are given in Fig. 4.2 for the positions V-c (right panel) and V-d. Line fluxes were derived from the 1D-spectra with the SPLOT package. Every line flux was determined from pixel integration. To get an estimate of the uncertainty in the flux due to noise and uncertainties in the position of the underlying continuum the flux was measured several times.

The extinction correction of the 1D-spectra was based on the Balmer decrements of Hα, Hγ and Hδ relative to Hβ. The Baker & Menzel (1938) Case B values from Storey & Hummer (1995) for T_e = 10 000 Kelvin and n_e = 100 cm^{-3} were taken as the dereddened decrements. Instead of using a standard extinction curve towards the Large Magellanic Cloud the necessary extinction correction was derived from the

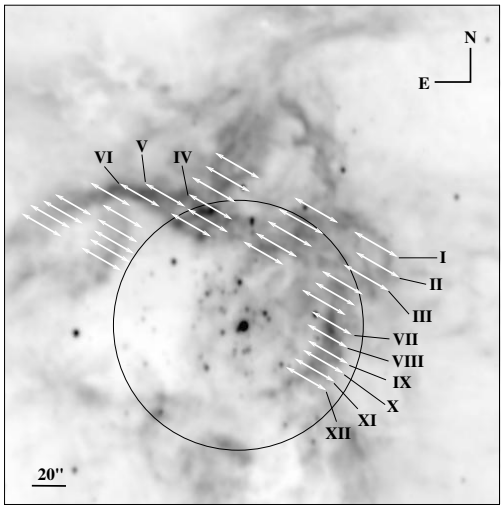

FIGURE 4.1— The positions of the extracted 1D-spectra. The slit positions are numbered I-XII from north to south. The circle defines the boundary between the inner and outer group of spectra.

spectra themselves. To this end, for every 1D-spectrum a function was fitted to the logarithmic ratio of the theoretical and observed Balmer-decrements. The function fitted was of the form

$$f(\lambda) = a\,\mathrm{e}^{-b\,\lambda} + c \equiv -0.4\,E(\beta - \lambda) \tag{4.1}$$

where the parameter c was constrained by the boundary condition $f(\mathrm{H}\beta) = 0$. The average of all the separately derived extinction curves is shown in Fig. 4.3. This average has been determined after having divided the extinction curves by their corresponding color excess $\mathrm{E}(\beta - \alpha)$. Also shown in this figure are the two most extreme of the normalized, separate curves, as well as the standard deviation in the average curve as a function of wavelength. We compared the average curve with the extinction curve towards the Magellanic Clouds as parametrized by Howarth (1983). We plot this curve in Fig. 4.3 for six wavelengths. The conversion factor between $\mathrm{E(B-V)}$ and $\mathrm{E}(\beta - \alpha)$ adopted for this comparsion was 0.84 (Caplan & Deharveng 1986). Our curves are flatter at the red end of the spectra and steeper at the blue end, but in the spectral range from 4500 Å to $\sim$ 7500 Å our curves are nearly indistinguishable from the average curve from Howarth (1983). The extinction correction was then applied to the 1D-spectra with the relation

$$\log(I_\lambda/I_\beta) = \log(F_\lambda/F_\beta) + f(\lambda), \tag{4.2}$$

where $\mathrm{I}_\lambda/\mathrm{I}_\beta$ and $\mathrm{F}_\lambda/\mathrm{F}_\beta$ are the dereddened and reddened fluxes relative to Hβ respectively. The dereddened 1D-spectra are given in Tables 4.2 to 4.8. The different 1D-spectra extracted from every slit position are given the numbers I through XII going from north to south, and the letters *a* through *d* going from west to east. The uncertainties in the fluxes arise from noise, uncertainties in the continuum fitting and a flux-calibration error of $\sim$4% (see chapter 2).

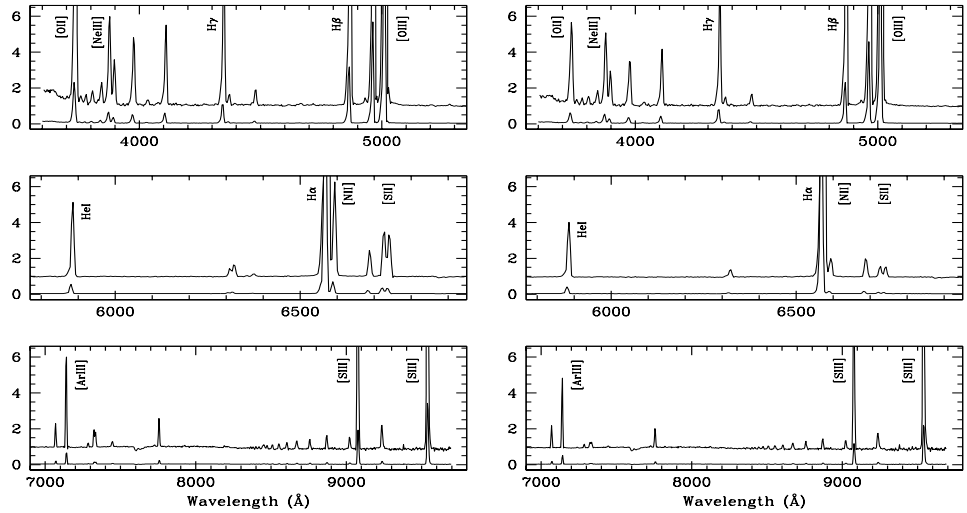

FIGURE 4.2— The least excited outer group spectrum (*left*) and most excited inner group spectrum (*right*) representing the extremes in terms of excitation (not corrected for extinction). The vertical axis shows the flux density in units of 10^{-13}ergs s^{-1}Å^{-1}. To bring out the fainter lines, every panel has been overplotted with the spectrum magnified by a factor of eight in the Y direction. The most important lines are labelled.

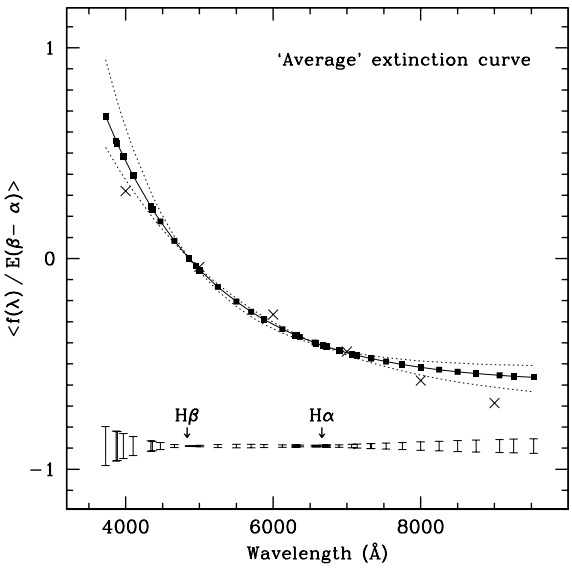

FIGURE 4.3— The average extinction curve $< f_\lambda/E(\beta-\alpha) >$ as derived from the fits to the separate spectra. The standard deviation of the average curve as function of wavelength is shown below. Shown as dotted lines are the two most extreme of the separate extinction curves. The positions of the Hα and Hβ lines are given. The crosses represent the extinction curve towards the Magellanic Clouds from Howarth (1983).

TABLE 4.2— The optical fluxes for the spectra I-a through II-b. The first and second column give the wavelength and identification of the lines, respectively. The fluxes are given relative to $H\beta \times 100$. The flux uncertainties are coded as follows : $A \leq 5\%$, $5\% < B \leq 10\%$, $10\% < C \leq 15\%$, $15\% < D \leq 20\%$, $20\% < E \leq 25\%$, $F > 25\%$.

λ (Å)	Identifier	I-a		I-b		I-c		II-a		II-b	
		I_λ/I_β	Err	I_λ/I_β	Err	I_λ/I_β	Err	I_λ/I_β	Err	I_λ/I_β	Err
3727	[O II]	55.9	C	119.4	B	116.9	B	119.3	B	84.8	B
3869	[Ne III]	32.5	C	31.1	C	31.2	C	26.2	C	32.8	C
3888	Hζ	14.2	E	15.2	D	15.5	D	16.0	D	15.8	D
3968	[Ne III] + Hϵ	23.3	C	24.6	D	23.6	C	24.0	D	24.7	B
4101	Hδ	26.2	C	25.7	C	22.7	C	26.2	C	26.1	C
4340	Hγ	44.4	B	47.1	B	45.2	B	48.1	B	46.9	B
4363	[O III]	3.6	F	3.4	F	3.5	E	2.8	F	3.5	E
4471	He I	4.9	E	5.0	D	4.1	E	3.5	F	4.0	D
4861	Hβ	100	A	100	A	100	A	100	A	100	A
4959	[O III]	178	A	162	A	164	A	160	A	179	A
5007	[O III]	525	A	478	A	489	A	482	A	530	A
5875	He I	12.3	B	12.2	B	12.0	B	12.7	B	12.1	B
6302	[O I]	–	–	0.9	F	0.8	F	1.1	E	–	–
6312	[S III]	2.0	E	1.6	E	1.7	D	1.6	D	1.6	C
6362	[O I]	–	–	–	–	–	–	–	–	–	–
6563	Hα	286	A	286	A	286	A	286	A	286	A
6585	[N II]	5.5	B	10.0	B	8.2	B	11.8	B	6.3	B
6678	He I	3.7	C	3.6	C	3.4	B	3.7	B	3.5	B
6717	[S II]	3.4	C	7.0	B	6.0	B	8.2	B	3.8	B
6730	[S II]	3.2	C	5.8	B	5.1	B	6.5	B	3.3	B
7065	He I	3.0	C	2.7	C	2.9	C	2.8	C	3.2	B
7137	[Ar III]	11.5	B	11.3	B	11.3	B	10.6	B	11.4	B
7320	[O II]	1.2	D	1.8	C	1.8	C	1.7	C	1.3	C
7330	[O II]	1.1	D	1.5	C	1.4	C	1.7	C	1.2	C
7751	[Ar III]	3.1	C	3.0	C	3.0	C	3.0	D	3.3	C
9069	[S III]	38.5	B	39.3	A	38.4	A	35.0	B	37.5	A
9532	[S III] + P8	84.9	B	86.0	A	83.7	A	75.4	B	83.8	A
	$E_{\beta-\alpha}$	0.29		0.29		0.23		0.32		0.27	

TABLE 4.3— The optical fluxes for the spectra II-c through IV-a. The first and second column give the wavelength and identification of the lines, respectively. The fluxes are given relative to $H\beta \times 100$. The flux uncertainties are coded as follows : $A \leq 5\%$, $5\% < B \leq 10\%$, $10\% < C \leq 15\%$, $15\% < D \leq 20\%$, $20\% < E \leq 25\%$, $F > 25\%$.

λ (Å)	Identifier	II-c		III-a		III-b		III-c		IV-a	
		I_λ/I_β	Err	I_λ/I_β	Err	I_λ/I_β	Err	I_λ/I_β	Err	I_λ/I_β	Err
3727	[O II]	108.1	B	129.9	B	77.1	B	120.7	B	134.9	B
3869	[Ne III]	38.1	C	32.0	C	33.8	B	38.9	C	38.4	C
3888	Hζ	19.2	C	18.0	C	16.8	C	18.9	C	19.3	D
3968	[Ne III] + Hϵ	26.9	C	24.7	C	24.3	B	28.5	C	29.0	D
4101	Hδ	25.3	B	23.7	C	24.4	B	23.7	C	26.1	C
4340	Hγ	47.7	B	46.7	B	46.9	B	46.7	B	46.1	B
4363	[O III]	3.8	D	3.7	E	3.1	D	3.1	F	3.6	F
4471	He I	3.7	D	4.2	F	4.4	D	3.6	E	4.3	D
4861	Hβ	100	A	100	B	100	A	100	A	100	A
4959	[O III]	175	A	161	A	181	A	168	A	179	A
5007	[O III]	512	A	481	A	534	A	500	A	529	A
5875	He I	12.1	B	11.4	B	12.0	B	11.6	B	11.5	B
6302	[O I]	–	–	–	–	–	–	0.9	F	0.8	E
6312	[S III]	1.5	C	1.8	D	1.8	D	1.7	D	1.7	D
6362	[O I]	–	–	–	–	–	–	–	–	–	–
6563	Hα	286	A	286	A	286	A	286	A	286	A
6585	[N II]	7.0	B	11.6	B	5.7	B	8.7	B	8.7	B
6678	He I	3.5	B	3.5	B	3.4	B	3.4	B	3.3	B
6717	[S II]	4.9	B	7.6	B	3.3	B	5.8	B	5.7	B
6730	[S II]	4.2	B	6.4	B	2.9	B	5.1	B	5.7	B
7065	He I	3.0	B	2.8	D	3.3	B	3.0	B	2.8	B
7137	[Ar III]	11.4	B	10.9	B	11.4	B	12.0	B	11.2	B
7320	[O II]	1.6	B	1.7	D	1.2	B	1.7	C	1.9	C
7330	[O II]	1.3	B	1.6	D	1.2	B	1.6	D	1.6	C
7751	[Ar III]	3.2	C	3.2	C	3.2	B	3.4	C	2.9	C
9069	[S III]	38.8	A	39.1	B	35.1	A	40.4	A	37.8	B
9532	[S III] + P8	84.1	A	82.5	B	77.5	B	89.8	A	59.5	B
	$E_{\beta-\alpha}$	0.34		0.36		0.24		0.36		0.40	

TABLE 4.4— The optical fluxes for the spectra IV-b through V-c. The first and second column give the wavelength and identification of the lines, respectively. The fluxes are given relative to $H\beta \times 100$. The flux uncertainties are coded as follows : $A \leq 5\%$, $5\% < B \leq 10\%$, $10\% < C \leq 15\%$, $15\% < D \leq 20\%$, $20\% < E \leq 25\%$, $F > 25\%$.

λ (Å)	Identifier	IV-b		IV-c		V-a		V-b		V-c	
		I_λ/I_β	Err	I_λ/I_β	Err	I_λ/I_β	Err	I_λ/I_β	Err	I_λ/I_β	Err
3727	[O II]	134.8	B	93.7	B	92.9	B	138.6	B	54.7	B
3869	[Ne III]	37.3	B	40.0	B	38.9	B	41.5	C	39.4	B
3888	Hζ	19.4	C	16.3	C	16.5	C	18.8	D	17.3	C
3968	[Ne III] + Hϵ	25.3	D	28.1	B	27.4	B	22.2	D	26.8	B
4101	Hδ	26.3	B	25.7	B	27.3	B	25.7	B	26.2	B
4340	Hγ	46.7	B	46.9	A	46.3	B	45.3	B	46.4	B
4363	[O III]	3.5	D	3.7	C	3.4	D	3.1	E	3.2	D
4471	He I	4.6	D	4.7	C	4.1	E	5.0	F	3.9	C
4861	Hβ	100	A	100	A	100	A	100	A	100	A
4959	[O III]	168	A	182	A	183	A	169	A	186	A
5007	[O III]	497	A	531	A	544	A	493	A	553	A
5875	He I	11.4	B	11.3	C	11.5	B	11.1	B	12.0	B
6302	[O I]	0.7	E	–	–	–	–	0.8	D	–	–
6312	[S III]	1.5	D	1.9	C	2.0	D	1.5	C	1.5	C
6362	[O I]	–	–	–	–	–	–	0.3	F	–	–
6563	Hα	286	A	286	A	286	A	286	A	286	A
6585	[N II]	7.3	B	5.7	B	5.7	B	7.9	B	3.5	B
6678	He I	3.3	B	3.3	B	3.4	B	3.3	C	3.5	B
6717	[S II]	5.2	B	3.2	B	4.3	B	6.0	B	1.9	B
6730	[S II]	4.9	B	3.3	B	3.7	B	5.0	B	1.8	B
7065	He I	2.9	B	3.4	D	2.9	B	2.7	C	3.7	B
7137	[Ar III]	10.5	B	11.5	B	11.0	B	10.4	B	11.4	B
7320	[O II]	1.9	C	1.8	D	1.4	B	1.8	C	1.0	B
7330	[O II]	1.5	C	1.5	D	1.2	C	1.6	C	1.0	B
7751	[Ar III]	3.0	B	3.1	B	3.0	B	2.9	C	3.3	B
9069	[S III]	34.2	B	34.9	A	35.7	B	32.0	A	34.0	A
9532	[S III] + P8	65.5	B	73.8	A	60.8	B	62.3	B	72.0	A
	$E_{\beta-\alpha}$	0.38		0.40		0.39		0.40		0.40	

TABLE 4.5— The optical fluxes for the spectra V-d through VII-a. The first and second column give the wavelength and identification of the lines, respectively. The fluxes are given relative to $H\beta \times 100$. The flux uncertainties are coded as follows : $A \leq 5\%$, $5\% < B \leq 10\%$, $10\% < C \leq 15\%$, $15\% < D \leq 20\%$, $20\% < E \leq 25\%$, $F > 25\%$.

λ (Å)	Identifier	V-d		VI-a		VI-b		VI-c		VII-a	
		I_λ/I_β	Err	I_λ/I_β	Err	I_λ/I_β	Err	I_λ/I_β	Err	I_λ/I_β	Err
3727	[O II]	152.6	B	74.8	B	84.1	B	128.2	A	83.2	C
3869	[Ne III]	34.6	B	40.4	C	38.6	B	33.8	C	36.3	C
3888	Hζ	16.4	B	17.7	D	17.0	C	16.7	C	15.9	E
3968	[Ne III] + Hϵ	27.4	B	28.8	C	27.5	B	27.4	C	27.8	D
4101	Hδ	26.6	B	26.2	C	26.6	B	27.2	B	27.2	D
4340	Hγ	46.2	A	47.4	B	47.5	B	45.2	C	46.5	C
4363	[O III]	2.8	D	3.9	E	3.7	D	3.1	D	3.9	F
4471	He I	3.7	D	3.6	E	4.2	D	3.5	C	4.3	F
4861	Hβ	100	A	100	A	100	A	100	A	100	A
4959	[O III]	166	A	188	A	181	A	168	A	185	A
5007	[O III]	490	A	556	A	538	A	502	A	559	A
5875	He I	11.5	B	11.7	B	11.7	B	11.5	B	11.8	B
6302	[O I]	1.2	C	–	–	–	–	1.0	C	–	–
6312	[S III]	1.8	B	1.6	D	1.8	D	1.7	C	2.0	F
6362	[O I]	0.4	F	–	–	–	–	0.4	F	–	–
6563	Hα	286	A	286	A	286	A	286	A	286	A
6585	[N II]	12.3	B	4.0	C	5.6	B	10.3	B	5.2	D
6678	He I	3.4	B	3.5	C	3.4	C	3.5	B	3.5	C
6717	[S II]	6.9	B	2.8	B	3.6	B	5.9	B	3.8	C
6730	[S II]	6.3	B	2.6	C	3.3	B	5.4	B	3.3	C
7065	He I	2.9	B	3.0	B	3.5	B	2.9	B	3.2	C
7137	[Ar III]	12.0	A	10.9	B	11.8	A	11.7	B	11.0	B
7320	[O II]	2.2	B	1.0	D	1.5	B	2.0	B	1.2	D
7330	[O II]	2.0	B	0.9	D	1.4	B	1.6	C	1.2	D
7751	[Ar III]	3.4	C	3.2	C	3.4	C	3.4	B	3.2	C
9069	[S III]	41.9	A	34.2	B	36.6	A	40.3	B	33.6	B
9532	[S III] + P8	81.0	A	57.4	B	77.1	A	81.0	A	60.5	A
	$E_{\beta-\alpha}$	0.38		0.37		0.36		0.39		0.39	

TABLE 4.6— The optical fluxes for the spectra VII-b through IX-b. The first and second column give the wavelength and identification of the lines, respectively. The fluxes are given relative to Hβ × 100. The flux uncertainties are coded as follows : A ≤ 5%, 5% < B ≤ 10%, 10% < C ≤ 15%, 15% < D ≤ 20%, 20% < E ≤ 25%, F > 25%.

λ (Å)	Identifier	VII-b		VIII-a		VIII-b		IX-a		IX-b	
		I_λ/I_β	Err	I_λ/I_β	Err	I_λ/I_β	Err	I_λ/I_β	Err	I_λ/I_β	Err
3727	[O II]	110.4	C	85.2	B	95.5	D	98.0	B	81.0	B
3869	[Ne III]	33.1	C	44.9	B	34.1	D	44.8	A	33.4	B
3888	Hζ	18.0	D	14.7	C	24.9	D	14.8	B	18.6	B
3968	[Ne III] + Hϵ	23.5	D	33.1	C	32.3	D	28.8	B	25.4	B
4101	Hδ	25.3	D	26.8	B	24.0	D	24.8	B	25.5	B
4340	Hγ	48.7	B	44.3	B	47.1	C	46.3	B	46.0	B
4363	[O III]	4.1	E	5.4	F	–	–	4.2	D	1.9	F
4471	He I	6.6	E	–	–	–	–	–	–	4.0	C
4861	Hβ	100	B	100	A	100	B	100	A	100	A
4959	[O III]	163	A	190	A	154	B	198	A	167	A
5007	[O III]	488	A	563	A	464	A	584	A	489	A
5875	He I	11.5	C	11.4	B	11.4	B	11.7	A	11.8	B
6302	[O I]	0.9	E	0.4	F	–	–	–	–	–	–
6312	[S III]	1.5	D	1.6	B	1.7	F	1.9	C	1.5	C
6362	[O I]	–	–	–	–	–	–	–	–	–	–
6563	Hα	286	A	286	A	286	A	286	A	286	A
6585	[N II]	8.5	B	4.5	B	7.6	B	4.6	B	6.1	B
6678	He I	3.7	D	3.4	D	3.7	D	3.2	B	3.3	B
6717	[S II]	5.3	B	2.7	B	3.9	C	3.2	B	4.0	B
6730	[S II]	4.2	B	2.7	B	3.2	C	2.9	B	3.6	B
7065	He I	3.0	D	3.6	B	3.1	C	3.5	C	2.8	B
7137	[Ar III]	11.7	B	11.2	A	12.2	B	11.5	A	12.3	B
7320	[O II]	1.7	D	1.6	B	1.3	F	1.5	C	1.1	C
7330	[O II]	1.7	D	1.4	B	2.2	F	1.3	C	1.1	C
7751	[Ar III]	4.0	D	3.6	B	3.5	E	3.3	B	3.4	B
9069	[S III]	41.6	B	35.5	A	38.4	B	40.6	A	38.5	A
9532	[S III] + P8	83.6	B	67.8	A	77.8	A	81.0	A	77.0	B
	$E_{\beta-\alpha}$	0.47		0.40		0.28		0.42		0.31	

TABLE 4.7— The optical fluxes for the spectra IX-c through XI-a. The first and second column give the wavelength and identification of the lines, respectively. The fluxes are given relative to $H\beta \times 100$. The flux uncertainties are coded as follows : $A \leq 5\%$, $5\% < B \leq 10\%$, $10\% < C \leq 15\%$, $15\% < D \leq 20\%$, $20\% < E \leq 25\%$, $F > 25\%$.

λ (Å)	Identifier	IX-c		X-a		X-b		X-c		XI-a	
		I_λ/I_β	Err	I_λ/I_β	Err	I_λ/I_β	Err	I_λ/I_β	Err	I_λ/I_β	Err
3727	[O II]	123.8	B	79.6	B	99.0	C	89.2	B	126.5	B
3869	[Ne III]	34.5	B	39.9	B	34.8	C	32.6	C	35.4	C
3888	Hζ	18.2	C	15.3	C	18.9	D	18.9	C	15.1	D
3968	[Ne III] + Hϵ	26.9	C	27.5	C	27.1	C	26.4	C	26.8	C
4101	Hδ	25.9	B	25.7	C	24.0	C	26.3	B	25.5	C
4340	Hγ	46.7	B	45.1	B	44.7	C	48.3	B	47.1	B
4363	[O III]	1.7	E	4.2	C	3.8	F	3.6	F	3.7	D
4471	He I	4.2	D	4.9	C	4.5	E	5.1	F	4.1	D
4861	Hβ	100	A	100	A	100	A	100	A	100	A
4959	[O III]	162	A	179	A	163	A	158	A	163	A
5007	[O III]	479	A	531	A	476	A	475	A	487	A
5875	He I	11.5	B	10.5	D	11.8	B	11.4	B	11.7	B
6302	[O I]	1.0	C	0.5	E	0.7	E	0.9	C	1.0	C
6312	[S III]	1.5	B	1.6	D	1.2	D	1.5	C	1.8	B
6362	[O I]	0.4	F	–	–	–	–	–	–	–	–
6563	Hα	286	A	286	A	286	A	286	A	286	A
6585	[N II]	10.7	B	4.4	B	11.4	B	9.4	B	8.3	B
6678	He I	3.6	B	3.1	B	3.5	B	3.3	B	3.5	B
6717	[S II]	6.2	B	3.1	B	5.2	B	5.8	B	6.3	B
6730	[S II]	5.4	B	2.9	B	4.7	B	4.5	B	5.0	B
7065	He I	2.8	B	3.2	B	3.0	B	2.6	C	3.7	B
7137	[Ar III]	11.4	A	10.8	A	12.1	B	11.2	B	11.8	A
7320	[O II]	1.8	B	1.3	B	1.5	B	1.5	C	2.3	B
7330	[O II]	1.6	B	1.1	B	1.3	C	1.2	C	1.8	B
7751	[Ar III]	3.3	B	3.1	B	3.6	B	3.1	B	3.1	B
9069	[S III]	41.9	A	36.0	A	42.2	A	41.5	B	41.5	A
9532	[S III] + P8	84.1	A	65.3	A	83.6	A	84.5	B	69.5	A
	$E_{\beta-\alpha}$	0.49		0.47		0.42		0.54		0.52	

TABLE 4.8— The optical fluxes for the spectra XI-b through XII-c. The first and second column give the wavelength and identification of the lines, respectively. The fluxes are given relative to H$\beta \times 100$. The flux uncertainties are coded as follows : A $\leq 5\%$, $5\% <$ B $\leq 10\%$, $10\% <$ C $\leq 15\%$, $15\% <$ D $\leq 20\%$, $20\% <$ E $\leq 25\%$, F $> 25\%$.

λ (Å)	Identifier	XI-b		XI-c		XII-a		XII-b		XII-c	
		I_λ/I_β	Err	I_λ/I_β	Err	I_λ/I_β	Err	I_λ/I_β	Err	I_λ/I_β	Err
3727	[O II]	77.7	B	82.9	C	76.3	B	84.9	B	69.3	D
3869	[Ne III]	34.0	B	33.4	D	33.0	C	31.3	D	29.1	E
3888	Hζ	16.8	B	20.4	E	14.4	D	17.0	E	15.5	E
3968	[Ne III] + Hϵ	25.9	C	29.1	D	28.5	D	26.4	D	23.2	E
4101	Hδ	25.5	C	25.5	C	25.8	C	25.8	D	25.4	E
4340	Hγ	44.9	B	49.1	B	46.6	B	46.7	C	47.7	C
4363	[O III]	3.5	D	3.9	F	5.4	F	3.3	F	4.9	F
4471	He I	4.2	E	4.9	F	4.0	F	3.2	F	2.3	F
4861	Hβ	100	A	100	A	100	A	100	A	100	B
4959	[O III]	167	A	161	A	181	A	166	A	155	B
5007	[O III]	497	A	483	A	539	A	489	A	470	A
5875	He I	11.6	B	11.2	B	11.8	B	12.1	B	11.4	B
6302	[O I]	–	–	–	–	0.6	D	0.7	E	–	–
6312	[S III]	1.5	C	1.7	D	1.6	C	1.5	D	1.4	C
6362	[O I]	–	–	–	–	–	–	–	–	–	–
6563	Hα	286	A	286	A	286	A	286	A	286	A
6585	[N II]	9.7	B	8.2	8	4.8	B	11.0	B	7.2	B
6678	He I	3.7	B	3.5	C	3.4	B	3.8	B	3.7	C
6717	[S II]	3.6	B	5.1	B	3.5	B	4.7	B	3.7	B
6730	[S II]	3.5	B	3.7	B	3.0	B	4.4	B	3.9	B
7065	He I	2.9	B	2.8	C	3.4	B	3.2	B	2.6	D
7137	[Ar III]	12.8	B	11.3	B	11.4	B	8.6	C	11.0	B
7320	[O II]	1.5	C	1.4	C	1.6	B	1.7	C	1.2	D
7330	[O II]	1.2	C	1.3	C	1.4	C	1.8	C	1.2	D
7751	[Ar III]	3.3	C	3.1	B	3.0	B	3.8	C	3.4	D
9069	[S III]	38.5	A	41.3	B	36.5	A	43.2	A	41.9	B
9532	[S III] + P8	80.0	A	85.3	A	61.5	A	89.5	A	84.7	A
	$E_{\beta-\alpha}$	0.44		0.61		0.55		0.58		0.66	

4.3 Analysis

A five-level atom was used as a model for the analysis involving the fine-structure lines. The relative populations of the five levels were calculated by taking into account the (de)population mechanisms of collisonal excitation and de-excitation by electrons, and radiative transitions. The slow variation of the effective collision strengths with temperature has been included in the model. For an exhaustive list of the sources from which we took the necessary transition probabilities and effective collision strengths we refer to Vermeij & Van der Hulst (2002b, hereafter VvdH). The first step in the analysis consisted of determining the electron temperature (T_e) and density (n_e) for every 1D-spectrum.

The electron density has been derived from the classical [S II] 6717 / [S II] 6730 line ratio. Nowhere did the electron density exceed the value of 1000 cm^{-3}. The average density across the nebula was 350 cm^{-3} with a standard deviation of 140 cm^{-3}. The spectral positions with the highest densities were XII-c (670 cm^{-3}) and IV-c (620 cm^{-3}). This last position is centered on a bright and compact blob (30 Doradus#3, see chapter 2 of this thesis).

We determined the electron temperature from the [O III] $(5007 + 4959)$/[O III] 4363 line ratio. The electron temperature did not vary much from position to position; the average T_e [O III] across the nebula was 10 330 K±700 (standard deviation). This isothermal nature of 30 Doradus was also noticed by Mathis et al. (1985) in their photometric study of the nebula, but their average temperature was slightly higher. A more recent study by Krabbe & Copetti (2002) also showed 30 Dor to be highly isothermal. Five positions, however, showed temperatures significantly different from this average. These were the positions VIII-a, XII-a and XII-c (11 450 K, 11 630 K and 11 810 K) and the positions IX-b and IX-c (8710 K and 8510 K). Excluding these positions in deriving the average temperature resulted in an average of 10 330 K±410. For position VIII-b no temperature could be derived because of the absence of the [O III] 4363 line. We assumed a T_e [O III] of 10 000 K for this position.

In deriving the ionic fractions, one should take into account the large-scale temperature stratification inside an H II region. The use of T_e [O III] is in principal only correct for the derivation of the O^{++} and Ne^{++} ionic fractions (the high-ionization species). For the low-ionization species like O^+ and the 'intermediate' species like S^{++}, the electron temperature applicable for their respective ionization zone should be used instead (T_e [O II] and T_e [S III], respectively). In order to derive the different electron temperatures, we used the relations between these as derived by Garnett (1992)

$$T_e\,[\mathrm{O\,II}] = 0.70\,T_e\,[\mathrm{O\,III}] + 3000 \tag{4.3}$$

$$T_e\,[\mathrm{S\,III}] = 0.83\,T_e\,[\mathrm{O\,III}] + 1700 \tag{4.4}$$

with T_e [O III] the electron temperature in Kelvin as measured from the optical spectra.

In the calculation of the ionic fractions we used T_e [O III] for the high-ionization species O^{++}, Ne^{++} and He^+. We used T_e [O II] for the low-ionization species O^+, N^+, and S^+, and T_e [S III] for the 'intermediate' ionic species S^{++} and Ar^{++}. Given the fact that most of our electron temperatures are near 10 000 K, the differences between the

TABLE 4.9— The full elemental abundances and heavy element-to-oxygen ratios for the positions in the outer zone (upper panel) and inner zone (lower panel). The notation a(−b) is shorthand for a×10^{-b}.

Position	O/H	O^+/O	S/H	log(S/O)	Ne/H	log(Ne/O)
I-a	1.89(−4)	0.12	7.41(−6)	−1.41	3.33(−5)	−0.75
I-b	1.91(−4)	0.23	6.38(−6)	−1.48	3.49(−5)	−0.74
I-c	1.91(−4)	0.23	6.19(−6)	−1.49	3.55(−5)	−0.73
II-a	2.32(−4)	0.23	6.38(−6)	−1.56	4.12(−5)	−0.75
II-c	1.90(−4)	0.21	6.22(−6)	−1.48	4.05(−5)	−0.67
III-a	1.79(−4)	0.25	5.99(−6)	−1.48	3.42(−5)	−0.72
III-c	2.27(−4)	0.23	5.97(−6)	−1.58	4.60(−5)	−0.69
V-d	2.60(−4)	0.28	7.24(−6)	−1.56	5.34(−5)	−0.69
VI-c	2.32(−4)	0.24	6.90(−6)	−1.52	4.55(−5)	−0.71
VII-b	1.58(−4)	0.22	6.16(−6)	−1.41	2.96(−5)	−0.73
VIII-b	1.99(−4)	0.20	6.72(−6)	−1.47	4.26(−5)	−0.67
IX-b	3.32(−4)	0.16	9.07(−6)	−1.56	7.24(−5)	−0.66
IX-c	3.79(−4)	0.23	9.47(−6)	−1.60	8.91(−5)	−0.63
X-b	1.64(−4)	0.21	6.50(−6)	−1.40	3.29(−5)	−0.70
X-c	1.66(−4)	0.19	6.77(−6)	−1.39	3.20(−5)	−0.71
XI-b	1.83(−4)	0.17	6.64(−6)	−1.44	3.57(−5)	−0.71
XI-c	1.54(−4)	0.17	6.69(−6)	−1.36	2.95(−5)	−0.72
XII-b	1.92(−4)	0.18	7.54(−6)	−1.41	3.52(−5)	−0.74
XII-c	1.12(−4)	0.17	5.80(−6)	−1.29	1.86(−5)	−0.78

Position	O/H	O^+/O	S/H	log(S/O)	Ne/H	log(Ne/O)
II-b	2.09(−4)	0.16	6.81(−6)	−1.49	3.69(−5)	−0.75
III-b	2.37(−4)	0.15	6.91(−6)	−1.54	4.41(−5)	−0.73
IV-a	2.25(−4)	0.25	6.11(−6)	−1.57	4.67(−5)	−0.68
IV-b	2.06(−4)	0.26	5.38(−6)	−1.58	4.41(−5)	−0.67
IV-c	2.05(−4)	0.19	5.88(−6)	−1.54	4.38(−5)	−0.67
V-a	2.28(−4)	0.17	6.59(−6)	−1.54	4.72(−5)	−0.68
V-b	2.31(−4)	0.25	5.45(−6)	−1.63	5.57(−5)	−0.62
V-c	2.34(−4)	0.11	7.24(−6)	−1.51	4.91(−5)	−0.68
VI-a	2.01(−4)	0.15	6.11(−6)	−1.52	4.18(−5)	−0.68
VI-b	2.03(−4)	0.17	6.40(−6)	−1.50	4.18(−5)	−0.69
VII-a	2.03(−4)	0.16	5.95(−6)	−1.53	3.80(−5)	−0.73
VIII-a	1.50(−4)	0.17	5.15(−6)	−1.46	3.20(−5)	−0.67
IX-a	2.14(−4)	0.18	6.79(−6)	−1.50	4.65(−5)	−0.66
X-a	1.72(−4)	0.16	5.92(−6)	−1.46	3.57(−5)	−0.68
XI-a	1.82(−4)	0.24	6.39(−6)	−1.45	3.68(−5)	−0.69
XII-a	1.34(−4)	0.16	5.30(−6)	−1.40	2.20(−5)	−0.78

TABLE 4.10— The full elemental abundances and heavy element-to-oxygen ratios for the positions in the outer zone (upper panel) and inner zone (lower panel). The notation a(−b) is shorthand for a×10^{-b}.

Position	Ar/H	log(Ar/O)	N/H	log(N/O)	He/H
I-a	1.45(−6)	−2.11	8.50(−6)	−1.35	0.093
I-b	1.17(−6)	−2.21	7.87(−6)	−1.39	0.091
I-c	1.17(−6)	−2.21	6.43(−6)	−1.47	0.089
II-a	1.24(−6)	−2.27	1.04(−5)	−1.35	0.093
II-c	1.18(−6)	−2.21	5.90(−6)	−1.51	0.090
III-a	1.05(−6)	−2.23	8.04(−6)	−1.35	0.088
III-c	1.35(−6)	−2.23	7.39(−6)	−1.49	0.085
V-d	1.36(−6)	−2.28	9.00(−6)	−1.46	0.085
VI-c	1.30(−6)	−2.25	8.42(−6)	−1.44	0.087
VII-b	1.10(−6)	−2.16	6.36(−6)	−1.40	0.090
VIII-b	1.41(−6)	−2.15	7.35(−6)	−1.43	0.089
IX-b	2.00(−6)	−2.22	9.56(−6)	−1.54	0.084
IX-c	1.76(−6)	−2.33	1.22(−5)	−1.49	0.082
X-b	1.20(−6)	−2.14	9.24(−6)	−1.25	0.090
X-c	1.17(−6)	−2.15	8.63(−6)	−1.28	0.085
XI-b	1.45(−6)	−2.10	1.04(−5)	−1.25	0.089
XI-c	1.17(−6)	−2.12	8.12(−6)	−1.28	0.086
XII-b	9.81(−7)	−2.29	1.14(−5)	−1.23	0.093
XII-c	9.67(−7)	−2.06	6.06(−6)	−1.27	0.090

Position	Ar/H	log(Ar/O)	N/H	log(N/O)	He/H
II-b	1.36(−6)	−2.19	7.44(−6)	−1.45	0.090
III-b	1.50(−6)	−2.20	7.73(−6)	−1.49	0.088
IV-a	1.17(−6)	−2.28	6.48(−6)	−1.54	0.085
IV-b	1.06(−6)	−2.29	5.12(−6)	−1.60	0.085
IV-c	1.27(−6)	−2.21	5.42(−6)	−1.58	0.084
V-a	1.33(−6)	−2.23	6.53(−6)	−1.54	0.086
V-b	1.14(−6)	−2.31	6.16(−6)	−1.57	0.083
V-c	1.64(−6)	−2.15	6.49(−6)	−1.56	0.089
VI-a	1.28(−6)	−2.20	4.88(−6)	−1.61	0.089
VI-b	1.35(−6)	−2.18	6.06(−6)	−1.53	0.087
VII-a	1.27(−6)	−2.20	5.94(−6)	−1.53	0.089
VIII-a	1.04(−6)	−2.16	4.02(−6)	−1.57	0.088
IX-a	1.26(−6)	−2.23	4.61(−6)	−1.67	0.086
X-a	1.15(−6)	−2.17	4.69(−6)	−1.56	0.079
XI-a	1.16(−6)	−2.20	6.00(−6)	−1.48	0.088
XII-a	1.05(−6)	−2.11	4.42(−6)	−1.48	0.089

three temperatures are small. The ionic fractions have been derived with the relation

$$\frac{\mathrm{X}^+}{\mathrm{H}^+} = \left[\frac{I_\lambda}{I_{H^+}}\right]\left[\frac{\epsilon\,(n_\mathrm{e}, T_\mathrm{e})}{A_\lambda E_\lambda}\right]\left[\frac{n_\mathrm{e}}{F\,(n_\mathrm{e}, T_\mathrm{e})}\right] \tag{4.5}$$

with $\mathrm{X}^+/\mathrm{H}^+$ the ionic fraction, $I_\lambda/I_{\mathrm{H}^+}$ the line flux relative to Hβ, A_λ and E_λ the radiative rate and energy of the transition from which the line originates, $\epsilon\,(n_\mathrm{e}, T_\mathrm{e})$ the emissivity of the hydrogen recombination line taken from Storey & Hummer (1995), n_e the electron density as derived from the [S II] lines, T_e the electron temperature, and $F\,(n_\mathrm{e}, T_\mathrm{e})$ the level-distribution function. For the calculation of the He^+ ionic fraction the following equation was used

$$\frac{\mathrm{He}^+}{\mathrm{H}^+} = \left[\frac{I_\lambda}{I_{\mathrm{H}_\beta}}\right]\left[\frac{\epsilon_{\mathrm{H}_\beta}\,(n_\mathrm{e}, T_\mathrm{e})}{\epsilon_\lambda\,(n_\mathrm{e}, T_\mathrm{e})}\right], \tag{4.6}$$

with $I_\lambda/I_{\mathrm{H}_\beta}$ the helium line flux relative to the Hβ line, $\epsilon_{\mathrm{H}_\beta}\,(n_\mathrm{e}, T_\mathrm{e})$ the Hβ emissivity from Storey & Hummer (1995), and $\epsilon_\lambda\,(n_\mathrm{e}, T_\mathrm{e})$ the helium recombination line emissivity from Benjamin et al. (1999). The He I recombination lines used in deriving the He^+ fraction were the $\lambda\,5875$ Å and the $\lambda\,6680$ Å lines. The two fractions were averaged to produce the final result.

To derive the full elemental abundances from the observed ionic fractions one needs to take into account the unobserved ionization stages of an element. The correction for these stages is made using Ionization Correction Factors (ICFs). The schemes adopted in our analysis for the elements oxygen, neon and nitrogen are

$$\frac{\mathrm{O}}{\mathrm{H}} = \frac{\mathrm{O}^+ + \mathrm{O}^{++}}{\mathrm{H}^+}, \tag{4.7}$$

$$\mathrm{Ne}^{++}/\mathrm{O}^{++} \;=\; \mathrm{Ne/O}, \tag{4.8}$$

$$\mathrm{N}^+/\mathrm{O}^+ \;=\; \mathrm{N/O} \tag{4.9}$$

with $\mathrm{O}/\mathrm{O}^{++}$ and O/O^+ as the ICFs for neon and nitrogen. For sulfur and argon the ICFs are somewhat more complicated. We adopt the following prescription from Stasińska (1978) for sulfur

$$\frac{\mathrm{S}}{\mathrm{S}^+ + \mathrm{S}^{++}} = \left[1 - \left(1 - \frac{\mathrm{O}^+}{\mathrm{O}}\right)^3\right]^{-1/3} \tag{4.10}$$

and similar for $\mathrm{Ar}/\mathrm{Ar}^{++}$. This prescription turned out to be fairly accurate for sulfur for $\mathrm{O}^+/\,\mathrm{O} > 0.2$ (VvdH). For helium we take $\mathrm{He} \simeq \mathrm{He}^+$ which is a very good approximation for highly ionized nebulae like 30 Doradus. The consistent He I 5875/Hβ of ~ 0.12 throughout the sample supports this assumption. The complete absence of He II recombination lines in our optical spectra indicates that the He^{++} fraction is negligibly small. The final results are presented in Tables 4.9 and 4.10. For a discussion on the error analysis we refer to VvdH.

4.4 Discussion

In our discussion we focus on the excitation, ionization and chemical properties of 30 Doradus, and we are particularly interested in how the latter two properties change as a function of the projected distance from the main ionizing source R 136. To simplify the spatial identification of the spectra, these have therefore been divided into two roughly equally sized groups. The spatial boundary between the two groups, a circle centered on R 136, is shown in Fig. 4.1. Throughout this chapter, the group of spectra inside the circle will be referred to as the inner group, and the second set as the outer group.

4.4.1 Ionization structure

4.4.1.1 General spectral characteristics

The global ionization structure and the excitation of the nebula are directly reflected in its spectral characteristics. This is demonstrated by the spectra shown in Fig. 4.2, which represent the two extremes in terms of excitation. The spectral lines used to constrain the ionization structure and excitation are the strong oxygen and sulfur lines complemented with the [Ne III] 3869 Å and [N II] 6858 Å lines. The differences in the strength of these lines is clearly visible in the spectra of Fig. 4.2. We plot these lines against each other in Fig. 4.4. Two sets of lines are distinguished, those of the low-ionization ionic species, and those of the high-ionization species (including S^{++}).

A first look at Fig. 4.4 already reveals a few interesting things. First of these is the often very clear separation between the spectral characteristics of the inner group of spectra and those of the outer group. This separation is most easily seen for the high-ionization [O III] 5007 Å and [S III] 9068 Å lines (see e.g. Fig. 4.4, panel *a*). The [Ne III] 3869 Å line shows less variation between the two groups. A similar separation is seen for the low-ionization [S II] 6717,6730 Å, [O II] 3727 Å and [N II] 6585 Å lines, although for these the separation between the two groups of spectra is less pronounced. The second thing that is immediately apparent is the difference in the range of line strengths covered by not only the different lines but also the two groups of spectra. In the case of the high-ionization lines, both groups of spectra occupy their own narrow, clearly separated niche. The two groups of spectra, however, behave differently in the case of the low-ionization lines. The range in line strengths covered by the outer group of spectra is considerably larger than that of the inner group and even shows some overlap with the inner group spectra. These differences in range for the low-ionization lines is most likely due to the placing of the spectra apertures; the outer group spectra are more widely distributed and are generally positioned in a morphologically more complex part of the nebula than the inner group spectra. The dominant O^{++} and S^{++} ionization zones are much less affected by these effects than e.g. the N^{+} zone.

Several correlations between the various line strengths can be seen in Fig. 4.4. The tightest correlations are found between the low-ionization lines (see Fig. 4.4, panels *c* and *d*), especially between those of S^{+} and O^{+}. The correlation between the [N II] and [O II] lines is much less tight, but this is due to the scatter in the [N II] 6585 Å line. For the high-ionization species, we see a positive trend for the [O III] and [Ne III] lines (Fig. 4.4, panel *b*). As far as the correlations between the low and high-ionization lines are concerned, we see, not surprisingly, a negative trend for the [O III] and [O II] lines

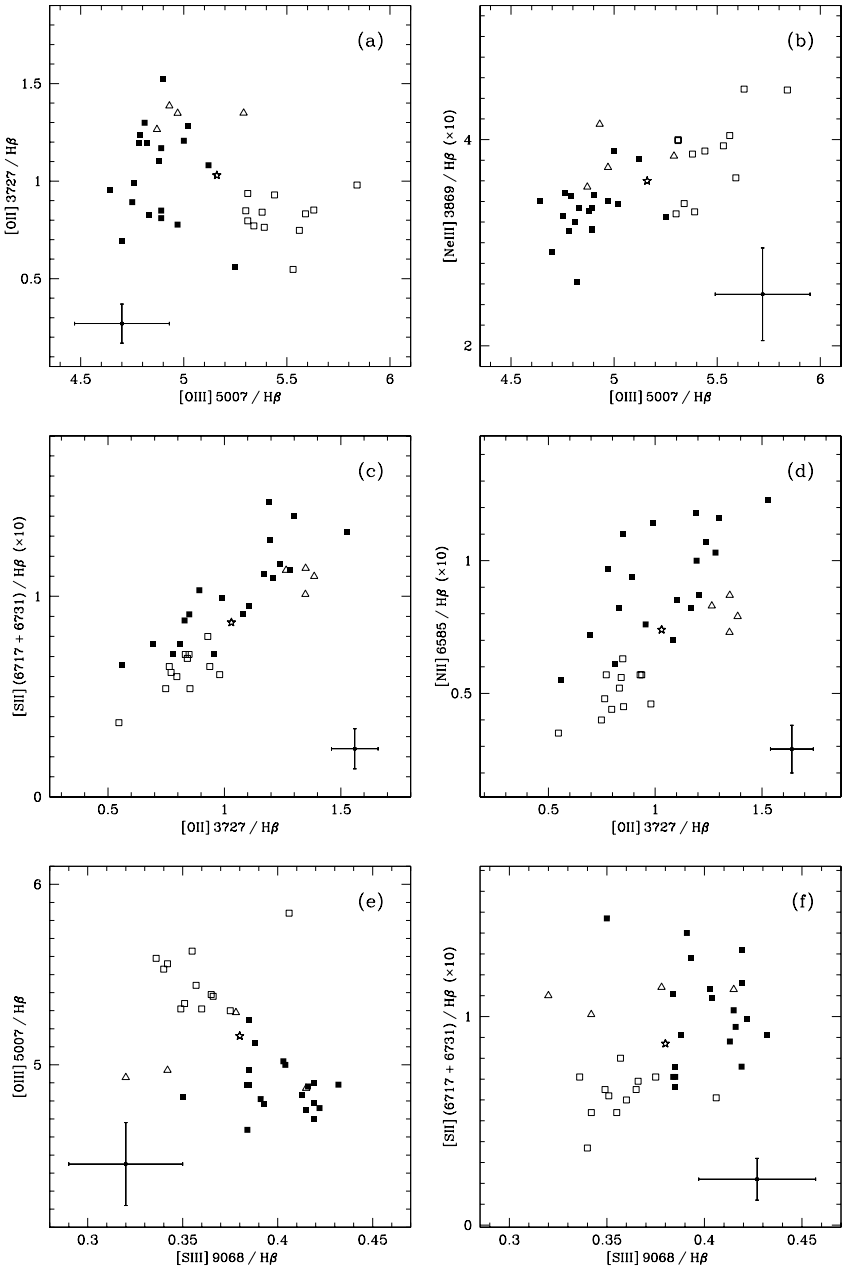

FIGURE 4.4— The relation between the various spectral indicators of the ionization structure of the nebula. The spectra from the inner group are designated by open symbols, those from the outer group by closed symbols. The result for the global spectrum is plotted as a star (see Sect. 4.6). The four deviant positions IV-a, IV-b, V-b and XI-a are shown as triangles. Given in every panel is a typical error bar.

(Fig. 4.4, panel *a*). More interesting, however, are the correlations involving the [S III] lines shown in panels *e* and *f* of Fig. 4.4. There is a negative trend between the [O III] and the [S III] lines, whereas the [S II] and [S III] lines show a positive one. We clearly see here the shift in the ionization balance from S^{++} to S^{+3} when we go from the outer zone of the nebula to the inner zone. The presence in 30 Dor of significant amounts of S^{+3} has been shown by VvdH.

These findings show the change in the ionization structure throughout 30 Doradus, becoming less highly excited when we go further out from the central ionizing source of the nebula. Four positions belonging to the inner group of spectra, however, deviate from this picture and seem to be less highly ionized than the rest of the positions in this group. These positions (IV-a, IV-b, V-b and XI-a) are shown in Fig. 4.4 as open triangles. The reason for the anomalous behaviour of these positions is not clear, but one should take into account that the projected distance of these positions from R 136 is of course deceptive. The internal kinematics of the core of 30 Dor has proven to be very turbulent with expanding structures as small as ~ 1 pc and expansion velocities in the range of 20-200 $\mathrm{km\,s^{-1}}$ (Chu & Kennicutt 1994), so the actual distance of these anomalous inner positions from R 136 could in fact be larger than those of the surrounding positions.

4.4.1.2 The excitation parameter η'

The ionization balance inside an H II region depends directly on the spectral energy distribution (SED) of the main exciting source(s). Combinations of line ratios from elements in various ionization stages therefore form a tool with which to constrain the stellar effective temperature. One such a parameter with which to probe the effective temperature has been proposed by Vilchez & Pagel (1988). Their parameter η' was defined as

$$\eta' = \frac{[\mathrm{O\,II}]\,3727\,/\,[\mathrm{O\,III}]\,4959,5007}{[\mathrm{S\,II}]\,6717,6730\,/\,[\mathrm{S\,III}]\,9068,9532}, \tag{4.11}$$

and the parameter composed of the corresponding ions as

$$\eta = \frac{\mathrm{O^{+}}\,/\,\mathrm{O^{++}}}{\mathrm{S^{+}}\,/\,\mathrm{S^{++}}}. \tag{4.12}$$

The η' parameter is sensitive to changes in the slope of the SED between the ionization potentials of S^+ and O^+ (23.3 and 35.1 eV, respectively). Note that the use of ratios of different ionization stages of the same element makes the parameter independent from the local abundances of these elements. The spatial coverage of our spectra enables us to test the variation of the parameter η' when measured at different points in the H II region. The results are shown in Fig. 4.5. Also plotted in this figure are the 32 positions in 30 Doradus from the work of Kennicutt et al. (2000).

The upper panel of Fig. 4.5 shows a strong correlation between the [S II]/[S III] and [O II]/ [O III] line ratios over ranges that span at least a full decade. This is, of course, indicative of a monotonically decreasing ionization parameter. The inner zone spectra, not surprisingly, show a higher ionization parameter than the outer zone spectra. The spectral positions from Kennicutt et al. (2000) mostly lie in the more outlying parts of 30 Dor. The picture of the ionization parameter monotonically decreasing with distance

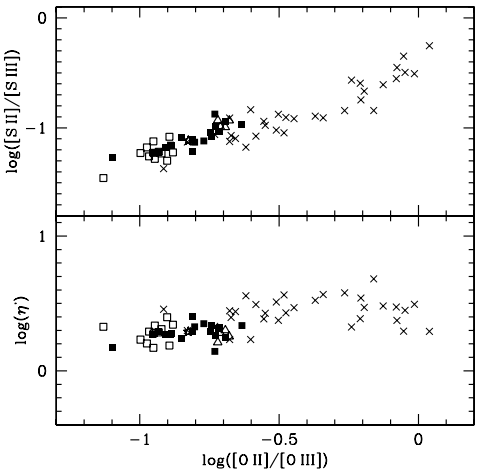

FIGURE 4.5— The excitation parameter η'. The top panel shows the strong correlation between the [S II]/[S III] and [O II]/[O III] line ratios. The bottom panel shows their ratio η'. The data from Kennicutt et al. (2000) are given as crosses. For an explanation of the other symbols see Fig. 4.4.

from the ionizing source R 136 is thus maintained. The relevant thing to note here is that the ionization parameter as measured through the sulfur and oxygen lines seems to be very well determined and can even be traced back to the ionizing source, this despite the morphological complexity of 30 Dor.

The η' parameter shown in the lower panel of Fig. 4.5 turns out to be remarkably constant across the face of 30 Doradus, a constant value that persists going from the inner to the outer group of spectra. The same is true for the positions from Kennicutt et al. (2000). Over the entire range of [O II]/[O III] the value of η' changes only slightly, increasing from ~ 2 at the low end of the range to ~ 4 at the high end. Apparently, the temperature of the local radiation field which is probed by the η' parameter does not change notably over the spatial scale covered by the data.

This result for the η' parameter is quite encouraging, and is especially interesting for the study of the stellar content of extragalactic H II regions which are usually not spatially resolved. The insensitivity of η' to changes in the ionization parameter makes it a much more useful probe of the ionizing source of the nebula than the crude [O III] 5007/ Hβ line ratio which is quite sensitive to changes in ionization parameter and metallicity.

4.4.2 Chemical characteristics

To investigate the global chemical characteristics of 30 Dor we plot in Fig. 4.6 the elemental abundances against the projected radial distance from R 136. It is immediately apparent from this figure that the chemical composition across the nebula is quite homogeneous. The occasional outliers are the positions with an anomalous temperature (cf. Sect. 4.3). If we recalculate the abundances for these points assuming an electron temperature of 10 000 K, we see that the abundances for the outlying points agree with the results of the other positions. The behaviour of the neon abundance in the upper part of the lefthand panel of Fig. 4.6 closely follows that of oxygen. The abundances averaged over all our positions are given in Table 4.11.

The case for nitrogen is considerably less simple. The nitrogen abundance as a

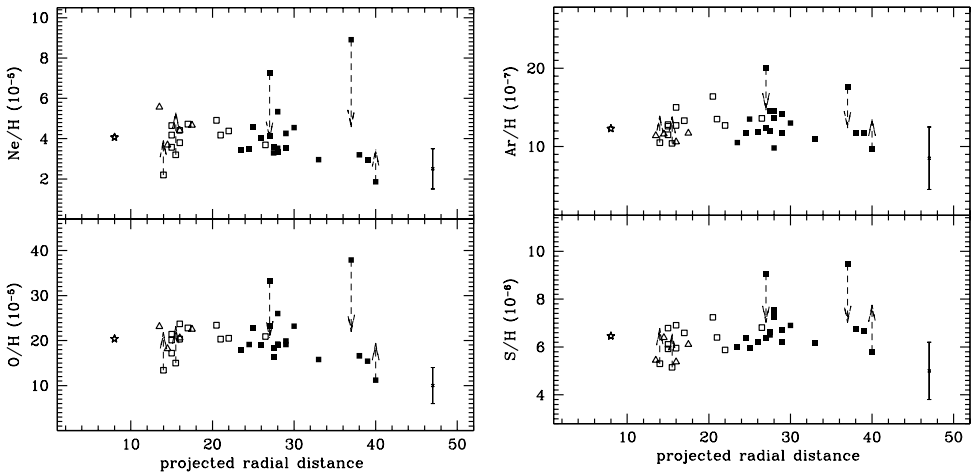

FIGURE 4.6— The neon, oxygen, argon and sulfur abundances as a function of the projected radial distance from the ionizing source. The dashed arrows show the shift in the derived abundances if we recalculate these for the temperature-anomalous points assuming an electron temperature of 10 000 K (see Sect. 4.3). Given in every panel is a typical error bar. For an explanation of the symbols see Fig. 4.4.

function of projected radial distance is plotted in Fig. 4.7. We can clearly see an increase in the nitrogen abundance as we progress outwards from the ionizing source. Recalculating the nitrogen abundances for the temperature-anomalous points results in a shift of these points that only strengthens the trend. Given the importance of nitrogen as a tracer of star-formation history this result is rather disturbing. Whether the observed trend is real or that some systematic effect in the data reduction and analysis plays a role here is not directly clear. The four most likely sources of error are (i) erroneous measurements of the [N II] 6585 Å line fluxes, (ii) errors in the extinction correction for these line fluxes, (iii) gradients in the electron temperature that might influence the derived N^+ ionic fraction, and (iv) the ionization correction factor used to derive the full nitrogen abundance. We discuss these four possibilities in turn.

As far as the first possible source of error is concerned, things are pretty clear. Given the resolution of our spectra of ~ 4 Å pix^{-1} the [N II] 6585 Å line is always clearly separated from the strong Hα line (cf. Fig. 4.2). The measurement of the [N II] 6585 Å line is therefore rather straightforward and no serious errors in the derived flux are expected.

Possible effects due to an incorrect extinction correction of the [N II] 6585 Å line do not play a role here either. We checked this by determining the [N II] 6585 Å/Hα ratio from the *reddened* fluxes. The extinction on the Hα line is the same as on the [N II] 6585 Å line because of their close proximity, so if we take the reddened fluxes for both lines and divide them, the extinction simply drops out. These [N II] 6585 Å/Hα ratios were then converted to [N II] 6585 Å/Hβ ratios by multiplying them with 2.86, the theoretical Hα/Hβ decrement. The [N II] 6585 Å/Hβ ratios thus derived turned out

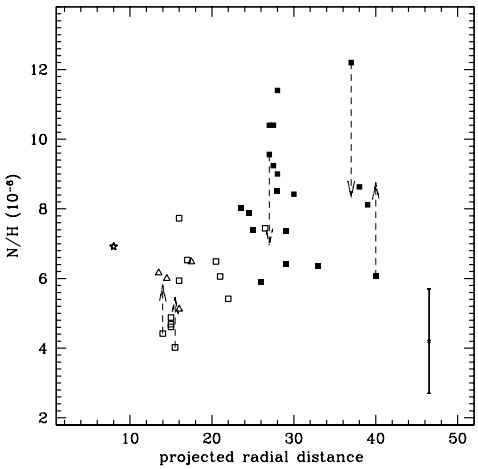

FIGURE 4.7— The nitrogen abundance as a function of the projected radial distance from the ionizing source. The dashed arrows show the shift in the derived abundance if we recalculate this for the temperature-anomalous points assuming an electron temperature of 10 000 K (see Sect. 4.3). Given is a typical error bar. For an explanation of the symbols see Fig. 4.4.

to be identical to the ones from the dereddened spectra.

To test the possibility that the cause of the observed trend in the nitrogen abundance lies in a radial temperature gradient, we plot in the lower panel of Fig. 4.8 the electron temperatures T_e [O III] against the projected radial distance. There is no obvious gradient in T_e [O III] in 30 Dor, and the scatter present is mainly the result of the temperature-anomalous points. The conversion of the T_e [O III] to the T_e [O II] actually used in deriving the N^+ ionic fraction will reduce the scatter in the temperatures even more. It is evident that the presence of a temperature gradient does not play a role here; this could already have been surmised from the lack in variation in the other abundances.

The question of whether the observed radial increase in N is caused by the ICF used in the derivation of the full nitrogen abundance is more difficult to address. The use of Eqn. 4.9 as the ICF for nitrogen has always been somewhat controversial. Its validity hinges on the assumption that the ionization structures of nitrogen and oxygen are essentially similar, and that both are fully sampled by the spectra. However, a considerable difference between the ionization potential of N^+ ($\sim$29 eV) and O^+ ($\sim$35 eV) exists. The discrepancies often found between the N^+/O^+ ratio derived from optical lines and the N^{++}/O^{++} ratio derived from far-infrared lines are in this respect also worrisome (e.g. Lester et al. 1983; Rubin et al. 1991; Walter et al. 1992). On the other hand, in many abundance studies of extragalactic H II regions, the nitrogen ICF and its underlying assumption seem to hold fairly well (e.g. Garnett 1990; Vila-Costas & Edmunds 1993; Thurston et al. 1996). The question therefore shifts from whether there is something fundamentally wrong with the nitrogen ICF itself, to whether the input parameters for the correction factor (i.e. N^+ and O^+) are somehow 'distorted'. In the following discussion we investigate the latter question.

As can be seen in the top panel of Fig. 4.8, the range covered by the parameter O^+/O used in the nitrogen ICF is quite narrow and does not change much with projected radial distance. It is true that many of the inner group positions cluster around a value $\sim$0.16, but the range in O^+/O covered is roughly the same for both groups of spectra;

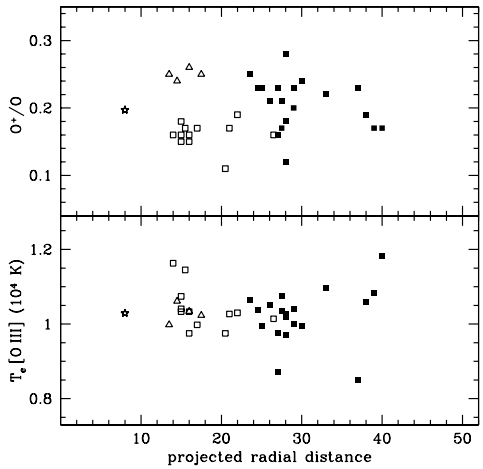

FIGURE 4.8— The O^+/O and T_e [O III] as a function of projected radial distance. For an explanation of the symbols see Fig. 4.4.

the difference in the average O^+/O ratio for the inner and outer group of spectra is only marginal (0.18±0.04 and 0.21±0.04, respectively). Furthermore, the positions with the lowest O^+/O will have the *largest* correction for unseen nitrogen, but these positions turn out to have the *lowest* nitrogen abundance. Any variation in O^+/O therefore can not be solely responsible for the observed variations in the nitrogen abundance. If we combine this finding with the isothermal nature of the nebula as discussed above, we conclude that the range in the derived nitrogen abundances simply reflects the range in the [N II] 6585 Å line strengths seen in panel *d* of Fig. 4.4; this range is roughly similar to the one found for the nitrogen abundance. One might ask oneself if there is any mechanism other than an actual nitrogen gradient that could cause the observed range in the [N II]/Hβ ratio.

One mechanism that can influence the emission in the low-ionization lines, and in particular the [N II] 6585 Å line, is shock enhancement (e.g. Dopita & Sutherland 1995, 1996). The turbulent kinematics of the core of 30 Dor with velocities in the proper range for shock enhancement to occur make this mechanism a possible candidate. However, none of our spectra show evidence of shock enhancement. Any shock enhancement of the [N II] 6585 Å line should be accompanied by a similar enhancement of the [S II] 6717, 6730 Å and [O I] 6302, 6362 Å lines, but this is not seen in any of our spectra. The [O I] lines are hardly even detected, and in those cases where they are present, they are all well in the range for a purely photoionized nebula (Stasińska 1990). We therefore can rule out local shock enhancement as an explanation for the range in the [N II] 6585 Å/Hβ ratios seen in Fig. 4.4.

One other factor that should be taken into account is the very nature of our observations itself, i.e. the use of 1D-spectra extracted from stationary longslit spectra. The fact that 30 Dor is spatially resolved and that every one of our 1D-spectra has its own line-of-sight through the likewise spatially resolved ionization structure of the nebula can have serious repercussions for the analysis. Theoretical studies based on photoionization models have shown that the global, integrated spectral properties of planetary nebulae (PNe) and H II regions can differ considerably from those derived

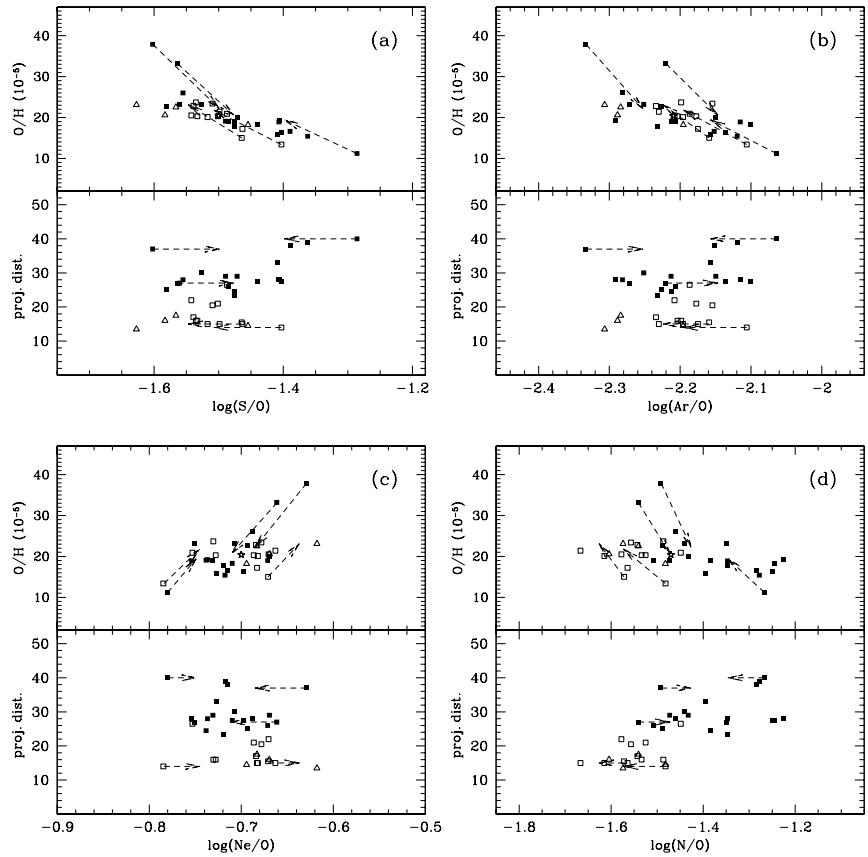

FIGURE 4.9— The variation of the heavy element-to-oxygen ratios with oxygen abundance and projected radial distance from R 136. The dashed arrows show the shift in the derived abundance if we recalculate this for the temperature-anomalous points assuming an electron temperature of 10 000 K (see Sect. 4.3). For an explanation of the symbols see Fig. 4.4.

from line-of-sight spectra at various fractions of the Strömgren radius (e.g. Gruenwald & Viegas 1992, 1998; Alexander & Balick 1997). These spatial effects turned out to be especially important for the emission in the [N II] 6585 Å line, with severe implications for the analysis of the N^+ ionization zone. The oxygen lines, however, were much less affected. The gradient in the nitrogen abundance observed by Balick et al. (1994) in several PNe could at least be partially explained by these effects. These results clearly show that spectral observations at or near the edge of an ionization front should be treated with caution in the analysis.

Recently, the ionization structure of the core of 30 Dor has been studied by Scowen et al. (1998) using narrow-band WFPC2 images in the [S II] (6717+6731) Å, Hα and [O III] 5007 Å lines. One of the main results of this study was the detection of a very narrow and highly stratified ionization front. Our spectral positions all coincide with

this ionization front. It is not inconceivable then that both the observed narrow range of the O^+/O parameter as well as the large range of [N II]/Hβ ratios are a direct result of line-of-sight effects in the spatially resolved ionization structure of 30 Dor.

Any spatial mismatch of the [N II] and [O II] emitting zones plays less of a role in the analysis of global, spatially integrated spectra. In their work, Alexander & Balick (1997) conclude that the nitrogen abundance derived from the spatially integrated model spectra, using the standard ICF for nitrogen, compared well with the input nitrogen abundance of the models. These differences in behaviour for the two types of spectra (resolved/unresolved) might therefore explain why in extragalactic abundance studies based on observations of *un*resolved H II regions, the nitrogen ICF given in Eqn. 4.9 seems to be quite accurate.

Given the influence of spatial effects on the observation of the [N II] and [O II] emitting zones, it may be clear that the use of Eqn. 4.9 as nitrogen ICF can be dubious for spatially resolved spectra and nebulae. We therefore conclude that the nitrogen gradient observed in this study is not real, but the result of line-of-sight effects.

4.4.2.1 The heavy element-to-oxygen ratios

Information on star-formation history and on possible local enrichment of the interstellar gas is contained in the heavy element-to-oxygen abundance ratios. The heavy element-to-oxygen ratios for our positions in 30 Dor are shown in Fig. 4.9. The values for the heavy element-to-oxygen ratios averaged over all our positions are given in Table 4.11.

The S/O and Ar/O ratios given in panels *a* and *b* of Fig. 4.9, respectively, show no correlation with the projected radial distance. At first sight, the S/O and Ar/O ratios appear to be slightly anticorrelated with O/H. This anticorrelation, however, is not real. The sulfur and argon abundances are very constant across the nebula (cf. Sect. 4.4.2, Table 4.11), whereas the oxygen abundance shows a range of ~ 0.20 dex, comparable to the one in the S/O and Ar/O ratios seen in this Figure. These facts combine to produce an artificial anticorrelation in an O/H versus X/O plot (with X being sulfur or argon).

The picture for Ne/O is somewhat different from that of S/O and Ar/O (Fig. 4.9, panel *c*). Like for S and Ar, we find no correlation with the projected radial distance from the ionizing source. However, contrary to what we found for the S/O and Ar/O ratios, the oxygen abundances derived for the various spectral positions tightly cluster around a single value of log(Ne/O). This correspondence between the neon and oxygen abundances is exemplified by the fact that for any given value of Ne/O the full range of the oxygen abundance is covered. The scatter in the Ne/O ratio for a fixed value of O/H is roughly 10%, which is equal to the typical uncertainty found in the measured [Ne II] 3869 Å line flux. These findings are indicative of the strong coupling between the oxygen and neon abundances which was already mentioned in Sect. 4.4.2.

It is not clear whether the observed range in the oxygen abundance is really due to local enrichment, or that it only reflects fluctuations in the measured electron temperature. Being the major coolant in an H II region, a physical relation does exist between the 'real' nebular temperature and O/H. However, a similar relation also exists between the *measured* electron temperature and the derived oxygen abundance, and this rela-

TABLE 4.11— The average elemental abundances and heavy element-to-oxygen ratios for the 35 positions in 30 Doradus.

	This work	VvdH[a]	IT99[b]	G00[c]
log<O/H>	−3.69±0.10	−3.74±0.02		−3.6
log<S/H>	−5.19±0.06	−5.16±0.04		−5.3
log<S/O>	−1.48±0.08	−1.42±0.04	−1.55±0.06	
log<Ar/H>	−5.89±0.08	−5.86±0.06		−5.8
log<Ar/O>	−2.20±0.08	−2.12±0.07	−2.27±0.10	
log<Ne/H>	−4.38±0.15	−4.12±0.05		−4.4
log<Ne/O>	−0.70±0.04	−0.38±0.05	−0.72±0.06	
log<N/H>	−5.14±0.14	−5.32±0.16		−5.1
log<N/O>	−1.44±0.13	−1.57±0.16	−1.46±0.14	
log<He/H>	−1.06±0.02	−1.05±0.02	–	

(*a*) Mean 30 Dor abundances from VvdH.
(*b*) Mean heavy element-to-oxygen ratios of the high-metallicity sub-sample from Izotov & Thuan (1999).
(*c*) Mean LMC abundances from Garnett (2000).

tion is unfortunately nearly indistinguishable from the former (Mathis 1985; Mathis et al. 1995). The derived oxygen abundances are plotted against the measured T_e [O III] in the upper panel of Fig. 4.10. It might be clear from this Figure that no conclusions can be drawn with respect to oxygen enrichment. The Ne^{++} ionic fraction reacts in roughly the same way to temperature variations as the O^{++} ionic fraction. The Ne/O ratio is therefore rather insensitive to these, which mimicks the effect of a simultaneous enrichment in both neon and oxygen. The Ne/O ratios plotted in Fig. 4.10 clearly show their robustness against temperature variations.

Not surprisingly, a strong correlation is seen between N/O and the projected radial distance from the ionizing source (Fig. 4.9, panel *d*). That this correlation is due to the apparent radial gradient in the nitrogen abundance (cf. Sect. 4.4.2) rather than to the range in O/H can be seen in the upper part of this panel; the points in the upper part cover a range of N/O of $\sim$0.4 dex while O/H remains constant over this range.

The heavy element-to-oxygen ratios for 30 Dor averaged over all our positions are given in Table 4.11. In general, the values agree well with the ones derived for 30 Dor from VvdH. The Ne/O ratio found in their work is $\sim$0.30 dex higher than found here, but this reflects the large discrepancies between the Ne^{++} ionic fractions derived by these authors from either the infrared or optical lines. The relative contribution of the Ne^{+} ionic fraction to the neon abundance was also suspected to be too high.

We can summarize the results of this Section as follows. The central part of 30 Dor is chemically homogeneous, and our data show no evidence of enrichment of the local interstellar medium. This chemical homogeneity was also noted by Mathis et al. (1985). The heavy element-to-oxygen ratios do not differ from the commonly found values, and are quite constant across the nebula. A special case, however, is nitrogen. In our data,

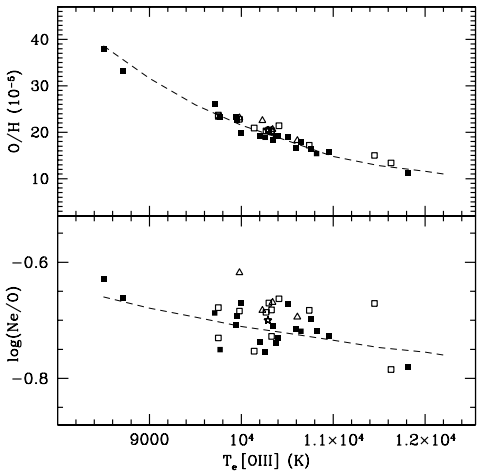

FIGURE 4.10— The derived oxygen abundances and Ne/O ratios plotted against the measured T_e [O III]. The effect of temperature variations on the oxygen abundance and Ne/O ratio is also plotted (dashed line). For an explanation of the symbols see Fig. 4.4.

a radial gradient was found in the nitrogen abundance and N/O ratio. This apparent gradient is believed not to be real, but the result of line-of-sight effects in the spatially resolved ionization structure of the nebula.

4.5 The R23 and S23 abundance indicators

In those cases where no electron temperature can be determined, other means of deriving abundances must be employed. Important tools for determining the oxygen and sulfur abundances in the absence of an electron temperature are the so called 'bright line' methods. In these methods, the bright lines of all the important ionization stages of an element are summed to get an estimate of its abundance. The 'bright line' indicators for oxygen (R23, Pagel et al. 1979) and sulfur (S23, Vílchez & Esteban 1996) are defined respectively as

$$\mathrm{R23} = \frac{[\mathrm{O\,III}]\,5007, 4959 + [\mathrm{O\,II}]\,3727}{\mathrm{H}\beta}, \tag{4.13}$$

and

$$\mathrm{S23} = \frac{[\mathrm{S\,III}]\,9068, 9532 + [\mathrm{S\,II}]\,6717, 6730}{\mathrm{H}\beta}. \tag{4.14}$$

To test the reliability of these parameters in the case of a spatially resolved nebula, their values and their associated oxygen and sulfur abundances are plotted in Fig. 4.11. We overplot the data points with a small grid of general photoionization models, which was calculated using CLOUDY for a range of metallicities between 0.1 and 1.0 $Z_\odot$, and for the ionization parameters $\log U = -3$, -2, -1 and 0. The stellar atmosphere used was the D2 CoStar model from Schaerer & de Koter (1997). The hydrogen density was fixed at 500 cm^{-3} and the inner radius of the central cavity of the model was set at 10^{17} cm. Also plotted in Fig. 4.11 are the results for 30 Doradus from VvdH.

It turns out that the R23 and S23 parameters are very well constrained across the face of the nebula; the parameter values lie in a rather narrow range, and are tightly

correlated with the O and S abundances. The inner and outer group of spectra largely overlap in the R23 plot despite the differences in excitation between the two groups of spectra (see Fig. 4.4). This is, however, much less the case for S23. The R23 parameter is also very consistent with regard to the ionization parameter; most points fall between the $\log U = -1$ and $\log U = -2$ model curves. Again, this consistency in $\log U$ is less clear for S23. Note the difference in the model $\log U$ as predicted by using either R23 or S23.

If we compare the results for S23 with those of 30 Dor from VvdH, we find a good agreement between the two. This is very interesting given the fact that the results from VvdH are obtained from spatially integrated spectra rather then from stationary longslit spectra. Comparing R23 for 30 Dor from VvdH with the present work would be less meaningful since for oxygen some of the spectra from the present work have been used in their analysis. However, work by Kobulnicky et al. (1999) on the use of the R23 parameter as an abundance indicator in the case of globally integrated spectra showed the parameter to be fairly robust.

Based on the present results, we draw the following conclusions. The abundance indicators R23 and S23 give consistent results when measured at various locations in the nebula, both in their measured value as in the associated directly determined oxygen or sulfur abundance. This robustness seems to extent to globally integrated spectra; the result for S23 suggest that the use of either global or local spectra does not make much difference for the final result. Caution should be exercised though, because the driftscan spectra used by VvdH only sample selected parts of 30 Dor, so whether our conclusion also holds for spectra which are integrated over the *full* spatial extent of an H II region is not clear.

One final note should be made about the differences in the degree of overlap between the outer and inner group spectra for R23 and S23. The separation between the two groups of spectra seen in the case of S23 is due to neglecting the important S^{+3} ion in the equation, which makes S23 more sensitive to the ionization parameter. That the inclusion of all the relevant ionization stages in the abundance indicator is important for a correct interpretation was clearly demonstrated by VvdH. This problem does not play a role for oxygen, since nearly all the oxygen is in the form of O^{+} and O^{++} of which both are included in R23.

4.6 The global spectrum

In extragalactic abundance studies, the H II region usually fills the entire beam. Any analysis of the nebula is thus based on spatially integrated spectra which can incorporate a large range in e.g. temperature and ionization parameter across the beam. An important question therefore is how the analysis results from a global, spatially integrated spectrum compare with those derived from separate spectra in a spatially resolved nebula.

To get a very rough approximation of a global spectrum for 30 Dor, we summed the reddened fluxes of the separate spectra for all the relevant lines. These integrated fluxes where then divided by the summed Hβ flux to get the resultant, reddened spectrum. The sum spectrum was dereddened using the average extinction curve for 30 Dor (see Fig, 4.3) and the Balmer decrements from the sum spectrum itself. The resultant,

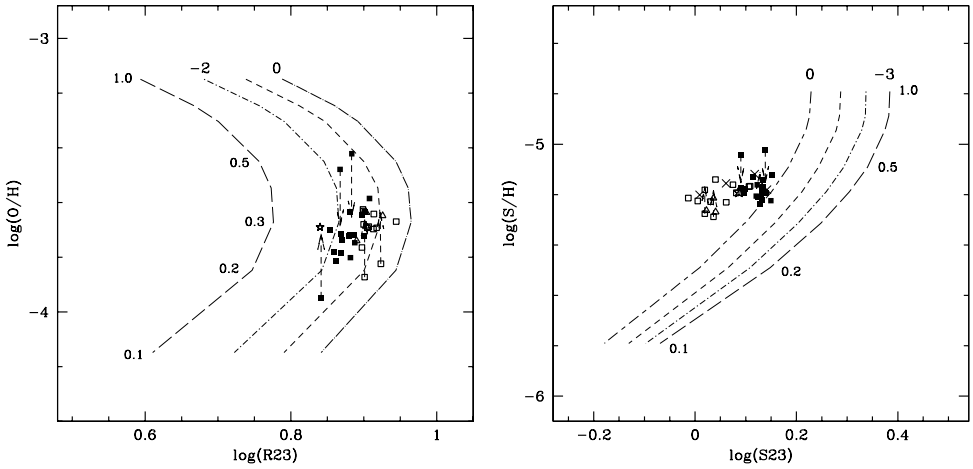

FIGURE 4.11— The oxygen and sulfur abundances plotted against the R23 and S23 abundance indicators, respectively. The model calculations for $\log U = 0$, -1, -2 and -3 are shown for metallicities in the range from 0.1 to 1.0 $Z_\odot$. The dashed arrows show the shift in the derived abundances if we recalculate these for the temperature-anomalous points assuming an electron temperature of 10 000 K (see Sect. 4.3). The crosses in the righthand panel indicate the results from VvdH. For an explanation of the other symbols see Fig. 4.4.

dereddened spectrum is given in Table 4.12 together with the analysis results.

The analysis results from the global spectrum agree very well with the average results for the separate spectra. The electron temperature and density are close to the average values from the separate spectra. However, more important is the good agreement of the global spectral characteristics; all the characteristics of the global spectrum give a good representation of the sample as a whole. The abundances and heavy element-to-oxygen ratios are comparable to those derived from the separate spectra, but this is, of course, a reflection of the overal chemical homogeneity of 30 Dor. The nitrogen abundance and N/O ratio from the global spectrum are also well-behaved, despite the apparent gradient found in the nitrogen abundance for the separate positions.

This little exercise shows that the spectral characteristics found in a global spectrum appear to be reasonably representative of the nebula as a whole. One should remember, however, that our approximation to a real spatially integrated spectrum is only rough.

4.7 Summary

In this work, a study of the spectral and chemical characteristics of the giant LMC H II region 30 Doradus was presented. Based on 35 spectral positions located in the core of the nebula, we investigated the variation in spectral characteristics and chemical composition of 30 Dor as a function of the distance from the ionizing source R 136. We were in particular interested in the robustness of commonly used spectral parameters like R23 when measured at various positions in a spatially resolved nebula.

Good correlations were found between the various high and low-ionization lines

TABLE 4.12— The global optical spectrum of 30 Doradus and the analysis results derived from it. The electron temperature and density are in units of Kelvin and cm^{-3}, respectively.

		I_λ/I_β			I_λ/I_β	Analysis results			
3727	[O II]	1.03	5875	He I	0.12	T_e [O III]	= 10290	n_e [S II]	= 360
3869	[Ne III]	0.36	6563	Hα	2.86				
4101	Hδ	0.26	6585	[N II]	0.074	log(η')	= 0.29		
4340	Hγ	0.47	6717	[S II]	0.046	log(R23)	= 0.84	log(S23)	= 0.086
4363	[O III]	0.035	6730	[S II]	0.041				
4861	Hβ	1.00	7137	[Ar III]	0.11	log(O/H)	= −3.69	log(He/H)	= −1.06
4959	[O III]	1.74	9068	[S III]	0.38	log(S/H)	= −5.19	log(S/O)	= −1.50
5007	[O III]	5.16	9532	[S III]	0.76	log(Ar/H)	= −5.91	log(Ar/O)	= −2.21
						log(Ne/H)	= −4.39	log(Ne/O)	= −0.70
	$E_{\beta-\alpha}$	0.38				log(N/H)	= −5.16	log(N/O)	= −1.47

(see Fig. 4.4). This well correlated behaviour of the various line strengths when moving outwards from R 136 is indicative of a well-defined ionization structure. The ionization parameter as traced by the [O II]/[O III] and [S II]/[S III] line ratios is well constrained across the nebula, and the Vilchez & Pagel (1988) η' parameter varies only slightly from position to position. The data from Kennicutt et al. (2000) strengthen this result and extend it to larger distances from R 136.

We found no evidence for chemical enrichment in 30 Dor, and no variation of the abundances with increasing projected radial distance from R 136 was seen. The abundances are all comparable to the mean LMC abundances (Garnett 2000), and the heavy element-to-oxygen ratios for sulfur, argon and neon do not deviate from the commonly found values. However, we did find a radial increase in the nitrogen abudance and a subsequent radial increase in the N/O ratio. We discussed the possible cause of the apparent nitrogen gradient and we concluded that this is the result of line-of-sight effects.

The bright-line abundance parameters for oxygen (R23) and sulfur (S23) turned out to be very constant across the nebula, with a well defined connection between the measured abundance parameter and the derived abundance. For R23, the different spectral positions show a much tighter overlap than for S23, which is the result of neglecting the S^{+3} ion in the S23 parameter.

To investigate to what extent the results from spatially resolved spectra are retained in a spatially integrated spectrum, we created an 'artificial' global spectrum by summing the fluxes from the separate spectra. All the analysis results from the global spectrum agreed very well with those derived from the separate spectra. This is especially important for spectral parameters like R23, which are often used in extragalactic abundance studies where the spectra are spatially unresolved.

A recurring theme in this work was the contrast between spatially resolved and spatially integrated spectra, and how differences in the type of spectra might affect the analysis results. The robustness of the η' and, more importantly, the bright-line abundance diagnostics observed in this study of 30 Doradus strongly support their

applicability in the case of spatially unresolved spectra of extragalactic H II regions. The nitrogen problem encountered in Sect. 4.4.2 clearly shows that for some purposes the use of spatially integrated spectra might even be preferable.

References

Alexander, J., Balick, B. 1997, AJ **114**, 713
Baker, J.G., Menzel, D.H. 1938, ApJ **88**, 52
Balick, B., Perinotto, M., Maccioni, A., Terzian, Y., Hajian, A. 1994, ApJ **424**, 800
Benjamin, R.A., Skillman, E.D., Smits, D.P. 1999, ApJ **514**, 307
Caplan, J., Deharveng, L. 1986, A&A **155**, 297
Chu, Y.-H., Kennicutt Jr, R.C. 1994, ApJ **425**, 720
Dopita, M.A., Sutherland, R.S. 1995, ApJ **455**, 468
Dopita, M.A., Sutherland, R.S. 1996, ApJS **102**, 161
Garnett, D.R. 1990, ApJ **363**, 142
Garnett, D.R. 1992, AJ **103**, 1330
Garnett, D.R. 2000, in IAU symposium 190 *New Vieuws of the Magellanic Clouds* eds. Y.-H. Chu, N.B. Suntzeff, J.E. Hesser, D.A. Bohlender, p. 266
Gruenwald, R.B., Viegas, S.M. 1992 ApJS **78**, 153
Gruenwald, R.B., Viegas, S.M. 1998, ApJ **501**, 221
Howarth, I.D. 1983, MNRAS **203**, 301
Izotov, Y.I., Thuan, T.X. 1999, ApJ **511**, 639
Kennicutt Jr., R.C., Bresolin, F., French, H., Martin, P. 2000, ApJ **537**, 589
Kobulnicky, H.A., Kennicutt, R.C., Pizagno, J.L. 1999, ApJ **514**, 544
Krabbe, A.C., Copetti, M.V.F. 2002, A&A **387**, 295
Lester, D.F., Dinerstein, H.L., Werner, M.W., Watson, D.M., Genzel, R.L. 1983, ApJ **271**, 618
Massey, P., Hunter, D.A. 1998, ApJ **493**, 180
Mathis, J.S. 1985, ApJ **291**, 247
Mathis, J.S., Chu, Y.-H., Peterson, D.E. 1985, ApJ **292**, 155
Pagel, B.E.J., Edmunds, M.G., Blackwell, D.E., Chun, M.S., Smith, G. 1979, MNRAS **189**, 95
Rubin, R.H., Simpson, J.P., Haas, M.R., Erickson, E.F. 1991, ApJ **374**, 564
Schaerer, D., De Koter, A. 1997, A&A **322**, 598
Scowen, P.A., Hester, J.J., Sankrit, R. et al. 1998, AJ **116**, 163
Stasińska, G. 1978, A&A **66**, 257
Stasińska, G. 1990, A&AS **83**, 501
Storey, P.J., Hummer, D.G. 1995, MNRAS **272**, 41
Thurston, T.R., Edmunds, M.G., Henry, R.B.C. 1996, MNRAS **283**, 990
Vermeij, R., Van der Hulst, J.M. 2002b, A&A, in press (VvdH)
Vila-Costas, M.B., Edmunds, M.G. 1993, MNRAS **265**, 199
Vílchez, J.M., Pagel, B.E.J. 1988, MNRAS **231**, 257
Vílchez, J.M., Esteban, C. 1996, MNRAS **280**, 720
Walborn, N.R., Blades, J.C. 1997, ApJS **112**, 457
Walter, D.K., Dufour, R.J & Hester, J.J. 1992, ApJ **397**, 196

Chapter 5

The stellar content, metallicity and ionization structure of H II regions

OBSERVATIONS of infrared fine-structure lines provide direct information on the metallicity and ionization structure of H II regions and indirectly on the hardness of the radiation field ionizing these nebulae. We have analyzed a sample of Galactic and Magellanic Cloud H II regions observed by the Infrared Space Observatory (ISO) to examine the interplay between stellar content, metallicity and the ionization structure of the H II regions. The observed [S IV] 10.5/[S III] 18.7 μm and [Ne III] 15.5/[Ne II] 12.8 μm line ratios are shown to be highly correlated over more than two orders of magnitude. We have compared the observed line ratios with the results from photoionization models using various stellar energy distributions. The derived characteristics of the ionizing star depend critically on the adopted stellar model as well as the (stellar) metallicity. For a few well-studied H II regions, we have compared the stellar effective temperatures derived from these model studies with published direct spectroscopic determinations of the spectral type of their ionizing stars. This comparison supports our interpretation that both the stellar and nebular metallicity influence the observed infrared ionic line ratios. We can explain the observed increase in the degree of ionization, as traced by the [S IV]/[S III] and [Ne III]/[Ne II] line ratios, by the hardening of the radiation field due to the decrease of metallicity. The implications of our results for the determination of the ages of starbursts in starburst galaxies are assessed.

5.1 Introduction

The spectral type of the ionizing stars and the stellar and nebular metallicity are intimately interwoven in controlling the ionization structure of H II regions. Hotter stars will ionize trace elements to higher ionization stages. Metallicity, on the other hand, modifies the spectral energy distribution (SED) of the ionizing stars and thus, influences

the ionization structure indirectly. In particular, line blocking/blanketing is directly coupled to the metallicity and controls the stellar wind of massive stars. The stellar wind, in turn, also modifies the SED of the star. The interlocking of these different effects hampers the determination of the stellar content from ionic line observations. This has clear repercussions for the study of starburst regions in galaxies as well, where the stellar content is used as an indicator of the starburst age. Current models of stellar atmospheres have started to take the effects of metallicity into account (e.g. Schaerer & De Koter 1997; Pauldrach et al. 2001). Such models can fit the observed line ratios in H II regions reasonable well (e.g. Giveon et al. 2002; Morisset et al. 2002). The derived spectral types for the ionizing sources, however, depend on the stellar model adopted and can be very different.

The Infrared Space Observatory (ISO, Kessler et al. 1996) has provided a powerful tool for the study of the ionization structure of H II regions (Giveon et al. 2002; Martín-Hernández et al. 2002, hereafter MHP02). The ratios of fine-structure lines originating in the ionized gas (e.g. [Ar III] 9.0/[Ar II] 7.0 μm, [S IV] 10.5/[S III] 18.7 μm and [Ne III] 15.5/[Ne II] 12.8 μm) are widely used to constrain the properties of the ionizing stars in these nebulae (e.g. Watarai et al. 1998; Takahashi et al. 2000; Morisset et al. 2002). The systematic studies of the ionization structure of H II regions via these ionic line ratios as a function of Galactocentric distance in the Milky Way by Martín-Hernández et al. (2002) and in the Large and Small Magellanic Clouds by Vermeij & Van der Hulst (2002a) have now provided us with a 'natural' sample of H II regions over a wide range in metallicity. Such a sample allows us to study the effect of stellar type and metallicity on the ionization structure. Moreover, while the ionizing stars in most H II regions are heavily extincted in the visible by tens to hundreds of magnitudes, the opening up of the infrared window has favoured in recent years the use of infrared spectra to infer the spectral types of the ionizing stars. An important effort has now started to identify the ionizing stars of Galactic H II regions in the K-band (Hanson et al. 1996; Watson & Hanson 1997) and the first results are now becoming available (Kaper et al. 2002a,b).

In this chapter, we examine this interplay between stellar content, metallicity and ionization structure of H II regions based upon the ISO sample. This chapter is structured as follows. Sect. 5.2 describes the combined sample of Galactic and LMC/SMC H II regions; Sect. 5.3 shows the correlation between the observed [Ne III]/[Ne II] and [S IV]/[S III] line ratios. In Sect. 5.4 and Sect. 5.5, we investigate the influence of the SEDs and the stellar/nebular metallicity, respectively, on the ionization structure. Sect. 5.6 discusses the implications for the interpretation of the spectra of starburst galaxies. Finally, in Sect. 5.7 we discuss and summarize the results.

5.2 The sample

We combined the ISO Short Wavelength Spectrometer (de Graauw et al. 1996) observations of the Galactic and Magellanic Cloud H II regions as described in the catalogues by Peeters et al. (2002) and Vermeij et al. (2002b). These catalogues present the atomic fine-structure line fluxes of 43 Galactic nebulae and 12 Magellanic Cloud sources. The first analysis of the observed fine-structure lines is presented in MHP02 and Vermeij & van der Hulst (2002a). This analysis includes, among others, the derivation of elemental abundances and a discussion on the ionization state of the nebulae.

TABLE 5.1— Selected H II regions in the Milky Way, Small Magellanic Cloud (SMC) and Large Magellanic Cloud (LMC). Given are the object name, the distance in kpc of the Galactic objects from the center of the Galaxy and the coordinates of the ISO pointing.

Object	Rgal (kpc)	RA (J2000.0) (h , m , s)	δ (J2000.0) (^{o}, $'$, $''$)	Object	RA (J2000.0) (h , m , s)	δ (J2000.0) (^{o}, $'$, $''$)
Milky Way :				**SMC :**		
IR 01045+6506	13.8	01 07 50.7	+65 21 21.7	N66	00 59 03.7	−72 10 39.9
IR 02219+6125	11.0	02 25 44.6	+62 06 11.3	N81	01 09 13.6	−73 11 41.1
IR 10589−6034	9.5	11 00 59.8	−60 50 27.1			
IR 11143−6113	9.7	11 16 33.8	−61 29 59.4	**LMC :**		
IR 12063−6259	9.3	12 09 01.1	−63 15 54.7			
IR 12073−6233	10.1	12 10 00.3	−62 49 56.5	N4A	04 52 08.4	−66 55 23.4
IR 12331−6134	6.9	12 36 01.9	−61 51 03.9	N83B	04 54 25.2	−69 10 59.8
IR 15384−5348	6.4	15 42 17.1	−53 58 31.5	N11A	04 57 16.2	−66 23 18.3
IR 15502−5302	4.6	15 54 06.0	−53 11 36.4	30 Dor#1	05 38 33.5	−69 06 27.1
IR 17221−3619	5.2	17 25 31.7	−36 21 53.5	30 Dor#2	05 38 35.5	−69 05 41.2
IR 17455−2800	0.5	17 48 41.5	−28 01 38.3	30 Dor#3	05 38 46.0	−69 05 07.9
IR 18116−1646	4.3	18 14 35.2	−16 45 20.6	30 Dor#4	05 38 54.2	−69 05 15.3
IR 18317−0757	4.5	18 34 24.9	−07 54 47.9	N160A1	05 39 43.3	−69 38 51.4
IR 18434−0242	4.6	18 46 04.0	−02 39 20.5	N160A2	05 39 46.1	−69 38 36.6
IR 18479−0005	7.5	18 50 30.8	−00 01 59.4	N159-5	05 40 02.4	−69 44 33.4
IR 18502+0051	4.7	18 52 50.2	+00 55 27.6			
IR 19598+3324	9.8	20 01 45.6	+33 32 43.7			
Dr 21	8.6	20 39 00.9	+42 19 41.9			
IR 21190+5140	12.7	21 20 44.9	+51 53 26.5			
IR 23030+5958	11.4	23 05 10.6	+60 14 40.6			

From this combined set of H II regions, we selected those for which both information on their elemental abundances (through Ne/H) and ionization state (through the [S IV] 10.5/[S III] 18.7 μm and [Ne III] 15.5/[Ne II] 12.8 μm line ratios) could be derived. The selected H II regions are listed in Table 5.1, where the source name, the distance of the Galactic objects from the center of the Galaxy and the ISO pointing coordinates are given. We chose to use Ne/H as a tracer of the nebular metallicity. The neon abundance can be determined from the IR fine-structure lines to a higher precision than other elements because it is less sensitive to ionization correction factors and assumptions regarding electron densities (see MHP02 for a complete discussion). Moreover, as a primary element, the abundance of neon closely follows that of oxygen (e.g. Henry & Worthey 1999 and references therein). As far as the choice of the ionization tracers is concerned, the choice of the [S IV]/[S III] and [Ne III]/[Ne II] line ratios was an obvious one as [Ar III]/[Ar II] has only been detected in a few LMC H II regions.

In total, our sample consists of 20 Galactic H II regions located at Galactocentric distances between 0 and 15 kpc, 7 H II regions in the LMC (including 4 positions in 30 Doradus) and 2 in the SMC. Also included are the SWS observations of Sgr A*, our own Galactic Center (Lutz et al. 1996), and the Orion nebula, for which an "integrated" infrared spectrum was obtained by Simpson et al. (1998) using the Midcourse Space Experiment (MSX) satellite. The MSX field of view (6'× 9') included most of the Orion nebula.

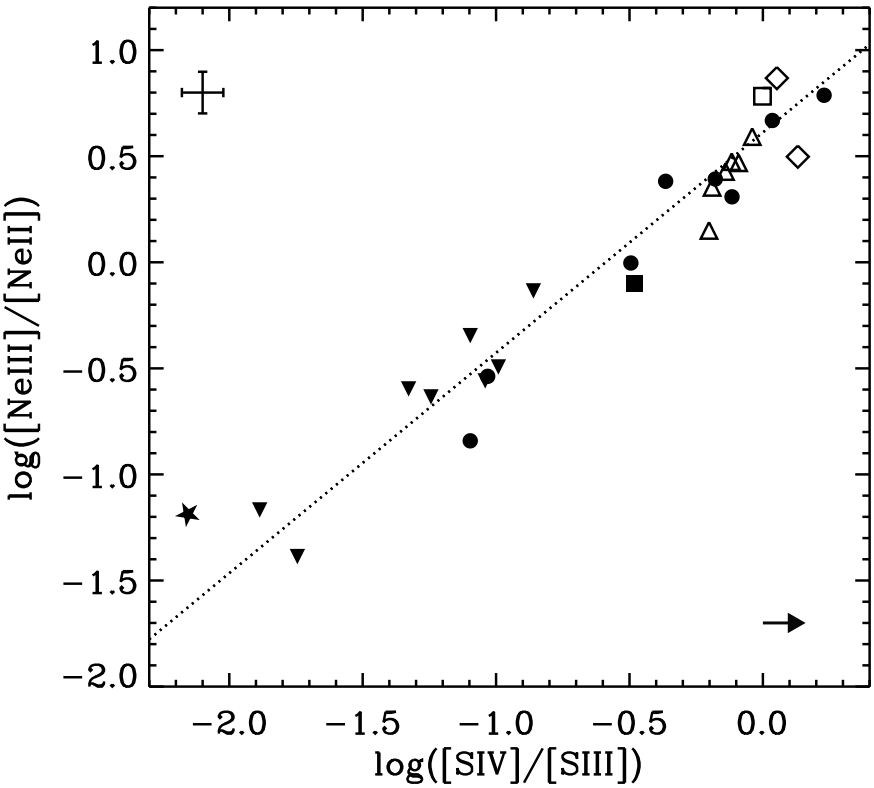

FIGURE 5.1— The relationship between the [S IV] 10.5/[S III] 18.7 μm and [Ne III] 15.5/[Ne II] 12.8 μm line ratios for the combined sample of H II regions. Indicated by various symbols are the Galactic nebulae at $R_{\rm Gal}< 7$ kpc (solid triangles), the Galactic nebulae at $R_{\rm Gal}> 7$ kpc (solid circles), the LMC nebulae (open triangles, except 30 Doradus, which is indicated by an open square) and the SMC nebulae (open diamonds). To avoid confusion, only the averaged location of the 4 SWS positions in 30 Doradus is indicated. The positions of Sgr A* (Lutz et al. 1996) and the Orion nebula (Simpson et al. 1998) are indicated by a solid star and a solid square, respectively. The dotted line is a least squares fit to the data. A typical error bar of the ISO data is given in the upper left corner. The arrow in the lower right corner indicates the extinction correction for an $A_{\rm K}$ of 2 mag.

5.3 Variations in the ionization structure

The ionization structure of a nebula basically depends on the shape of the SED of the ionizing source and on the nebular geometry. In the case of an ionized sphere of constant gas density and filling factor, the geometrical effect can be defined by the ionization parameter $U = Q_{\rm H}/(4\pi R^2 nc)$, where $Q_{\rm H}$ is the number of stellar photons above 13.6 eV emitted per second, R the Strömgren radius, n the gas density, and c the speed of light. The ionization structure can be traced by the ratio of successive stages of ionization X^{+i} and X^{+i+1} of a given element. Such a ratio depends, for a given U, on the number of photons able to ionize X^{+i} (Vilchez & Pagel 1988).

In Fig. 5.1, we present the relation between the [S IV]/[S III] and the [Ne III]/[Ne II] line ratios for the combined sample of H II regions in the Milky Way and the LMC/SMC. The line ratios have not been corrected for extinction. The [Ne II] 12.8 and [Ne III] 15.5 μm lines are very close in wavelength, so the [Ne III]/[Ne II] ratio is practically insensitive to extinction. However, the differential extinction between the [S IV] 10.5 and [S III] 18.7 μm lines ($\sim 0.08 A_{\rm K}$ if a standard extinction curve is considered, see MHP02) can affect the [S IV]/[S III] line ratio. The effect of this differential extinction is indicated in the lower right corner of Fig. 5.1 for a typical $A_{\rm K}$ of 2 mag (MHP02).

The data shown in Fig. 5.1 span a range in ionization of more than 2 orders of magnitude. The LMC/SMC points nicely overlap the Galactic trend at the high ionization end. The least squares fit to the data, displayed as a dotted line, gives a slope of 1.04 ± 0.05 and an intercept of 0.61 ± 0.04. Fig. 5.1 also illustrates the change in the degree of ionization of the Galactic H II regions with increasing distance from the Galactic center. The more highly ionized objects are located at larger Galactocentric distances, while the less highly ionized objects, including Sgr A*, are located at smaller distances. In line with the known metallicity gradient in the Galaxy (e.g. see review by Henry & Worthey 1999; Rolleston et al. 2000 and references therein), the location of the high metallicity Galactic Center at the low ionization end of the correlation and the low metallicity LMC/SMC H II regions at the high ionization end suggests that metallicity is somehow involved in the change of degree of ionization and hence, in the hardening of the radiation field shown in Fig. 5.1.

We consider in the next sections both the influence of the SED and the metallicity on the ionization structure of H II regions.

5.4 Influence of the SEDs

In order to investigate the dependence of the [Ne III]/[Ne II] and [S IV]/[S III] line ratios on the SED, a set of nebular models has been calculated with the photoionization code CLOUDY (Ferland et al. 1998) using MICE, the IDL interface for CLOUDY created by H. Spoon[1]. The parameters varied in the modelling are the stellar effective temperature ($T_{\rm eff}$) and the ionization parameter (U). We compute nebular models for a static, spherically symmetric, homogeneous gas distribution with one ionizing star in the center. An inner cavity with a radius equal to 10^{17} cm is set, while the outer radius of the H II region is defined by the position where the electron temperature, $T_{\rm e}$, reaches 100 K. Two different stellar atmosphere models are taken to describe the SED:

[1] see http://www.astro.rug.nl/∼spoon/mice.html

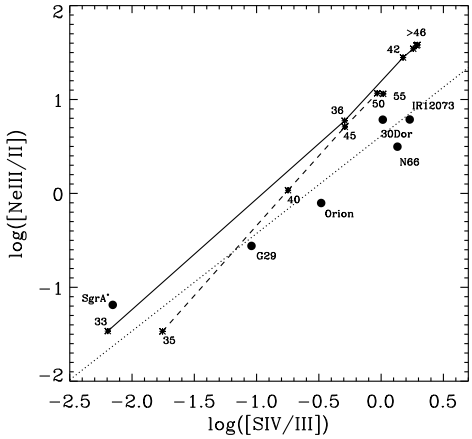

FIGURE 5.2— The dependence of the [S IV]/[S III] and [Ne III]/[Ne II] line ratios on the stellar $T_{\rm eff}$ (crosses) as given by the CoStar (solid lines) and Pauldrach (dashed lines) SEDs. Only photoionization models for $n_{\rm H}$=10^3 cm^{-3} are plotted. The observed line ratios for the reference sources (Sgr A*, G29.96−0.02, the Orion nebula, IRAS 12073−6233, N66 and 30 Dor) are indicated by solid circles. The dotted line is the least squares fit to the data also plotted in Fig. 5.1.

the CoStar models by Schaerer & De Koter (1997) and the models by Pauldrach et al. (2001). Previous studies of these ionization ratios have concentrated on either the CoStar models (e.g. Morisset et al. 2002, MHP02) or on the Pauldrach models (Giveon et al. 2002). For a detailed study of the influence of these and other stellar SEDs on the ionization ratios, we refer to the work by Morisset et al. (in prep.). We use stellar models for main sequence (dwarf) stars, i.e. CoStar models A2, B2, C2, D2, E2 and F2, and Pauldrach models D-35, D-40, D-45, D-50 and D-55. The metallicity of the star and the nebula is chosen to be solar. The number of hydrogen ionizing photons emitted by the central source is fixed to the typical value of $Q_{\rm H} = 10^{48}\,{\rm photons\,s^{-1}}$. The parameter U is varied by changing the hydrogen density ($n_{\rm H}$). For each of the stellar atmosphere models selected, which span a range in $T_{\rm eff}$ from approximately 30 to 55 kK, photoionization models are calculated for $n_{\rm H}$= $10^2, 5\times10^2, 10^3, 5\times10^3$ and 10^4 cm^{-3}.

The output of this grid of models for $n_{\rm H}$=10^3 cm^{-3} is presented in Fig. 5.2. The variation of [Ne III]/[Ne II] and [S IV]/[S III] with $T_{\rm eff}$ is shown separately for the two selected SED models. An increase in density of two orders of magnitude produces an increase of the line ratios of at most 0.5 dex approximately along the lines drawn in Fig. 5.2. For reference, the observed line ratios of the Galactic sources Sgr A*, G29.96−0.02 (IRAS 18434−0242), the Orion nebula and IRAS 12073−6233, the SMC H II region N66, and 30 Doradus are indicated by solid circles. Sgr A* and IRAS 12073 delimit the observed parameter space for [Ne III]/[Ne II] and [S IV]/[S III] as they are, respectively, the lowest and highest ionized source in Fig. 5.1. Several points can be gleaned from inspection of Fig. 5.2:

(a) The [Ne III]/[Ne II] and [S IV]/[S III] line ratios strongly depend on the stellar $T_{\rm eff}$, but they can no longer discriminate between models when most of the Ne and S is in the higher ionization stage (see also Giveon et al. 2002, MHP02). When this happens, these line ratios remain constant even with large changes in the SED. When using the CoStar SEDs, both [Ne III]/[Ne II] and [S IV]/[S III] become insensitive to the stellar $T_{\rm eff}$ for $T_{\rm eff}>$ 42 kK, while when using the Pauldrach

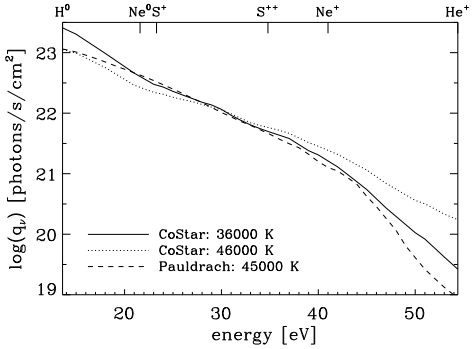

FIGURE 5.3— The number of ionizing photons in $cm^{-2}s^{-1}$ above a certain energy from the CoStar B2 (36000 K), D2 (46000 K) and Pauldrach D-45 (45000 K) SED models is plotted as a function of this energy. The curves are normalized so that the total number of hydrogen ionizing photons Q_H is 10^{48} photons s^{-1}, the value used in the photoionization models. These curves define the ionization structure in the nebula for a given ionization parameter U. Labeled at the top of the figure are the ionization energies for H, He, S^{++}, Ne^{+} and He^{+}.

SEDs, the hardness of the stellar ionizing flux changes less rapidly with $T_{\rm eff}$, and it is not until $T_{\rm eff}>$ 50 kK that the star fully ionizes S^{++} and Ne^{+}.

(b) The slope of the observed log([Ne III]/[Ne II]) versus log([S IV]/[S III]) is practically equal to 1 (cf. Fig. 5.1), suggesting that the spectral hardening affects the range of ionizing energies for S^{++} ($h\nu > 35$ eV) and Ne^{+} ($h\nu > 41$ eV) equally. The model trends are, however, slightly steeper than the data, i.e. for a given $T_{\rm eff}$ the models overpredict [Ne III]/[Ne II] (underpredict [S IV]/[S III]) by a factor up to 5 for a given [S IV]/[S III] ([Ne III]/[Ne II]). As has been discussed by Oey et al. (2000) and Morisset et al. (2002), there is an indication that the CoStar models overpredict the stellar spectrum at these ionizing energies.

(c) When using the CoStar SEDs to describe the emergent flux, practically the entire observed ionization range spanning more than 2 orders of magnitude can be modeled by a rather narrow $T_{\rm eff}$ range between $\sim$ 33 kK and $\sim$ 42 kK. This effect is less dramatic with the Pauldrach SEDs, for which the entire range up to 55 kK is suitable for modelling the observed line ratios.

We see that large differences appear when we compare the predictions by the CoStar models to those by the Pauldrach ones for a given $T_{\rm eff}$. These differences are primarily caused by the different treatment of the line blocking and blanketing between the two SED models. This causes the Pauldrach models to have a much softer spectrum than the analogous CoStar model at a similar $T_{\rm eff}$. Note, for instance, the case of the CoStar SED with $T_{\rm eff}$=36000 K (model B2) and the Pauldrach SED with $T_{\rm eff}$=45000 K (model D-45) in Fig. 5.2, which predict practically the same values for [S IV]/[S III] and [Ne III]/[Ne II].

It is instructive to calculate the integrated ionizing photon flux above a certain energy as a function of this energy for these two stellar models (CoStar B2 and Pauldrach D-45). The number of ionizing photons in $cm^{-2}\,s^{-1}$ with energies larger than $h\nu_i$ is defined as $q_{\nu_i} = \int_{\nu_i}^{\infty} F_\nu/(h\nu)d\nu$, with F_ν being the astrophysical flux in erg s^{-1} cm^{-2} Hz^{-1}.

TABLE 5.2— Comparison of the stellar properties predicted via the [Ne III]/[Ne II] and [S IV]/[S III] line ratios with the spectral type derived directly from infrared/optical stellar spectra. The objects are sorted by increasing degree of ionization.

Object name	Observed Spectral Type and $T_{\rm eff}$			Predicted $T_{\rm eff}$		
	(a)	(b)	(c)	CoStar[(d)]	Pauldrach[(e)]	Ref.[(f)]
G 29.96−0.02	O5–O3	46–51	42–49	33–36	35–40	1
Orion nebula	O6	44	39	33–36	40–45	2
N66	O6.5 and earlier	> 42	> 37	33–42	>40	3
30 Doradus	O4–O3	49–51	43–49	36–42	>45	4,5
IRAS 12073−6233	O7.5–O6	40–44	36–39	> 36	>45	1

(a) Spectral type determined from infrared/optical stellar spectra. (b) $T_{\rm eff}$ in kK derived from the observed spectral type using the calibration by Vacca et al. (1996). (c) $T_{\rm eff}$ in kK derived from the observed spectral type using the calibration by Martins et al. (2002). (d) $T_{\rm eff}$ in kK predicted by the CoStar SEDs. (e) $T_{\rm eff}$ in kK predicted by the Pauldrach SEDs. (f) Reference of the observed spectral type. REFERENCES: (1) Kaper et al. (2002a,b) and private communication; (2) SIMBAD database; (3) Massey et al. (1989); (4) Walborn & Blades (1997); (5) Massey & Hunter (1998).

The results are shown in Fig. 5.3. For a meaningful comparison with the photoionization model results, the total number of hydrogen ionizing photons has been scaled to 10^{48} photons s^{-1}, the value used in these models. We note that the stellar models differ in their radii. The [S IV]/[S III] and [Ne III]/[Ne II] line ratios are basically sensitive to the slope of the curve between the energies able to produce and ionize S^{++} and Ne^{+}, i.e. between 23.3 and 34.8 eV, and 21.6 and 41.0 eV, respectively. The slopes of the CoStar B2 and the Pauldrach D-45 SEDs are very similar between these energies; hence, their match in the predicted [S IV]/[S III] and [Ne III]/[Ne II] line ratios. The ionization structure of a nebula with such values of [S IV]/[S III] and [Ne III]/[Ne II] can, therefore, be equally well described by any of these two SEDs. However, the interpretation of this ionization structure in terms of the stellar properties, e.g. $T_{\rm eff}$, depends on the stellar model adopted. For comparison, we also show the shape of the hotter CoStar model D2 with a $T_{\rm eff}$ of 46000 K. The ionizing flux of this hotter CoStar model starts to be higher than the corresponding Pauldrach model above $\sim$ 30 eV. This hotter CoStar model will, consequently, produce a larger amount of S^{+3} and Ne^{++}.

In this respect, closely related to the problem of determining the $T_{\rm eff}$ of the ionizing sources is that of their spectral type classification. It is illustrative to consider at this point the cases of G29.96−0.02, the Orion nebula, IRAS 12073−6233, N66 and 30 Doradus, for which the spectral types of the ionizing star(s) are known. The Orion nebula is ionized by the Trapezium cluster, the dominant source of ionizing radiation being the O6 star θ^1C Ori. 30 Dor is known to be powered by a stellar cluster containing a large number of O3–O4 stars (Walborn & Blades 1997; Massey & Hunter 1998). N66 is the most prominent H II region in the SMC. It contains a rich stellar cluster of at least 33 O stars of which 11 are of type O6.5 or earlier (Massey et al. 1989). Recent high resolution K-band spectral observations of G29 and IRAS 12073 (Kaper et al. 2002a,b, private communication) allow the determination of the spectral type of the ionizing stars based mainly upon the presence and strength of photospherical lines of C IV and

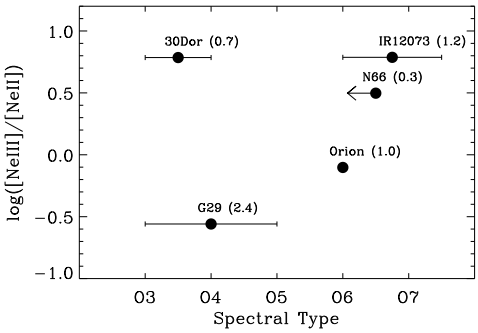

FIGURE 5.4— The ionization ratio [Ne III]/[Ne II] is compared to the observed spectral type of the ionizing sources of G29.96−0.02, the Orion nebula, IRAS 12073−6233, N66 and 30 Doradus. The numbers in brackets indicate the Ne/H abundance by number in units of 10^{-4}. References for the Ne/H abundances are: G29 and IRAS 12073 (MHP02); N66 and 30 Dor (Vermeij & Van der Hulst 2002a); Orion (Simpson et al. 1998).

N III (Hanson et al. 1996). These observations indicate that IRAS 12073 is ionized by a cluster of young O6–O7.5 stars, while the spectral type of the main ionizing star in G29 is confirmed to be O3–O5 (we note that lower resolution K-band spectral observations by Watson & Hanson 1997 classified this star as being O5–O8).

As mentioned above, the interpretation of the [S IV]/[S III] and [Ne III]/[Ne II] line ratios observed for these objects in terms of the stellar $T_{\rm eff}$ depends on the stellar model used to describe the ionization structure traced by these ratios. The subsequent spectral classification of the ionizing source depends on the spectral type attributed to the SED used in the modelling of the H II region. We can try to compare the $T_{\rm eff}$ determined from the observed line ratios by using either CoStar or Pauldrach SEDS (cf. Fig. 5.2) with the observed spectral type of the ionizing star(s). To do so, we need a $T_{\rm eff}$–spectral type calibration for O stars. The $T_{\rm eff}$ calibration of the different spectral types is based on modelling the observed photospheric hydrogen, helium and metal lines and it is by no means certain. For instance, the commonly used $T_{\rm eff}$–spectral type calibration by Vacca et al. (1996) is based on plane-parallel models which do not incorporate stellar winds and line blocking/blanketing. The more recent calibration by Martins et al. (2002), based on non-LTE line blanketed atmosphere models with stellar winds computed with the *CMFGEN* code of Hillier & Miller (1998), gives substantially lower effective temperatures than the Vacca et al. (1996) calibration for the same spectral type. We will use both calibrations.

The result of the comparison between the observed spectral types and the predicted stellar properties is summarized in Table 5.2. The calibration by Martins et al. (2002) gives effective temperatures for the observed spectral types $\sim$ 4000 − 5000 K lower than Vacca et al. (1996). Even considering this most recent calibration, the CoStar models systematically predict a lower temperature for the ionizing stars than observed. A better match is found by using the Pauldrach SEDs, although the predicted $T_{\rm eff}$ for G29 is still low. The opposite is true for IRAS 12073, for which the Pauldrach models predict a hotter star than observed. Moreover, while our photoionization models predict that an increase in the degree of ionization is coupled to an increase in $T_{\rm eff}$ and thus in spectral type, observationally this trend is less clear (cf. Fig. 5.4). In particular,

G29 and 30 Dor are both ionized by very early O stars, yet their ionization ratios are very different. Similarly, IRAS 12073 and 30 Dor are ionized by stars with very different spectral types but their ionization ratios are very similar. It is clear that the stellar spectral type as determined from optical or infrared spectroscopy is not the only controlling factor of the ionization structure of H II regions. In line with the discussion in Sect. 5.3 (cf. Fig. 5.1), we infer that both the metallicity of the star and the metallicity of the H II region are involved as well. At this respect, the differences in spectral type between G29 and 30 Dor, and in ionization structure between 30 Dor and IRAS 12073 may be a consequence of the differences in metallicity. G29 has a Ne/H abundance more than 3 times higher than 30 Dor; 30 Dor, on the other hand, has a lower abundance than IRAS 12073 (cf. Fig. 5.4).

It is well known that a stellar wind modifies the SED of a star. This effect is directly coupled to the strength of the wind, which in turn depends on the metallicity. Metallicity also controls the degree of attenuation of the UV and EUV stellar radiation due to line blocking and blanketing. Changes in metallicity can, therefore, transform the stellar spectrum to that of a cooler or hotter star than what is determined from the solar metallicity stellar models.

5.5 Influence of the metallicity

The ionization tracer [Ne III]/[Ne II] is compared with the metallicity tracer Ne/H in Fig. 5.5. The data show a loose trend of decreasing degree of ionization with increasing metallicity. No selection effect is thought to influence this relationship. While some of the LMC/SMC H II regions are among the brightest in these galaxies − 30 Dor (LMC) and N66 (SMC) are powered by luminous stellar clusters containing many early O stars −, the LMC sample also contains sources such as N11A, which are comparable to the H II regions in the Galactic sample in terms of luminosity and Lyman continuum flux. Besides, no selection effect is apparent in the Galactic H II regions, for which no obvious variation in the density of the ionized gas or the stellar luminosity with Galactocentric distance is observed (cf. MHP02). There is some systematic effect, however, due to the influence of metallicity on the electron temperature of the ionized gas. The Galactic Ne/H abundances were derived using Brα to determine the H^+ emission associated with the nebula assuming a constant T_e of 7500 Kelvin. Hence, a high metallicity nebula, which is expected to have a lower electron temperature, will actually have a higher Brα emission coefficient than the one adopted in the evaluation of the Ne/H abundance, and vice versa. For reasonable electron temperatures between 5000 and 10000 K (Shaver et al. 1983; Afflerbach et al. 1996; Deharveng et al. 2000), this effect is less than a factor of 2 (cf. MHP02). The Magellanic Cloud abundances, however, are not expected to be influenced by this systematic effect because they were evaluated using electron temperatures derived from optical lines. Hence, we consider that the trend in Fig. 5.5 is not due to a selection effect, and that there is a general correlation albeit with a large spread. On average, the most highly ionized H II regions have the lowest metallicity, and vice versa.

Based on a set of photoionization models computed using the Pauldrach SEDs, Giveon et al. (2002) investigated the influence of varying the stellar and nebular metallicity on the [Ne III]/[Ne II] line ratio. They found that, for a given $T_{\rm eff}$, the SED hardens

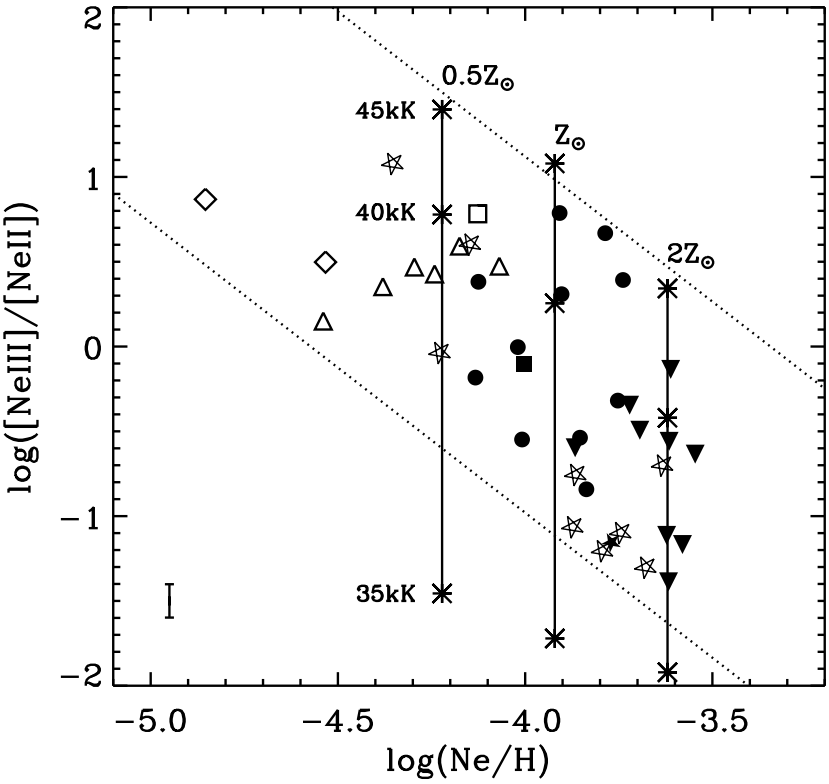

FIGURE 5.5— The relationship between the [Ne III]/[Ne II] line ratio and the metallicity indicator Ne/H for the combined sample of H II regions. Symbols are as in Fig. 5.1. The data collected on starburst galaxies (open stars) are compared to the Galactic and LMC/SMC H II regions. The parallel lines delineate the parameter space span up by the data. A typical error bar for log([Ne III]/[Ne II]) is shown in the left bottom corner. No error bar for Ne/H is indicated as the main uncertainty (which can be as large as a factor of 2 for the Galactic sources, see Sect. 5.5) comes from the abundance derivation method itself and is very hard to determine. The solid lines show the results of the photoionization models calculated by Giveon et al. (2002) using Pauldrach SEDs for subsolar, solar and supersolar stellar and nebular metallicities.

with decreasing metallicity due to the decreased line blocking in the stellar atmosphere winds. Quantitatively, for a 40 kK star, an increase in the nebular and stellar metallicity from $0.5Z_\odot$ to $2Z_\odot$ would reduce [Ne III]/[Ne II] by a factor of 20. We compare the results of these calculations to the observed correlation between metallicity and degree of ionization (cf. Fig. 5.5) for $T_{\rm eff}$=35, 40, 45 kK, Z=$0.5Z_\odot$, $1Z_\odot$, $2Z_\odot$ and $n_{\rm H}$=800 cm^{-3}. In view of these results, we see that the large spread in degree of ionization at a given metallicity observed in our data reflects a true variation in $T_{\rm eff}$. Moreover, the observed increase in the degree of ionization of the H II regions (cf. Fig. 5.1) reflects clearly a hardening of the SEDs due to the decreased metallicity and it is not necessarily due to a rise of the effective temperature of the ionizing star.

Returning to the individual sources considered in Sect. 5.4 and in view of Fig. 5.5, the Galactic H II region G29, with a metallicity of roughly $2Z_\odot$, would be powered by a star with a temperature slightly higher than the one indicated in Fig. 5.2, which are solar metallicity models. The Magellanic sources N66 and 30 Dor, with sub-solar metallicities, would be, on the other hand, ionized by cooler stars because of the decreased line blocking. However, a proper comparison of the effective temperature derived from the modelling of the H II region line data with the effective temperature derived directly from the stellar spectra will require a proper calibration of stellar spectra for different metallicities. In particular, the 'calibration' of ionizing stars based upon K-band spectra (Hanson et al. 1996) may require spectra of stars with different metallicities. Also, the comparison of the strength of hydrogen and helium lines with predictions of stellar atmospheres will require a proper treatment of the influence of metallicity.

5.6 The case of starburst galaxies

Information on starburst galaxies has been collected in order to make a comparison with the H II region results. The data obtained for a sample of 9 galaxies observed by ISO are presented in Table 5.3 and are plotted in Fig. 5.5 as open stars. These galaxies show a similar distribution as the H II regions: high metallicity–low ionization, low metallicity–high ionization. In particular, we note that the low metallicity dwarf irregular galaxy II Zw 40 coincides well with the H II regions in the LMC, further reinforcing our interpretation that metallicity and degree of ionization are strongly interconnected. Among the low ionized galaxies are M 82 and NGC 253, which are the prototypical starburst galaxies. With a [Ne III]/[Ne II] ratio similar to that of M 82, NGC 3256 is a recent galaxy merger. The highly ionized galaxies include NGC 5253, a young Wolf-Rayet galaxy, and NGC 4038/4039 (the Antennae), where an extensive burst of star formation is ongoing in the overlap region between the two merger systems.

The [Ne III]/[Ne II] line ratio and other ionization ratios observed in starburst galaxies have been used to infer the spectral type of the ionizing stars and hence, the age of the starburst (e.g. Schaerer & Stasińska 1999; Crowther et al. 1999; Thornley et al. 2000; Spoon et al. 2000). However, as this discussion has emphasized, the stellar type is only one of the parameters influencing the ionization structure. Furthermore, the uncertain spectral classification of the ionizing sources through ionization line ratios makes a proper age estimate of the starburst difficult. The other factor influencing the ionization structure, metallicity, measures the cumulative effect of star formation over the galaxy's history.

TABLE 5.3— [Ne III]/[Ne II] line ratios and Ne/H abundances for a sample of galaxies, including Sgr A*. The notation a (−b) is shorthand for a×10^{-b}.

Object name	[Ne III]/[Ne II]	Ne/H†	Ref.	Object name	[Ne III]/[Ne II]	Ne/H†	Ref.
M83	0.05	2.1 (−4)	1,+	M82	0.18	1.4 (−4)	4
Sgr A*	0.06	1.8 (−4)	2,+	NGC 3256	0.20	2.3 (−4)	5
NGC 7552	0.08	1.8 (−4)	1,+	NGC 4038/39◇	0.92	0.6 (−4)	6
NGC 253	0.08	1.8 (−4)	1,+	NGC 5253	4.0	0.7 (−4)	7
NGC 4945‡	0.09	1.3 (−4)	3	II ZW 40	12	0.4 (−4)	1,+

(†) Calculated from the mid-infrared [Ne II] 12.8 μm, [Ne III] 15.5 μm and Brα 4.0 μm lines assuming T_e= 10^4 K and the low-density limit. No extinction correction is applied. (‡) The nature of this galaxy is uncertain. The infrared diagnostics show no evidence for the existence of the AGN inferred from hard X-ray observations (see Spoon et al. 2000). (◇) ISO pointing centered on the overlap region between the two interacting systems.
REFERENCES: (1) Thornley et al. (2000); (2) Lutz et al. (1996); (3) Spoon et al. (2000); (4) Förster Schreiber et al. (2001); (5) Rigopoulou et al. (1996); (6) Kunze et al. (1996); (7) Crowther et al. (1999); (+) ISO archive.

5.7 Summary and conclusions

In this chapter, we have examined the interplay between the ionization structure of H II regions, the SEDs of their ionizing stars and metallicity. To this end, we combined the near– and mid–infrared ISO spectra of a set of Galactic and Magellanic Cloud H II regions. This wavelength range gives us access to the [S IV] 10.5/[S III] 18.7 μm and [Ne III] 15.5/[Ne II] 12.8 μm line ratios, which are sensitive to the ionization structure of the nebula. The [S IV]/[S III] and [Ne III]/[Ne II] line ratios are found to span a range of more than 2 orders of magnitude and to be highly correlated. The low-metallicity LMC and SMC H II regions overlap the trend found for the Galactic objects at the high ionization end.

The dependence of the [S IV]/[S III] and [Ne III]/[Ne II] line ratios on the $T_{\rm eff}$ of the ionizing star is investigated using a grid of photoionization models at solar metallicity. The models are calculated using two different stellar atmosphere models: the CoStar SEDs from Schaerer & De Koter (1997) and the more recent SEDs from Pauldrach et al. (2001). The interpretation of the observed ionization line ratios in terms of the stellar content of the H II region depends critically on the adopted SED. In particular, we note that the CoStar SEDs systematically predict much cooler stars than the Pauldrach SEDs for the same ionization conditions. As a result, practically the whole observed ionization range can be fit by a very narrow $T_{\rm eff}$ range between $\sim$ 33000 and 42000 K when the CoStar models are adopted, while the entire range up to 55000 K is suitable when using the Pauldrach models. These differences originate principally from the different treatment of the line blanketing/blocking and wind properties.

For a few sources, spectral types of the ionizing sources are presently available from infrared (K-band) or optical stellar spectroscopy. The comparison of these spectral types with those derived indirectly from the ionized gas through the [S IV]/[S III] and [Ne III]/[Ne II] line ratios confirms that metallicity has an important influence on the stellar spectra. As impetus for this, we have investigated the relation between the ionization structure and the metallicity comparing the observed [Ne III]/[Ne II] line ratios

and Ne/H abundances. Although a large scatter is present, a loose correlation between the two parameters is found. This observed trend is compared to photoionization models calculated varying self-consistently the nebular and stellar metallicity (Giveon et al. 2002). The comparison shows that the observed increase in degree of ionization can be explained by the hardening of the SED due to a decrease of the metallicity.

We note, moreover, that the $T_{\rm eff}$ calibration of the different spectral types is based on modelling the observed photospheric hydrogen, helium and metal lines. This calibration is uncertain as it is very sensitive to the input physics of the stellar model used. The widely used calibration of early stars by Vacca et al. (1996) is based on plane-parallel, non-LTE models which do not incorporate stellar winds and line blanketing. It has been shown, for instance, that the inclusion of line blanketing, stellar wind and a spherical geometry in the models (Martins et al. 2002) lowers the predicted $T_{\rm eff}$ substantially when compared to the calibration by Vacca et al. (1996) for the same spectral type. A new calibration is needed if predictions of the stellar content of H II regions are to be compared with the observed spectral types of the ionizing stars. Such a recalibration will have to include the effects of metallicity.

In view of this analysis, the main conclusions are the following:

- The interpretation of the observed X^{+i+1}/X^{+i} ratios is valid only when the stellar metallicity of the SED used in the modelling properly matches the metallicity of the local ISM. Not taking into account the effect of the stellar metallicity correctly can lead to wrong conclusions on the stellar content of the nebula and thus on the local stellar population.

- The adequate treatment of the effects of stellar wind and line blocking and blanketing on the ionizing spectra of early O stars, and the availability of grids of stellar models at different metallicities, is needed. In this respect, the new models by Pauldrach et al. (2001) constitute an improvement over previous ones.

- A $T_{\rm eff}$-spectral type calibration of early stars is insufficient if the effects of metallicity are not accounted for. A detailed new calibration is, therefore, necessary.

- The determination of starburst ages in starburst galaxies based on X^{+i+1}/X^{+i} ratios is likely incorrect if metallicity is not taken into account.

Concluding, it is important to further study the ionization structure of H II regions, particularly using different tracers such as the He I recombination lines. Furthermore, from a theoretical point of view, it may be important to investigate the origin of the actual spectral classification, such as the K band spectral classification via the C IV and N III photospherical lines and their dependence on the stellar metallicity.

Acknowledgements

We thank the anonymous referee, whose comments greatly improved this article. MICE is supported at MPE by DLR (DARA) under grants 50 QI 86108 and 50 QI 94023.

References

Afflerbach, A., Churchwell, E., Acord, J. M. et al. 1996, ApJS **106**, 423

Crowther, P.A., Beck, S.C., Willis, A.J. et al. 1999, MNRAS **304**, 654
de Graauw, T., Haser, L.N., Beintema, D.A. et al. 1996, A&A **315**, L49
Deharveng, L., Peña, M., Caplan, J., Costero, R. 2000, MNRAS **311**, 329
Förster Schreiber, N.M., Genzel, R., Lutz, D., Kunze, D., Sternberg, A. 2001, ApJ **552**, 544
Ferland, G.J., Korista, K.T., Verner, D.A. et al. 1998, PASP **110**, 761
Giveon, U., Sternberg, A., Lutz, D., Feuchtgruber, H., Pauldrach, A.W.A. 2002, ApJ **566**, 880
Hanson, M.M., Conti, P.S., Rieke, M.J. 1996, ApJS **107**, 281
Henry, R.B.C., Worthey, G. 1999, PASP **111**, 919
Hillier, D.J., Miller, D.L. 1998, ApJ **496**, 407
Kaper, L., Bik, A., Hanson, M., Comerón, F. 2002a, in *Hot Star Workshop III: The Earliest Phases of Massive Star Birth*, ed. P.A. Crowther, in press
Kaper, L., Bik, A., Hanson, M., Comerón, F. 2002b, in ESO workshop on The Origins of Stars and Planets: The VLT view, ed. J. Alves & M. McCaughrean (ESO Astr. Symp.), in press
Kessler, M.F., Steinz, J.A., Anderegg, M.E. et al. 1996, A&A **315**, L27
Kunze, D., Rigopoulou, D., Lutz, D. et al. 1996, A&A **315**, L101
Lutz, D., Feuchtgruber, H., Genzel, R. et al. 1996, A&A **315**, L269
Martín-Hernández, N.L., Peeters, E., Morisset, C. et al. 2002, A&A **381**, 606
Martins, F., Schaerer, D., Hillier, D.J. 2002, A&A **382**, 999
Massey, P., Hunter, D.A. 1998, ApJ **493**, 180
Massey, P., Parker, J.W., Garmany, C.D. 1989, AJ **98**, 1305
Morisset, C., Schaerer, D., Martín-Hernández, N.L. et al. 2002, A&A **386**, 558
Oey, M.S., Dopita, M.A., Shields, J.C., Smith, R.C. 2000, ApJS **128**, 511
Pauldrach, A.W.A., Hoffmann, T.L., Lennon, M. 2001, A&A **375**, 161
Peeters, E., Martín-Hernández, N.L., Damour, F. et al. 2002, A&A **381**, 571
Rigopoulou, D., Lutz, D., Genzel, R. et al. 1996, A&A **315**, L125
Rolleston, W.R.J., Smartt, S.J., Dufton, P.L., Ryans, R.S.I. 2000, A&A **363**, 537
Schaerer, D., De Koter, A. 1997, A&A **322**, 598
Schaerer, D., Stasińska, G. 1999, A&A **345**, L17
Shaver, P.A., McGee, R.X., Newton, L.M., Danks, A.C., Pottasch, S.R. 1983, MNRAS **204**, 53
Simpson, J.P., Witteborn, F.C., Price, S.D., Cohen, M. 1998, ApJ **508**, 268
Spoon, H.W.W., Koornneef, J., Moorwood, A.F.M., Lutz, D., Tielens, A.G.G.M. 2000, A&A **357**, 898
Takahashi, H., Matsuhara, H., Watarai, H., Matsumoto, T. 2000, ApJ **541**, 779
Thornley, M.D., Schreiber, N.M.F., Lutz, D. et al. 2000, ApJ **539**, 641
Vacca, W.D., Garmany, C.D., Shull, J.M. 1996, ApJ **460**, 914
Vermeij, R., Van der Hulst, J.M. 2002a, A&A, in press
Vermeij, R., Van der Hulst, J.M., Damour, F., Baluteau, J.-P. 2002b, A&A **390**, 649
Vílchez, J.M., Pagel, B.E.J. 1988, MNRAS **231**, 257
Walborn, N.R., Blades, J.C. 1997, ApJS **112**, 457
Watarai, H., Matsuhara, H., Takahashi, H., Matsumoto, T. 1998, ApJ **507**, 263
Watson, A.M., Hanson, M.M. 1997, ApJ **490**, L165

Chapter 6

The PAH emission spectra of Large Magellanic Cloud H II regions

A set of ISOPHOT spectra from a sample of H II regions in the Large Magellanic Cloud (LMC) is presented. In all the spectra, emission bands arising from Polycyclic Aromatic Hydrocarbons (PAHs) are clearly present. These features are observed to vary considerably in relative strength to each other from source to source and even within 30 Doradus. The LMC spectra have been compared with ISO-SWS spectra from Galactic H II regions and with an ISOCAM observation towards a quiescent molecular cloud in the SMC (Reach et al. 2000). A correlation is found between the $I_{7.7}/I_{11.2}$ versus $I_{6.2}/I_{11.2}$ and the $I_{8.6}/I_{11.2}$ versus $I_{6.2}/I_{11.2}$ ratios. A segregation between the sources in the different types of environment (Milky Way – LMC – SMC) is present. Furthermore, within the LMC observations, a clear distinction between 30 Doradus and the non-30 Doradus pointings is found. We discuss the variations in the relative strength of the PAH features in view of the different physical environments and highlight the relation with the PAH/dust ratio and the extinction curve. We conclude that 1) the same conditions responsible for the observed trends in the relative PAH-feature strengths also affect the carrier of the 2175 Å bump leading to the differences in strength of the latter, and 2) the molecular structure is the major cause of the observed variations in the relative strength of the PAH features. In the SMC and 30 Doradus compact PAH species dominate, while PAHs with an open, uneven structures dominate in the Galactic H II regions and the non-30 Dor LMC sources.

6.1 Introduction

Ground-based, airborne, and space-based observations have shown that the mid-infrared spectra of many objects with associated dust and gas are dominated by the well-known emission features at 3.3, 6.2, 7.7, 8.6 and 11.2 μm commonly called the unidentified infrared (UIR) bands (cf. Gillett et al. 1973; Geballe et al. 1985; Cohen et al. 1986; Roche et al. 1989). These bands are now generally attributed to vibrational relaxation of UV-pumped Polycyclic Aromatic Hydrocarbons (PAHs) containing $\simeq$ 50 carbon atoms (Léger & Puget 1984; Allamandola et al. 1985, 1989; Puget & Léger 1989; Tielens et al. 2000). The band at 3.3 μm is due to CH stretching vibrations, the 6.2 μm band corresponds largely to pure CC stretching motions, whereas the 7.7 μm feature arises from combinations of CC stretching and CH in-plane bending motions. The 8.6 and 11.2 μm features arise from CH in-plane and out-of-plane bending motions, respectively. Underlying the 6.2 μm, 7.7 μm and 8.6 μm bands as well as underlying the 11.2 μm band, is a quasi-continuum or pedestal originating from larger PAHs and clusters of small PAHs.

Since the emission arises not from a single species but from a complex mixture of PAHs (Léger & Puget 1984; Allamandola et al. 1985), the interstellar PAH spectra reflect a combination of individual molecular features, and hence the overall PAH spectrum appears very similar from source to source. The exact PAH family (molecular structure and size) present in a source fine-tunes the PAH spectrum in terms of relative strengths and peak positions of the individual PAH features (Schutte et al. 1993; Verstraete et al. 1996; Allamandola et al. 1999; Moutou et al. 1999; Hony et al 2001; Peeters et al. 2002b). Laboratory studies and quantum-chemical calculations have shown that ionization of the PAH molecules has a remarkable effect on the spectrum. While the peak positions of the UIR bands are modestly affected by ionization, the influence on the intensity is striking - particularly in the 5 to 10 μm region (Allamandola et al. 1999; Bakes et al. 2001). As a result, the emitted spectrum will depend on the local physical conditions. In addition, dehydrogenation may also influence the PAH spectrum, in particular in the strength of the different CH modes (Pauzat et al. 1997).

With the launch of the Infrared Space Observatory (ISO), a huge amount of infrared spectral data became available, showing the omnipresent nature of these PAH features. By now, the features have been detected in a wide range of objects and environments, from post-AGB stars and planetary nebulae, to H II regions, reflection nebulae, the diffuse interstellar medium and extragalactic sources. As demonstrated by the galaxy survey by Helou (1999), the mid-IR spectrum of the ISM in galaxies is dominated by the UIR bands. A spectroscopic survey of the nuclei of nearby ($z < 0.3$) starburst galaxies has also revealed the presence of bright UIR bands (Bosselli et al. 1997; Lutz et al. 1998; Bosselli et al. 1997).

Studies have also been performed for the Magellanic Clouds. ISOCAM studies of the large SMC H II region N 66 (Contursi et al. 2000) and of the SMC molecular cloud B1#1 (Reach et al. 2000) show the presence of PAHs even in such a metal-deficient environment. A similar study of the H II region complex N4 in the LMC also hints at the presence of PAHs (Contursi et al. 1998). An ISO-SWS AOT1 spectrum of 30 Doradus taken at our position #3 also shows the clear presence of Polycyclic Aromatic Hydrocarbons (Sturm et al. 2000).

TABLE 6.1— The ISOPHOT and ISO-SWS pointings and dates of the observations. The coordinates are J2000.0. The designations for the Magellanic Cloud sources, except for 30 Doradus, are those of Henize (1956). The Galactic sources (except the Orionbar) are designated by their IRAS number.

LMC				Milky Way			
Object	RA (h m s)	δ (^{o} $'$ $''$)	Date	Object	RA (h m s)	δ (^{o} $'$ $''$)	Date
N4A	4 52 08.4	-66 55 23.4	29-04-96	Orion bar#1	05 35 21.4	-05 25 40.1	11-10-97
N83B	4 54 25.8	-69 10 56.7	31-10-97	Orion bar#2	05 35 19.8	-05 25 10.0	24-02-98
N11A	4 57 16.3	-66 23 22.9	16-08-96	Orion bar#3	05 35 18.2	-05 24 39.9	11-10-97
N159-5	5 40 04.2	-69 44 42.9	24-09-97	12331−6134	12 36 01.9	-61 51 03.9	10-09-96
30 Dor#1	5 38 33.5	-69 06 27.1	05-12-97	15384−5348	15 42 17.1	-53 58 31.5	10-09-96
30 Dor#2	5 38 35.4	-69 05 41.2	13-04-96	18317−0757	18 34 24.9	-07 54 47.9	08-03-97
30 Dor#3	5 38 46.0	-69 05 07.9	20-07-97	18434−0242	18 48 04.1	-02 39 20.0	12-04-97
30 Dor#4	5 38 54.2	-69 05 15.3	05-08-97	21190+5140	21 20 44.9	+51 53 27.0	30-11-97
				22308+5812	22 32 45.9	+58 28 21.0	12-05-96
				23030+5958	23 05 10.6	+50 14 41.0	06-12-97
				23133+6050	23 15 31.4	+51 07 08.0	06-06-97

The study of PAHs in the Magellanic Clouds is of interest because of the different physical environment encountered there. The best known of these differences is the low metallicity of the Magellanic Clouds relative to the Galaxy. Furthermore, the prodigious starformation activity inundates the Magellanic Clouds with diffuse UV radiation (e.g. Cole et al. 1999).

In this chapter, a set of mid-IR spectra from a sample of H II regions in the Large Magellanic Cloud is presented, and all of these show the strong presence of PAH features. These spectra give us the opportunity to investigate the influence of the completely different environment in the LMC on the PAH spectra and their carriers. We therefore make a comparison between our sample H II regions in the LMC and those of our own Milky Way and the SMC. In section 6.2 the data are presented, with special emphasis on the way the PAH-feature strengths have been determined. Section 6.3 describes the general trends in the observed PAH-feature strengths. In section 6.4, the connection with extinction is highlighted and the possible underlying causes for the observed trends are examined. Finally, in section 6.5 we summarize our results.

6.2 Data

6.2.1 Observations

The sample includes a set of Large Magellanic Cloud H II regions. The spectra were obtained with the ISOPHOT/PHT-S instrument on board ISO in staring mode using the PHT-40 template. The observation log is given in Table 6.1. The PHT-S instrument covers the spectral ranges from 2.5 - 4.8 μm (the PHT-SS part) and from 5.8 - 11.6 μm (the PHT-SL part). Both spectral ranges have their own linear detector block consisting of 64 pixels each with a spectral resolution of 85 in the SS part and 95 in the SL part. The ISOPHOT spectra were reduced with PIA V8.4 using standard routines. Special attention was paid to the de-glitching of the signal from every separate pixel. This

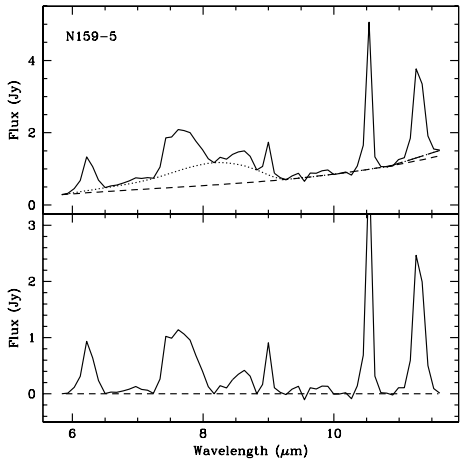

FIGURE 6.1— The ISOPHOT spectrum of N159-5. The upper panel shows the spectrum and the components of the fitted continuum. The lower panel shows the continuum subtracted spectrum.

was done to make sure that no spurious feature would contaminate the spectra. In addition to these ISOPHOT data, the ISO-SWS AOT 01 spectrum of 30 Dor#3 (Sturm et al. 2000) was taken from the ISO archive and reduced in a similar way as the spectra of the Galactic H II regions. Representing the Small Magellanic Cloud in this work is the ISOCAM observation from Reach et al. (2000) of the molecular cloud B1#1.

The sample of H II regions in the Milky Way was taken from the Galactic 'Ultra Compact H II region' ISO program (Peeters et al. 2002a) complemented with spectra of the Orion bar also taken from the ISO archive (Orion bar#3 : Cesarsky et al. 2000). The spectra have been obtained with the Short Wavelength Spectrometer (SWS) in the AOT 01/AOT 06 scanning mode (see Table 6.1). A detailed account of the reduction of the AOT 01 spectra can be found in Peeters et al. (2002a). The AOT 06 spectra were reduced in a similar way as the AOT 01 data.

6.2.2 The spectra

The ISOPHOT spectra of the LMC sources are shown in the Figures 6.1 and 6.2. Only the part of the spectra ranging from 5.9 to 11.6 μm is shown here. The spectra of the LMC H II regions resemble the spectra of Galactic H II regions very much. All the major PAH features, i.e. the 6.2, 7.7, 8.6 and 11.2 μm bands, are clearly present. Only in some cases (e.g. N4A), a trace of the 3.3 μm feature was seen. This is not surprising since this feature is known to contribute typically only 6% to the total luminosity carried by the PAH features (Cohen et al. 1989) and can therefore easily be hidden in the noise in the ISOPHOT spectra. Even the weak PAH features at 6.0 and 11.0 μm (Hony et al. 2001; Peeters et al. 2002b) can be discerned in some of the spectra (e.g. N4A, 30Dor#4). In addition to the PAH emission bands, the [Ar II] 6.9 μm, [Ar III] 8.9 μm and [S IV] 10.5 μm fine-structure lines are observed, the former being rather weak. The Pfα line at 7.5 μm might be present in the spectra, but at the resolution of PHT-S it is not possible to disentangle the Pfα line from the 7.7 μm PAH feature. This line and the PAH feature are easily separated at the resolution of SWS. In the SWS spectrum of 30 Dor#3, this Pfα line is clearly present. The silicate absorption feature at 9.7 μm

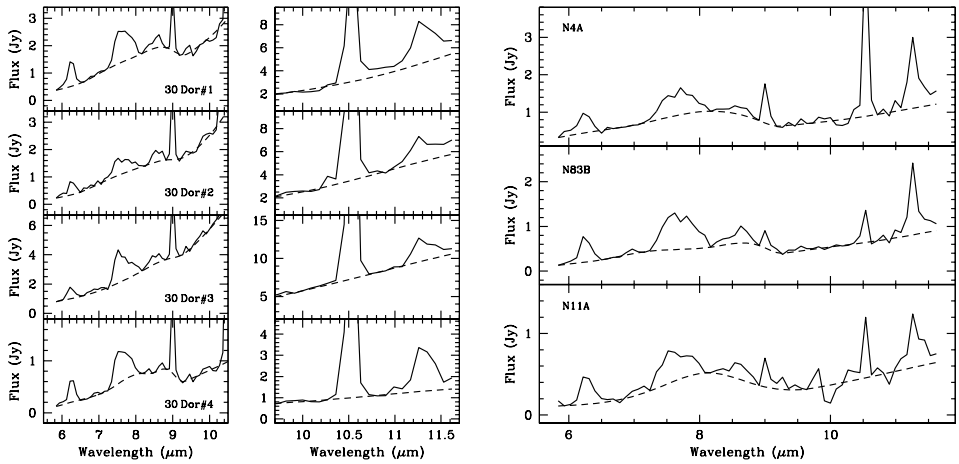

FIGURE 6.2— The ISOPHOT spectra of the sample objects in the Large Magellanic Cloud. The left panel shows the 30 Doradus spectra from which the spectral region near 11 μm is blown up for clarity.

was not detected in any of the spectra of the Magellanic sources.

Already at first glance, variations in the relative PAH-feature strengths from one object to another are obvious. These variations are not only present when comparing different H II regions, but also for the different pointings within the giant H II region 30 Doradus. At first sight, the shape of the features also seems to vary. This is the most pronounced for the 7.7 μm feature, but here the possible presence of the Pfα line at 7.5 μm should be taken into account. While tantalizing, we conclude that these profile variations may not be significant due to the low resolution of the PHT-S instrument. Note, however, that the Galactic H II regions show little profile variations for the 6.2, 7.7 and 8.6 μm features (see Peeters et al. 2002b). Small variations are present in the 11.2 μm PAH feature (see Peeters et al. 2002, in prep.) but these cannot be seen at the PHT-S resolution. Furthermore, the PAH profiles in extragalactic sources are similar to those in the Galactic H II regions (see Peeters et al. 2002b).

6.2.3 Continuum fitting and flux determination

For both the ISOPHOT and the ISO-SWS spectra the continuum subtraction was done with the same two-step procedure by fitting a spline through selected points in the spectra.

In the first step of the continuum subtraction, an underlying dust continuum was defined. For the ISOPHOT spectra, the spline points for this continuum were located at $\sim$5.8 μm, in the 9 - 10 μm region, and at the blue base of the [S IV] 10.5 μm line. The wavelength coverage of ISOPHOT (ending at 11.6 μm) hampers the determination of the continuum redwards of the [S IV] 10.5 μm line. Without continuum points beyond 11.6 μm, it is difficult to ascertain the presence of a broad plateau underlying the 11.2 μm feature and, if present, to distinguish it from the underlying dust continuum.

TABLE 6.2— The ISOPHOT fluxes of the different PAH features in units of 10^{-18} W cm^{-2}. The errors given in this table are only the measurement errors. Also included are the fluxes from SMC B1#1 and the SWS-AOT1 spectrum of 30 Doradus#3.

Object	3.3 μm	6.2 μm	7.7 μm	8.6 μm	11.2 μm
N4A	d	0.92 ± 0.05	1.67 ± 0.02	0.29 ± 0.01	0.68 ± 0.03
N83B	n	0.85 ± 0.01	2.05 ± 0.02	0.46 ± 0.04	0.56 ± 0.02
N11A	n	0.60 ± 0.01	0.92 ± 0.02	0.26 ± 0.01	0.29 ± 0.01
N159-5	n	1.45 ± 0.02	2.83 ± 0.02	0.54 ± 0.05	1.14 ± 0.01
30 Dor#1	d	1.59 ± 0.03	2.87 ± 0.02	0.51 ± 0.01	1.48 ± 0.01
30 Dor#2	n	0.79 ± 0.05	1.50 ± 0.03	0.48 ± 0.01	0.92 ± 0.02
30 Dor#3°	d	1.27 ± 0.02	4.50 ± 0.04	0.81 ± 0.01	1.51 ± 0.02
30 Dor#3*	0.23	1.16	3.66	0.74	1.23
30 Dor#4	n	0.65 ± 0.02	1.38 ± 0.02	0.11 ± 0.05	1.07 ± 0.04
SMC B1#1†	-	0.37	0.76	0.11	1.26

° : flux derived from the ISOPHOT data. n : not detected. d : detected.
* : flux derived from the ISO-SWS AOT 01 spectrum (Sturm et al. 2000.)
† : flux derived from the ISOCAM spectrum (Reach et al. 2000), see Section 6.2.3.

Therefore, no points were added in this region to constrain the fit to the underlying continuum. However, as can be seen in, for example, Figure 6.1, some residual flux is present underneath the 11.2 μm feature. In the spectra where such a residual flux was present, it was removed by defining a simple straight-line continuum superimposed on the underlying continuum.

For H II regions, the 5 - 9 μm spectral range is characterized by a broad plateau underlying the features (Peeters et al. 2002b). In the second step of the continuum subtraction, a continuum was fit to this plateau and subtracted. Anchor points for the fit to this plateau were located at $\sim 5.8\,\mu$m, between the 6.2 μm and the 7.7 μm features, at the blendpoint of the 7.7 μm and 8.6 μm features, and at the base of the [Ar III] 8.9 μm line. As an example, the resulting composite continuum and the continuum-subtracted spectrum of N159-5 are shown in Figure 6.1.

For fitting the underlying continuum in the SWS spectra, points in roughly the same wavelength ranges were taken. A spline was fitted through points in the range from 5 - 6 μm, between the 6.2 μm and the 7.7 μm features (near 7 μm), between the 7.7 μm and 8.6 μm features (near 8.2 μm), in the 9 - 11 μm range and through points near 11.7 μm.

In this way, a local continuum around the 6.2 μm and the 11.2 μm features is determined. The presence of a silicate absorption feature at 9.7 μm (in some Galactic H II regions) has been ignored in determining the fit but will strongly influence the 8.6 μm feature. Hence, when examing the 8.6 μm feature, the Galactic H II regions with obvious silicate absorption (IRAS 15384, IRAS 18317, IRAS 18434) are disregarded.

The fluxes of the PAH features have been derived from the continuum subtracted spectra by simple pixel integration. The fluxes of the 6.2 μm, 7.7 μm, 8.6 μm and 11.2 μm features were derived by integration over the wavelength intervals of 6.1 - 6.6 μm, 7.1 - 8.2 μm, 8.3 - 8.9 μm and 11.1 - 11.6 μm, respectively. To make sure that the fluxes

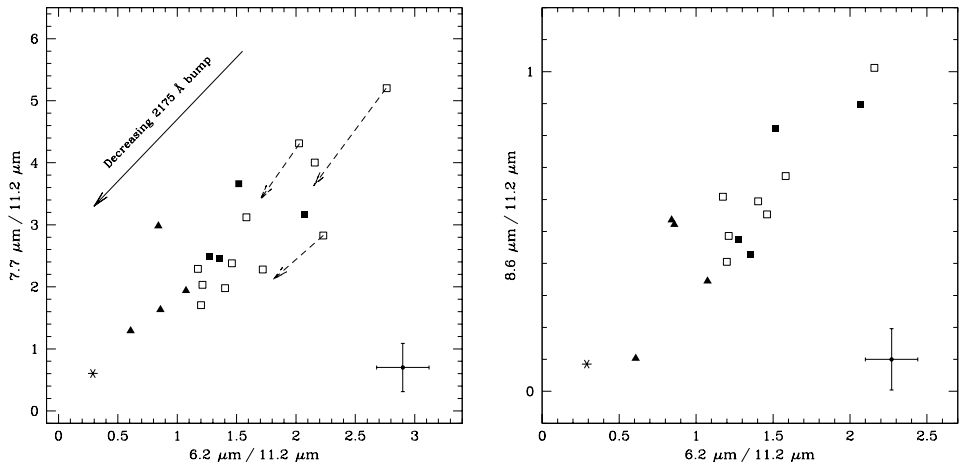

FIGURE 6.3— The correlations between the different relative PAH-feature strengths. The feature fluxes have been normalized relative to the 11.2 μm flux so as to eliminate the differences in the distance to the source. The Galactic sources are shown as open squares, the non-30 Dor sources as solid squares and the 30 Dor pointings as solid triangles. The asterisk represents the SMC B1#1 molecular cloud. Shown in the lower right corner is a typical error bar. The dashed arrows show the shift in position of the observed ratios when an extinction correction is applied (see text). The solid arrow shows the direction in which the contrast of the 2175 Å bump to the general extinction decreases.

for the SMC B1#1 cloud can be compared, these have been rederived in the same way rather than taking the fluxes from Reach et al. (2000). The fluxes will be sensitive to the continuum determination and to the decomposition of the 6 to 9 μm region in terms of the PAH features and the PAH plateau. However, this will influence all spectra in the same way. In particular, this will not introduce spurious differences between the Galactic and the LMC sources.

The fluxes for the LMC and SMC sources are given in Table 6.2. For 30 Doradus#3, both the flux derived from the ISOPHOT data as well as from the SWS data is given in Table 6.2. The only uncertainty quoted in the Table is the one arising from noise in the spectra. The relative flux calibration uncertainty of the ISOPHOT spectra is estimated to be around 10% (Acosta-Pulido & Ábrahám 2001). The 7.7 μm flux could be contaminated by the Pfα line, but a comparison between the 7.7 μm fluxes and the Pfα fluxes for the same objects from Vermeij et al. (2002) showed this contamination to be not higher than $\sim$10%. For the Galactic H II regions, the intensity of the Pfα line is less than 8% of the intensity of the 7.7 μm PAH band.

6.3 Correlations

Given the differences in the physical environments of the Milky Way and the Magellanic Clouds, it is of interest to investigate the differences - if any - in the PAH spectra between the Galactic and Magellanic Cloud H II regions. Here we want to study variations in the relative strength of the PAH bands to each other, not the differences in absolute

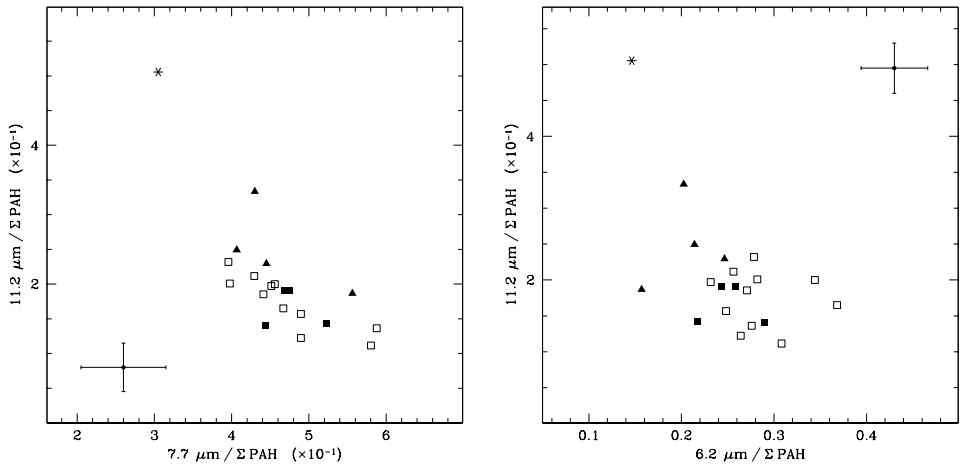

FIGURE 6.4— The relative contribution of the 6.2, 7.7 and 11.2 μm PAH features to the total energy output within all the PAH bands. For an explanation of the symbols see Figure 6.3. Shown in both panels is a typical errorbar.

intensities due to intrinsic luminosity and distance of the sources. We therefore use 3-feature intensity-ratio plots. The relation between the different relative PAH-feature strengths is shown in Figure 6.3.

Three of our Galactic sources suffer from extinction (IRAS 15384, IRAS 18317, IRAS 18434; Martín-Hernández et al. 2002). For these sources, both the observed and intrinsic ratios are shown in the left panel of Figure 6.3 (the dashed arrows). The extinction A_K is derived from hydrogen recombination lines. These sources are not shown in the right panel of Figure 6.3 since silicate absorption influences the relative strength of the 8.6 μm feature. For the LMC sources, the pointing with the highest extinction (30 Dor#4) has an A_V of 1.7 (Vermeij et al. 2002). Therefore, extinction has only a minor influence on the observed strengths of the PAH features in the LMC.

Both panels in Fig. 6.3 clearly show linear correlations between the different PAH-feature strengths. Most striking is a segregation between the sources of different type of environment, i.e. from the Milky Way to the LMC and to the SMC. Interesting, however, is the fact that for 30 Doradus the measured PAH-feature ratios lie further down the sequence than those of the other LMC pointings, showing a clear distinction between the pointings in 30 Doradus and the non-30 Doradus sources. This distinction is clearly visible for the $I_{6.2}/I_{11.2}$ ratio, but is less pronounced for the $I_{7.7}/I_{11.2}$ and the $I_{8.6}/I_{11.2}$ ratios; three of the pointings in 30 Doradus show a $I_{7.7}/I_{11.2}$ and $I_{8.6}/I_{11.2}$ ratio similar to those of the Galactic and non-30 Dor sources. Note that the non-30 Dor LMC H II regions behave more like the Galactic H II regions in our sample.

We also investigated the relative contribution of every PAH feature to the total emitted PAH flux in all the features. These are shown in Figure 6.4. The SMC point in this figure is in both panels clearly separated from the other objects. The Galactic and Magellanic Cloud sources show a similar range in the fraction of the PAH emission

emitted in the 7.7 μm and the 8.6 μm band. In contrast, there is a clear difference between the Galactic sources and the 30 Dor and SMC sources when considering the 6.2 and 11.2 μm bands (Figure 6.4, right panel). The 6.2 μm feature is relatively stronger in the Galactic sources whereas its 11.2 μm band is relatively weaker. This latter difference, however, is only slight. Here too, the 30 Dor pointings and the SMC source are situated in different regions in the plot compared to the Galactic sources and the non-30 Dor sources. A similar separation is not noticed for the $I_{7.7}/\Sigma$ PAH versus $I_{11.2}/\Sigma$ PAH ratio (Figure 6.4, left panel).

6.4 Discussion

6.4.1 Extinction : the 2175 Å bump

Much work has been done on determining the extinction characteristics of many lines-of-sight towards the LMC and also the SMC (e.g. Borgman et al. 1975; Nandy et al. 1981; Koornneef & Code 1981; Prévot et al. 1984). A common result found in this work for the LMC is that the extinction in the UV is significantly higher and rises more sharply than for Galactic lines-of-sight and that the 2175 Å bump is about 50% weaker. These differences in the characteristics of the extinction curve are even more pronounced for the SMC. It has also been pointed out that there seems to be an anti-correlation between the 2175 Å bump strength and the slope of the FUV rise.

For a long time, it was assumed that the extinction curve derived for the LMC was applicable for the galaxy as a whole. However, this early work was based solely on stars near 30 Doradus. Later work by Fitzpatrick (1985, 1986) and Clayton & Martin (1985) showed the extinction curve outside the 30 Doradus region to be much less different from the Galactic ones than previously thought, with the 2175 Å feature significantly stronger than in 30 Doradus. The carrier of the 2175 Å bump has not yet been positively identified, but one of the possible candidates could be PAHs (Joblin et al. 1992).

Our pointings are nicely distributed over the LMC and can be divided into a 30 Dor group and a non-30 Dor group. Some of the stars used by Fitzpatrick (1986) in the derivation of his non-30 Dor curves are located near our sample objects N11A, N4A and N83B (e.g. Sk 19-66, Sk 2-67, Sk 19-69). It is therefore interesting to compare our PAH spectra with the properties of the extinction curves.

A comparison between the absolute PAH-feature fluxes for our 30 Dor pointings and for our other LMC objects does not show many differences (see Table 6.2). The relative intensity ratios though show a clear sequence, going from the Galaxy and the non-30 Dor pointings to 30 Dor and the SMC object B1#1 (see Figure 6.3). A similar sequence can be found for the 2175 Å bump strength, wich decreases in strength going from the Milky Way to the non-30 Dor and the 30 Dor sources and is even completely absent in the SMC (e.g. Rodrigues et al. 1997). The latter suggests a possible connection between the strength of the 2175 Å bump on one hand and the PAHs and their structure on the other hand. The direction in which the contrast of the 2175 Å feature decreases relative to the general extinction is shown in Figure 6.3.

The confirmation or refutation of PAHs as carrier of the 2175 Å bump is difficult though. Extinction curves are commonly derived from lines-of-sight towards hot stars, and it is not easy to asses the impact of the environment on the molecules. Moreover, the possibility exists that the same physical conditions responsible for our observed

trends in the relative PAH-feature strengths also affect the carrier of the 2175 Å bump leading to the differences in strength of the latter. To really settle the problem of the possible PAH nature of the bump carrier, observations of PAHs and extinction curves in the same line-of-sight are needed. In the next section, we will discuss several of the processes affecting the strength of the different PAH features.

6.4.2 Variations in the observed PAH spectrum

Many different factors play a role in shaping the PAH spectra and their relative PAH-feature strengths. Among these are the balance between ionized and neutral PAHs, the degree of hydrogenation of the PAHs, and the size and molecular structure of the PAHs present in the source (e.g. Schutte et al. 1993; Allamandola et al. 1999; Bakes et al. 2001; Hudgins & Allamandola 1999). The problem one faces when analyzing a PAH spectrum is the fact that all these possible factors are interconnected, which makes it hard to single out one of those as the decisive one in shaping the spectrum. In this section, the possible contribution of these different factors to the observed trends is investigated. The connection with the PAH/dust ratio is also highlighted.

6.4.2.1 Ionization balance

The PAH charge is known to influence the PAH spectrum remarkably. Upon ionization, the intrinsic strength of the features in the 5-10 μm region increases while the intrinsic strength of those in the 10-15 μm region decreases (Langhoff 1996; Allamandola et al. 1999; Hudgins et al. 1999; Peeters et al. 2002b). The PAH charge is governed by the photoionization rate and the electron recombination rate, and is therefore a function of the local physical conditions (Bakes & Tielens 1994; Bakes et al. 2001); in particular, the electron density and the strength of the FUV field illuminating the PDR (generally measured in units of the interstellar radiation field in the solar neighbourhood).

To investigate the possible role of the ionization balance in the observed trends, these two quantities have been determined for our sample sources. The Lyman continuum flux and the rms electron density of the H II regions were derived from radio measurements. For the LMC objects N4A, N11A, N83B and N159-5, this was based on new 6 cm radio data obtained with the Australia Compact Array radio telescope. For the Galactic sources, the radio data were taken from the literature when available (for an overview, see Martín-Hernández et al. 2002). The Lyman continuum flux was converted to solar luminosities using the models from Vacca, Garmany & Shull (1996). By using the radio sizes, the local radiation field is obtained expressed in units of 1.6×10^{-6} W cm^{-2}. A distance of 55 kpc was adopted for the LMC, the distances of the Galactic sources were taken from Peeters et al. (2002a).

For 30 Doradus the estimate for the local radiation field was based on stellar population studies. Assumed was that all the radiation is emitted by R136, the stellar cluster at the core of 30 Doradus. The stellar content of R136 was taken from the stellar population list of Massey & Hunter (1998). From this stellar list a total luminosity was derived by using the same stellar atmosphere models as for the other sample objects. The flux at the pointing position was then determined from the projected distance from the center of R136 to the ISOPHOT pointings. For the derivation of the rms electron density at our positions, a 6 cm radio map of 30 Doradus was used that

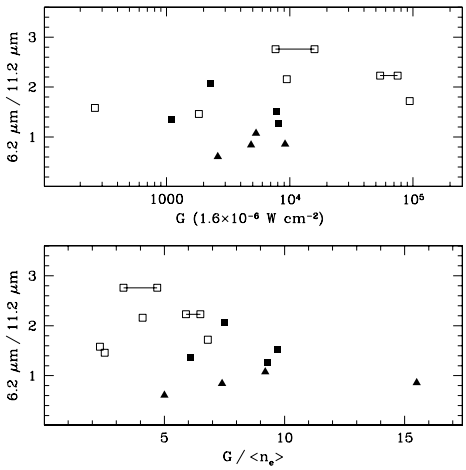

FIGURE 6.5— The $I_{6.2}/I_{11.2}$ ratio versus the local radiation field G and the parameter $G/< n_e >$. The full lines join G and $G/< n_e >$ as derived using both the near and far solar distance.

was kindly provided to us by Lazendic et al. (in prep.) prior to publication. As a check on the results for the radiation field as determined from the stellar population study, the Lyman continuum has also been derived from this radio data. The two different results were in very good agreement.

The balance between neutral and ionized PAHs is governed by the ratio of the local radiation field and the electron density, $G/< n_e >$. The Galactic H II regions are found to have a systematically lower $G/< n_e >$ than the Magellanic sources. However, no correlation is found between this parameter and any of the possible relative PAH-feature strengths. As an example, the relative PAH-feature strength $I_{6.2}/I_{11.2}$ as a function of G and $G/< n_e >$ is shown in Figure 6.5. We therefore conclude that the differences between the relative PAH-feature strengths cannot be attributed to the ionization balance of the PAHs. It is interesting to see that, although for the four 30 Dor positions $G/< n_e >$ shows a reasonable variation, the $I_{6.2}/I_{11.2}$ ratio for these pointings is roughly the same.

To provide us with a further check on the local radiation field and also to get an additional constraint on the derived electron density, PDR diagnostic fine-structure line ratios have been determined from the SWS and LWS data of all our LMC objects (except N11A for which no LWS data is available - Vermeij et al. 2002) and all the IRAS sources (Peeters et al. 2002a). This is necessary because the PAH spectrum is formed in the PDR, whereas the physical parameters derived from the radio data are more indicative of the body of ionized gas making up the H II region.

The combination of the [C II] 158 μm/[O I] 63 μm line ratio with the ([C II] 158 + [O I] 63 + [Si II] 35)/FIR ratio defines a unique set of density and radiation field G (e.g. Wolfire, Tielens & Hollenbach 1990). It turns out that the Galactic and Magellanic sources have similar diagnostic ratios. Our sources lie between the log $G = 3$ and log $G = 4$ tracks in the diagnostic diagrams from Wolfire, Tielens & Hollenbach (1990), which is in reasonable agreement with our values of the local radiation field from the radio data. The LMC and Galactic H II regions show a similar efficiency of photoelectric heating as measured by the ([C II] 158 + [O I] 63 + [Si II] 35)/FIR ratio.

The photoelectric effect is governed by the ionization state of the PAHs, so these findings lend further support to our conclusion that the ionization balance of the PAHs is not responsible for the observed differences in the PAH-feature strenghts.

6.4.2.2 Dehydrogenation

Theoretical studies of dehydrogenation of interstellar PAHs have shown that for PAHs larger than ~ 25 carbon atoms hydrogenation through reactions with atomic hydrogen is more important than *de*hydrogenation through FUV photo-dissociation (Tielens et al. 1987; Allamandola et al. 1989; Jochims et al. 1994, 1999; Allain et al. 1996). With a typical PAH size of 50 C-atoms (Tielens et al. 2000), dehydrogenation should therefore be minimal and no effect on the PAH spectrum should be seen.

Observationally, the degree of dehydrogenation can be probed best by the features in the 10 - 15 μm region. The peak position and strength of the PAH features present in this range depend on the structure of the molecule and then in particular on the number of neighbouring H-atoms per ring (e.g. Bellamy 1958; Hudgins & Allamandola 1999; Hony et al. 2001). Isolated CH groups on the aromatic ring are termed 'solo' CH groups, two adjacent CH groups 'duet' CH groups, and so on. Other ways to assess the degree of dehydrogenation include a non-linear behaviour between the 3.3 and 11.2 μm PAH features upon dehydrogenation (Hony et al. 2001) and the change in the ratio of the CC and CH modes.

In their observational study, Hony et al. (2001) conclude that dehydrogenation is unimportant for the objects in their sample, which includes the Galactic sources contained in ours. The LMC source with the smallest $I_{6.2}/I_{11.2}$ ratio for which there is also a reliable 3.3 μm flux (30 Dor#3), has a $I_{3.3}/I_{11.2}$ ratio that is consistent with those found in Hony et al. (2001) implying that the PAHs in this source are not dehydrogenated. This can unfortunately not be confirmed by its 10 - 15 μm region since the PAH features there are very weak and no significant 12.7 μm feature has been detected (Sturm et al. 2000, see Section 6.4.2.4). Nevertheless, our conclusion is that the effect of dehydrogenation cannot fully account for the observed differences in the PAH-feature strengths.

6.4.2.3 Molecular size

With decreasing size of the molecules, the ratio of CC to CH bonds also decreases. This CC/CH ratio is most clearly reflected in the $I_{6.2}/I_{3.3}$ ratio, since the 3.3 μm band is produced by *all* the CH bonds. The 3.3 μm feature though is hardly detected in our ISOPHOT spectra, so we have to rely on the $I_{6.2}/I_{11.2}$ ratio.

Since the 11.2 μm band is only produced by the solo CH groups, the $I_{6.2}/I_{11.2}$ ratio is influenced by both the molecular structure as well as the size. If we assume that there is only a size effect and restrict ourselves to PAHs with more than 50 carbon atoms, the lower $I_{6.2}/I_{11.2}$ ratio observed in the 30 Doradus and the SMC would at first suggest that the PAHs are smaller than those in the Galaxy and the non-30 Dor LMC sources (Schutte et al. 1993). However, the position with the lowest $I_{6.2}/\Sigma$ PAH and $I_{6.2}/I_{11.2}$ ratio (30 Dor#3) has a $I_{6.2}/I_{3.3}$ ratio that is consistent with the range observed for the Galactic H II regions. This would suggest that differences in molecular size are not responsible for the observed PAH-feature strengths.

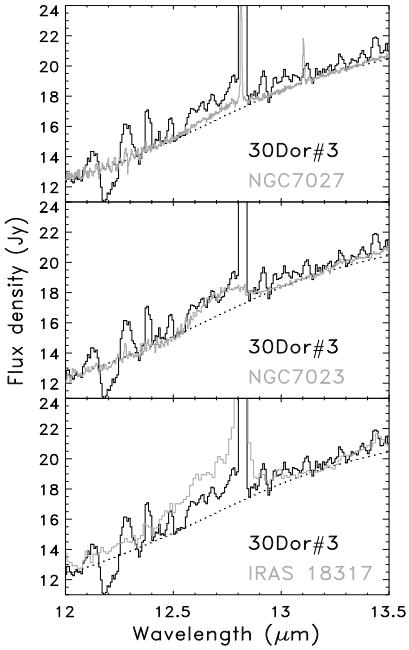

FIGURE 6.6— A comparison between the 12.7 μm feature of 30 Dor#3 and the scaled 12.7 μm feature of NGC 7027 (top), NGC 7023 (middle) and IRAS 18317 (bottom). The scaling is such that the 11.2 μm feature is equally strong in all spectra. The 30 Dor#3 spectrum is shown in solid black and the scaled spectra in grey. The dotted line represents the continuum.

6.4.2.4 *Molecular structure*

As was already mentioned in section 6.4.2.2, the strength of the PAH features in the 10 - 15 μm region depends on the number of neigbouring CH groups. The strength of the 11.2 μm feature, and hence the $I_{6.2}/I_{11.2}$ ratio, is therefore influenced by the molecular structure. If the observed trend in this ratio were only due to the molecular structure, this would imply that the PAH emission in the SMC source and 30 Doradus is dominated by 'smooth-edged' species (the so-called 'compact' species in Hony et al. 2001 which have long straight edges and few corners) while open, 'rough-edged' structures (the so-called open, uneven species in Hony et al. 2001 with many corners) are the dominant ones in the Galactic and non-30 Doradus H II regions. To have a strong handle on this, the features in the 10-15 μm spectral region are indispensible.

We carefully re-examined the spectrum of 30 Dor#3. A hint of the 12.7 μm feature is found, but it is clearly no 3 σ detection. In order to get a feeling for the $I_{12.7}/I_{11.2}$ ratio, we took the spectra from Hony et al. (2001) with the lowest and highest $I_{12.7}/I_{11.2}$ ratio and scaled them in such a way that their 11.2 μm feature is as strong as in the 30 Dor#3 spectrum (see Figure 6.6). It is obvious from Fig. 6.6 that for the Galactic source with the highest $I_{12.7}/I_{11.2}$ ratio (IRAS 18317), the scaled 12.7 μm feature cannot be hidden in the noise of the spectrum of 30 Dor#3. The same is not true, however, for the Galactic source with the lowest $I_{12.7}/I_{11.2}$ ratio (NGC 7027). The source with a similar $I_{12.7}/I_{11.2}$ ratio as 30 Dor#3, is the reflection nebula NGC 7023, which is an intermediate in the range of $I_{12.7}/I_{11.2}$ ratios studied by Hony et al. (2001). We can therefore conclude that the PAHs in 30 Dor#3 are certainly more compact when compared to those in IRAS 18317 and are probably similar to those in NGC 7023.

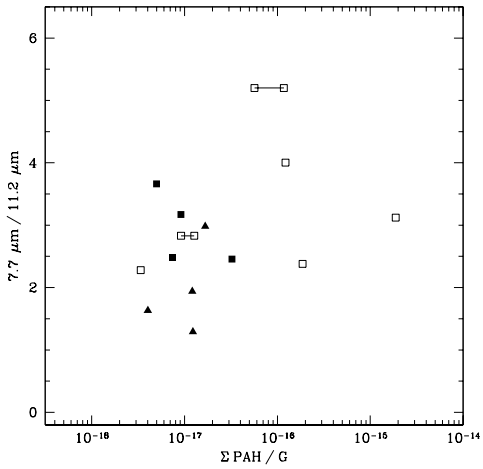

FIGURE 6.7— The correlation between the $I_{7.7}/I_{11.2}$ ratio and the Σ PAH / G ratio. The full lines join the Σ PAH / G as derived using both the near and far solar distance.

The quiescent molecular cloud SMC B1#1 exhibits a strong 12.7 μm feature (Reach et al. 2000). The observed $I_{12.7}/I_{11.2}$ and $I_{6.2}/I_{11.2}$ ratios for this source also point towards species that are more compact compared to those in the Galactic H II regions (Hony et al. 2001).

We can summarize our conclusions by stating that the few observations present to date point towards the dominance of compact PAH species in the SMC and 30 Doradus while open uneven structures are the dominant ones in Galactic H II regions and the non-30 Dor LMC sources.

6.4.2.5 PAH/dust abundance

An indicator of the PAH/dust abundance is the ratio between the total emission in the PAHs and the far-infrared (FIR) emission. We derived the FIR emission from LWS spectra of the objects (Vermeij et al. 2002; Peeters et al. 2002a). The Σ PAH / FIR ratios are very similar for the Galactic and LMC sources except that the four pointings towards 30 Doradus show lower values. However, the LWS aperture is much larger compared to the ISOPHOT and ISO-SWS apertures. This ratio will therefore be influenced by the aperture differences for sources more extended than the mid-IR beam or for sources which are not isolated. It is quite certain that the mid-IR and FIR beams receive radiation from different regions in 30 Doradus. After correcting for the aperture difference (assuming a uniform, infinitely extended source), the Σ PAH / FIR ratios for the 30 Doradus observations are similar to the ratio of the other sources. Note, however, that some of the other sources are not isolated or are more extended then the mid-IR beam (but certainly smaller then the FIR beam) and could therefore suffer from the same problem.

If we assume that all the UV radiation absorbed by the dust is re-emitted in the IR, the Σ PAH/G ratio is an additional indicator for the PAH/dust abundance. As can be seen in Figure 6.7, the Σ PAH/G ratio in the LMC lies at the lower end of the range covered by our sample H II regions. Both the 30 Doradus and non-30 Doradus observations have a similar Σ PAH/G ratio. The PAH/dust abundance thus appears

to be very similar for the LMC sources. However, the difference in the Σ PAH/G ratio between the Magellanic Cloud and Galactic sources seems significant.

It is currently believed that PAHs form either as byproducts or intermediares in soot formation (Frenklach & Freigelson 1989, Cherchneff et al. 1992) or as shattering products of grains (Jones et al. 1996). Apparently, the differences in metallicity and general conditions in the ISM or in soot-forming regions have some influence on the PAH/dust ratio.

6.5 Summary

In this chapter, a set of ISOPHOT spectra from H II regions in the Large Magellanic Cloud has been presented. In all the spectra, emission bands arising from Polycyclic Aromatic Hydrocarbons (PAHs) were clearly present. These features are observed to vary considerably in relative strength to each other from source to source and even within 30 Doradus. The LMC spectra have been compared with ISO-SWS spectra from Galactic H II regions and with an ISOCAM observation towards a quiescent molecular cloud in the SMC (Reach et al. 2000).

A correlation was found between the $I_{7.7}/I_{11.2}$ versus $I_{6.2}/I_{11.2}$ ratios and the $I_{8.6}/I_{11.2}$ versus $I_{6.2}/I_{11.2}$ ratios. A segregation between the sources of different type of environment, i.e. from the Milky Way to the LMC and the SMC, is present. Furthermore, within the LMC observations, a clear distinction between 30 Doradus and the non-30 Doradus pointings was found. The relative strengths of the IR emission features, therefore, correlate with the local environment.

A similar sequence was found for the 2175 Å bump strength, which decreases in strength from the Milky Way to the non-30 Dor pointings, the 30 Dor pointings and is even completely absent in the SMC (e.g. Rodrigues et al. 1997). Since the lines-of-sight for the extinction derivation and for our ISOPHOT observations were very similar, this suggests that the same conditions responsible for the observed trends in the relative PAH-feature strengths probably also affect the carrier of the 2175 Å bump leading to the differences in strength of the latter.

We have discussed the different factors that influence the spectra and might explain the observed variations. Most important of these factors is the ionization balance of the PAHs which showed no difference between the Magellanic and Galactic sources. The Σ PAH/G ratio, which is an indicator of the PAH/dust abundance, appeared to be very similar for the LMC sources, but the difference in the Σ PAH/G ratio between the Magellanic Cloud and Galactic sources seemed significant. The differences in metallicity and general conditions in the ISM or in soot-forming regions have apparantly some influence on the PAH/dust ratio.

The few observations present to date point towards the molecular structure as the major cause of the observed variations. Compact PAH species dominate in the SMC and in 30 Doradus, while PAH species with an open, uneven structure are the dominant ones in Galactic H II regions and in the non-30 Dor LMC sources. This may reflect the effects of the local physical conditions on the composition and characteristics of the family of PAH molecules present in the source.

Acknowledgements

PIA is a joint development by the ESA Astrophysics Division and the ISO-PHT consortium.

References

Acosta-Pulido, J.A., Ábrahám, P. 2001 ESA SP-481 *The calibration legacy of the ISO mission* in press, eds. Metcalfe, L. and Kessler, M.F.K.
Allain, T., Leach, S., Sedlmayr, E. 1996, A&A **305**, 616
Allamandola, L.J., Tielens, A.G.G.M., Barker, J.R. 1985, ApJ **290**, L25
Allamandola, L.J., Tielens, A.G.G.M., Barker, J.R. 1989, ApJS **71**, 733
Allamandola, L.J., Hudgins, D.M., Sandford, S.A. 1999, ApJ **511**, L115
Bakes, E.L.O., Tielens, A.G.G.M., Bauschlicher, C.M. 2001, ApJ **556**, 501
Bellamy, L. 1958 in *The infrared spectra of complex molecules* 2nd edition, John Wiley & Sons, Inc., New York
Borgman, J., van Duinen, R.J., Koorneef, J. 1975, A&A **40**, 461
Bosselli, A. et al. 1997, A&A **324**, L13
Cesarsky, D., Jones, A. P.,Lequeux, J.,Verstraete, L. 2000, A&A **358**, 708
Clayton, G.C., Martin, P.G. 1985, ApJ **288**, 558
Cherchneff, I., Barker, J.R., Tielens, A.G.G.M. 1992, ApJ **401**, 269
Cohen, M., Dopita, M.A., Schwartz, R. 1986, ApJ **302**, 737
Cohen, M., Tielens, A.G.G.M., Bregman, J. et al. 1989, ApJ **341**, 246
Cole, A.A., Nordsieck, K.H., Gibson, S.J., Harris, W.M. 1999, AJ **118**, 2280
Contursi, A., Lequex, J., Hanus, M. et al. 1998, A&A **336**, 662
Contursi, A., Lequex, J., Cesarsky, D. et al. 2000, A&A **362**, 310
Fitzpatrick, E.L. 1985, ApJ **299**, 219
Fitzpatrick, E.L. 1986, AJ **92**, 1068
Frenklach, M. & Feigelson, E.D. 1989, ApJ **341**, 372
Geballe, T.R., Lacy, J.H., Persson, S.E. et al. 1985, ApJ **292**, 500
Gillett, F.C., Forrest, W.J., Merrill, K.M. 1973, ApJ **183**, 87
Helou, G. 1999, ESA SP-427 *The Universe as seen by ISO* p. 727, eds. P. Cox
Henize, K.G. 1956, ApJS **2**, 315
Hony, S., Van Kerckhoven, C., Peeters, E. et al. 2001, A&A **370**, 1030
Hudgins, D.M. & Allamandola, L.J. 1999, ApJ **516**, L41
Joblin, C., Léger, A., Martin, P. 1992, ApJ **393**, 79
Jochims, H.W., Ruhl, E., Baumgärtel, H., Tobita, S., Leach, S. 1994, ApJ **420**, 307
Jochims, H.W., Baumgärtel, H., Leach, S. 1999, ApJ **512**, 500
Jones, A.P., Tielens, A.G.G.M., Hollenbach, D.J. 1996, ApJ **469**, 740
Koornneef, J., Code, A.D. 1981, ApJ **247**, 860
Langhoff, S.R. 1996, J. Phys. Chem. A **100**, 2819
Léger, A., Puget, J.L. 1984, A&A **137**, L5
Léger, A., Puget, J.L. 1989, ARA&A **27**, 161
Lutz, D., Spoon, H.W.W., Rigopoulou, D. et al. 1998, ApJ **505**, L103
Martín-Hernández, N.L., Peeters, E., Damour, F. et al. 2002, A&A **381**, 606
Massey, P, Hunter, D.A. 1998, ApJ **493**, 180

Moutou, C., Verstraete, L., Sellgren, K., Léger, A. 1999, ESA SP-427 *The Universe as seen by ISO* p. 727, eds. P. Cox
Nandy, K., Morgan, D.H., Willis, A.J., Wilson, R., Gondhalekar, P.M. 1981, MNRAS **196**, 955
Pauzat, F., Talbi, D., Ellinger, Y. 1997, A&A **319**, 318
Peeters, E., Martín-Hernández, N.L., Damour, F. et al. 2002a, A&A **381**, 571
Peeters, E., Hony, S., Van Kerckhoven, C. et al. 2002b, A&A **390**, 1089
Prévot, M.L., Lequeux, J., Maurice, E., Prévot, L., Rocca-Volmerange, B. 1984, A&A **132**, 389
Puget, J.L., Léger, A. 1989, ARA&A **27**, 161
Reach, W.T., Boulanger, F., Contursi, A., Lequeux, J. 2000, A&A **361**, 895
Roche, P.F., Aitken, D.K., Smith, C.H. 1989, MNRAS **236**, 485
Rodrigues, C.V., Magalhães, A.M., Coyne, G.V., Piirola, V. 1997, ApJ **485**, 618
Schutte, W.A., Tielens, A.G.G.M., Allamandola, L.J. 1993, ApJ **415**, 397
Sturm, E., Lutz, D., Tran, D. et al. 2000, A&A **358**, 481
Tielens, A.G.G.M., Allamandola, L.J., Barker, J.R., Cohen, M.J. 1987, in *Polycyclic Aromatic Hydrocarbons and Astrophysics* p. 273
Tielens, A.G.G.M., Van Kerckhoven, C., Peeters, E., Hony, S. 2000, IAUS **197**, 349
Vacca, W.D., Garmany, C.D., Shull, J.M. 1996, ApJ **460**, 914
Vermeij, R., Damour, F., Van der Hulst, J.M., Baluteau, J.-P. 2002, A&A **390**, 649
Verstraete, L, Puget, J.L., Falgarone, E., Drapatz, S., Wright, C.M., Timmerman, R. 1996, A&A **315**, L337
Wolfire, M.G., Tielens, A.G.G.M., Hollenbach, D. 1990, ApJ **358**, 116

Chapter 7

Summary and outlook

Several aspects of the physical structure of H II regions have been addressed in this thesis. Focussing on the role of these regions as probes of the interstellar medium, the work presented covered the various ways in which an H II region can be used as an astrophysical tool through careful analysis of its spectrum. A flexible tool that can be used to gain insight into the nature of the engine at the core of the H II region, or to investigate the properties of its body of ionized gas. Centerstage in this work, however, was the H II region in its capacity of probe of the local gas-phase abundances.

The use of H II regions in their role as an astrophysical tool relies heavily on the fields of atomic physics and radiative transfer; it is the combination of these two fields that provides us with the necessary building blocks on which any analysis of a nebular spectrum is based. It is these elementary building blocks which have been our main concern, and the main goal of this thesis was to evaluate them critically.

7.1 Summary

The first part of this thesis dealt with the gas-phase elemental abundances and the analysis steps needed to derive these. The core data set upon which this work is based was presented in chapter 2. The data set comprises new optical as well as infrared spectra. The optical spectra have been obtained with the ESO 1.52m telescope, and the infrared spectra with the spectrometers on board the *Infrared Space Observatory* (Kessler et al. 1996). The sample objects were introduced in this chapter, and an account was given of the reduction of the data. The major sources of uncertainty in the data and their impact on the analysis were discussed. The main problem limiting the accuracy of the analysis lies in the large number of different beams and apertures of the instruments used in obtaining the data.

The abundance analysis was presented in chapter 3. Giving an in-depth discussion of every single analysis step, we derived improved gas-phase abundances for our sample objects. Using as many different optical/optical and infrared/infrared line-ratios as possible, we derived the run of the electron density and temperature throughout the nebula. In the derivation of the ionic fractions, care was taken to use the appropriate electron density and temperature. Theoretical relations between the various electron

temperatures often used in abundance studies were confronted with our temperature results and were found to agree well. The full elemental abundances could in many cases be calculated without using ionization correction factors (ICFs), which allowed us to check the commonly used recipes for the sulfur and neon ICFs. We found the ICF for the important element sulfur from Stasińska (1978) with $\alpha = 3$ to be fairly accurate for $O^+/O > 0.2$, but its validity for $O^+/O < 0.2$ was less clear. Given the uncertainty in the neon abundance, no reliable comparison with the ICF for neon could be made. Combining our spectra with the newly derived abundances, we checked the robustness of the 'bright-line' abundance indicators R23 and S23(4) for spatial undersampling of the sample objects and variations in their spatial extent. These indicators showed themselves to be very robust to these effects. The availability of the [S IV] 10.5 μm line in our data base and the S^{+3} ionic fraction derived from this line allowed us to calibrate the S234 parameter empirically. The parameter turned out to be very well constrained and almost completely insensitive to the ionization parameter. We ended this chapter by discussing briefly the heavy element-to-oxygen ratios found.

In chapter 4, we gave a detailed case study of the giant LMC H II region 30 Doradus. With 35 spectral positions densely covering the core of the nebula, the spatial variation of the chemical composition of the nebula and of several diagnostic line ratios was investigated. We found 30 Dor to be chemically homogeneous and isothermal. The latter confirmed the result from Krabbe & Copetti (2002). We did, however, find an apparent gradient in the nitrogen abundance which we explained as the result of line-of-sight effects in the spatially resolved ionization structure of the nebula (Gruenwald & Viegas 1992, 1998; Alexander & Balick 1997). Similar gradients have also been observed in planetary nebulae (Balick et al. 1994), but these could also be explained by invoking line-of-sight effects. An important theme underlying this chapter was the contrast between spatially resolved and unresolved data, and how the differences between the two types of data can affect the analysis results. We found that, despite the complex morphology of 30 Dor, diagnostic tools such as the 'bright-line' abundance indicators turn out to be very robust and constant across the nebula, which underlines their usefulness in the case of the analysis of a spatially unresolved nebula.

The issue of the stellar content of an H II region and how this is reflected in the spectral characteristics of the nebula was the subject of chapter 5. We investigated the connection between the nebular metallicity, the stellar metallicity, and the spectral energy distribution (SED) of the ionizing source, and how the interplay of these three affects the ionization structure of the nebula. To cover as wide a range in excitation and nebular metallicity as possible, we combined the Magellanic sample of objects with the Galactic sample from Peeters et al. (2002). The interpretation of the nebular spectrum in terms of the stellar content of the nebula is based on photoionization modelling, and depends strongly on the stellar atmosphere used in the modelling and to the stellar parameters attributed to this atmosphere (i.e. effective temperature and spectral type). We found that several factors conspire to make the identification of the stellar content based on modelling dubious. First of all, depending on the choice of stellar model grid (e.g. CoStar or Pauldrach01), different results for the stellar content of a nebula can be obtained while predicting the same nebular spectrum. The differences between the stellar model grids are the result of how the influence of the stellar metallicity on the SED is taken into account. Secondly, having chosen a particular grid, it is

important to match the stellar and nebular metallicity. Failing to do so leads to a misinterpretation of the effective temperature of the ionizing source(s). On top of this, the effective temperature assigned to the various stellar models and their spectral classification were found to be deficient. We concluded that a proper matching between the nebular metallicity on the one hand and the metallicity of the stellar atmosphere used in the modelling on the other hand is of crucial importance for a good analysis. These findings have repercussions for the age estimates of starbursts, which are based on photoionization modelling of the observed spectrum.

Based on ISOPHOT spectra of our objects, we investigated the properties of Polycylic Aromatic Hydrocarbons (PAHs) in the low-metallicity environment of the LMC in chapter 6. We compared the relative PAH-feature strengths from our sample with those of a subsample of Galactic H II regions from Peeters et al. (2002). The SMC was represented in the sample by observations of the molecular cloud SMC B1#1 (Reach et al. 2000). Several correlations between the different PAH-feature strengths were observed which were interpreted in terms of the molecular structure of the carrier. In all these correlations we noticed the same separation of the sample sources going from the SMC to the LMC to the Milky Way. Furthermore, the 30 Dor spectra were in all cases clearly separated from the other LMC sources. We concluded that the molecular structure of the PAHs in the LMC is similar to that of the PAHs in our Galaxy, but that the PAHs in 30 Doradus are more compact than in the other LMC sources. We also observed an anticorrelation between the relative PAH-feature strengths and the strength of the 2175 Å bump in the extinction curves towards our sources. Although the carrier of the 2175 Å bump has not yet been identified, it appears that the conditions that affect the PAHs also seem to affect the carrier of this bump.

7.2 Future work

It may have become clear that the combination of different spectral regimes is essential for a full and detailed analysis of the structure of a nebula. However, one important condition has to be met in order for this spectral information to be exploited to the fullest. This condition is that the various spectral lines used in the analysis must be 'compatible', i.e. over the full spectral range the slit or aperture used in the observation must cover the same part of the nebula. This is especially important when using several spectral lines from one and the same ionic species. The often unavoidable use of many different instruments in obtaining the necessary data, however, makes it difficult to meet this requirement.

One of the longstanding problems in the study of nebulae is that of small-scale temperature fluctuations in a given ionization zone. Even after decades of study, the size of these fluctuations and their origins are not completely clear. Given the importance of an accurately known electron temperature for abundance studies, this is a serious problem. Deriving the electron temperature from different combinations of spectral lines from one and the same ion makes it, in principle, possible to measure these temperature fluctuations. Prerequisite for this to work, however, is that the different spectral lines can be combined in a meaningful way (see previous paragraph).

Scheduled for launch at the beginning of 2003, the *Space Infrared Telescope Facility* (SIRTF) will include, amongst others, a spectrograph. This instrument, the Infrared

Spectrograph (IRS), will provide spectral coverage over the range from 5 μm to 40 μm. The most interesting feature of this instrument is its longslit design capable of making 2D-spectra in the infrared. Spatial information is retained in these spectra just as in the case of optical 2D-spectra. It is therefore in principle possible to obtain a combined optical/infrared data set that at least goes a long way at fullfilling the requirement of overall compatibility.

Another mission that could also be of interest in this respect is the *Next Generation Space Telescope* (NGST). Although with its launch date still far in the future and with many features still under development, the telescope will have spectroscopic capabilities covering a continuous spectral range from 0.6 μm to $\sim$30 μm. This continous coverage will remove many of the ambiguities that come with using separate instruments for the optical and infrared, and in combination with its 8 meter primary mirror, this will allow us to perform accurate nebular studies in galaxies at higher redshift, where the optical regime and a significant part of the adjoining infrared will be shifted into the spectral window covered by NGST.

Although space-borne instruments play an increasingly important role in present-day research, groundbased optical spectroscopy is still important. As was mentioned several times throughout this thesis, the major ingredient needed to derive a reliable metallicity is the electron temperature. However, the important [O III] 4363 Å line needed to derive this parameter is unfortunately quite often too weak. This is either because the galaxy is too far away to measure this line reliably, or because of the high metallicity of the galaxy which suppresses the line. This is a major problem, both for the study of chemical abundances in galaxies at cosmological distances as well as for tracing the spatial variations in the metallicity throughout a galaxy into the high-metallicity regime. With several telescopes in the 8+ meter class coming on line or already in use, these problems can largely be solved, not only because of the larger ligh-collecting areas of these telescopes but also because of the higher spectral resolutions allowed.

References

Alexander, J., Balick, B. 1997, AJ **114**, 713
Balick, B., Perinotto, M., Maccioni, A., Terzian, Y., Hajian, A. 1994, ApJ **424**, 800
Gruenwald, R.B., Viegas, S.M. 1992 ApJS **78**, 153
Gruenwald, R.B., Viegas, S.M. 1998, ApJ **501**, 221
Kessler, M.F., Steinz, J.A., Anderegg, M.E. et al. 1996, A&A **315**, L27
Krabbe, A.C., Copetti, M.V.F. 2002, A&A **387**, 295
Peeters, E., Martín-Hernández, N.L., Damour, F. et al. 2002, A&A **381**, 571
Reach, W.T., Boulanger, F., Contursi, A., Lequeux, J. 2000, A&A **361**, 895
Stasińska, G. 1978, A&A **66**, 257

List of publications

Publications in refereed journals

The physical structure of Magellanic Cloud H II regions I. Dataset
Vermeij, R., Damour, F., Van der Hulst, J.M., Baluteau, J.-P 2002, A&A, 390, 649

The physical structure of Magellanic Cloud H II regions II. Elemental abundances
Vermeij, R., Van der Hulst, J.M. 2002, A&A, in press

The stellar content, metallicity and ionization structure of H II regions
Martín-Hernández, N.L., Vermeij, R., Tielens, A.G.G.M., Van der Hulst, J.M., Peeters, E. 2002, A&A, 389, 286

The PAH emission spectra of Large Magellanic Cloud H II regions
Vermeij, R., Peeters, E., Tielens, A.G.G.M., Van der Hulst, J.M. 2002, A&A, 382, 1042

Publications in conference proceedings

SWS Observations of H II regions in the Magellanic Clouds
Van der Hulst, J.M., Vermeij, R. 1997 in the Proc. of the 'First ISO Workshop on Analytical Spectroscopy', ESA SP-419

The physical structure of Magellanic Cloud H II regions
Vermeij, R., Van der Hulst, J.M. 1999 in the Proc. of 'The universe as seen by ISO' conference, ESA SP-427

Nederlandse samenvatting

Wie zich op een heldere winteravond wel eens buiten heeft gewaagd en in de richting van het sterrenbeeld Orion heeft gekeken zal het vast niet zijn ontgaan dat er zich vlak onder de gordel van Orion een vage vlek bevindt. Als we deze vlek bekijken door een kleine sterrenkijker blijkt deze een complexe structuur te hebben en zijn kleine kluitjes van sterren zichtbaar. Deze vlek die bekend staat als de Orion nevel (zie Fig. 7.1) is hoogstwaarschijnlijk het meest beroemde voorbeeld van een stervormingsgebied: een kraamkamer van recentelijk gevormde sterren.

Sterren kennen een levenscyclus van geboorte, leven en dood; geboren uit het interstellaire gas, stralen sterren voor enige tijd om vervolgens op meer of minder gewelddadige wijze te sterven. Sterren ontstaan nooit geïsoleerd maar in grote groepen tegelijk, en de leden van een dergelijke groep variëren onderling sterk in massa. De meeste sterren hebben een kleine massa, vergelijkbaar met of zelfs kleiner dan die van onze Zon. Een zeer select deel van de groep echter is aanzienlijk zwaarder dan dat, tot wel 100 keer zwaarder dan de Zon, en het zijn deze zwaargewichten onder de sterren die de hoofdrol spelen in de rest van het verhaal.

Direct nadat de meest massieve sterren zich hebben bevrijd uit hun geboortecocon beginnen deze hun omgeving drastisch te veranderen. De oppervlaktetemperatuur van deze sterren is behoorlijk hoog, meer dan 40 000 °C is vrij normaal, en deze sterren stralen dan ook een enorme hoeveelheid energie uit. Het grootste deel van deze energie wordt uitgestraald op golflengtes die korter zijn dan waargenomen kan worden met het oog, namelijk in het ultraviolet. Figuur 7.2 geeft een overzicht van het volledige bereik van het electromagnetische spectrum. Als gevolg van de hoge helderheid van deze sterren in het ultraviolette deel van het spectrum wordt het lokale moleculaire gas afgebroken tot losse atomen en worden deze losse atomen vervolgens nog eens beroofd van hun buitenste electronen. Dit laatste proces wordt ionisatie genoemd, en de aldus van hun electronen beroofde atomen noemen we ionen. De sterren creëren zo voor zichzelf een omgeving van geïoniseerd gas.

Het meest voorkomende en tevens lichtste element in het heelal is waterstof (chemisch symbool H). Het grootste deel van het geïoniseerde gas bestaat uit waterstof, en het is dit geïoniseerde waterstofgas waaraan stervormingsgebieden hun naam ontlenen: H II gebieden (spreek uit H-twee). Het licht dat het H II gebied zijn karakteristieke rode kleur geeft wordt geproduceerd wanneer het kale waterstofion zijn verloren electron terugwint.

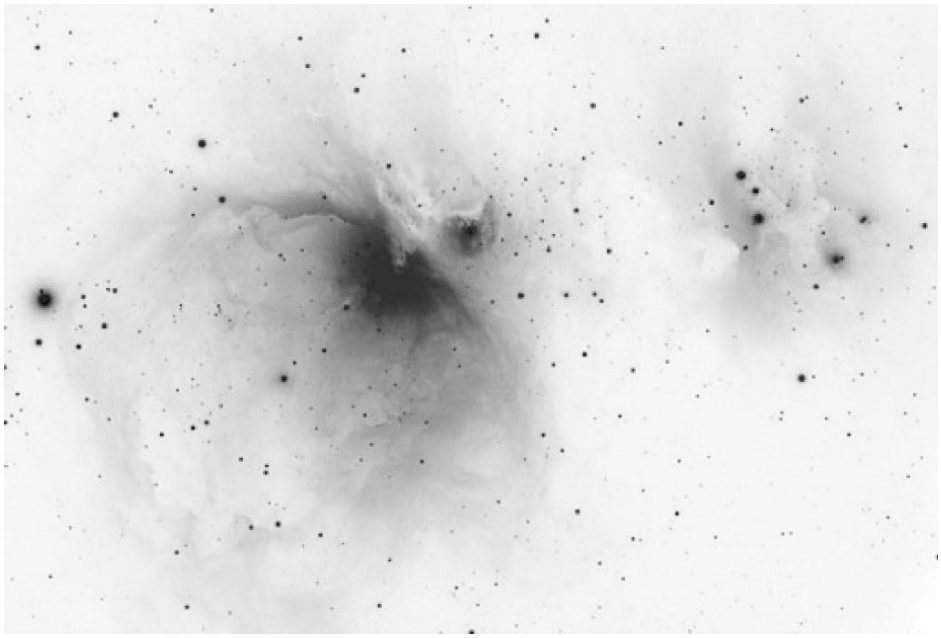

FIGUUR 7.1— Het meest beroemde voorbeeld van een H II of stervormingsgebied: de Orion nevel.

De levensloop van een massieve ster

Over de hele Melkweg verspreid treffen we grote wolken van moleculair gas aan. Deze wolken bestaan voornamelijk uit simpele moleculen als koolstofdioxide en moleculair waterstof, zijn zeer koud (hooguit enige tientallen graden boven het absolute nulpunt) en hebben een hoge dichtheid. Het zijn nu precies deze moleculaire wolken waaruit sterren worden gevormd.

Het stervormingsproces begint op het moment dat een moleculaire wolk onder het eigen gewicht begint in te storten. Tijdens dit proces breekt de wolk in allemaal kleine klonten die vervolgens nog verder samentrekken. Ieder van deze klonten afzonderlijk vormt de kiem van een toekomstige ster. Bij het samentrekken van een dergelijke klont nemen de dichtheid en de temperatuur van het gas continue toe en vormt er zich uiteindelijk een protoster. Deze protoster blijft verder krimpen totdat de temperatuur en dichtheid in het centrum van de protoster hoog genoeg zijn opgelopen om de primaire energiebron van iedere ster op te starten: kernfusie. Bij dit proces wordt in de kern van een ster energie geproduceerd door simpele, lichte atoomkernen samen te laten smelten tot zwaardere elementen. Vanaf dit moment kunnen we spreken van een echte ster.

Een ster brengt het grootste deel van haar leven door met het rustig omzetten van waterstof in helium. Echter, op een bepaald moment raakt deze primaire brandstof uitgeput waarop de energieproductie stagneert. Voor het soort massieve ster waarover

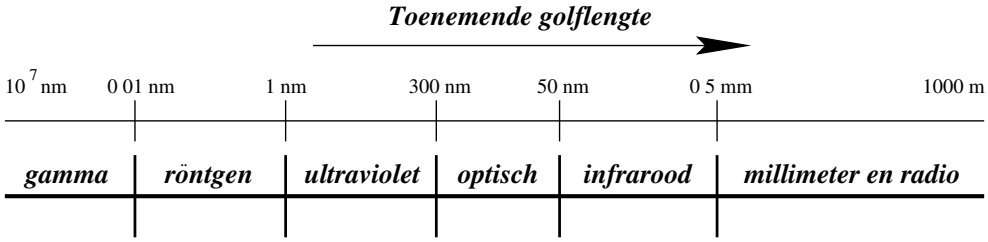

FIGUUR 7.2— Het electromagnetisch spectrum van gamma-stralen tot radiogolven. De voor H II gebieden meest interessante gedeelten zijn het ultraviolet, optisch en infrarood.

we hier praten gebeurt dat al na een paar miljoen jaar. De ster reageert op dit gebrek aan brandstof met een stevige reorganisatie van haar inwendige structuur en schakelt over op een zwaarder type brandstof; waar voorheen waterstof werd gefuseerd tot helium wordt nu het helium zelf als brandstof gebruikt. De fusie van waterstof gaat op bescheiden schaal door in een dunne schil net buiten de kern van de ster. Dit proces herhaalt zich een aantal keer waarbij een steeds zwaardere brandstof wordt gebruikt net zolang totdat er geen enkele brandstof meer voorhanden is.

Aangekomen op dit punt is de ster geheel verstoken van enig bron van energie en stort de kern van deze onder invloed van de zwaartekracht in elkaar. Tegelijkertijd worden de buitenlagen van de ster met heel veel geweld het heelal ingeslingerd in een explosie die bekend staat als een supernova. Wat overblijft van de ster is een neutronenster of een zwart gat. Door de supernova-explosie worden de fusieproducten die zich hebben opgehoopt in de ster toegevoegd aan het interstellaire gas waar het zich vermengd met het al aanwezige gas. Het aldus met zware elementen verrijkte gas staat aan de basis van een nieuwe generatie van sterren en de hele cyclus van stervorming en sterdood herhaald zich.

Spectrale en fysische eigenschappen

Naast watersof bevat het gas in een H II gebied ook sporen van zwaardere elementen zoals stikstof, zuurstof, zwavel en neon. In tegenstelling tot waterstof dat slechts één electron kan verliezen tijdens de ionisatie, beschikken deze zwaardere elementen over meer electronen. Bijgevolg kunnen deze dan ook meerdere malen worden geïoniseerd. Het element zuurstof bijvoorbeeld kan van één electron zijn beroofd maar ook van twee. Deze verschillende stadia van ionisatie (ionisatietrappen) kunnen naast elkaar bestaan in een H II gebied. Door het hele H II gebied heen vinden we dan ook een mix van elementen in allerhande verschillende ionisatietrappen. Deze mix duiden we collectief aan als de ionisatiestructuur van de nevel.

De grote aantrekkingskracht van H II gebieden als studieobject komt voort uit het ongelooflijk rijke spectrum dat wordt uitgezonden door het geïoniseerde gas. Van het verre infrarood helemaal tot aan het extreme ultraviolet wordt het spectrum gedomineerd door nauwe emissielijnen. Elk van deze emissielijnen vormt een vingerafdruk van een chemisch element in één van zijn verschillende ionisatietrappen. Het zijn deze lijnen die de astronoom in staat stellen om verschillende parameters van het geïoniseerde gas

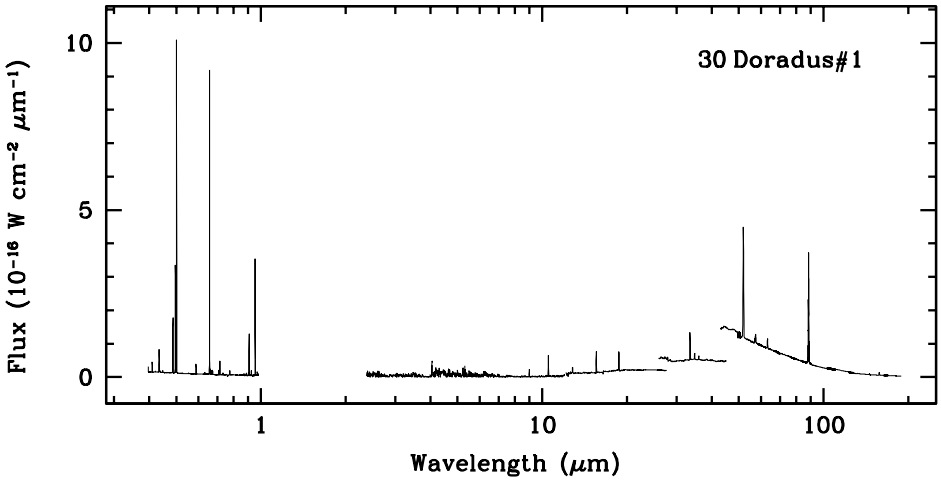

FIGUUR 7.3— Een voorbeeld van een emissielijn-spectrum waarbij het optische en het infrarode deel van het electromagnetische spectrum zijn gecombineerd. Iedere 'spike' verraadt de aanwezigheid van een bepaald ion. De golflengte uitgezet op de horizontale as is in eenheden van 0.001 millimeter.

te bepalen en zich zo een beeld te vormen van de fysische structuur van het H II gebied. Een mooi voorbeeld van een spectrum waarin het optische en infrarode deel van het electromagnetische spectrum zijn gecombineerd is gegeven in Fig. 7.3.

De belangrijkste stukjes informatie die men kan verkrijgen uit het spectrum van een H II gebied zijn de variatie van de temperatuur en dichtheid van het gas door het H II gebied heen, de ionisatiestructuur van het gebied, en de chemische samenstelling van het plaatselijk aanwezige gas. Op een meer indirecte wijze geeft de ionisatiestructuur van de nevel inzicht in het soort ster dat gevormd is in het stervormingsgebied.

Het astrofysische belang van H II gebieden

Zoals al werd genoemd in de sectie over de levensloop van massieve sterren wordt het gas waaruit sterren ontstaan keer op keer gerecycled. Iedere generatie van sterren voegt weer meer zwaardere elementen toe aan het interstellaire gas. De lokale chemische compostitie van het gas zegt ons dan ook iets over de lokale stervormingsgeschiedenis. Deze compositie nu vinden we terug in het spectrum van een H II gebied. Door een dergelijk spectrum nauwkeurig te analyseren kunnen we dan ook de lokale chemische compositie achterhalen en vervolgens herleiden tot een lokale stervormingsgeschiedenis.

Niet alleen op lokaal niveau maar ook op de schaal van hele sterrenstelsels spelen H II gebieden een belangrijke rol bij het sonderen van de eigenschappen van het interstellaire gas. Sterrenstelsels zijn grote collecties van sterren die op grond van hun vorm ruwweg in drie groepen ingedeeld kunnen worden. De eerste groep bestaat uit elliptische stelsels die, zoals de naam al doet vermoeden, rond of elliptisch van vorm zijn. De tweede groep

zijn de schijf- of spiraalstelsels. Deze bestaan uit een platte schijf met een verdikking in het midden. Onze eigen Melkweg behoort tot deze groep. De derde groep heeft een vorm die op geen enkele manier valt te beschrijven, en deze noemen we dan ook onregelmatige stelsels.

Doordat H II gebieden verspreid voorkomen over een sterrenstelsel is het mogelijk om de variatie van de chemische compositie van het interstellaire gas te meten door het hele sterrenstelsel heen. Dit levert inzicht in de globale stervormingsgeschiedenis van het sterrenstelsel. Bovendien leert deze variatie in chemische compositie ons iets over de mechanismen die zorgen voor de verspreiding van het gas door het sterrenstelsel.

Naast zijn betekenis als een sonde waarmee het interstellaire gas kan worden onderzocht is een H II gebied natuurlijk ook een tracer van recente stervorming. In een recent gevormd H II gebied zijn de meest massieve sterren die verantwoordelijk zijn voor het ontstaan van de nevel in het algemeen niet zichtbaar. De enige manier waarop deze sterren kunnen worden 'waargenomen' is op indirecte wijze, namelijk via hun invloed op de ionisatiestructuur van de nevel en hoe deze zich vertaalt in het spectrum van het H II gebied. Omdat deze sterren zo kort leven kunnen we ze nooit direct waarnemen, en daarom is er maar weinig bekend over de zware kant van de gewichtsverdeling van sterren. De precieze gewichtsverdeling van sterren is echter een cruciaal element in theorieën over stervorming. Via het spectrum van het H II gebied is het mogelijk om informatie hierover te achterhalen.

Problemen in de analyse

Het zal duidelijk zijn geworden uit het voorgaande dat een H II gebied een hoge waarde heeft als een diagnostisch stuk gereedschap. Dit stuk gereedschap staat echter niet op zichzelf. Om de informatie vervat in het spectrum van een H II gebied te kunnen lezen moet een zwaar beroep worden gedaan op verschillende takken van de natuurkunde. De belangrijkste van deze zijn de gebieden van de atoomfysica en van het stralingstransport. Het laatste houdt zich bezig met de interactie tussen de door het ster uitgezonden licht en het gas en hoe deze interactie de voortplanting van het licht beïnvloedt.

Het proces van de interpretatie van het spectrum van een H II gebied kent vele stappen, en het verkregen eindresultaat is sterk afhankelijk van de betrouwbaarheid van ieder van deze stappen. Eén van de belangrijkste factoren die de betrouwbaarheid van het uiteindelijke analyseresultaat beperkt is de hoeveelheid spectrale informatie die men heeft. Gaten in de analyseresultaten die voortkomen uit lacunes in de beschikbare spectrale informatie moeten worden opgevuld met 'lapmiddellen' waardoor extra onzekerheden worden geïntroduceerd in de afgeleide resultaten.

Een belangrijk voorbeeld van een situatie waarin vaak een beroep moet worden gedaan op een dergelijk 'lapmiddel' is in de bepaling van de chemische compositie van het interstellaire gas. Om de totale hoeveelheid van een gegeven element (zijn abundantie) goed te kunnen bepalen moeten alle ionisatietrappen waarin dit element kan voorkomen worden meegenomen. Echter, de spectrale informatie benodigd hiervoor is zelden tot nooit voor handen, zodat de gevonden abundantie achteraf naar boven toe moet worden bijgesteld. De grootte van deze correctie is echter heel moeilijk te bepalen.

Deze en soortgelijke problemen beperken het gebruik en het nut van H II gebieden als astrofysisch gereedschap. Om deze beperkingen op te heffen is het noodzakelijk om

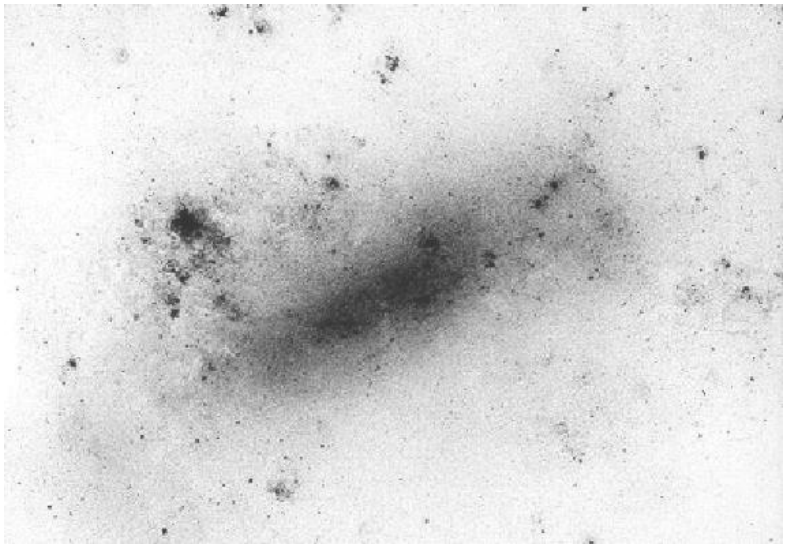

FIGUUR 7.4— Het onregelmatige sterrenstelsel de Grote Magellaanse Wolk. Dit stelsel en de onregelmatige Kleine Magellaanse Wolk zijn twee satelietstelsels van onze Melkweg. De verspreide kleine zwarte vlekken zijn H II gebieden. De grote vlek links van het midden is het reusachtige H II gebied 30 Doradus.

zoveel mogelijk spectrale informatie van een gegeven H II gebied te combineren. Een dergelijke set van gecombineerde spectrale informatie nu vormt de basis waarop dit proefschrift is gebouwd.

Inhoud van het onderzoek

In dit proefschrift belichten we diverse aspecten van het gebruik van H II gebieden als astrofysisch gereedschap. Daartoe wordt gebruik gemaakt van een set van zorgvuldig uitgekozen H II gebieden alle waargenomen in zowel het optische als het infrarode spectrale regime. Een belangrijk doel van het onderzoek bestaat uit de kritische evaluatie van de methoden die in het algemeen in de analyse van de spectra van H II gebieden worden gebruikt. Hiervoor is de combinatie van optische en infrarood spectra noodzakelijk. De infrarood spectra zijn verkregen met een Europese sateliet die vloog van 1995 tot en met 1998 : de *Infrared Space Observatory*. Door deze twee spectrale regimes met elkaar te combineren kunnen niet alleen veel van de beperkingen die het analyseresultaat nadelig beïnvloeden worden omzeild, maar is het ook mogelijk om de 'lapmiddelen' die in het algemeen gebruikt worden in de analyse aan een empirische test te onderwerpen.

De H II gebieden in onze collectie bevinden zich allemaal in de Magellaanse Wolken. Deze twee onregelmatige sterrenstelsels, de Grote en Kleine Magellaanse Wolk, zijn satellietstelsels van onze Melkweg. Deze sterrenstelsels zijn om meerdere redenen zeer geschikt voor ons doel. Ten eerste bevinden de Magellaanse Wolken zich op 'loopafstand' van ons (170 000 - 200 000 lichtjaar). Hierdoor zijn de H II gebieden in deze sterrenstelsels ruimtelijk opgelost wat een nauwkeurige studie van hun ruimtelijke structuur

mogelijk maakt. Ten tweede is de positie van de stelsels aan de hemel heel erg gunstig. Hoog verheven boven de band van sterren die we de Melkweg noemen, kunnen we de H II gebieden in deze stelsels onbelemmerd waarnemen in alle relevante spectrale gebieden. Dit is niet mogelijk in het vlak van de Melkweg zelf, waar de aanwezigheid van stof het gebruik van het optische deel van het spectrum beperkt tot H II gebieden in de buurt van de Zon. Tenslotte zijn de Magellaanse Wolken zelf interessant als studieobject in de context van stervormingsgeschiedenis; de lage verrijkingsgraad van het gas in deze stelsels met zware elementen en de hoge snelheid waarmee nieuwe sterren worden gevormd creëren een omgeving die sterk afwijkt van die in onze eigen Melkweg. Figuur 7.4 laat de Grote Magellaanse Wolk zien.

De spectrale gegevens gebruikt in dit onderzoek en de H II gebieden die zijn geobserveerd worden gepresenteerd in hoofdstuk 2 van het proefschrift. In hoofdstuk 3 gebruiken we deze gegevens voor een analyse van de chemische compositie van het gas in onze bronnen. Speciale aandacht wordt hier besteed aan de temperatuurstructuur van de bronnen en aan de correcties benodigd voor het verkrijgen van de 'volledige' abundantie van ieder element. Een uitgebreide studie van het reuze H II gebied 30 Doradus in de Grote Magellaanse Wolk wordt gepresenteerd in hoofdstuk 4. We bestuderen in dit hoofdstuk de ruimtelijke variatie door het H II gebied heen van de chemische compositie van het gas. Tevens bestuderen we hier de toepasbaarheid van verschillende spectrale diagnostische stukken gereedschap in het geval van ruimtelijk opgeloste nevels. Het gebruik van het spectrum van een H II gebied als indicator van de sterinhoud van het gebied is het onderwerp van hoofdstuk 5. De rol die gespeeld wordt door de modelsteratmosfeer gebruikt in de interpretatie staat centraal. In hoofdstuk 6 onderzoeken we de eigenschappen van een bepaalde klasse van grote organische moleculen die 'leven' op het grensgebied van het H II gebied en de moleculaire wolk waaruit de ioniserende sterren zijn gevormd. Het betreft hier Polycyclische Aromatische Koolwaterstoffen, en de belangrijkste vraag die we hier stellen is in hoeverre de drastisch andere omstandigheden in de Grote Magellaanse Wolk in vergelijking met die in de Melkweg de structuur van deze moleculen beïnvloedt. In hoofdstuk 7 wordt een samenvatting gegeven van het proefschrift en worden er suggesties gedaan voor toekomstig onderzoek.